THE EFFECT OF A BOUNDARY NEAR A TURBULENT BUOYANT JET

A thesis
submitted in partial fulfilment
of the requirements for the Degree
of
Doctor of Philosophy in Civil Engineering
at the
University of Canterbury,
Christchurch, New Zealand.

by

M. GRANT WEBBY

May 1981

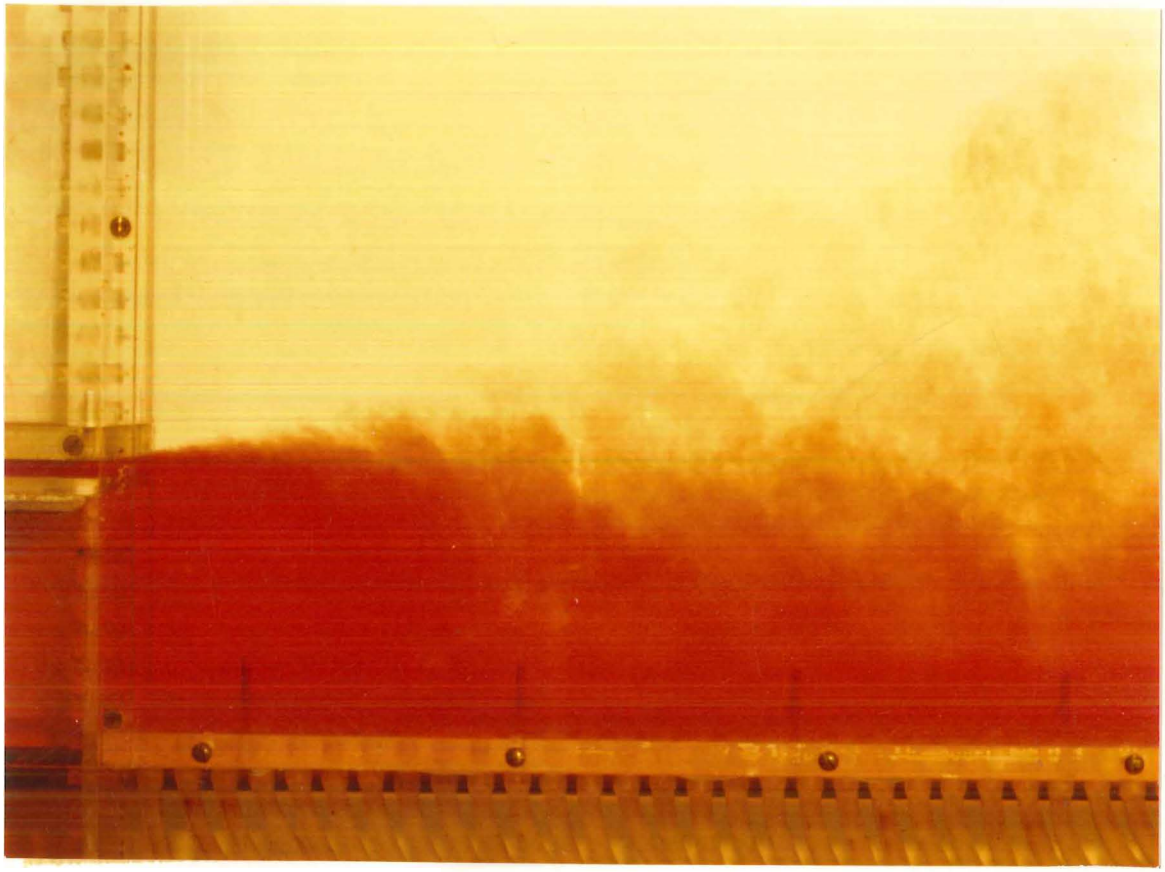

A two-dimensional attached buoyant jet
in the region of attachment.

ABSTRACT

A simple entrainment model has been developed to describe the flow configuration of an attached buoyant jet up to the point of attachment. The effect of curvature on entrainment is ignored and self-similarity of all mean profiles at all cross sections normal to the locus of maximum velocity is assumed. Momentum effects are dominant near the jet source so that initially the flow has been treated as a non-buoyant jet. An understanding of the effect of buoyancy without the added complications that it introduces is gained by studying the addition of a passive tracer to the non-buoyant jet. The steady state concentration distribution in the eddy is found to be approximately uniform which means that the net influx of tracer at attachment balances the net efflux entrained by the jet. The balanced condition is modelled by linearly superimposing two solutions of the tracer conservation equation for different concentration boundary and initial conditions. The basic entrainment model is then extended to the buoyant situation. The model suggests that, for certain boundary and initial conditions, no solution is possible and attachment of a buoyant jet will not occur.

The attached jet configuration is characterised by certain basic parameters. Some simple experiments have been conducted to verify the model predictions of these parameters for the non-buoyant situation. The finer details of the model have been compared with measurements of the horizontal velocity field in both attached buoyant and non-buoyant jets and with temperature field measurements in the buoyant case. Satisfactory agreement is found.

The detailed measurements of velocity and temperature indicate that the attached buoyant jet develops similarly to a plane buoyant jet. The jet remains momentum dominated at least to the point of attachment. The eddy is found to be not only an area of approximately uniform temperature or density deficit but also of low turbulent intensity.

ACKNOWLEDGEMENTS

Many people have contributed to this study in various ways and I am profoundly grateful to them all.

I owe the most to my supervisor, Professor I. R. Wood. He originally suggested the topic and was always a source of enthusiasm and patient guidance during the course of the study. I particularly appreciate all that he has taught me.

The experimental results obtained in the study could not have been achieved without the assistance of the technical staff of the Civil Engineering Department. Mr. A. Stokes constructed the physical model and the traversing system by which it was moved. Mr. H. Pearce constructed the thermistor probes, a task that was so demanding of concentration and patience. He also assisted in the performance of the experiments and his encouragement when nothing seemed to go right was greatly appreciated. Mr. J. Ritchie set up the data acquisition system and solved all of the teething troubles. Mr. K. Mulvey designed and constructed the thermistor bridge circuits for measuring temperatures.

Others have contributed to the preparation of this thesis. Miss B. V. Nottingham typed the manuscript. Mr. B. Kay, Mr. W. McClelland and Mrs. V. Grey traced the illustrations. Mr. L. Gardner was responsible for the photographic work.

This study has not been without its share of frustrations. I am grateful to my flatmates for bearing with me during such times. My parents have also offered their encouragement and support. Above all, I want to thank Rosemary for her companionship and assistance during the

experimental phase and in the thesis preparation.

The research for this thesis was undertaken using the facilities provided by the Department of Civil Engineering, University of Canterbury. For the duration of the study the writer was assisted financially by the New Zealand University Grants Committee.

TABLE OF CONTENTS

LIST OF FIGURES

PAGE

PAGE

PAGE

PAGE

PAGE

PAGE

PAGE

LIST OF TABLES

LIST OF SYMBOLS

(Note: only the more important symbols are listed)

b characteristic length parameter defining the transverse mean profiles of velocity, concentration and density deficit.

b_i length parameter defining the growth of the turbulent shear layers in the initial flow region = $y_2 - y_1$.

b_o half width of jet exit = $Q_o^2/2M_o$.

B buoyancy flux = $\int_{-\infty}^{+\infty} \frac{g}{\rho_a} (\rho_a - \rho(s,n))\ u(s,n)\ dy$.

B_o buoyancy flux at jet exit = $\left(\frac{\rho_a - \rho_o}{\rho_a}\right) g\ u_o\ 2b_o$.

c concentration of passive tracer.

c_f concentration of tracer in the eddy or in a uniform field.

c_o concentration of tracer at jet exit.

g gravitational constant.

h step height.

$H(\ )$ Heaviside or unit step function.

l eddy length.

l_l lower limit of eddy length.

l_u upper limit of eddy length.

M momentum flux parameter = $\int_{-\infty}^{+\infty} u^2(s,n)\ dn$.

M_o momentum flux at jet exit = $u_o^2\ 2b_o$.

n distance normal to the centreline.

n_e transverse distance of the eddy streamline from the centreline ($n_e < 0$).

p pressure.

p_a ambient pressure.

Δp average negative pressure difference across an attached buoyant jet.

Q volume flux parameter = $\int_{-\infty}^{+\infty} u(s,n)dn$.

Q_o volume flux at jet exit = $u_o\ 2b_o$.

Q_t tracer flux parameter = $\int_{-\infty}^{+\infty} c(s,n)u(s,n)dn$.

Q_{t_o} flux of tracer at jet exit = $c_o u_o 2b_o$.

Re jet Reynolds number = $\rho_o Q_o/\mu_o$,

Ri_o initial jet Richardson number = $Q_o^3 B_o/M_o^3$.

s centreline distance from the jet exit.

s_3 centreline length denoting the position at which the jet senses the boundary.

s_4 centreline length defining the attachment point on the boundary.

sgn( ) sign of the quantity.

T temperature.

T_a ambient temperature.

T_o temperature at the jet exit.

$\bar{T}$ mean temperature.

T' turbulent fluctuation of temperature.

u velocity in x (s in the case of the curved jet flow) direction.

u_c centreline velocity in the x (s in the case of the curved jet flow) direction.

u_o jet exit velocity = M_o/Q_o .

u_x velocity in the x direction in the case of curved jet flow.

$\bar{u}$ mean velocity in the direction of motion.

u' turbulent fluctuation of velocity in the direction of motion.

V eddy volume.

x horizontal distance from the jet exit.

x_1 length of the concentration potential core (replaced by s_1 for the curved jet flow) = $b_o/\tan \gamma_3$.

x_2 length of the velocity potential core (replaced by s_2 for the curved jet flow) = $b_o/\tan \gamma_1$.

x_{or} distance of the virtual origin from the jet exit (replaced by s_{or} for the curved jet flow.

y vertical distance from the centre of the jet exit (from the boundary for the experimental data).

y_1 edge of the velocity potential core (replaced by n_1 for curved jet flow) = $b_o - x \tan \gamma_1$.

y_2 distance normal to the centreline at which $u/u_o = 0.5$ in the turbulent shear layers of the initial region = $b_o + x \tan \gamma_2$.

y_3 edge of the concentration potential core (replaced by n_3 for curved jet flow) = $b_o - x \tan \gamma_3$.

y_4 distance normal to the centreline at which $c/c_o = 0.5$ in the turbulent shear layers of the initial region for an efflux of tracer from the source = $b_o + x \tan \gamma_4$.

α entrainment coefficient.

α_i entrainment coefficient in the initial flow region = $(\tan \gamma_1)/2$.

β angle defining the geometry of the circular extrapolation of the eddy streamline to the boundary in the attached non-buoyant jet model.

γ_1, γ_2 angular parameters defining spread of tracer in the shear layers of the initial flow region.

γ_3, γ_4 angular parameters defining spread of tracer in the shear layers of the initial flow region.

δ absolute value of the centreline slope at the station $\chi_3 = |(\theta)_{\chi_3}|$

ε_m eddy viscosity.

ε_D eddy mass diffusivity.

ζ dimensionless parameter defining the buoyancy in the jet for the region $0 \leq \chi \leq \chi_1$.

η dimensionless distance normal to the centreline = $\sigma n/b$.

η_e dimensionless transverse distance of the eddy streamline from the jet centreline ($\eta_e < 0$).

η_{15} dimensionless length normal to the centreline denoting the position of the inner jet edge ($\eta<o$), defined by $u/u_c = 0.15$.

θ angle denoting slope of the jet trajectory with respect to the (x,y) coordinate system.

λ^2 ratio of the eddy mass diffusivity to the eddy viscosity = $\varepsilon_D/\varepsilon_m$.

μ viscosity.

ν dimensionless distance normal to the centreline in the initial region = $\sigma(y-\text{sgn}(y)\,y_3)/(y_4-y_3)$.

§ dimensionless parameter defining the buoyancy in the jet for the region $\chi_1 \leq \chi \leq \chi_2$.

ρ density.

$\bar{\rho}$ mean density.

ρ_a ambient density.

ρ_f density in the eddy or in a uniform field.

ρ_o density at the jet exit.

σ constant = $\cosh^{-1}\sqrt{2}$

τ angle defining the geometry of the circular extrapolation of the eddy streamline in an attached non-buoyant jet.

χ dimensionless centreline distance = $2M_o\, s/Q_o^2$.

χ_1 dimensionless centreline length of the velocity potential core.

χ_2 dimensionless centreline length of the velocity potential core and the initial region.

χ_3 dimensionless length along the centreline of the position at which the jet senses the boundary.

χ_4 dimensionless length along the centreline defining the attachment point on the boundary.

χ_{or} dimensionless centreline distance of the virtual origin from jet exit.

ψ denotes a streamline.

ψ_t denotes a line of constant tracer flux.

ψ_{t_n} value of the line of constant tracer flux at the transverse distance n $= \int_n^{+\infty} c(s,n)u(s,n)dn$.

$\psi_{t_{+\infty}}$ value of the line of constant tracer flux at a large transverse distance. By definition $\psi_{t_{+\infty}} = 0$.

Subscripts

* denotes a dimensionless quantity.

a denotes a quantity of the ambient fluid.

c denotes a quantity along the jet centreline.

e denotes a quantity along the eddy streamline.

f denotes a quantity in the eddy or in a uniform field.

i denotes a quantity in the initial flow region.

o denotes a quantity at the jet exit.

x denotes a quantity in the x direction.

Abbreviations

CEDACS Civil Engineering Department data acquisition system.

LDA Laser Doppler Anemometer.

CHAPTER 1

INTRODUCTION

1.1 THE ATTACHMENT OF A TWO-DIMENSIONAL JET TO AN ADJACENT BOUNDARY

The attachment of a two-dimensional turbulent jet to an adjacent boundary (Fig. 1.1) is an example of a phenomenon termed the "Coanda effect" in the literature. The jet curves over towards the boundary and divides upon contact with it. Some of the flow is recirculated and the major portion continues downstream as a wall jet before separating and rising as a plume. The geometry of the recirculation region, henceforth termed the eddy, is constant for the steady flow situation. A limiting condition exists for attachment and if this is exceeded the jet behaves as a free one. The presence of a buoyancy force decreases the curvature of the jet and changes the limiting condition.

A physical explanation of the attachment phenomenon has been postulated by Squire (1950). Initially the jet behaves freely. Turbulent shear layers develop on either side of the jet and ambient fluid is entrained. The entrainment process is confined on one side by the boundary and a slight counter flow is induced, sufficient to cause a pressure difference across the jet. The jet subsequently begins to follow a curved trajectory, accelerating towards the attached equilibrium state (Fig. 1.1).

The attachment phenomenon has a number of practical applications. It is discussed in the context of waste water disposal into the ocean in the next section.

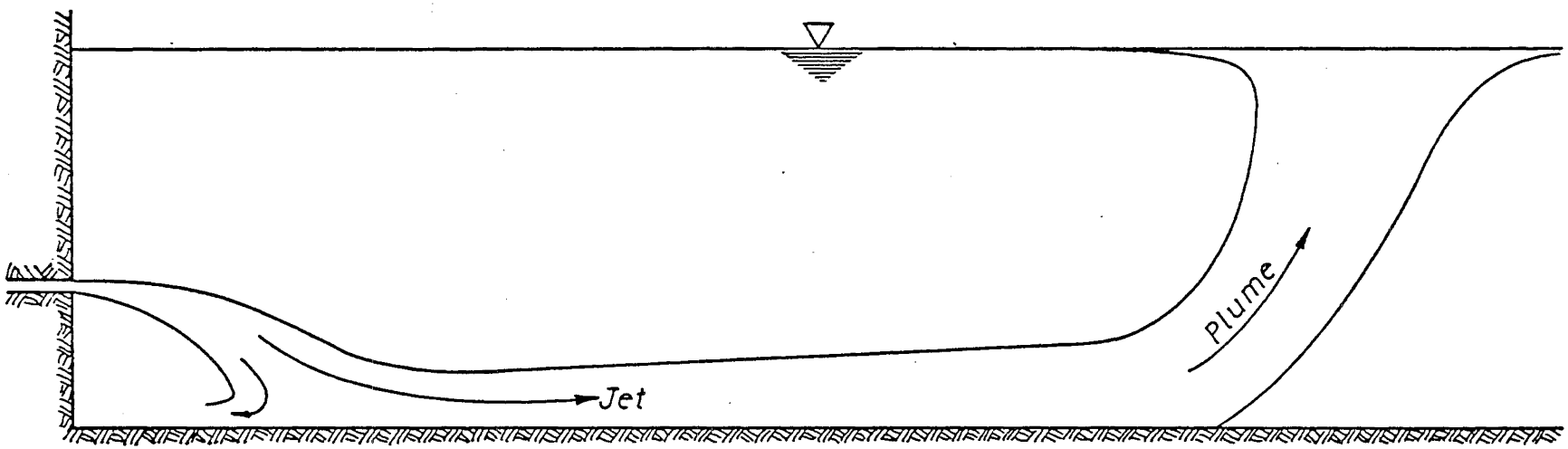

FIGURE 1.1 A two-dimensional attached buoyant jet.

1.2 APPLICABILITY OF THE ATTACHMENT PHENOMENON TO WASTE WATER DISPOSAL

Waste water is normally discharged into the ocean through a long pipeline extending along the sea bed from the shore (known as an outfall). The effluent emerges from a multi-port diffuser at the far end and rises towards the ocean surface due to buoyancy. The velocity gradient between the jets thus formed and the receiving water causes ambient fluid to be entrained into the flow and the waste water is thereby diluted.

The discharge from an outfall operating in the free jet mode may effectively meet the minimum water quality standards specified for the receiving water. However modifications to the diffuser geometry can produce a more efficient design in which the dilution exceeds that achieved by the free jet configuration. This is particularly beneficial when density stratification of the ambient receiving water occurs and the buoyant jet rises to an equilibrium level below the ocean surface.

The use of an attached jet configuration to improve the dilution obtainable from a submerged outfall has been proposed by Sharp (1975). A two-dimensional buoyant jet discharging parallel to an adjacent horizontal boundary (Fig. 1.1) describes the flow from a long prototype diffuser which occurs sufficiently close to the sea-bed. The spacing of the diffuser ports is assumed small enough for the individual jets to merge together. The buoyant wall jet flowing downstream is more efficient at mixing the jet fluid with the ambient fluid than an equivalent free jet. This is due to the instability of the interface between the less dense underflowing layer and the ambient layer which promotes entrainment and also to the greater effective length over which entrainment occurs. Therefore the dilution is much greater making it desirable to achieve the attachment phenomenon in a prototype situation.

Investigations of similar configurations for the purpose of waste water disposal have previously been reported. Anwar (1973) has studied a two-dimensional buoyant jet discharging into a crossflow. The magnitude of the crossflow was sufficient to cause the jet to curve over and attach to the horizontal boundary and flow downstream as a wall jet. Daniel and Wood (1976) have studied the warm water discharge under a submerged gate down a slope. The buoyant discharge flowed down the slope before breaking free and rising to the surface.

1.3 NATURE OF THE INVESTIGATION

Previous investigations of an attached buoyant jet have been confined largely to the wall jet flowing downstream. Thus attachment of the jet to the boundary has been implicitly assumed. Scant attention has been given to the region of flow up to the point of attachment and, in particular, the conditions for which attachment will occur. This theoretical and experimental study has been conducted to gain a better understanding of the two-dimensional attached buoyant jet in the region of attachment.

While a prototype situation is a complex one, an initial understanding of the attachment phenomenon demands a simplified approach. Therefore the investigation has been confined to the case of a two-dimensional buoyant jet discharging into a stagnant environment. The assumption of a stagnant ambient reservoir means that the effects of ocean currents likely to be present in a prototype location are ignored.

The two-dimensional approximation for flow from a prototype diffuser is valid so long as the port spacing is close and the diffuser is infinitely long. The former assumption is entirely satisfactory, but a prototype diffuser is of finite length and the flow from it is strictly three-

dimensional due to the shearing action between the lateral edges and the ambient receiving water. However the flow from the centre of the diffuser will be two-dimensional and, if edge effects due to shear are ignored, the two-dimensional assumption is a reasonable first approximation. Understanding the simpler two-dimensional situation is the first step towards understanding the more realistic three-dimensional situation.

Some preliminary experiments with a two-dimensional attached buoyant jet had indicated that the cling length of the wall jet (and therefore the dilution) was greatest when the initial momentum of the jet was directed horizontally. For this reason a two-dimensional buoyant jet discharging horizontally has been studied rather than a jet directed down towards the boundary.

1.4 THESIS OUTLINE

The parameters defining the geometry of the attachment region of a two-dimensional attached jet are identified in the next chapter (Chapter 2). The literature relevant to the investigation is also discussed.

Momentum effects are expected to dominate close to the jet exit so that initially the flow is treated as a pure jet (Chapter 3). A simple entrainment model is constructed to describe the flow in the attachment region.

An initial understanding of the effect of buoyancy is gained by analysing the addition of a passive tracer to the non-buoyant jet case (Chapter 4). The entrainment model developed in Chapters 3 and 4 is then extended to describe the buoyant situation (Chapter 5).

An experimental investigation to verify the model predictions is outlined in Chapter 6. Measurements of some parameters defining the

the geometry of the eddy in the non-buoyant jet case are presented in Chapter 7. Detailed measurements of velocity in the attachment region of both non-buoyant and buoyant jets are analysed in Chapter 8. Buoyancy was produced by increasing the jet inflow temperature relative to the ambient temperature and detailed measurements of the temperature field in an attached buoyant jet were also made. The results are reported in Chapter 9. A comparison between the experimental data and the predictions of the attached buoyant jet model is made in Chapter 10.

The essential results of the investigation are summarised in Chapter 11. Conclusions and recommendations for future research are also discussed.

Material related to the investigation but of secondary importance is presented in the appendices.

CHAPTER 2

LITERATURE REVIEW

2.1 INTRODUCTION

A number of theories have been postulated for turbulent incompressible jets and plumes. These are reviewed briefly in this chapter. The essential details discussed are the same for both axisymmetric and two-dimensional jets and plumes although for the purposes of the review two-dimensionality is assumed.

The theories of turbulent incompressible jets and plumes have generally been developed for the simplest flow configuration in which the jet is rising vertically in a stagnant homogeneous environment remote from any confining boundaries. They have then been extended to more complex flow configurations such as the attached jet. Recent models of the two-dimensional attached jet are also reviewed in this chapter along with the experimental data available for comparison with the theoretical predictions.

2.2 THEORIES OF TURBULENT JETS AND PLUMES

A buoyant jet, or forced plume as it is sometimes called, possesses initial momentum and buoyancy fluxes. It has two limiting cases. When buoyancy forces are absent the jet is termed a pure or non-buoyant one. When the initial momentum flux is zero the buoyant jet flow is described as a pure plume. In a uniform ambient environment a buoyant jet is always in transition to a pure plume no matter how large the initial momentum flux is.

Observations of turbulent jet flows have identified three distinct flow regions (List and Imberger, 1973) as shown in Fig. 2.1.

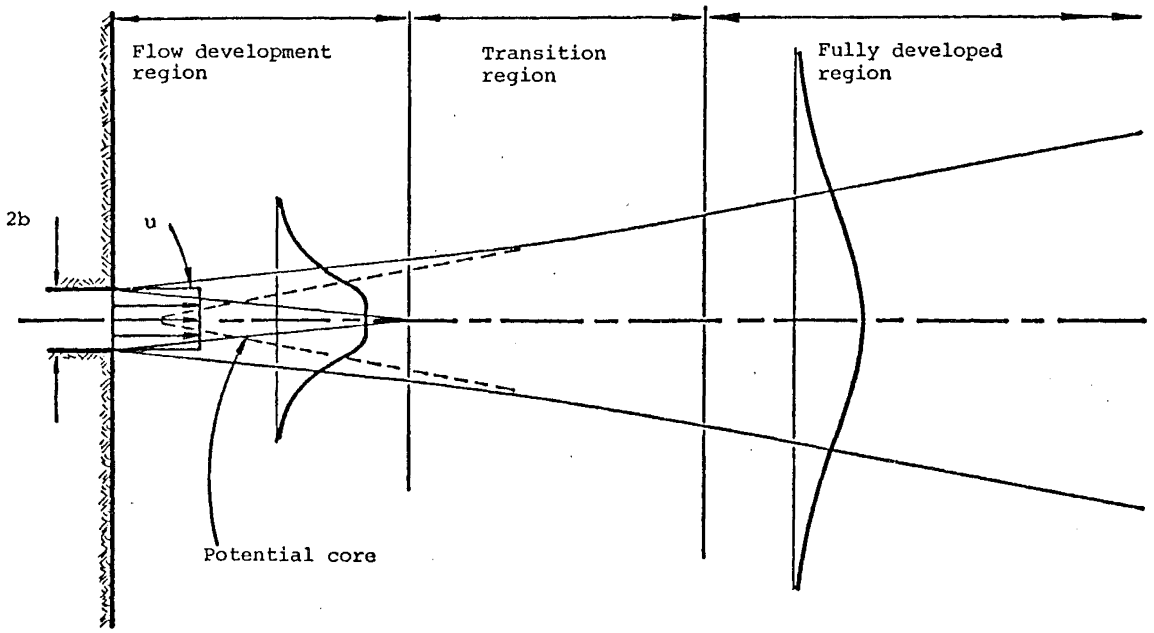

Figure 2.1 Flow regions of a turbulent incompressible jet.

In the initial or flow development region turbulent shear layers on either side of a potential core of uniform velocity spread until their inner boundaries coalesce. After the end of the potential core (transition region) it is some distance before all mean quantities begin to vary systematically with longitudinal distance and fully developed flow is established. In the fully developed region the flow is self-similar or self-preserving meaning that the transverse distributions of each of the mean quantities retain the same functional form and only their transverse length scale and the scales of the mean quantities change with longitudinal distance. A fully developed jet therefore behaves as though it originates as a virtual line source of momentum flux and or buoyancy flux. Since jet behaviour

far from the real source is of greater practical interest most theories have concentrated on describing flow in the fully developed region.

Fluid motion whether laminar or turbulent is described by the Navier-Stokes equations. In the turbulent case the velocity components, pressure and density can each be expressed as the sum of a mean value, denoted by an overbar, and a randomly varying perturbation, denoted by a prime (Raudkivi and Callander, 1975). Application of the Boussinesq approximation produces only minor error when the density variations are small (Turner, 1973). The approximation consists basically of replacing the local mean density $\bar{\rho}$ with the ambient density ρ_a in all terms except the buoyancy ones where the density difference $\rho_a - \bar{\rho}$ is essential. Viscous diffusion of momentum and molecular diffusion of heat (where heat is responsible for the density variations) can be neglected in comparison with the turbulent diffusion of those quantities. The resultant time-averaged partial differential equations of motion for turbulent incompressible flow contain more unknown variables than there are equations and boundary conditions. The closure of these equations is the fundamental problem of turbulent fluid mechanics and several semi-empirical methods have been proposed to deal with it.

Early workers in the field of turbulent fluid mechanics assumed the self-preservation of all mean quantities for a pure jet and attempted to formulate a constitutive relationship between the Reynolds stress, $-\overline{u'v'}$, and the velocity gradient, $\frac{\partial \bar{u}}{\partial y}$ (u is the velocity component in the mean flow direction x and v is the velocity component in the transverse direction y). Prandtl pioneered this approach with his mixing length and constant eddy viscosity hypotheses (Schlichting, 1960). While successful predictions of the mean velocity distribution are made on the basis of these hypotheses, they fail altogether at predicting the distributions

of other quantities. The basic criticism of them though is that they assume a physical picture which is in conflict with experimental evidence (Batchelor, 1950). Nevertheless they remain a useful approximation for predicting mean velocity profiles.

More complex constitutive equations relating the Reynolds stress to the mean velocity field have been postulated due to the failure of Prandtl's hypotheses. Such relations essentially define a turbulence model which describes the turbulence state throughout the flow. The resulting system of partial differential equations generally requires a numerical solution. No assumptions regarding entrainment rates and the forms of mean profiles are necessary as these are obtained as part of the solution. A review of models in this category is given by Launder and Spalding (1972).

Another more recent approach has been to assume mean transverse distributions of velocity and density deficit and integrate the partial differential equations of motion across the flow. The integrated equations are simplified by neglecting certain terms which it is argued are zero or small in magnitude and closure is achieved through an entrainment hypothesis based on dimensional reasoning. An irrotational entrainment flow outside the boundary of the turbulent jet, responding to the induced pressure gradient, sees the jet as a distribution of planar sinks (Taylor, 1958). Hence it is argued that the velocity of the potential flow is proportional to some characteristic velocity of the jet flow (Morton et al, 1956). The constant of proportionality, known as the entrainment coefficient and denoted by α, must be determined experimentally.

Morton (1959) assumed the entrainment coefficient to have the same value for jets and plumes, an assumption which leads to the result for Gaussian profiles that the linear spreading rate of a pure jet is twice

the spreading rate of a pure plume. This is contradicted by experimental evidence that the rate of spread is approximately the same for both jets and plumes (Chen and Rodi, 1980), even though the driving force in each case is quite different. The difficulty can be overcome by assuming different values of entrainment coefficient for a pure jet and a pure plume although this implies a variable entrainment coefficient for a buoyant jet which is always in transition towards a pure plume (Kotsovinos, 1975). Fortunately the solution of the equations of motion is relatively insensitive to the value of the entrainment coefficient (Turner, 1973) and a value depending on the nature of the flow can be assumed without much error.

List and Imberger (1973) have attempted to evaluate the variability of the entrainment coefficient for a buoyant jet rising vertically in a uniform environment. They reformulated the integral equations of motion in terms of the volume, momentum and buoyancy fluxes without making any assumptions regarding the self-similarity of the velocity and density deficit profiles. Using dimensional arguments they expressed an entrainment function in the continuity equation and the buoyancy force in the momentum equation as functions of a local jet Richardson number

$$Ri(x) = \frac{Q^3(x)\ B(x)}{M^3(x)}$$

and another dimensionless number

$$C(x) = \frac{Q(x)}{\sqrt{M(x)\ (x - x_o)}}$$

giving a measure of the local jet angle expansion (x is the centreline distance in the mean flow direction measured from the real source, x_o is the position of the virtual source and Q(x), M(x) and B(x) are the volume, momentum and buoyancy fluxes respectively). Kotsovinos (1975) in an

experimental study of a plane buoyant jet found that the number C is invariant and that the entrainment function is linearly dependent on Ri, which is a measure of the relative importance of the buoyancy and momentum fluxes.

2.3 THE TWO-DIMENSIONAL ATTACHED PURE JET

The flow configuration for the two-dimensional attached jet is shown in Fig. 2.2.

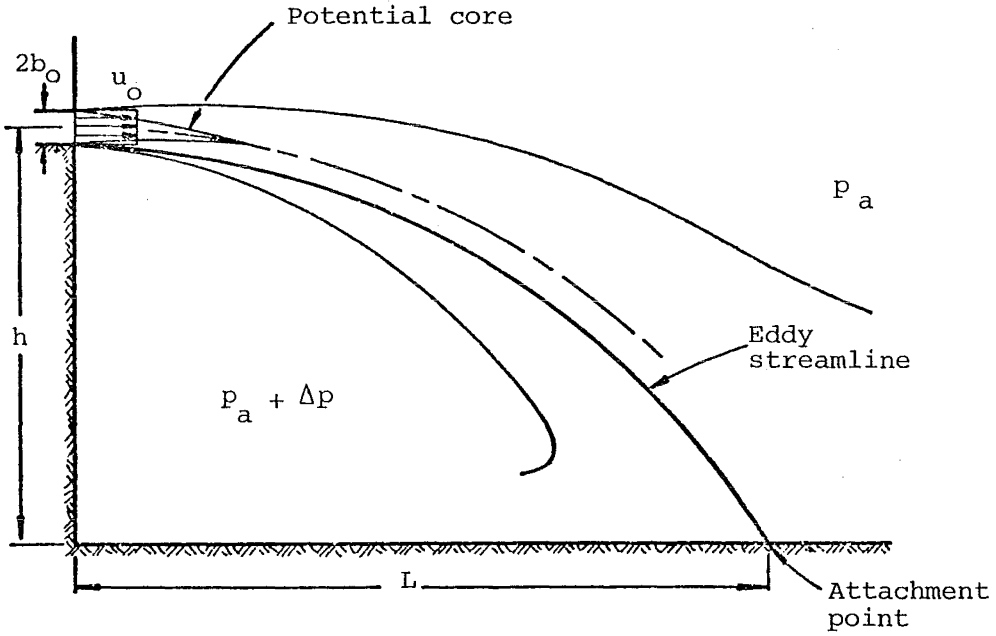

Figure 2.2 Basic parameters defining the configuration of a two-dimensional attached non-buoyant jet.

Across the eddy streamline there is no net flow. It is apparent then that the downstream flow is the sum of the jet efflux and the volume of fluid entrained along the upper edge of the jet. By implication the volume of fluid entrained along the lower edge of the jet is equal to the volume fed back into the eddy in the attachment region.

The independent variables which determine the physical features of the flow (Fig. 2.2) are the step height h, the half-width of the jet exit b, a characteristic jet exit velocity u_o, and for an incompressible fluid, the fluid properties of density ρ and viscosity μ. The dependent variables are an average negative pressure difference Δp across the jet and the length l of the eddy defined by the position of the eddy streamline on the boundary.

Expressed mathematically,

$$l, \Delta p = f(h, b_o, u_o, \rho, \mu) \tag{2.1}$$

Dimensional analysis then yields

$$\frac{l}{h}, \frac{\Delta p}{\rho u_o^2} = f\left(\frac{h}{b_o}, \rho\frac{u_o 2b_o}{\mu}\right) \tag{2.2}$$

where $\rho u_o 2b_o/\mu$ is a Reynolds number. Since the jet is fully turbulent Reynolds number effects will be small and

$$\frac{l}{h}, \frac{\Delta p}{\rho u_o^2} = f\left(\frac{h}{b_o}\right) \tag{2.3}$$

The relationships between the dimensionless numbers in eqs. 2.3 have been the subject of several experimental and theoretical studies.

2.3.1 Analytical studies

Borque and Newman (1960) and Sawyer (1960) first analysed the plane attached jet using the thin jet assumption ($h/b_o >> 1$). They

developed independently similar entrainment models of the equilibrium situation which treated the jet as fully developed throughout and ignored the effect of flow curvature on entrainment. For the purposes of this discussion, Sawyer's model will be briefly described because he subsequently improved it (Sawyer, 1963). His improvements are also described.

The steps that Sawyer (1960) followed in his approximate analysis are outlined in Fig. 2.3. He argued that the centrifugal force on the current flow balanced the force due to the average pressure difference across the jet. Jet curvature could therefore be expressed as the ratio of the average pressure difference to the mean momentum flux, a quantity that Sawyer implicitly assumed to be conserved. He adopted a mean velocity profile for a free jet obtained on the basis of Prandtl's constant eddy viscosity hypothesis and which incorporated an entrainment related constant spread parameter. This enabled him to calculate the position of the eddy streamline and the division of flow at attachment. He made further assumptions regarding the shapes of the initial reversed flow and initial downstream flow velocity profiles and then achieved closure of the set of equations by applying the momentum equation to a local control volume in the region of attachment, ignoring any pressure differences.

Manipulation of the equations derived produced the appropriate forms of the relationships suggested by eqs. 2.3. By a convenient choice of value for the floating constant spread parameter, reasonable agreement between theory and experiment (section 2.3.2) was obtained. The value of the spread parameter differed however from the value measured experimentally for a two-dimensional free jet.

Borque and Newman (1960) also applied the momentum equation to another control volume bounded upstream by the back of the step, but the

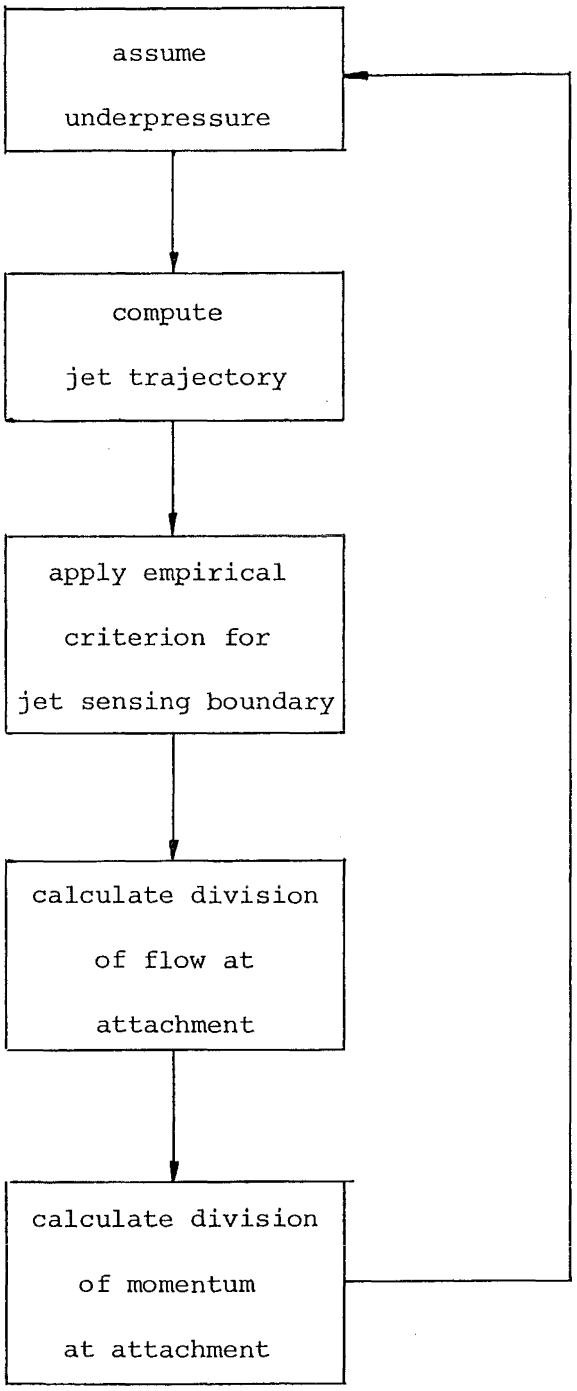

FIGURE 2.3 Outline of Sawyer's (1960) model for a two-dimensional attached non-buoyant jet.

average pressure difference across the jet was seriously underestimated and the eddy length overestimated by this approach.

Sawyer (1960) suggested that the effects of jet curvature on entrainment were responsible for the different value of the spread parameter from that determined experimentally for the free jet. He argued that due to centrifugal effects entrainment along the inner edge of the jet would be reduced and entrainment along the outer edge increased. Measurements of the growth of a two-dimensional wall jet flowing round a curved surface designed to maintain a constant ratio of jet thickness to surface radius of curvature confirmed this argument (Sawyer, 1963). However the argument implies that the mean velocity profile for a two-dimensional attached jet should be asymmetrical, a fact which was not observed experimentally. Neither did Sawyer (1960) observe the spread of the two-dimensional attached jet to differ markedly from that of a plane jet and he concluded that there must be a flow of fluid across the jet centreline for these observations to be consistent with differing entrainment rates on either side of the jet.

Sawyer (1963) modified his original analysis of the two-dimensional attached jet to account for different entrainment rates along the jet edges. He argued on the basis of a first-order mixing length theory that $(E_2 - E_1)/(E_1 + E_2)$ is proportional to b/R, where E_1 and E_2 are the entrainment rates along the inner and outer edges respectively, b is the jet width, and R is the radius of curvature of the flow. The sum $E = E_1 + E_2$ is the overall entrainment rate which Sawyer related to the constant spread parameter that he had used in his original analysis. The ratio b/R is not constant for an attached jet but Sawyer assumed an average value and confirmed the experimental observation that the mean velocity profile is virtually identical to that of a free jet.

Sawyer (1963) sought also to incorporate the initial development of the two-dimensional jet in his modified analysis (Fig. 2.1). He ignored the transition region and also the effects of curvature in the initial region, arguing that these would be small. The turbulent shear layers in the initial region are of a plane mixing layer type so that Sawyer assumed a velocity distribution described by the error function and obtained on the basis of Prandtl's constant eddy viscosity hypothesis. This necessitated appropriate adjustment of the length scales to match the mixing layer velocity profile to the fully developed profile at the transition station.

As a further improvement Sawyer (1963) assumed a pressure distribution across the jet when he applied the momentum equation to a local control volume in the region of attachment. The pressure distribution was of the form obtained by Wattendorf (1935) in a study of fully developed flow round a bend in a rigid-walled channel.

Sawyer's (1963) modified analysis showed improved agreement with experiment (section 2.3.2) for the relationships suggested by eqs. 2.3. The overall entrainment rate $E = E_1 + E_2$ was identical to that for a free jet, but the value of the ratio $(E_2 - E_1)/(E_1 + E_2)$ varied with step height in the range 0.1 to 0.17.

2.3.2 Experimental studies

Both Sawyer (1960) and Borque and Newman (1960) conducted experiments to determine the relationships between the dimensionless quantities in eqs. 2.3 for comparison with their model predictions. The experiments covered different ranges of Reynolds number ($Re \approx 9.5 \times 10^4$ for Sawyer, $0.8 \times 10^4 < Re < 1.5 \times 10^4$ for Borque and Newman), but their results, plotted in Figs. 2.4 and 2.5, are complementary, thereby confirming eqs. 2.3 to be independent of Reynolds number. The range of dimensionless

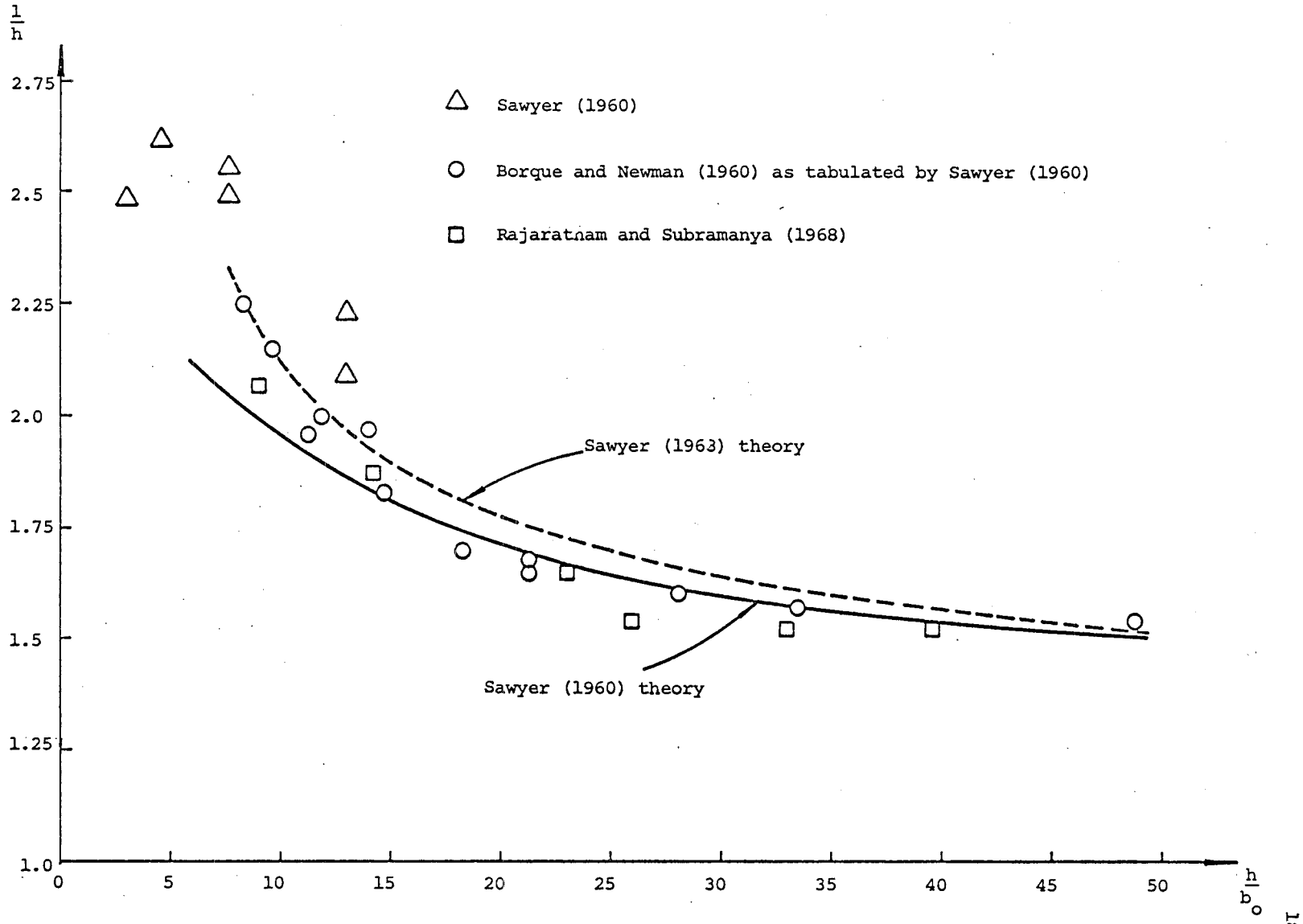

FIGURE 2.4 Comparison of the available experimental data and theoretical predictions for the eddy geometry of an attached non-buoyant jet.

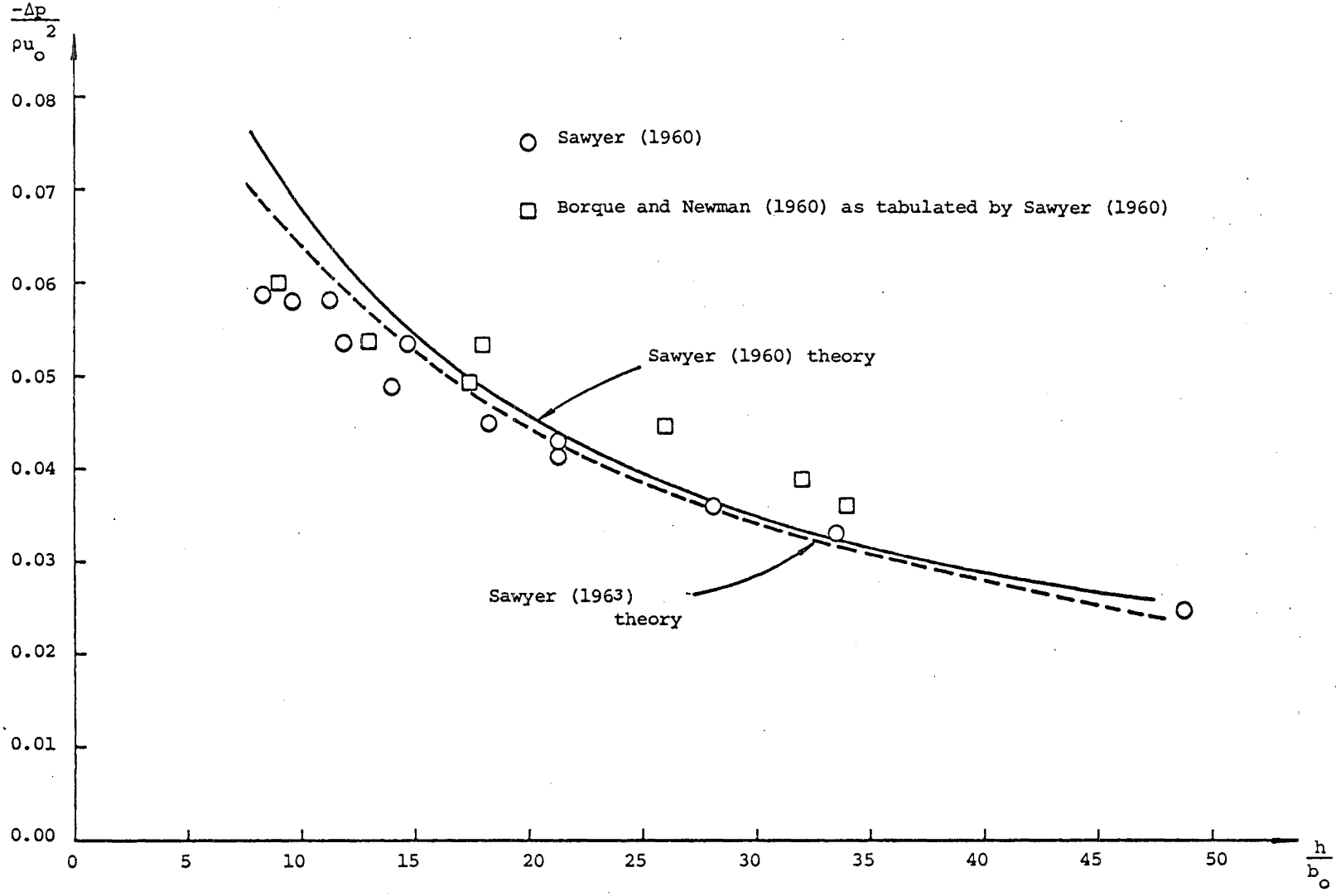

FIGURE 2.5 Comparison of the available experimental data and theoretical predictions for the average pressure difference across an attached non-buoyant jet.

step height covered was $10 < h/b_o < 50$.

Borque and Newman (1960) used a visual technique to measure eddy length. The division of reversed and downstream flow was indicated by hinged paper tufts lying in the direction of mean flow. Sawyer (1960) however traversed the boundary with two flattened pitot tubes, one facing backwards and the other forwards. He took the attachment point to be the point at which the two pitot tubes gave identical readings and found this to coincide with the position of maximum positive pressure along the boundary, measured by static pressure tappings. Sawyer also observed that the static pressure distribution (Fig. 2.6) along the boundary closely

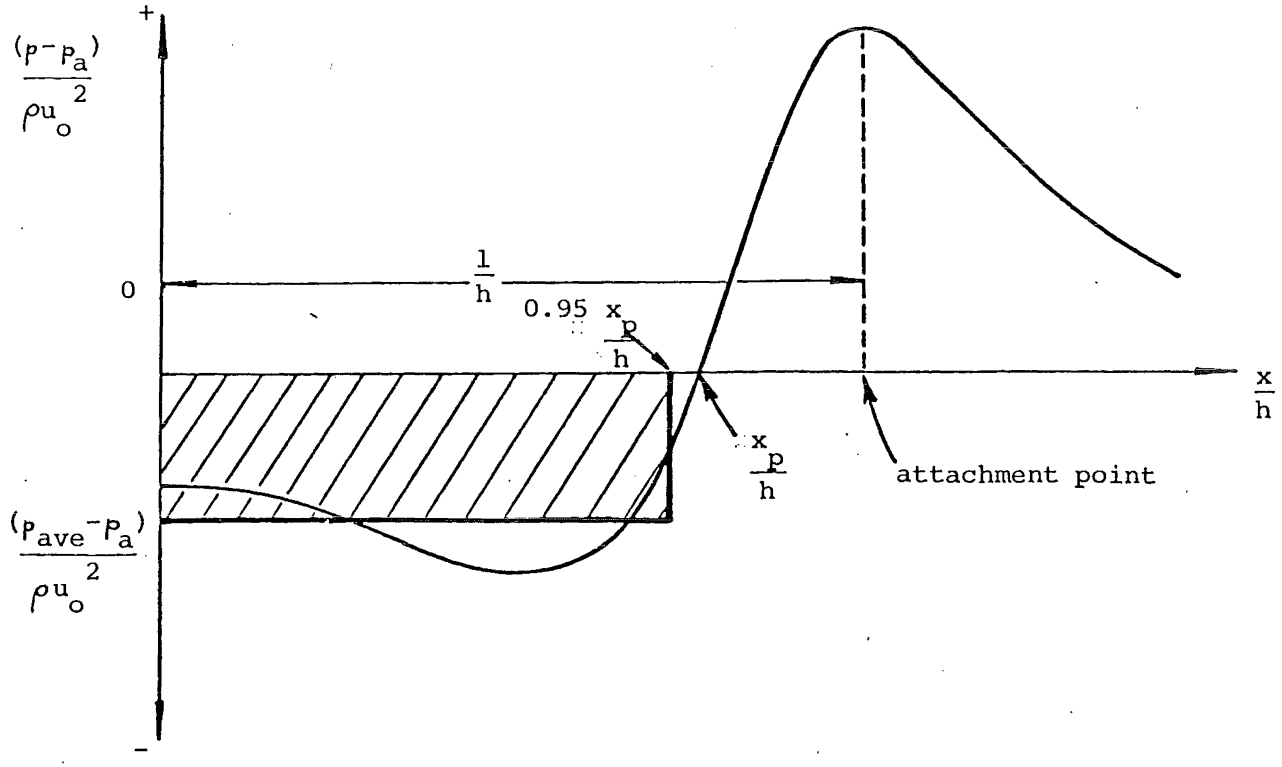

FIGURE 2.6 Typical static pressure distribution along the boundary as measured by Sawyer (1960) and showing Sawyer's definition of the average pressure difference across the jet.

resembled the static pressure in the eddy and he therefore defined the average pressure difference across the jet to be the negative mean of the pressure along the boundary over the range of dimensionless distance x/h between zero and 0.95 times its value at $p - p_a = 0$ (p is the static pressure and p_a is the ambient static pressure). He recalculated Borque and Newman's measurements using this definition.

In addition to measuring the dimensionless quantities in eqs. 2.3, Sawyer (1960) measured the static pressure distribution throughout the flow, and mean velocity profiles at various vertical cross-sections.

Rajaratnam and Subramanya (1968) measured the eddy length and the maximum positive pressure along the boundary as functions of step height for a water jet at a large depth of submergence, the Reynolds numbers lying in the range $5 \times 10^4 < Re < 10^5$. They covered a dimensionless step height range, $0 < h/b_o < 10$, lower than in the other experiments reported and outside the valid range of the theoretical model described in the previous section. Their measurements of the eddy geometry have been shown in Fig. 2.4. They did not report their static pressure measurements along the boundary so that the average pressure differences cannot be calculated using Sawyer's definition.

2.4 THE TWO-DIMENSIONAL ATTACHED BUOYANT JET

Few studies of the two-dimensional attached buoyant jet are known to the writer.

Yoshida and Nagata (1979) investigated experimentally the unsteady behaviour of a vertical two-dimensional buoyant jet as it attached to an adjacent parallel surface. Their results are of little significance to the present study of a steady state buoyant jet attached to a horizontal boundary.

Bates (1977) investigated the attachment criterion for a free buoyant jet and the detachment criterion for an attached buoyant jet where the jet discharges parallel to an adjacent horizontal boundary. On the basis of his experimental results he suggested for the former criterion that

$$Ri_o \left(\frac{h}{b_o}\right)^2 = 2.5 \tag{2.4}$$

and for the latter criterion that

$$Ri_o \left(\frac{h}{b_o}\right)^2 = 8 \tag{2.5}$$

where

$$Ri_o = \frac{(\rho_a - \rho_o)\, g\, b_o}{\rho_a\, u_o^2} \tag{2.6}$$

is the initial jet Richardson number.

This study makes a contribution towards understanding the two-dimensional attached buoyant jet.

CHAPTER 3

AN ANALYTICAL ENTRAINMENT MODEL OF A TWO-DIMENSIONAL ATTACHED NON-BUOYANT JET

3.1 INTRODUCTION

Momentum effects dominate near the source of a two-dimensional attached buoyant jet so that, as a first approximation, the flow can be treated as a pure jet. The two-dimensional attached pure jet case up to the point of attachment is examined in this chapter.

The essential parameters defining the flow configuration of an attached non-buoyant jet (Fig. 3.1) have previously been identified in section 2.3 as the step height h, the initial half-width of the jet b_o, a characteristic jet exit velocity u_o, and for an incompressible fluid, the fluid properties of density ρ and viscosity μ. The eddy length l and an average pressure difference Δp across the jet are the dependent variables. Dimensional reasoning indicates that

$$\frac{l}{h} \, , \; \frac{\Delta p}{\rho \, u_o^2} = f\left(\frac{h}{b_o} \, , \; Re\right) \tag{3.1}$$

although these equations will be substantially independent of the Reynolds number Re due to the turbulent nature of the flow.

An analytical entrainment model of the flow is developed to predict the form of the relationships suggested in eqs. 3.1. The usual assumptions of fully turbulent flow, incompressible fluid, a stagnant ambient environment (except for the induced entrainment motion) and similarity of all mean profiles are made. In addition the effects of curvature on entrainment are ignored and the jet is considered to be thin ($h/2b_o >> 1$).

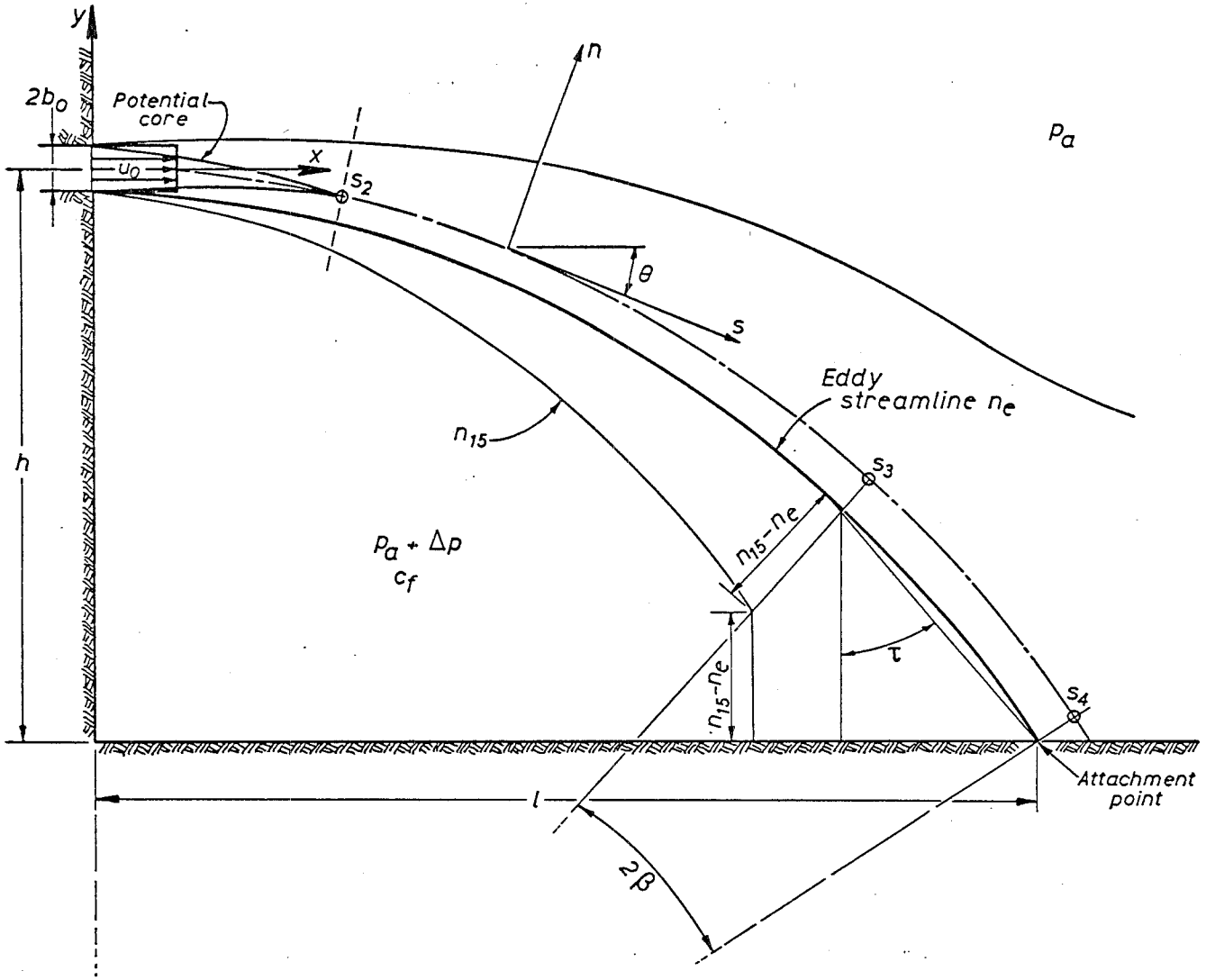

FIGURE 3.1 Configuration of a two-dimensional attached non-buoyant jet.

3.2 A DESCRIPTION OF THE FLOW CONFIGURATION

For most jet flow problems, behaviour far from the real source is generally of greater interest than behaviour in the vicinity of the source. It is sufficient for modelling purposes to disregard the initial and transition regions (Fig. 2.1) and to treat the jet as fully developed, emanating from a virtual source. In the case of an attached jet, the attachment region is in the neighbourhood of the real source and the influence of the flow development region is likely to be significant, particularly for small step heights. Therefore the initial growth of the jet from the real source cannot be neglected.

Beyond the initial flow development region the mean centreline velocity $\bar{u}_c$ begins to systematically decay. However it is not until further downstream that the root mean square centreline velocity fluctuation $\sqrt{\overline{u'^2_c}}$ attains a maximum value before decaying also (Chen and Rodi, 1980), and self-similarity is achieved. Prior to the establishment of fully developed flow, the deviation from the dynamically similar mean velocity profile is expected to be small so that little error will be involved if self-similarity is assumed. This assumption is tantamount to ignoring the transition region.

The analysis of the two-dimensional attached pure jet proceeds on the basis of this assumed picture of the flow. The treatment of the fully developed region is straightforward and follows that of Morton (1961) in which the flow is imagined as originating from a virtual source. The position of the virtual source is determined by the momentum and volume fluxes (and buoyancy flux in the case of a buoyant jet) characteristic of an equivalent source at the end of the initial region. The flux quantities at the equivalent source need to be related to their counterparts at the real source but this poses a difficulty because entrainment

in the initial region is not well understood.

In the flow development region turbulent shear layers grow on either side of a potential core of uniform velocity. Sawyer (1963) in his improved model of the two-dimensional attached pure jet treated the shear layers as self-similar plane mixing layers and assumed an appropriate mean velocity profile. In adopting this approach, the form of the velocity profile and the geometry of the potential core imply a constant entrainment coefficient. This coefficient differs from the experimemtal value of the entrainment coefficient in the fully developed region because of the length assumed for the potential core. Thus, in the assumed picture of the flow, there will be a discontinuity in the entrainment velocity at the transition from the initial region to the fully developed region.

Morton (1968) has argued that models in which the entrainment velocity is related to some characteristic jet velocity cannot properly apply in the neighbourhood of the source. In this region, the turbulent intensity (and hence entrainment) is strongly influenced by the turbulent intensity in the efflux and is unlikely to follow any assumed similarity relationship with the mean flow. Therefore, Morton suggests that entrainment must be related to the local turbulent flow rather than the mean velocity field. He develops a modified entrainment model of an asymmetric forced plume along these lines. The solution tends asymptotically towards that derived on the basis of the entrainment velocity being scaled in proportion to some characteristic jet velocity.

Morton's (1968) approach is more accurate as it is based on an order-of-magnitude analysis of the terms in the Navier-Stokes equations. Also it overcomes the deficiencies of Sawyer's (1963) approach. However,

the latter approach has been followed in this analysis of an attached pure jet (except that curvature of the trajectory has been included) because of its greater mathematical simplicity and the fact that it does not entail the risk of a major digression from the objectives of the study. It must be emphasised that the assumption of dynamic similarity in the turbulent mixing layers of the initial region merely enables a convenient mathematical description of the flow to be formulated. It does nothing to improve the present physical understanding of entrainment in the neighbourhood of the real source.

3.3 VELOCITY PROFILES

Gortler solved the Navier-Stokes equations for steady turbulent incompressible two-dimensional jet flow with the assumption of a constant eddy viscosity ε_m across a transverse section (Schlichting, 1960) and obtained

$$u(x,y) = u_c(x)\ \mathrm{sech}^2\ \eta \qquad (3.2)$$

where x and y are directions parallel to and normal to the mean flow (Appendix A). u is the mean velocity in the x direction, the subscript c denoting a centreline value. The dimensionless parameter $\eta = \sigma y/b$, where b is a characteristic length parameter defined as the transverse distance from the centreline to the point at which the mean velocity is equal to half of the mean centreline velocity

$$\frac{u\ (x,\ b(x))}{u_c\ (x)} = \frac{1}{2} \qquad (3.3)$$

The latter definition implies that the constant $\sigma = \cosh^{-1} \sqrt{2}$.

The turbulent shear layers on either side of the potential core in the initial region have been likened to self-similar plane mixing layers (Sawyer, 1963) for which Prandtl's constant eddy viscosity hypothesis

predicts a mean velocity distribution described by the error function. The assumption of a mean velocity profile of this type for the turbulent shear layers necessitates matching with the free jet profile (eq. 3.2) at the transition from the initial region to the fully developed region. Albertson et al (1950) circumvented this difficulty through adopting on the basis of experimental evidence a Gaussian profile which collapses by virtue of certain geometrical assumptions to a Gaussian free jet profile at the point of transition. A similar method is followed here.

For the turbulent shear layers in the initial region, the mean velocity distribution is approximated by a profile

$$u(x,y) = u_o \operatorname{sech}^2 \left(\frac{\sigma(y-\operatorname{sgn}(y)y_1)}{b_i}\right) \tag{3.4}$$

which is valid for $y_1 \lesssim y \lesssim -y_1$. y_1 marks the edge of the potential core (Fig. 3.2), y_2 is defined in a similar manner to the characteristic length parameter b by the equation

$$\frac{u(x,\, y_2(x))}{u_o} = \frac{1}{2} \tag{3.5}$$

and $b_i = y_2 - y_1$ (Fig. 3.2). Across the potential core, $-y_1 \lesssim y \lesssim y_1$,

$$u(x,y) = u_o \tag{3.6}$$

The parameters, y_1 and y_2, are assumed to be linear functions of x (Albertson et al, 1950)

$$\begin{aligned} y_1 &= b_o - x \tan \gamma_1 \\ y_2 &= b_o + x \tan \gamma_2 \end{aligned} \tag{3.7}$$

γ_1 and γ_2 are angular parameters defining the spread of the shear layers and hence are entrainment related. Integrating across the flow, the integral equations for the conservation of momentum and volume yield

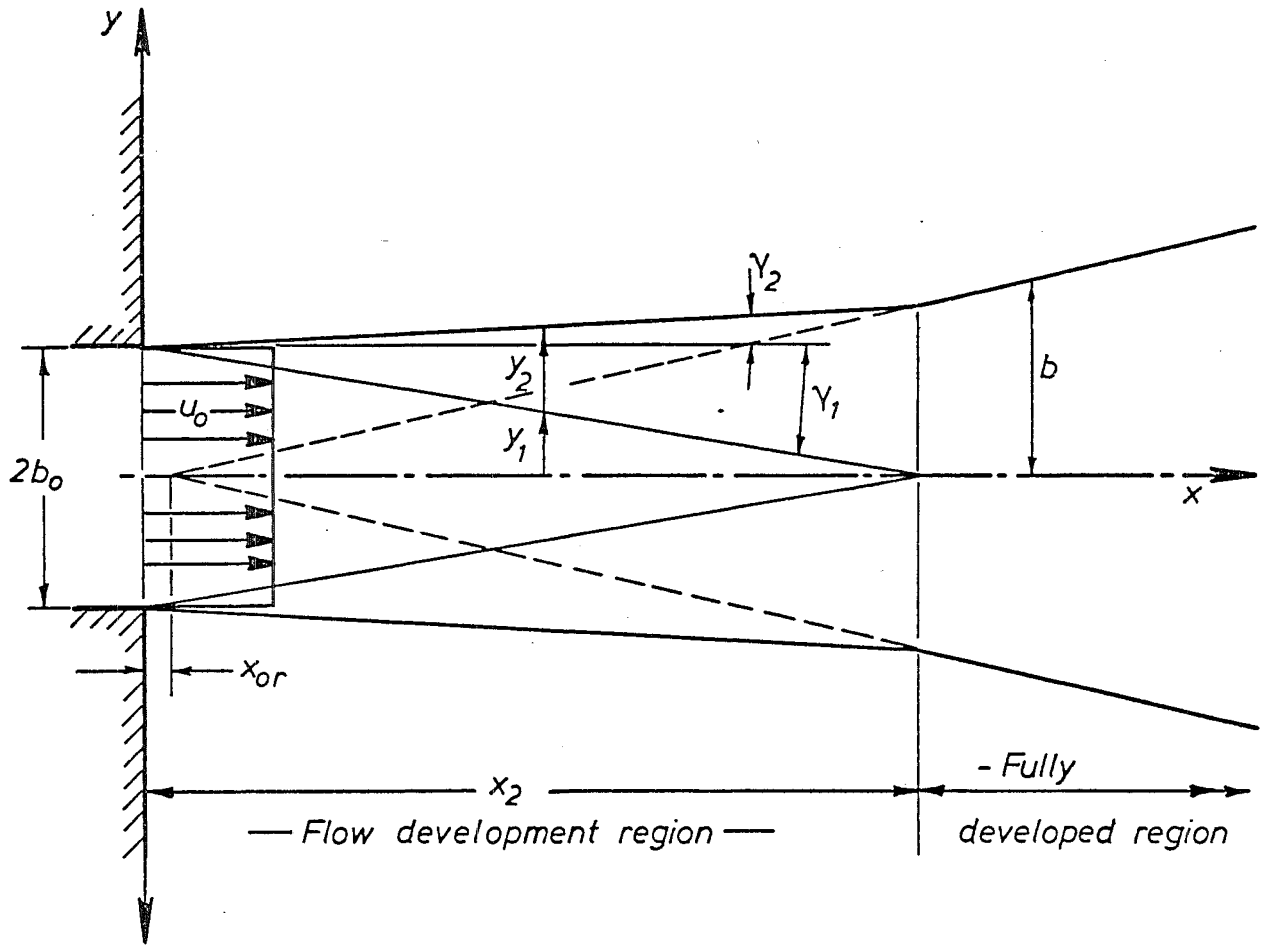

FIGURE 3.2 Geometry of the flow development region.

$$\gamma_2 = \tan^{-1}\left[(\tan\gamma_1)\left(\frac{3}{2}\sigma - 1\right)\right] \tag{3.8}$$

and

$$\alpha_i = \frac{1}{2}\tan\gamma_1 \tag{3.9}$$

where α_i is an entrainment coefficient. The specification of one of γ_1, γ_2 or α_i implies the other two, and the length of the potential core, x_2. For the purposes of this investigation, γ_1 has been assigned a value of 4.8^o (Rajaratnam, 1976) so that α_i is equal to 0.042 and x_2 is approximately $12b_o$.

Eqs. 3.4 and 3.7 indicate that at the exit the velocity profile across the jet becomes a top hat one of magnitude u_o and width $2b_o$. At the transition from the initial region to the fully developed region, the velocity profile defined by the same equations matches that defined by eq. 3.2.

3.4 FORMULATION OF THE INTEGRAL EQUATIONS OF MOTION

Similarity of all mean profiles at all cross-sections normal to the centreline is assumed for the curved jet flow in Fig. 3.1. Therefore the transverse distributions of mean velocity defined in section 3.3 are applicable.

Then, replacing x with s, the distance along the jet centreline measured from the real source, and y with n, the distance normal to the centreline, the integral equations for the conservation of volume, horizontal momentum and vertical momentum in the fully developed region can be written respectively as

$$\frac{d}{ds}\left\{u_c \frac{b}{\sigma} \int_{-\infty}^{+\infty} \operatorname{sech}^2 \eta \, d\eta\right\} = 2\alpha u_c \tag{3.10}$$

$$\frac{d}{ds}\left\{\rho u_c^2 \frac{b}{\sigma} \int_{-\infty}^{+\infty} \operatorname{sech}^4 \eta \, d\eta \cos\theta\right\} = -\Delta p \sin\theta \tag{3.11}$$

$$\frac{d}{ds}\left\{\rho\, u_c^2\, \frac{b}{\sigma} \int_{-\infty}^{+\infty} \operatorname{sech}^4\eta\, d\eta\, \sin\theta\right\} = \Delta p \cos\theta \tag{3.12}$$

The geometry of the coordinate system used (Fig. 3.1) yields two additional equations

$$\frac{dx}{ds} = \cos\theta \tag{3.13}$$

$$\frac{dy}{ds} = \sin\theta \tag{3.14}$$

The configuration equations 3.10, 3.11 and 3.12 are simplified by evaluating the integrals and defining volume and momentum flux parameters respectively as

$$Q = 2\, u_c \frac{b}{\sigma}, \quad M = \frac{4}{3}\, u_c^2 \frac{b}{\sigma} \tag{3.15}$$

Then

$$\frac{dQ}{ds} = 3\,\alpha\,\frac{M}{Q} \tag{3.16}$$

$$\frac{d}{ds}(M\cos\theta) = -\frac{\Delta p}{\rho}\sin\theta \tag{3.17}$$

$$\frac{d}{ds}(M\sin\theta) = \frac{\Delta p}{\rho}\cos\theta \tag{3.18}$$

Eqs. 3.17 and 3.18 are expanded and manipulated to yield

$$\frac{dM}{ds} = 0 \tag{3.19}$$

$$\frac{d\theta}{ds} = \frac{\Delta p}{\rho M} \tag{3.20}$$

Now using the nondimensionalisation

$$Q_* = \frac{Q}{Q_o}, \quad M_* = \frac{M}{M_o}, \quad \chi = \frac{2M_o}{Q_o^2}\, s, \quad x_* = \frac{2M_o}{Q_o^2}\, x, \quad y_* = \frac{2M_o}{Q_o^2}\, y \tag{3.21}$$

where $Q_o = u_o 2b_o$ and $M_o = u_o^2 2b_o$ are the reference volume and momentum flux parameters at the real source, eqs. 3.13, 3.14, 3.16, 3.19 and 3.20 reduce to

$$\frac{dQ_*}{d\chi} = \frac{3}{2}\,\alpha\,\frac{M_*}{Q_*} \tag{3.22}$$

$$\frac{dM_*}{d\chi} = 0 \tag{3.23}$$

$$\frac{d\theta}{d\chi} = \frac{\Delta p_*}{2M_*} \tag{3.24}$$

$$\frac{dx_*}{d\chi} = \cos\theta \tag{3.25}$$

$$\frac{dy_*}{d\chi} = \sin\theta \tag{3.26}$$

where by definition $\Delta p_* = \Delta p \; Q_o^2/\rho M_o^2$.

In the initial region, the integral equations for the conservation of volume, horizontal momentum, and vertical momentum are written by integrating across the flow zone in Fig. 3.2.

$$\frac{d}{ds}\left\{2 u_o \left[n_1 + \frac{b_i}{\sigma} \int_o^\infty \operatorname{sech}^2\left(\frac{\sigma(n-n_1)}{b_i}\right) d\left(\frac{\sigma(n-n_1)}{b_i}\right)\right\}\right. = 2 \alpha_i u_o \tag{3.27}$$

$$\frac{d}{ds}\left\{2\rho u_o^2 \left[n_1 + \frac{b_i}{\sigma} \int_o^\infty \operatorname{sech}^4\left(\frac{\sigma(n-n_1)}{b_i}\right) d\left(\frac{\sigma(n-n_1)}{b_i}\right)\right] \cos\theta \right\} =$$

$$-\Delta p \sin\theta \tag{3.28}$$

$$\frac{d}{ds}\left\{2\rho u_o^2 \left[n_1 + \frac{b_i}{\sigma} \int_o^\infty \operatorname{sech}^4\left(\frac{\sigma(n-n_1)}{b_i}\right) d\left(\frac{\sigma(n-n_1)}{b_i}\right)\right] \sin\theta \right\} =$$

$$\Delta p \cos\theta \tag{3.29}$$

The volume and momentum flux parameters are

$$Q = 2 u_o \left[n_1 + \frac{b_i}{\sigma} \int_o^\infty \operatorname{sech}^2\left(\frac{\sigma(n-n_1)}{b_i}\right) d\left(\frac{\sigma(n-n_1)}{b_i}\right)\right] \tag{3.30}$$

and

$$M = 2 u_o^2 \left[n_1 + \frac{b_i}{\sigma} \int_o^\infty \operatorname{sech}^4\left(\frac{\sigma(n-n_1)}{b_i}\right) d\left(\frac{\sigma(n-n_1)}{b_i}\right)\right] \tag{3.31}$$

Eqs. 3.28 and 3.29 are essentially of the same form as their counterparts for the fully developed region (eqs. 3.11 and 3.12) even though the

momentum flux parameter M is defined differently for the two flow regions. Thus they reduce to eqs. 3.17 and 3.18 respectively. Eq. 3.27 reduces to

$$\frac{dQ}{ds} = 2\alpha_i \frac{M_o}{Q_o} \tag{3.32}$$

The geometric relations expressed by eqs. 3.13 and 3.14 apply in the initial region and therefore the normalised ordinary differential equations 3.23 to 3.26 describe the initial region of flow development as well as the fully developed region. Eq. 3.32 in dimensionless form is

$$\frac{dQ_*}{d\chi} = \alpha_i \tag{3.33}$$

The initial conditions at $\chi = 0$ are $Q_* = M_* = 1$ and $\theta = x_* = y_* = 0$. Hence integrating eqs. 3.23 to 3.26 and 3.33 and substituting the initial conditions,

$$Q_* = 1 + \alpha_i \chi , \quad 0 \leq \chi \leq \chi_2 \tag{3.34}$$

$$M_* = 1 \tag{3.35}$$

$$\theta_* = \frac{\Delta p_*}{2M_*} \chi \tag{3.36}$$

$$x_* = \frac{2M_*}{\Delta p_*} \sin\theta \tag{3.37}$$

$$y_* = \frac{2M_*}{\Delta p_*} (1 - \cos\theta) \tag{3.38}$$

A virtual source defined by $Q_* = 0$ (Morton, 1961) can be imagined to exist at $\chi = \chi_{or}$ so that eq. 3.22 has the solution

$$Q_* = \sqrt{3 \alpha M_* (\chi - \chi_{or})} , \quad \chi_2 \leq \chi \tag{3.39}$$

The position of the virtual origin is dependent on the magnitude of the volume and momentum flux parameters at the equivalent source ($\chi = \chi_2$).

A constant pressure difference across the jet is seen from these solutions to cause a translation of the free jet trajectory such that the centreline follows a circular arc with radius of curvature $-2M_*/\Delta p_*$.

The entrainment coefficient α in the fully developed region has been assumed equal to 0.065 (Sawyer, 1963).

3.5 THE EDDY GEOMETRY

Across the eddy streamline there is zero net flow. Hence it is apparent that the volume flux of the downstream wall jet flow is equal to the initial jet efflux plus the entrained flux along the upper edge of the jet. By implication, the entrained flux along the lower edge of the jet is equal to the flux recirculated in the eddy.

For general centreline distance then, the position of the eddy streamline $\eta_e = \sigma n_e/b$ in the fully developed region is given by the equation

$$\int_{-\infty}^{n_e} u(s,n)\, dn = \int_{o}^{s_2} \alpha_i\, u_o\, ds + \int_{s_2}^{s} \alpha\ u_c(s)\, ds \qquad (3.40)$$

Evaluation and nondimensionalisation using the appropriate definitions yields

$$\sqrt{3\ \alpha\ (\chi - \chi_{or})}\quad \tanh \eta_e + 1 = 0 \qquad (3.41)$$

Eq. 3.41 defines the position of the eddy streamline relative to the centreline up to the station, $s = s_3$, (in dimensionless form $\chi = \chi_3$) at which the jet senses the proximity of the boundary. This station is defined to be where the inner edge of the jet meets the edge of the recirculating flow (Sawyer, 1963). The model is relatively insensitive to the position of the inner jet edge (Appendix G) and for the purposes of the investigation it is arbitrarily taken as the locus of points for which $u/u_c = 0.15$ ($\eta_{15} = \sigma n_{15}/b$). The intersection point of the edges

of the jet and the recirculating flow will be equidistant from the eddy streamline and the boundary (Fig. 3.1) if the velocity profile for the recirculating flow is assumed to be identical to that part of the free jet profile at $\chi = \chi_3$ for which $\eta_{15} < \eta < \eta_e$.

It is necessary to know the position of the eddy streamline on the boundary as this defines the attachment point and hence the eddy length. Suitable extrapolation of the eddy streamline to the boundary is required since eq. 3.41 is invalid as the jet divides upon impingement in the attachment region.

At best limits within which the attachment point is likely to lie can be defined. An obvious lower limit is the point vertically below the station, $\chi = \chi_3$, in which case the eddy length is the horizontal component of the centreline distance

$$l_{l_*} = (x_*)_{\chi_3} \tag{3.42}$$

An upper limit is defined by a linear extrapolation of the eddy streamline from the station, $\chi = \chi_3$, to the boundary so that the eddy length is

$$l_{u_*} = (x_*)_{\chi_3} + \frac{1}{\sigma}(b_*)_{\chi_3}\left[-\left|(\eta_e)_{\chi_3}\right| \sin\delta + \frac{\left(\left|(\eta_{15})_{\chi_3}\right| - \left|(\eta_e)_{\chi_3}\right|\right)(1 + \cos\delta)}{\tan\delta}\right] \tag{3.43}$$

where $\delta = \left|(\theta)_{\chi_3}\right|$.

A mean estimate of the attachment point is obtained by extrapolating the eddy streamline from the station, $\chi = \chi_3$, by means of a circular arc (Fig. 3.1) of radius $-(2M_*/\Delta p_* + \left|(\eta_e)_{\chi_3}\right|(b_*)_{\chi_3}/\sigma)$. The dimensionless eddy length is then

$$l_* = (x_*)_{\chi_3} + \frac{1}{\sigma}(b_*)_{\chi_3}\left[-|(\eta_e)_{\chi_3}|\sin\delta + \right.$$

$$\left.(|(\eta_{15})_{\chi_3}| - |(\eta_e)_{\chi_3}|)(1+\cos\delta)\tan\tau\right] \qquad (3.44)$$

where the angle τ, defined in Fig. 3.1, is given by the simultaneous solution of the two equations

$$\delta + \beta + \tau = \pi/2 \qquad (3.45)$$

and

$$\frac{(b_*)_{\chi_3}(|(\eta_{15})_{\chi_3}| - |(\eta_e)_{\chi_3}|)(1+\cos\delta)}{\sigma.\cos\tau} +$$

$$2\left(\frac{2M_*}{\Delta p_*} + \frac{1}{\sigma}(b_*)_{\chi_3}|(\eta_e)_{\chi_3}|\right)\sin\beta = 0 \qquad (3.46)$$

The dimensionless step height is given by

$$h_* = |(y_*)_{\chi_3}| + \frac{1}{\sigma}(b_*)_{\chi_3}\left[|(\eta_{15})_{\chi_3}|(1+\cos\delta) - \right.$$

$$\left.|(\eta_e)_{\chi_3}|\right] \qquad (3.47)$$

The geometry of the eddy is thus completely defined, enabling determination of the aspect ratio, l/h.

3.6 CONTROL VOLUME ANALYSES

A knowledge of the average pressure difference across the jet has so far been assumed. It will now be estimated by means of control volume analyses in which the jet is regarded as thin ($h/2b_o >> 1$).

Sawyer's (1960) measurements indicate that the static pressure distribution in the eddy is more complex than imagined in the assumed physical picture. This is particularly true in the attachment region. In a local control volume there (CGHIJ, Fig. 3.3), the error introduced when balancing momentum and ignoring pressure differences is likely to be

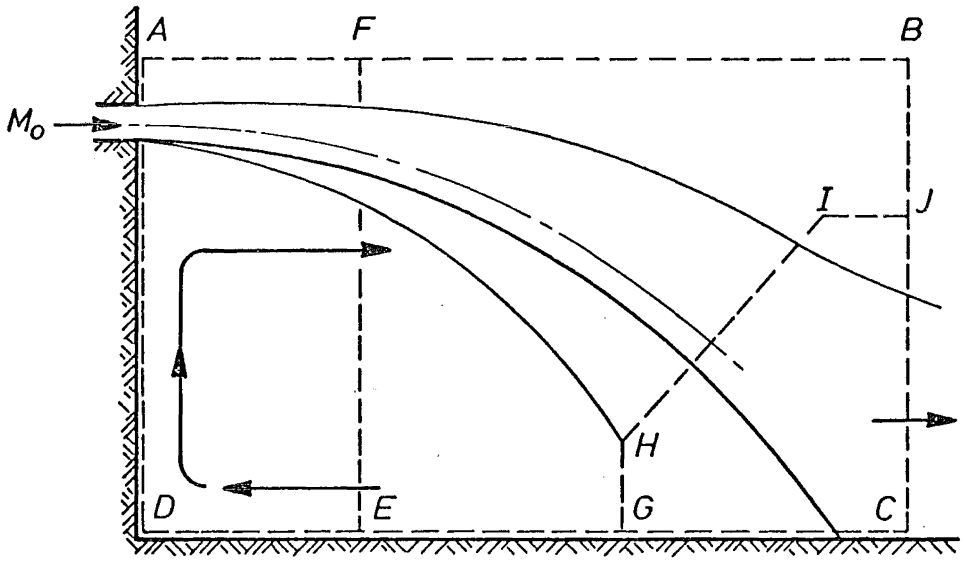

FIGURE 3.3 Control volumes used in the analyais of the attached jet.

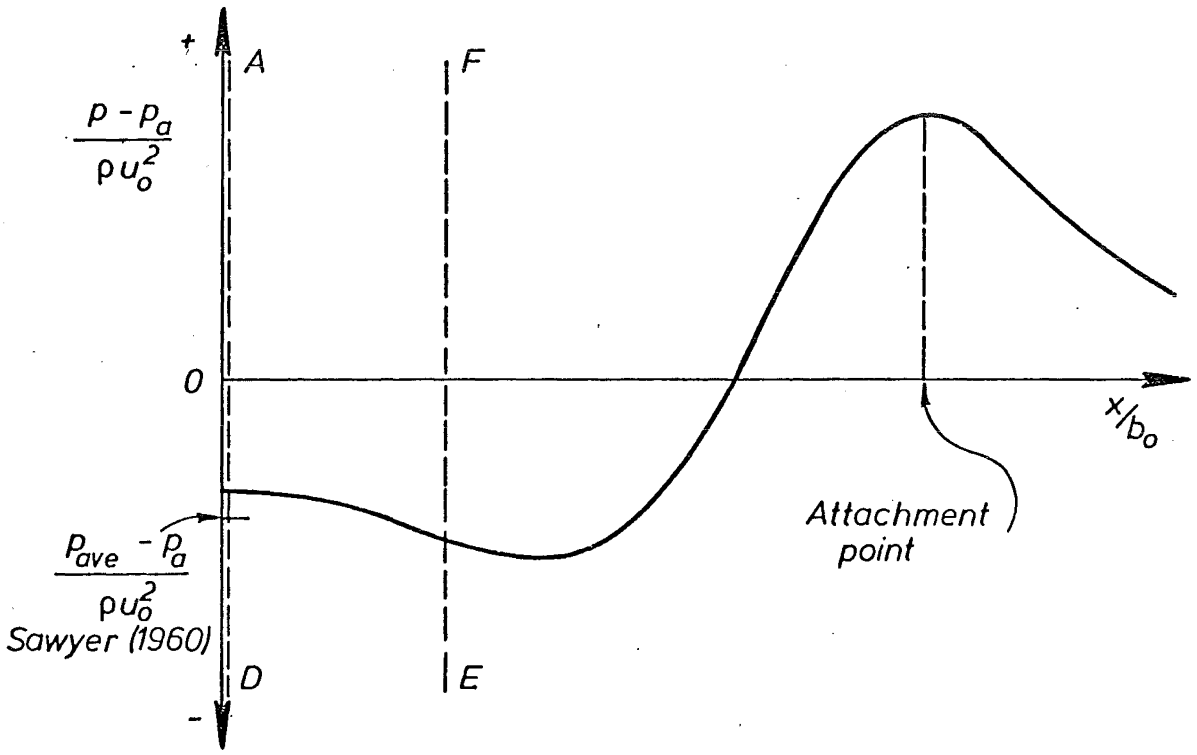

FIGURE 3.4 Static pressure distribution along the boundary as measured by Sawyer (1960).

significant. Thus other control volumes must be considered.

An estimate of the average pressure difference on the back of the step is obtained by considering a control volume ABCD (Fig. 3.3). The effects of skin friction along the boundary and the horizontal momentum component of the entrained fluid along the upper edge of the jet are ignored. At attachment the jet flow is assumed to divide in such a manner that the momentum flux is not dissipated. For a linear pressure difference gradient across the jet and a constant pressure difference Δp_{AD} on the back of the step, then

$$\Delta p_{AD}\, h = \rho \left[\left(u_c^2 \, \frac{b}{\sigma} \int_{\eta_e}^{+\infty} \operatorname{sech}^4 \eta \, d\eta \right)_{s_3} - M_o \right] \tag{3.48}$$

The magnitude of Δp_{AD} will be less than the magnitude of the average pressure difference across the jet (Fig. 3.4) because the step exerts a thrust on the recirculating flow to reverse its direction.

To model the reversal of the recirculating flow at the step, a second control volume AFED (Fig. 3.3) is considered. The jet flow at attachment is assumed to be non-dissipative so that the recirculating flow impinges on the step with momentum equal to that when it was turned by the horizontal boundary initially. As before, skin friction and momentum of the entrained fluid are neglected and a linear pressure difference gradient across the jet assumed.

Applying the momentum equation in the horizontal direction, the average pressure difference Δp_{AD} on the back of the step is related to an average pressure difference, Δp_{FE}, across the vertical section FE. It is supposed that this estimates a pressure difference nearer that corresponding to the negative peak along the boundary (Fig. 3.4)

$$(\Delta p_{AD} - \Delta p_{FE})\, h = 2\, \rho \left[\left(u_c^2 \, \frac{b}{\sigma} \int_{-\infty}^{\eta_e} \operatorname{sech}^4 \eta \, d\eta \right)_{s_3} \right] \tag{3.49}$$

The vertical section FE is regarded as sufficiently close to the step such that the slope of the jet trajectory is small and $(M \cos\theta)_{s_{FE}} \simeq (M)_{s_{FE}}$.

The average pressure difference Δp across the jet will lie between the average pressure differences on the vertical sections, AD and FE (Fig. 3.4). It is estimated by the mean of Δp_{AD} and Δp_{FE}.

$$\Delta p = \frac{1}{2} (\Delta p_{AD} + \Delta p_{FE})$$

$$= \frac{\rho}{h} \{ \left[u_c^2 \frac{b}{\sigma} \left(\int_{\eta_e}^{\infty} \operatorname{sech}^4 \eta \, d\eta - \int_{-\infty}^{\eta_e} \operatorname{sech}^4 \eta \, d\eta \right) \right]_{s_3} - M_o \} \qquad (3.50)$$

Expressed in dimensionless form with the integrals evaluated, the under pressure is

$$\Delta p_* = \frac{1}{h_*} \{ 3(M_*)_{\chi_3} \left[- \tanh(\eta_e)_{\chi_3} + \frac{1}{3} \tanh^3 (\eta_e)_{\chi_3} \right] - 2 \} \qquad (3.51)$$

Due to the non-buoyant nature of the flow (which implies that the momentum flux of the jet is constant) and the assumption of a non-dissipative division of flow at attachment, it is found that the average pressure differences across the vertical sections FE and AD are exactly ± 50% of the estimated under pressure Δp respectively. The model proves fairly sensitive to such a variation of under pressure.

A comparison of the model predictions for the under pressure across the vertical section FE with Sawyer's (1960) measurements of the static pressure distribution along the boundary indicates that the section FE generally occurs just to the left (on the step side) of the negative peak (Fig. 3.4). However, at the lower end of the step height range, the estimates of the average pressure difference across the section FE exceed the corresponding data for the magnitude of the maximum negative pressure difference along the boundary.

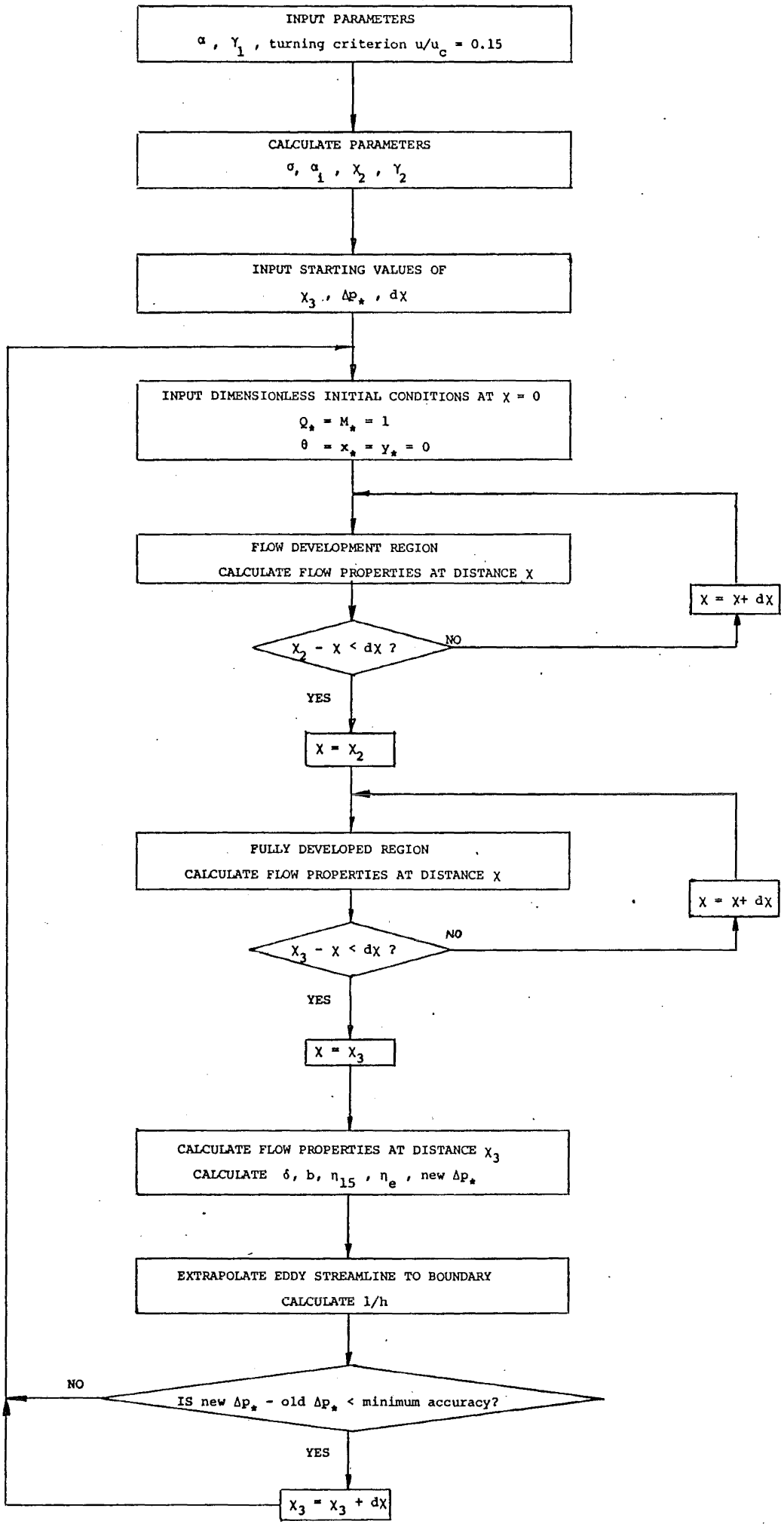

FIGURE 3.5 Solution procedure for attached non-buoyant jet model.

It is also found from Sawyer's (1960) measurements of the static pressure distribution along the boundary that the position at which the model defines the inner jet edge to intersect the edge of the recirculating flow lies directly above a point on the boundary to the left of the position where the pressure difference is zero ($p - p_a = 0$).

3.7 SUMMARY

A simple entrainment model of a two-dimensional attached pure jet has been developed. In this model, the eddy geometry, expressed by the aspect ratio, l/h, and the dimensionless pressure difference across the jet, Δp_*, have been found as functions of the dimensionless step height, h_*. The solution procedure for the model is outlined in Fig. 3.5.

The model predictions are compared with some experimental data in Chapter 7.

CHAPTER 4

THE ADDITION OF A PASSIVE CONTAMINANT TO AN ATTACHED JET

4.1 INTRODUCTION

It was argued in the previous chapter that, since momentum effects are dominant near the source of a two-dimensional buoyant jet, the flow in this region can be approximately treated as a pure jet. An analytical entrainment model of the flow up to the point of attachment was developed on this basis. The next logical step in understanding the buoyant situation is to study the addition of a passive contaminant to the pure jet.

Some preliminary experiments indicated that when a passive tracer is added to the jet efflux, a uniform concentration distribution eventually forms in the eddy. This means that in the steady buoyant situation where the buoyancy is produced by an excess inflow temperature, the temperature in the eddy will be constant throughout.

The formation of an equilibrium concentration in the eddy implies a zero net transfer of tracer flux across the eddy streamline. The problem is treated then by initially ignoring the curvature of the flow and incorporating a flux of tracer and a uniform field of tracer on one side of the flow in the solution of a horizontal non-buoyant jet into an unconfined reservoir. For there to be a zero net transfer of tracer flux across a particular streamline, the streamline must cut the same line of constant tracer flux twice. The constant tracer flux line ψ_{t_η} that is of interest is the one defining the mean tracer flux (measured from the upper jet edge) equal to the efflux. The position of this constant tracer flux line

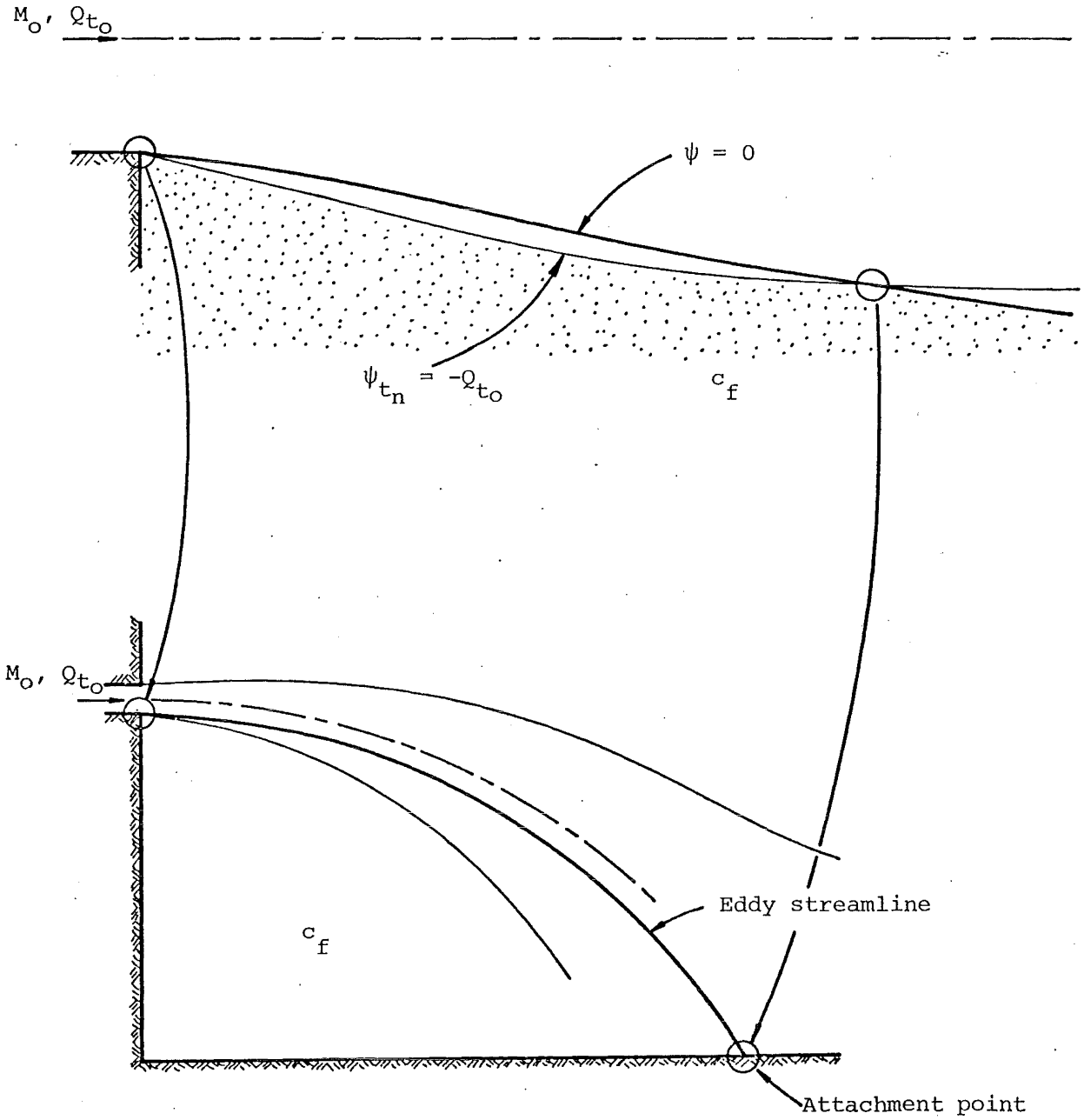

FIGURE 4.1 Relationship between the intersection point of a streamline and a line of constant tracer flux in a plane jet and the attachment point in an attached jet.

changes according to the relative strengths of the inflow concentration and the uniform field concentration. The streamline corresponding to the eddy streamline in the attached jet situation cuts the constant tracer flux line ψ_{t_η} at the jet exit and at some distance downstream (Fig. 4.1). Now the downstream intersection point can be related to the attachment point in the attached jet situation. Thus the ratio of the uniform field concentration (or eddy concentration), to the inflow concentration of tracer, can be expressed as a function of dimensionless step height

$$\frac{c_f}{c_o} = f(\frac{h}{b_o}) \tag{4.1}$$

which is consistent with the form of the dimensional analysis prediction. Reynolds number effects are implicitly assumed to be insignificant.

4.2 EQUATIONS FOR THE CONSERVATION OF A PASSIVE CONTAMINANT

For steady incompressible two-dimensional flow in which molecular diffusion can be ignored, the partial differential equation for the conservation of a passive contaminant is

$$u \frac{\partial c}{\partial x} + v \frac{\partial c}{\partial y} = 0 \tag{4.2}$$

where u and v are the components of velocity in the x and y directions and c is the tracer concentration. This conservation equation is linear in c meaning that solutions for different concentration boundary and initial conditions in the same flow field can be superimposed.

4.2.1 The Partial Differential Equation for the Conservation of a Passive Contaminant Incorporating a Constant Eddy Mass Diffusivity

Since the flow is turbulent, u, v and c in eq. 4.2 can each be expressed as the sum of a mean value (denoted by an overbar) and a randomly varying fluctuation (denoted by a prime). Therefore the time-averaged

equation for the conservation of a passive contaminant is

$$\bar{u}\frac{\partial \bar{c}}{\partial x} + \bar{v}\frac{\partial \bar{c}}{\partial x} + \frac{\partial}{\partial x}\left(\overline{c'u'}\right) + \frac{\partial}{\partial y}\left(\overline{c'v'}\right) = 0 \qquad (4.3)$$

Prandtl's eddy viscosity hypothesis relates the Reynolds stress $-\overline{u'v'}$ to the velocity gradient $\partial\bar{u}/\partial y$ by an eddy viscosity ε_m, assumed constant for a given normal cross-section (Schlichting, 1960). Along similar lines the quantity $-\overline{c'v'}$, representing the turbulent transfer of tracer by fluctuations in the transverse velocity, is related to the concentration gradient $\partial\bar{c}/\partial y$ by an eddy mass diffusivity ε_D (Prandtl, 1960), also assumed constant for a given normal cross-section.

$$-\overline{c'v'} = \varepsilon_D \frac{\partial \bar{c}}{\partial y} \qquad (4.4)$$

Adopting this hypothesis and regarding turbulent diffusion in the longitudinal direction as insignificant compared with advective transport of the tracer, e.g. 4.3 reduces to

$$u\frac{\partial c}{\partial x} + v\frac{\partial c}{\partial y} - \varepsilon_D \frac{\partial^2 c}{\partial y^2} = 0 \qquad (4.5)$$

in which the overbars denoting mean quantities are no longer essential. This partial differential equation is also linear in c implying that the superposition of solutions for different concentration boundary and initial conditions in the same flow field is valid.

The ratio of the eddy mass diffusivity to the eddy viscosity is assumed to be a constant, $\varepsilon_D/\varepsilon_m = \lambda^2$, and is a measure of the relative rate of spread of mass and momentum. It is generally agreed in the literature that $\lambda^2 > 1$ although there exists a degree of uncertainty over a suitable value due to the paucity of data. This is particularly true for the turbulent diffusion of mass in a liquid medium.

Forstall and Gaylord (1955) studied momentum and mass transfer in an axially symmetric water jet and concluded that the turbulent diffusion of mass in water is similar to the turbulent diffusion of heat in air. On the basis then of data collated by Abramovich (1963) from experiments with heated air jets and jets with an added gaseous tracer, a value of $\lambda^2 = 2$ for a plane jet seems reasonable. Chen and Rodi (1980) in their review of experimental data for vertical turbulent buoyant jets also recommend this value.

4.2.2 The Integral Equation for the Conservation of a Passive Contaminant

Integrating eq. 4.3 across the fully developed flow and using the entrainment approach yields

$$\frac{d}{dx}\left\{\int_{-\infty}^{+\infty} c(x,y)\ u(x,y)\ dy\right\} = \alpha\ u_c\left[\lim_{y\to+\infty} c(x,y) + \lim_{y\to-\infty} c(x,y)\right] \quad (4.6)$$

It is assumed that turbulent transport in the longitudinal direction is negligible in comparison with advective transport ($\bar{u}\bar{c} >> \overline{u'c'}$) and that turbulent transport in the transverse direction tends to zero at large distances from the centreline

$$\lim_{y\to\pm\infty} \overline{c'v'} = 0$$

The functions $u(x,y)$ and $c(x,y)$ are the time-averaged mean transverse distribution of velocity and concentration respectively (the overbars are unnecessary) and the integral with respect to y of their product represents the flux of tracer Q_t at any normal cross-section to the jet centreline

$$Q_t = \int_{-\infty}^{+\infty} c(x,y)\ u(x,y)\ dy \quad (4.7)$$

Eq. 4.6 is linear in c so that the linear superposition of solutions is valid.

4.3 DERIVATION OF CONCENTRATION PROFILES

When a passive tracer is added to the efflux of an attached jet, a uniform concentration distribution forms in the eddy. If the curvature of the flow is ignored then, this situation is equivalent to that of a line source of momentum and tracer flux discharging into an infinite reservoir with a uniform field of tracer on one side of the flow. The relevant equations (4.5 and 4.6) are linear in tracer concentration c and the solution for this case can be obtained from the linear superposition of the solutions for two simpler cases (Fig. 4.2):

(i) a line source of momentum flux and tracer flux discharging into an infinite reservoir

(ii) a line source of momentum flux only discharging into an infinite reservoir, uniformly contaminated on one side of the flow by a field of tracer of concentration, c_f.

The steps taken in the derivation of the solutions for cases (i) and (ii) are outlined in Fig. 4.3. Initially it is assumed for ease of argument that the lateral spreading rates of momentum and tracer are identical ($\lambda^2 = 1$). Since the presence of the initial region cannot be ignored, the problem again arises of how to relate a flux parameter at the real source to the same parameter in the fully developed region ($x > x_2$, Fig. 3.2). It is assumed that the tracer flux is known for an equivalent source (step 1, Fig. 4.3) at the transition from the initial region to the fully developed region ($x = x_2$, Fig. 3.2) (Morton, 1961). The solution to the integral tracer conservation equation in the fully developed region is found to be dependent on the solution to the integral continuity equation (eq. 4.6 is linear in c). Thus the line sources of momentum flux and tracer flux can be imagined to emanate from a common virtual origin (step 2, Fig. 4.3). The position of the virtual origin

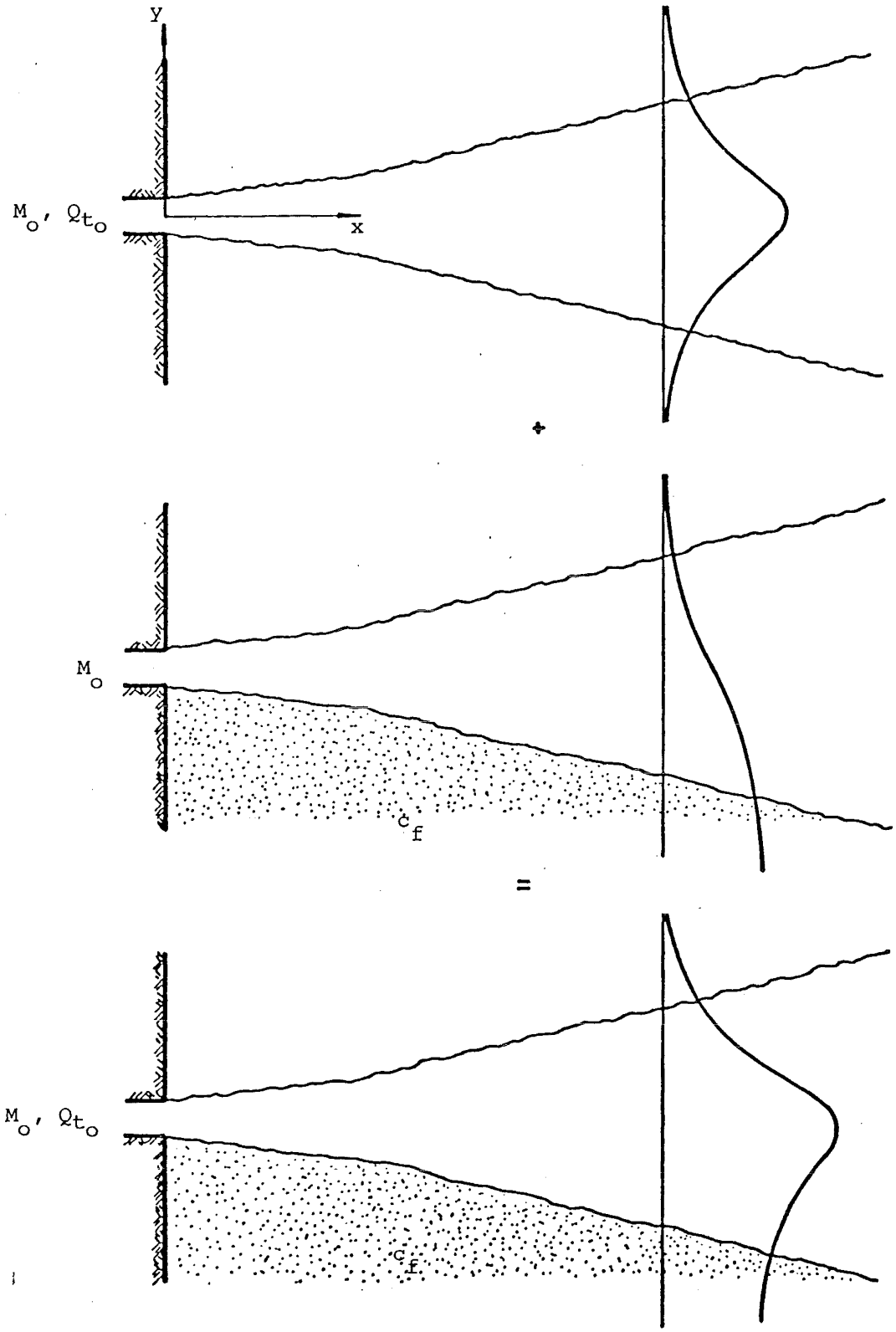

FIGURE 4.2 Linear superposition of solutions for a line source of momentum flux and tracer flux discharging into a large reservoir with a uniform field of tracer on one side of the flow.

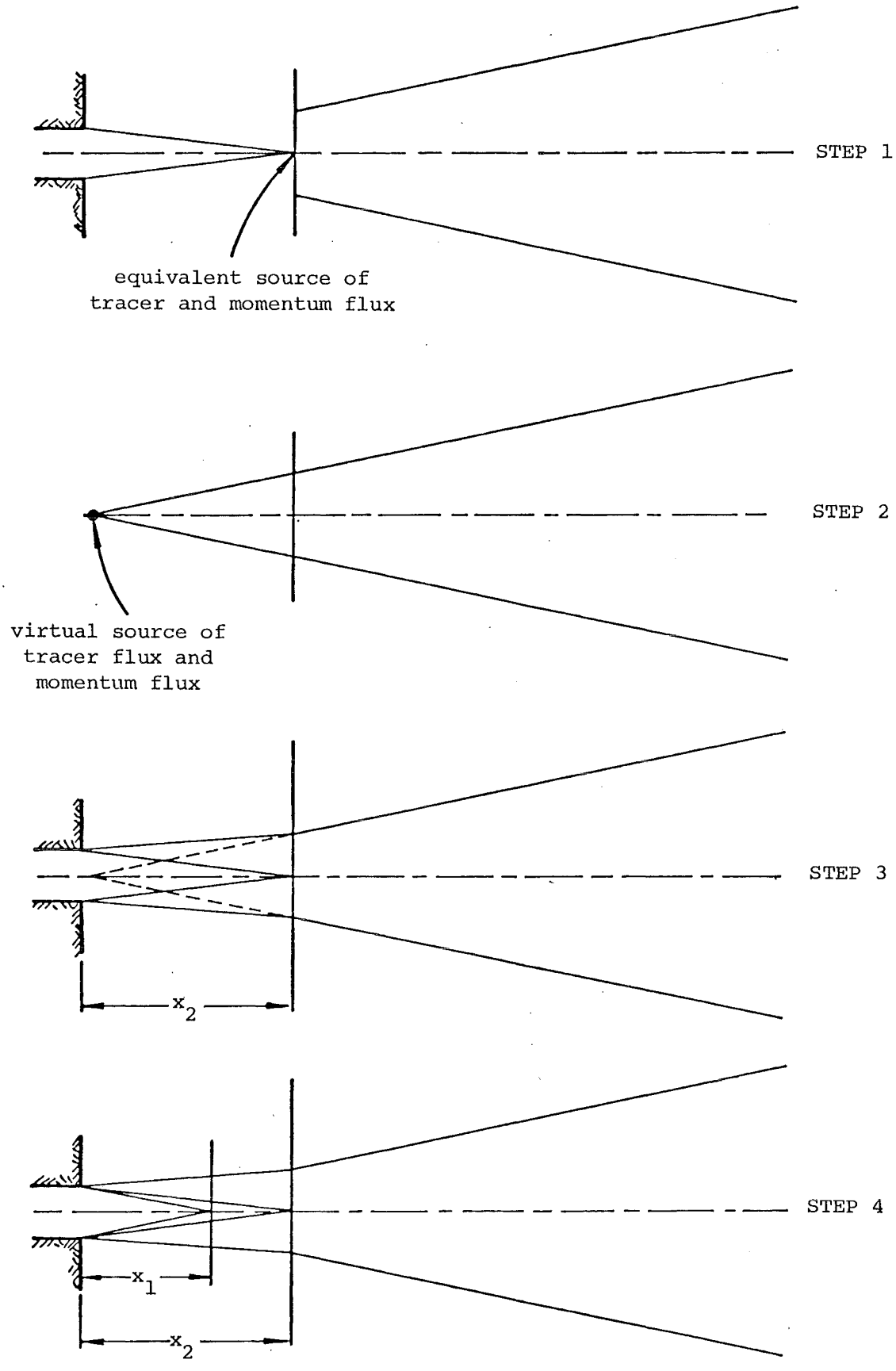

FIGURE 4.3 Outline of method to obtain solutions for cases (i) and (ii).

is determined by the characteristic momentum and volume fluxes of the equivalent source. Previously these same fluxes at the equivalent source have been related to their counterparts at the real source by an approximation to the geometry of the initial region and the assumption of a suitable velocity profile across the flow (section 3.3). In a similar way the tracer fluxes at the real and equivalent sources can be related (step 3, Fig. 4.3).

The positions of the equivalent sources for the line sources of momentum flux and tracer flux differ (Fig. 4.7) when the lateral spreading rates of momentum and tracer are assumed to differ ($\lambda^2 = 2$). The final step (step 4, Fig. 4.3) consists of relating the tracer fluxes at the real and equivalent sources for this situation.

4.3.1 Concentration Profiles for $\lambda^2 = 1$

For case (i) the solution of the integral equation for the conservation of tracer (eq. 4.6) indicates that $Q_t = Q_{t_o}$, where $Q_{t_o} = c_o u_o 2b_o$ is the reference flux of tracer at the real source assuming uniform velocity and concentration profiles. The jet can be imagined then to emanate as a line source of momentum flux, M_o, and trac er flux Q_{t_o}, from a common virtual origin at $x = x_{or}$. The solution to the partial differential equation for the conservation of tracer (eq. 4.5) gives a concentration profile across the jet (Appendix A)

$$c(x,y) = c_c(x) \operatorname{sech}^2 \eta \tag{4.8}$$

where the centreline concentration $c_c(x)$ is defined by

$$c_c(x) = \frac{3\, Q_{t_o}}{2\sqrt{6\, \alpha\, M_o\, (x-x_{or})}} \tag{4.9}$$

The variation of centreline concentration with distance from the virtual origin is shown in Fig. 4.4.

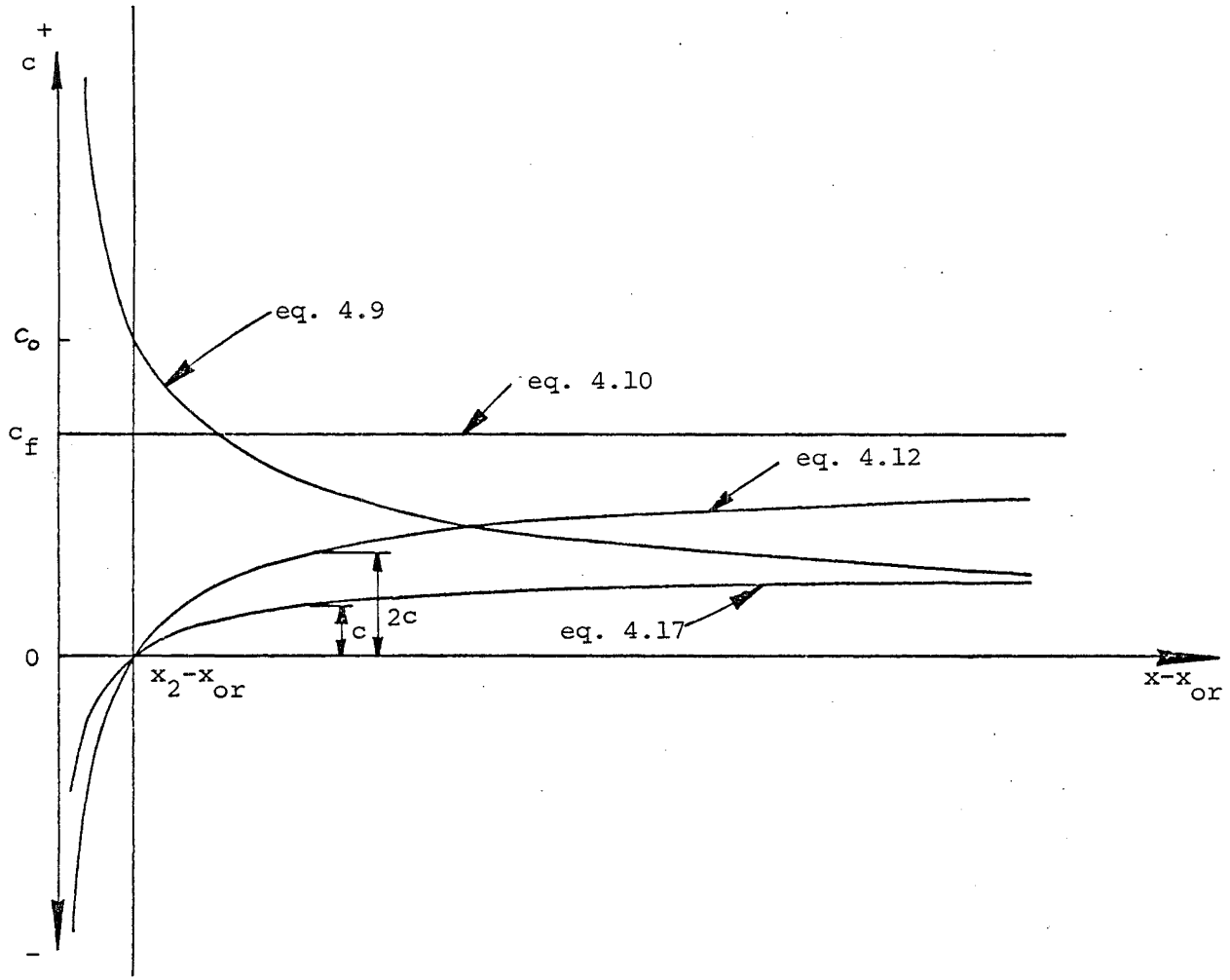

FIGURE 4.4 Variation of centreline concentration with distance.

For case (ii) the solution to the integral equation (eq. 4.6) suggests that the centreline concentration is independent of distance. The solution to eq. 4.5 then (Appendix A) gives a concentration profile across the jet

$$c(x,y) = \frac{1}{2} c_f(1 - \tanh \eta) \qquad (4.10)$$

where c_f is the concentration of tracer in the uniform field. The centreline concentration is apparently equal to a value of half of the uniform field concentration. Since the centreline concentration does not vary with distance, this solution cannot have a virtual origin.

The writer has recently become aware of a similar result obtained by Hestroni *et al* (1965) on the basis of Reichardt's inductive theory of turbulence (Schlichting, 1960). Hestroni *et al* studied a plane air jet subjected to asymmetric ambient temperatures.

The lack of a virtual origin implies that this line source solution (eq. 4.10) cannot take account of the initial region. The solution implicitly assumes turbulent diffusion of tracer across the jet centreline along the entire length of the flow from the momentum source, whereas in the real sense diffusion across the centreline is significant only beyond the initial flow region ($x > x_2$). The centreline concentration of tracer is expected to vary then as a function of distance, growing from zero at the transition from the initial region ($x = x_2$) and tending asymptotically towards that predicted by eq. 4.10. Suitable modification of the solution obtained for case (ii) (eq. 4.10) is required if the tracer concentration distribution across the jet is to be satisfactorily described in the region immediately beyond the initial one.

It has been argued previously that the linear superposition of solutions for different concentration boundary conditions and initial conditions in the same flow field is valid because the equations for the

conservation of tracer are linear in c. By the same reasoning, the linear decomposition of solutions is valid.

It is possible to obtain another solution for case (ii) which contains a virtual origin at the same position as in case (i) by linearly decomposing the solution for a line source of momentum flux discharging into an infinite reservoir that is uniformly contaminated throughout with tracer of concentration c_f (Fig. 4.5). The latter situation can be treated as a line source of momentum flux and concentration deficit flux flowing into a large reservoir, in which case the solution is by analogy with eqs. 4.8 and 4.9

$$c_f - c(x,y) = (c_f - c_c(x)) \ \mathrm{sech}^2\eta \tag{4.11}$$

where

$$c_f - c_c(x) = \frac{3\, c_f\, Q_o}{2\sqrt{6\, \alpha\, M_o\, (x-x_{or})}} \tag{4.12}$$

The centreline concentration is shown as a function of distance in Fig. 4.4. The virtual origin occurs at the same position as in case (i).

From the solution defined by eq. 4.11 two solutions, $c_1(x,y)$ and $c_2(x,y)$, can be obtained that correspond to the cases in which a line source of momentum flux discharges into a large reservoir uniformly contaminated on opposite sides of the flow (Fig. 4.5). The linear sum of $c_1(x,y)$ and $c_2(x,y)$ must equal the concentration profile $c(x,y)$ defined by eq. 4.11

$$c_1(x,y) + c_2(x,y) = c_f - \frac{3\, c_f\, Q_o}{2\sqrt{6\, \alpha\, M_o\, (x-x_{or})}}\ \mathrm{sech}^2\eta \tag{4.13}$$

and $c_1(x,y)$ and $c_2(x,y)$ must be mirror images of each other about the x axis

$$c_1(x,y) = c_2(x,-y) \tag{4.14}$$

$c_2(x,y)$ must also satisfy the boundary conditions

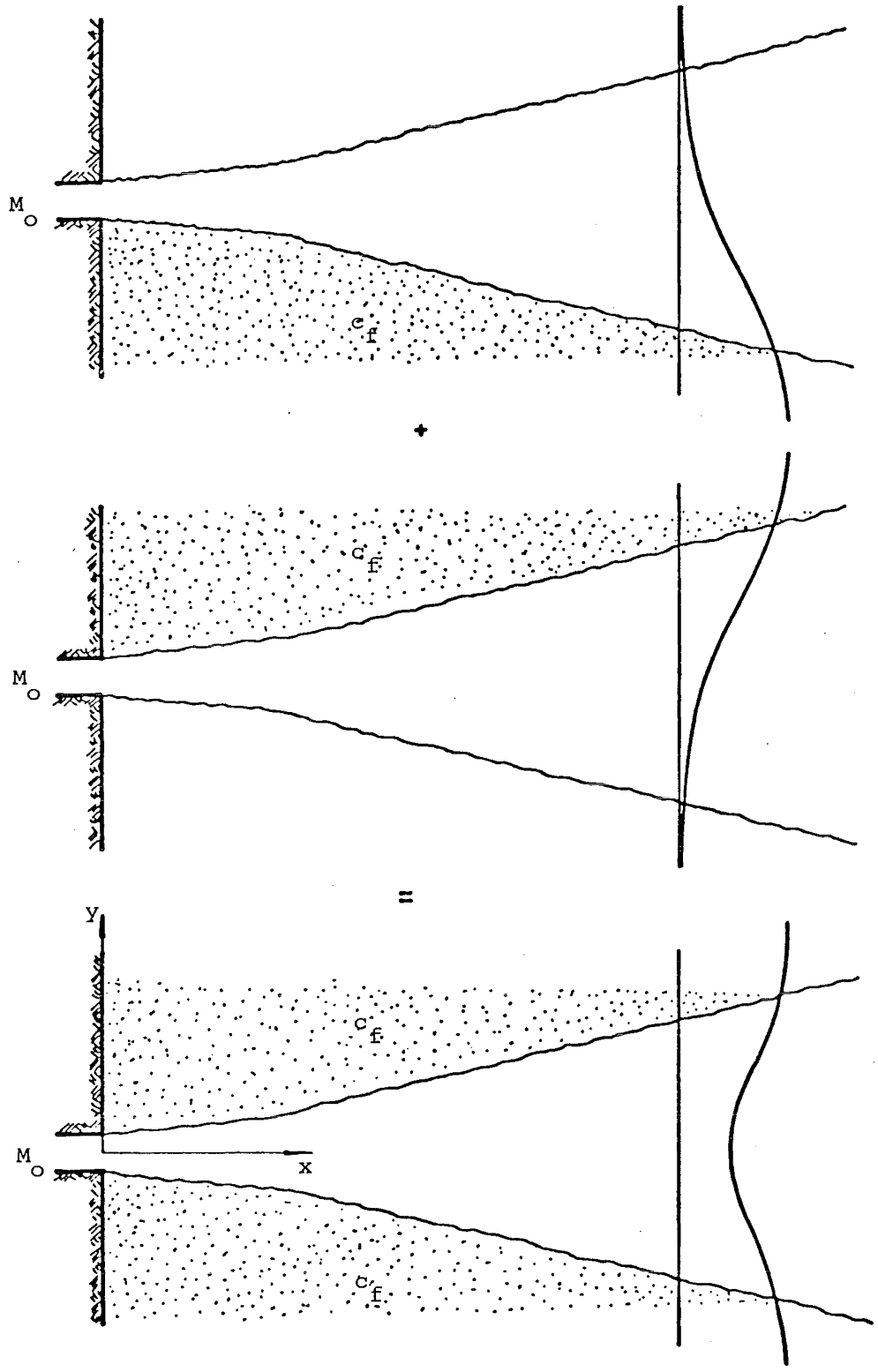

FIGURE 4.5 Linear superposition of solutions for a line source of momentum flux only discharging into a large reservoir uniformly contaminated throughout.

$$\lim_{y\to+\infty} c_2(x,y) = 0$$

$$\lim_{y\to-\infty} c_2(x,y) = c_f \qquad (4.15)$$

and, at large distances from the source, tend to the profile originally obtained

$$\lim_{x\to\infty} c_2(x,y) = \frac{1}{2} c_f(1 - \tanh \eta) \qquad (4.16)$$

The profile defined in eq. 4.11 is composed of a uniform part of magnitude $c_f(1 - 3 Q_o/(2\sqrt{6 \alpha M_o (x-x_{or})}))$ (AB, Fig. 4.6) and another part varying as $(3 c_f Q_o/(2\sqrt{6 \alpha M_o (x-x_{or})}))$ $(1-\text{sech}^2\eta)$. By treating the individual parts separately, the profile can be decomposed such that all the conditions expressed by eqs. 4.13 to 4.16 are satisfied (Fig. 4.6). It is found that

$$c_2(x,y) = \frac{1}{2} c_f \left(1 - \frac{3 Q_o}{2\sqrt{6 \alpha M_o (x-x_{or})}}\right) (1 - \tanh \eta)$$

$$+ \frac{3 c_f Q_o}{2\sqrt{6 \alpha M_o (x-x_{or})}} (1 - \text{sech}^2\eta) (1 - H(\eta)) \qquad (4.17)$$

$H(\eta)$ is the Heaviside or unit step function defined to be

$$H(\eta) = \begin{cases} 0 & \eta < 0 \\ 1 & 0 \leq \eta \end{cases} \qquad (4.18)$$

The profile defined by eq. 4.17 represents the solution for case (ii) which contains a virtual origin at the same position as in case (i). Fig. 4.3 illustrates the variation of centreline concentration with distance from the virtual origin. For a given centreline distance, the centreline concentration is exactly half that for the solution defined by eq. 4.11. At large distances from the origin the solution (eq. 4.17) tends to the one originally obtained (eq. 4.10).

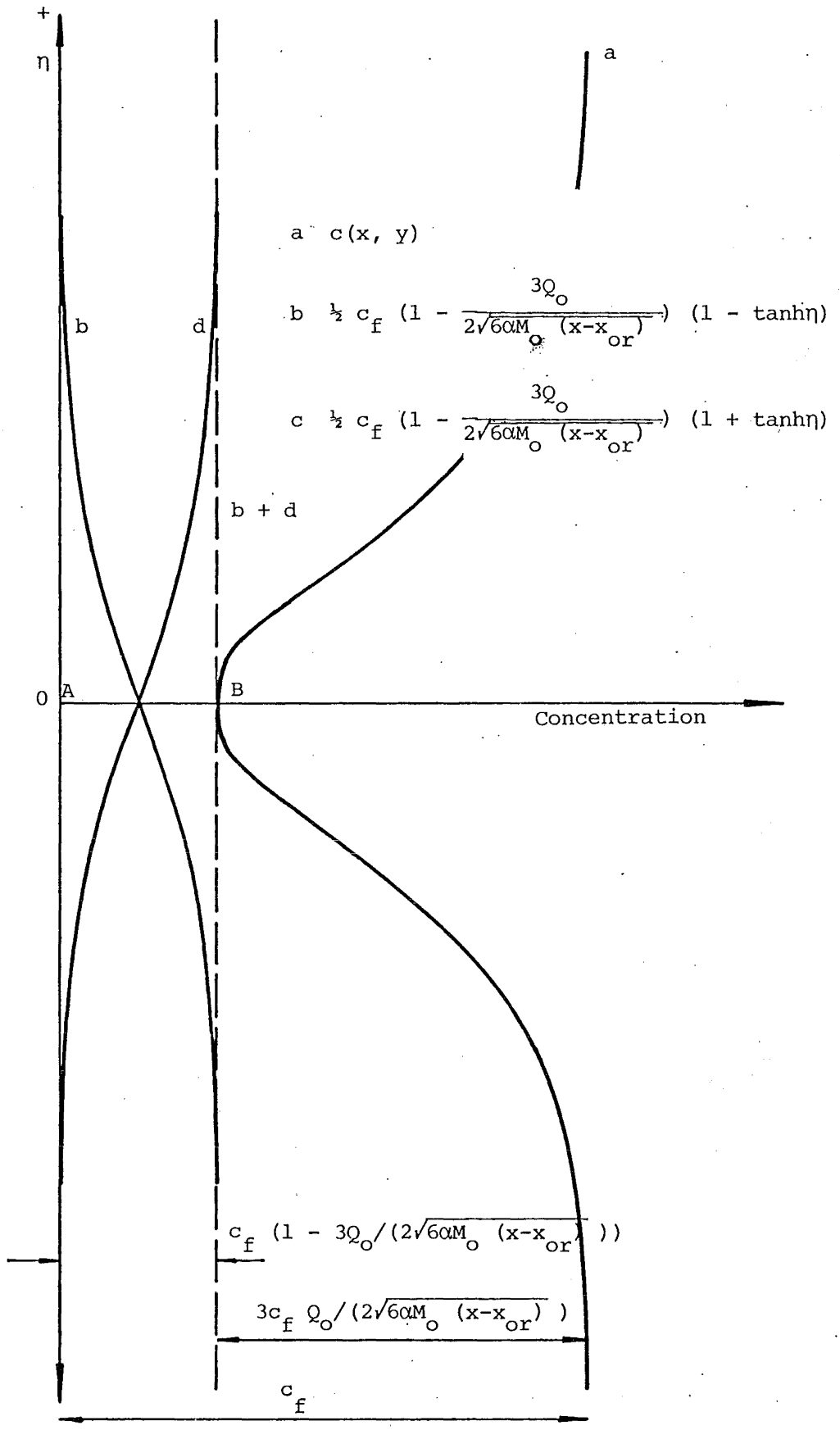

FIGURE 4.6 Linear decomposition of the concentration profile $c(x, y) = c_f \left(1 - \frac{3Q_o}{2\sqrt{6\alpha M_o (x-x_{or})}} \operatorname{sech}^2 \eta\right)$

The solutions derived so far for a line source emanating from a virtual origin (eqs. 4.8, 4.11 and 4.17) are meaningful in a physical sense only in the fully developed region ($x > x_2$, Fig. 4.4). In the same way that the volume and momentum fluxes characteristic of an equivalent source at the end of the initial region (the magnitudes of which determined the position of the virtual origin) were related back to their counterparts at the real source, the tracer flux at the same equivalent source must be related back to the reference flux at the real source also to obtain a solution in the initial region.

In the fully developed region, the solution for a line source of momentum flux and tracer flux discharging into an infinite reservoir uniformly contaminated on one side ($\eta < 0$) of the flow (the linear superposition of cases (i) and (ii), Fig. 4.2) is from eqs. 4.8 and 4.17

$$c(x,y) = \frac{3\, c_o\, Q_o}{2\sqrt{6\,\alpha\, M_o\,(x-x_{or})}}\ \mathrm{sech}^2\,\eta + \frac{1}{2}\, c_f\left(1 - \frac{3\, Q_o}{2\sqrt{6\,\alpha\, M_o\,(x-x_{or})}}\right)(1 - \tanh\eta) + \frac{3\, c_f\, Q_o}{2\sqrt{6\,\alpha\, M_o\,(x-x_{or})}}\,(1 - \mathrm{sech}^2\,\eta)\,(1 - H(\eta)) \qquad (4.19)$$

4.3.2 Concentration Profiles in the Flow Development Region

Solutions have been obtained for cases (i) and (ii) as though an imaginary line source emanates from a virtual origin at $x = x_{or}$ (Fig. 4.8). The solutions are not applicable in the initial region. They must be modified in an appropriate manner so that the tracer efflux at the real source is related to the flux of tracer at an equivalent source at the transition from the initial region to the fully developed region ($x=x_2$, Fig. 4.8).

Since turbulent diffusion of mass occurs at a greater rate than the diffusion of momentum, the velocity and concentration potential cores will not coincide. In particular, $x_1 < x_2$, where x_2 and x_1 denote the positions along the jet centreline of the apexes of the velocity and concentration potential cores respectively (Fig. 4.8). However, to simplify the presentation of the basic arguments, it has been assumed that $\lambda^2 = 1$ initially. Thus both potential cores coincide and the geometry defining the spread of momentum in the turbulent shear layers of the initial flow region is also suitable to define the spread of tracer.

The mean concentration distributions for cases (i) and (ii) in the initial region are approximated in a similar manner to the velocity distribution. Turbulent diffusion of tracer across the edges of the potential core is likely to be insignificant so that it is reasonable to assume a constant concentration along them. The forms of the profiles across the shear layers are determined by the forms of the corresponding profiles assumed for the fully developed region.

For cases (i) then, the mean concentration distribution across the jet is approximated by a profile

$$\begin{aligned} c(x,y) &= c_o && -y_1 \leq y \leq y_1 \\ c(x,y) &= c_o \operatorname{sech}^2(\sigma(y-\operatorname{sgn}(y)\, y_1)/(y_2-y_1)) && y_1 \leq y \leq -y_1 \end{aligned} \tag{4.20}$$

The profile defined in eq. 4.17 for case (ii) in the fully developed region is expressed as the linear sum of two terms, one of which tends conveniently to zero at the transition from the initial region. Thus the form of the second term determines the form of the approximation to the mean concentration distribution across the shear layer in the initial region. Across the remaining part of the jet, the concentration is zero.

Then

$$c(x,y) = c_f\left[1 - \operatorname{sech}^2(\sigma(y-\operatorname{sgn}(y)\ y_1)/(y_2-y_1))\right] \quad y \lesssim -y_3$$

$$c(x,y) = 0 \qquad -y_3 \lesssim y \tag{4.21}$$

For the linear superposition of cases (i) and (ii) (Fig. 4.2) the appropriate mean concentration profile in the initial region is

$$c(x,y) = c_o \qquad -y_1 \lesssim y \lesssim y_1$$

$$c(x,y) = c_o \operatorname{sech}^2(\sigma(y-\operatorname{sgn}(y)\ y_1)/(y_2-y_1)) + \tag{4.22}$$

$$c_f\left[1 - \operatorname{sech}^2(\sigma(y-\operatorname{sgn}(y)\ y_1)/(y_2-y_1))\right]$$

$$(1 - H(y-\operatorname{sgn}(y)\ y_1)) \quad y_1 \lesssim y \lesssim -y_1$$

4.3.3 Concentration Profiles for $\lambda^2 = 2$

The mean concentration profiles obtained previously have been derived assuming for simplicity that the turbulent diffusion of mass occurs at the same rate as the turbulent diffusion of momentum ($\lambda^2 = 1$). It is observed that the turbulent diffusion rates for mass and momentum are not equal. This means that the tracer flux at the real source must be related to the tracer flux at a different equivalent source ($x=x_1$, Fig. 4.8). Thus the velocity and concentration potential cores will not be coincident which complicates the assumed picture of the initial region.

The geometry defining the spread of mass in the initial region must necessarily differ from that defining the spread of momentum (Fig. 4.8) thereby requiring the definition of an additional concentration profile for the region $x_1 \lesssim x \lesssim x_2$ (x_1 and x_2 denote the apices of the concentration and velocity potential cores along the centreline respectively). The same basic arguments as before are now used to derive the concentration

profiles for cases (i) and (ii) assuming $\lambda^2 = 2$.

For case (i) the solution to the partial differential equation for the conservation of tracer (eq. 4.5) gives a concentration profile for the fully developed region

$$c(x,y) = \frac{4\, Q_{t_o}}{\pi \sqrt{6\, \alpha\, M_o\, (x-x_{or})}}\ \text{sech}\ \eta \qquad (4.23)$$

where $Q_{t_o} = c_o\, u_o\, 2b_o$ is the reference flux of tracer at the real source. For a flux of tracer deficit discharging into a large reservoir then, the appropriate concentration profile is by analogy

$$c_f - c(x,y) = \frac{4\, c_f\, Q_o}{\pi \sqrt{6\, \alpha\, M_o\, (x-x_{or})}}\ \text{sech}\ \eta \qquad (4.24)$$

where c_f is the magnitude of the deficit.

Decomposition of the profile defined by eq. 4.24 in the same manner as the one defined by eq. 4.11 must satisfy the same conditions expressed by eqs. 4.13 to 4.16. It is found that

$$c_2(x,y) = \frac{1}{2}\, c_f \left(1 - \frac{4\, Q_o}{\pi \sqrt{6\, \alpha\, M_o\, (x-x_{or})}}\right)\left(1 - \frac{2}{\pi} \tan^{-1}\ (\sinh \eta)\right) \qquad (4.25)$$

$$+ \frac{4\, c_f\, Q_o}{\pi \sqrt{6\, \alpha\, M_o\, (x-x_{or})}}\ (1 - \text{sech}\ \eta)(1 - H(\eta))$$

This represents the solution for case (ii) which contains a virtual origin at the same position as the solution for case (i). It is valid in the real sense for $x > x_2$. The solution must be suitably modified to describe the mean concentration profile in the region $x_1 \leq x \leq x_2$ since the solution of the integral continuity equation is not valid there. At the equivalent source of tracer flux ($x = x_1$) then, the contribution of the term corresponding to the first one in eq. 4.25 will be zero and the centreline concentration likewise.

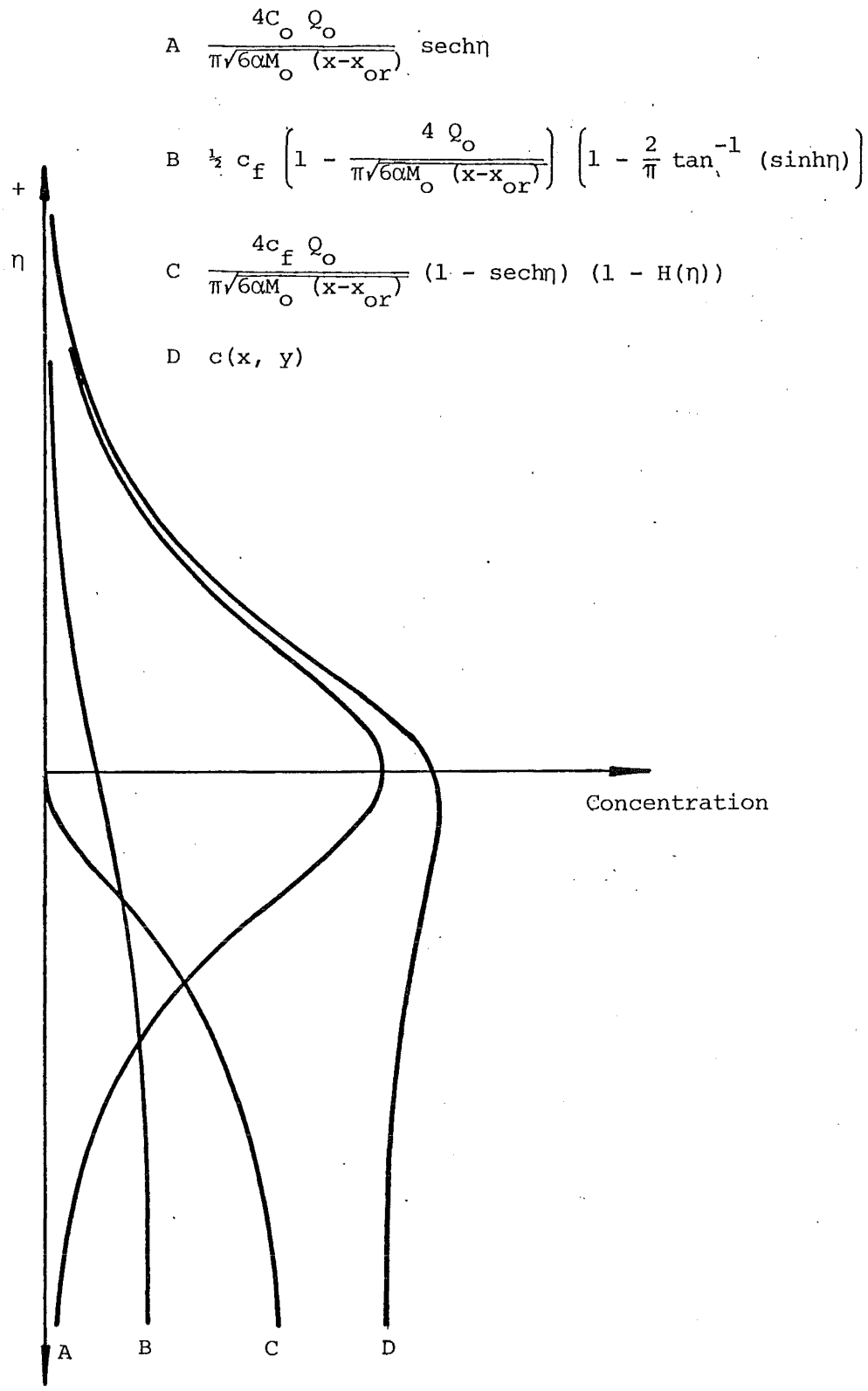

FIGURE 4.7 Concentration profile c(x, y) for the fully developed region assuming $\lambda^2 = 2$

From eqs. 4.23 and 4.25, the solution for the linear superposition of cases (i) and (ii) (Fig. 4.2) is

$$c(x,y) = \frac{4\, c_o\, Q_o}{\pi \sqrt{6\, \alpha\, M_o\, (x-x_{or})}}\ \text{sech}\ \eta$$

$$+ \frac{1}{2}\, c_f \left(1 - \frac{4\, Q_o}{\pi \sqrt{6\, \alpha\, M_o\, (x-x_{or})}}\right) \left(1 - \frac{2}{\pi} \tan^{-1} (\sinh \eta)\right)$$

$$+ \frac{4\, c_f\, Q_o}{\pi \sqrt{6\, \alpha\, M_o\, (x-x_{or})}} (1 - \text{sech}\ \eta)(1 - H(\eta)) \qquad (4.26)$$

The profile defined by this equation is illustrated in Fig. 4.7.

A similar geometry is assumed to define the spread of tracer in the turbulent shear layers of the initial region (Fig. 4.8) as for the spread of momentum. Again the forms of the concentration profiles in the fully developed region determine the forms of the profiles across the turbulent shear layers.

For case (i) then, the mean concentration distribution in the range $0 \lesssim x \lesssim x_1$ is approximated by a profile

$$\begin{aligned} c(x,y) &= c_o && -y_3 \lesssim y \lesssim y_3 \\ c(x,y) &= c_o\, \text{sech}\nu && y_3 \lesssim y \lesssim -y_3 \end{aligned} \qquad (4.27)$$

where $\nu = (y - \text{sgn}(y)\ y_3)/(y_4 - y_3)$. y_3 marks the edge of the concentration potential core (Fig. 4.8) and y_4 defines the locus of points at which the mean concentration is half the concentration in the potential core,

$$\frac{c(x,\ y_4(x))}{C_o} = \frac{1}{2} \qquad (4.28)$$

Both y_3 and y_4, like y_1 and y_2, are assumed to be linear functions of x,

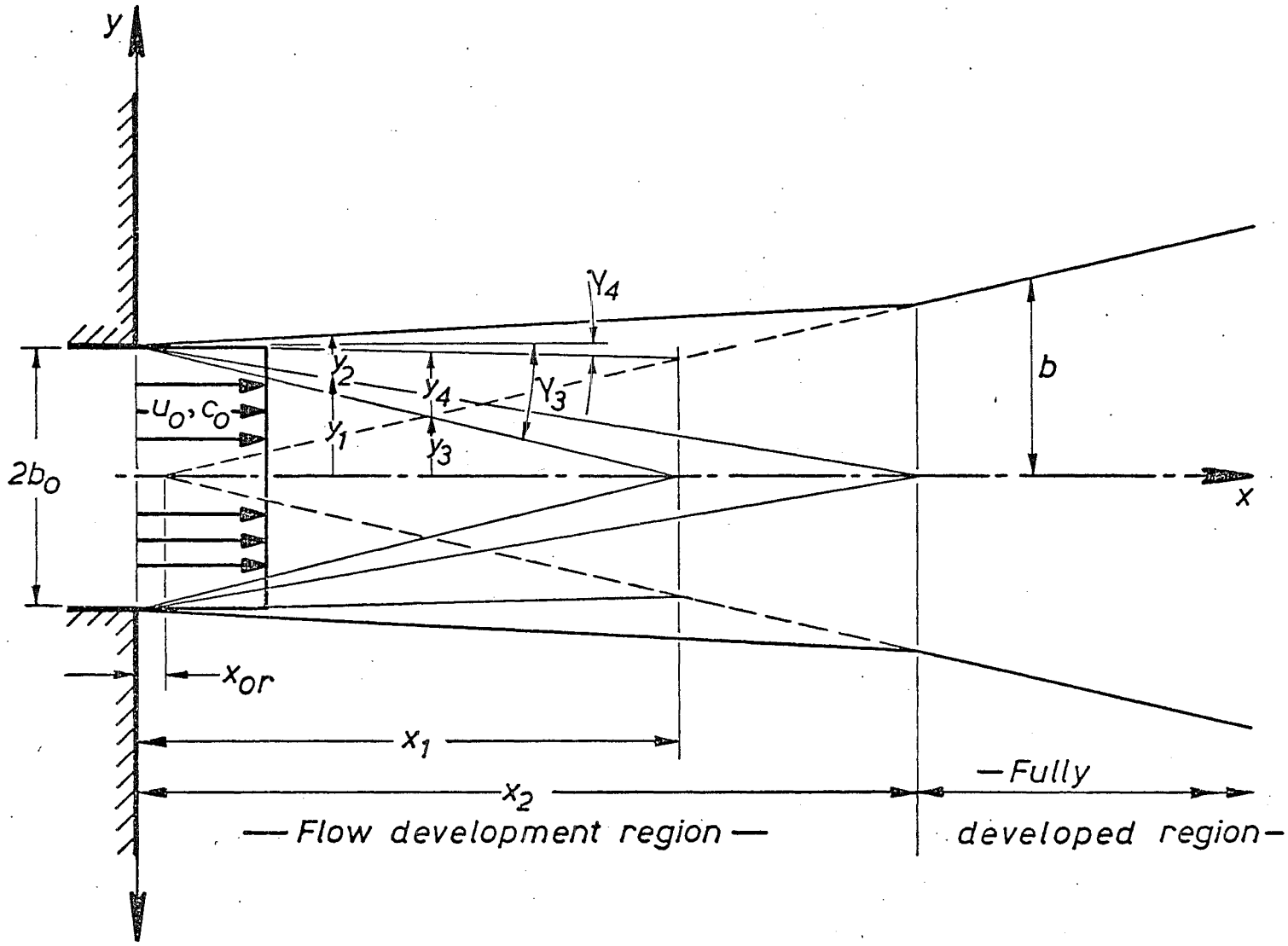

FIGURE 4.8 Geometry of flow development region for the spread of tracer.

$$y_3 = b_o - x \tan \gamma_3$$
$$y_4 = b_o + x \tan \gamma_4 \qquad (4.29)$$

in which the angular quantities, γ_3 and γ_4, specify the geometry of the mixing layers.

The tracer flux for general dimensionless centreline distance, $0 \leq \chi \leq \chi_1$, is found by integrating across the jet

$$\frac{Q_t}{c_o u_o 2b_o} = 1 - \chi \tan \gamma_3 + \frac{1}{\sigma} \chi(\tan \gamma_3 + \tan \gamma_4) \left[\tan^{-1}(\sinh \nu_1) + \int_{\nu_1}^{+\infty} \operatorname{sech} \nu \operatorname{sech}^2((\nu-\nu_1) \frac{(\tan \gamma_3 + \tan \gamma_4)}{(\tan \gamma_1 + \tan \gamma_2)}) d\nu \right] \qquad (4.30)$$

where $\nu_1 = \sigma(y_1-y_3)/(y_4-y_3)$ and $\chi = 2M_o x/Q_o^2$. The integral equation for the conservation of tracer flux indicates that at any normal cross-section, $Q_t = Q_{t_o}$, where $Q_{t_o} = c_o u_o 2b_o$ is the tracer flux at the real source assuming uniform velocity and concentration profiles. At $\chi = \chi_1$, the position along the jet centreline of the apex of the concentration potential core,

$$\chi_1 \tan \gamma_3 = 1$$

and

$$\chi_1(\tan \gamma_3 + \tan \gamma_4) = 2\alpha\sigma (\chi_1 - \chi_{or})$$

Thus eq. 4.22 can be evaluated to determine the magnitude of χ_1, and hence γ_3 and γ_4. The integral on the righthand side of eq. 4.22 must be calculated numerically and a four point Gauss-Legendre integration scheme (Stroud and Secrest, 1966) proves sufficiently accurate. For $\lambda^2 = 2$ and $\gamma_1 = 4.8^o$, it is found that $\chi_1 = 8.30$, $\gamma_3 = 6.9^o$ and $\gamma_4 = -0.6^o$.

For case (ii), the same geometry defining the spread of tracer in the turbulent shear layer of the initial region is assumed as in case (i). The form of the concentration profile is determined by the form of the second term in the equation (eq. 4.25) defining $c_2(x,y)$ in the fully developed region so that the centreline concentration is zero at the equivalent source of tracer flux ($x = x_1$). Thus the mean concentration distribution in the range $0 \leq x \leq x_1$ is approximated by the profile

$$\begin{aligned} c(x,y) &= 0 && -y_3 \leq y \leq y_3 \\ c(x,y) &= c_f(1 - \operatorname{sech} \nu)(1 - H(\nu)) && y_3 \leq y \leq -y_3 \end{aligned} \tag{4.31}$$

For the linear superposition of cases (i) and (ii) (Fig. 4.2) the appropriate concentration profile in the range $0 \leq x \leq x_1$ is then

$$\begin{aligned} c(x,y) &= c_o && -y_3 \leq y \leq y_3 \\ c(x,y) &= c_o \operatorname{sech} \nu + c_f(1 - \operatorname{sech} \nu)(1 - H(\nu)) && y_3 \leq y \leq -y_3 \end{aligned} \tag{4.32}$$

For the remaining part of the initial region ($x_1 \leq x \leq x_2$), turbulent diffusion of tracer begins to occur across the jet centreline and consequently the centreline concentration starts to vary as a function of distance. The concentration profiles for cases (i) and (ii) (and their linear superposition) in the fully developed region are modified so that they match those assumed for $0 \leq x \leq x_1$ and $x_2 \leq x$ at $x = x_1$ and $x = x_2$ respectively. The only change in the equations defining the fully developed region profiles (eqs. 4.23, 4.25 and 4.26) occurs in the coefficient $4\, Q_o/\pi\sqrt{6\, \alpha\, M_o\, (x-x_{or})}$. $\sigma_{Q_o^2}^{It}$ is replaced by another one

$$\frac{}{2\, M_o\, b\left[\tan^{-1}(\sinh \eta_1) + \int_{\eta_1}^{+\infty} \operatorname{sech} \eta \operatorname{sech}^2\left(\frac{(\eta-\eta_1)\, b}{b_i}\right) d\eta\right]}$$

where $\eta_1 = \sigma y_1/b$, $b_i = x(\tan \gamma_1 + \tan \gamma_2)$ and $b = 2\alpha\sigma(x-x_{or})$. The new coefficient is derived by integrating across the jet to obtain the tracer flux for case (i) and using the result from the integral equation for the conservation of tracer flux that $Q_t = Q_{t_o}$. Since the volume flux varies differently, the centreline concentrations follow a slightly different decay or growth relation from that valid in the range $x > x_2$.

4.4 THE INTEGRAL EQUATION SOLUTION

For the linear superposition of cases (i) and (ii) in section 4.3 (Fig. 4.2), the boundary conditions are

$$\lim_{y \to +\infty} c(x,y) = 0$$

and

$$\lim_{y \to -\infty} c(x,y) = c_f$$

so that the integral equation for the conservation of tracer (eq. 4.6) in the fully developed region reduces to

$$\frac{dQ_t}{dx} = \alpha u_c c_f \tag{4.33}$$

But using the integral equation for the conservation of volume (eq. 3.10) and the nondimensionalisation $c_* = c\, Q_o/Q_{t_o}$, eq. 4.25 can be simplified even further to

$$\frac{dQ_{t*}}{dQ_*} = \frac{1}{2} c_{f_*} \tag{4.34}$$

The integral equation for the conservation of tracer in the flow development region ($0 \leq x \leq x_2$)

$$\frac{dQ_t}{dx} = \alpha_i u_o c_f \tag{4.35}$$

reduces to the same result upon substitution of eq. 3.27. Then integrating eq. 4.34 and applying the initial condition that $Q_{t_*} = 1$ at $Q_* = 1$,

$$Q_{t_*} = \frac{1}{2} c_{f_*}(Q_*-1) + 1 \tag{4.36}$$

The solution to eq. 4.34 for the fully developed region is identical.

4.5 PREDICTION OF THE EQUILIBRIUM CONCENTRATION

Self-similarity of all mean profiles is assumed so that the mean concentration profiles derived in section 4.3 can be applied to the curved jet flow in Fig. 3.1. In all equations then, x is replaced with s and y with n.

For the attached jet (Fig. 3.1) the addition of a continuous flux of tracer at the source causes the establishment of a uniform concentration distribution in the eddy. In terms of the linear superposition of cases (i) and (ii) (section 4.3), the flux of tracer across the eddy streamline corresponding to case (i) balances that corresponding to case (ii), thereby making the net transfer zero.

For general centreline distance a zero net flux of tracer across the eddy streamline is expressed mathematically by the equation

$$\psi_{t+\infty} - \psi_{t_{n_e}} = \left[\psi_{t+\infty} - \psi_{t-\infty}\right]_{s=0} = Q_{t_o} \tag{4.37}$$

where Ψ_t denotes a line of constant tracer flux

$$\Psi_{t_n} = \int_n^\infty c(s,n)\ u(s,n)\ dn \tag{4.38}$$

and by definition $\Psi_{t+\infty} = 0$. Eq. 4.37 states that for zero net transfer at a general centreline distance, s, the flux of tracer above the eddy streamline ($n_e \lesssim n < +\infty$) is equal to the source flux. By implication the flux of tracer below the streamline ($-\infty < n \lesssim n_e$) is equal to the entrained flux along the lower edge of the jet.

Upon substitution of the mean velocity and concentration profiles, eq. 4.37 is evaluated and made dimensionless to yield the condition

$$c_{f_*} = \frac{\frac{1}{2}\left\{1 - \frac{2}{\pi}\left[\operatorname{sech}\eta_e \tanh\eta_e + \tan^{-1}(\sinh\eta_e)\right]\right\} - 1}{\frac{1}{2}\left(\frac{Q_*}{2} - \frac{2}{\pi}\right)\left\{\tanh\eta_e - \frac{2}{\pi}\left[\tan^{-1}(\sinh\eta_e)\tanh\eta_e + \operatorname{sech}\eta_e\right]\right\} + \frac{2}{\pi}\left\{\tanh\eta_e - \frac{1}{2}\left[\operatorname{sech}\eta_e \tanh\eta_e + \tan^{-1}(\sinh\eta_e)\right]\right\}} \qquad (4.39)$$

for which the eddy streamline and the line of constant tracer flux $\psi_{t_n} = -Q_{t_o}$ intersect downstream of the source. For a given dimensionless step height, the intersection point coincides with the attachment point (Fig. 4.1). The condition (eq. 4.39) is solved for a centreline distance, $\chi = \chi_4$, defined by the normal which passes through that position on the boundary (Fig. 3.1).

4.6 SUMMARY

The addition of a continuous flux of tracer at the source of an attached pure jet results in the establishment of a uniform concentration distribution in the eddy. The eddy concentration has been predicted as a function of centreline distance (and hence step height) and is compared with the results of some simple experiments in Chapter 7.

CHAPTER 5

AN ENTRAINMENT MODEL OF A TWO-DIMENSIONAL ATTACHED BUOYANT JET

5.1 INTRODUCTION

A two-dimensional attached buoyant jet (Fig. 5.1) will remain attached to the adjacent boundary like a non-buoyant one but only under certain limiting conditions. In the buoyant situation the negative pressure difference across the jet is countered by the uplift due to the buoyancy in the eddy (ABCD, Fig. 5.1) and if it is exceeded then detachment of the jet from the boundary is possible. A detached or free buoyant jet will follow a curved trajectory up towards the free surface. The experimentally determined criterion for detachment, which is a function of the boundary and initial conditions, differs from the more critical criterion for spontaneous attachment of a free buoyant jet (Bates, 1977).

The parameters which determine the basic features of the flow are the same ones as for the pure jet situation (h, b_o, u_o, ρ, μ) except that the inflow concentration of passive tracer c_o is replaced by an initial density deficit $\rho_a - \rho_o$ and an additional parameter is the gravitational constant g (Fig. 5.1). The reference density is chosen for convenience as the density of the ambient fluid ρ_a. The dependent variables are also

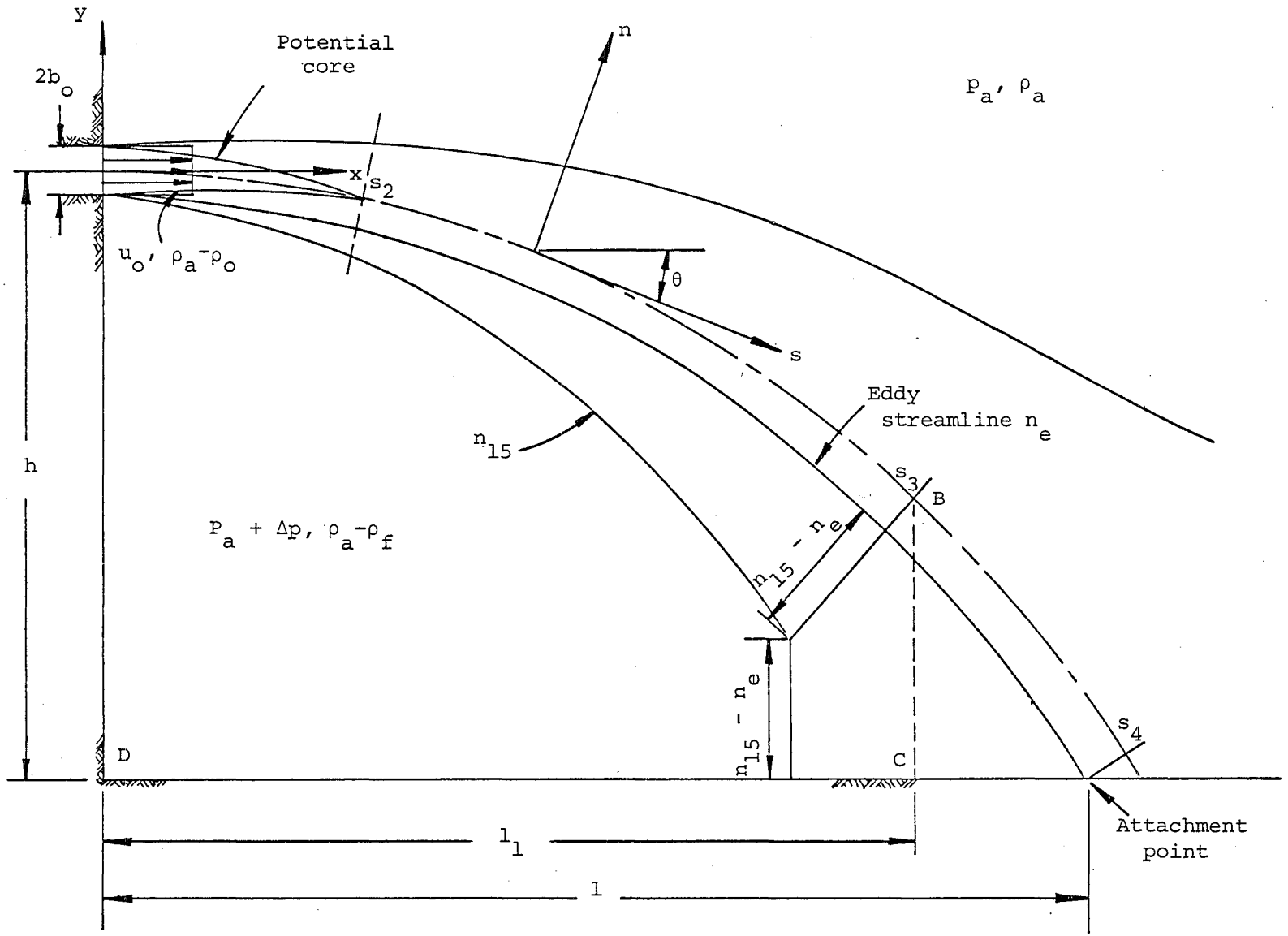

FIGURE 5.1 Configuration of a two-dimensional attached buoyant jet.

identical to those in the pure jet situation (1, Δp) although the eddy concentration of passive tracer c_f becomes an eddy density deficit $\rho_a - \rho_f$. Dimensional arguments are used to construct dimensionless numbers from these dependent variables and express them as functions of other dimensionless numbers involving the independent variables.

$$\frac{1}{h}\,,\ \frac{\Delta p}{\rho_a u_o^2}\,,\ \frac{\rho_a-\rho_f}{\rho_a-\rho_o} = f\left(\frac{h}{b_o}\,,\ \frac{\rho_o u_o 2b_o}{\mu_o}\,,\ \left(\frac{\rho_a-\rho_o}{\rho_a}\right)\ g\,\frac{2b_o}{u_o^2}\right) \tag{5.1}$$

All the dimensionless numbers may be alternatively written in terms of the initial volume, momentum and buoyancy fluxes which are defined assuming top hat profiles by the equations

$$Q_o = u_o\, 2b_o\,,\ M_o = u_o^2\, 2b_o\,,\ B_o = \left(\frac{\rho_a-\rho_o}{\rho_a}\right) g\, u_o\, 2b_o \tag{5.2}$$

Eqs. 5.1 then become

$$\frac{1}{h}\,,\ \frac{\Delta p\, M_o^2}{\rho_a Q_o^2}\,,\ \frac{\rho_a-\rho_f}{\rho_a-\rho_o} = f\left(\frac{2M_o h}{Q_o^2}\,,\ \frac{\rho_o Q_o}{\mu_o}\,,\ \frac{Q_o^3 B_o}{M_o^3}\right) \tag{5.3}$$

Since fully turbulent flow conditions are assumed the Reynolds number $Re = \rho_o Q_o/\mu_o$ is unlikely to be important in eqs. 5.3. In contrast the initial jet Richardson number $Ri_o = Q_o^3 B_o/M_o^3$ will be of particular significance as it expresses the importance of buoyancy relative to momentum.

In this chapter an entrainment model of the flow situation up to the point of attachment is developed along the same lines as the one outlined in Chapters 3 and 4. The same basic assumptions are made and steps followed. A numerical solution of the integral equations of motion is required because of their non-linearity.

5.2 ON THE CONSERVATION OF BUOYANCY FLUX

Where jet buoyancy is produced by an excess inflow temperature above ambient the temperature field in the flow must be related to the density field by the equation,

$$\frac{1}{\rho(T)} \quad \frac{d\rho(T)}{dT} = -\alpha_T(T) \tag{5.4}$$

$\rho(T)$ is the density at temperature T and $\alpha_T(T)$ is the variable coefficient of thermal expansion at the same temperature. For small temperature (and hence density) variations the coefficient of thermal expansion can be treated as being constant so that the relationship defined by eq. 5.4 is approximately linear

$$\frac{\Delta\rho}{\rho} = -\alpha\,\Delta T \tag{5.5}$$

Using this linear approximation it can be shown that the conservation of the initial heat flux released is equivalent to the conservation of the density deficit flux about the reference density ρ_a. Molecular diffusion of heat, turbulent diffusion of heat in the mean flow direction (compared with advective transport) and the transformation of work into heat by viscous forces are all regarded as insignificant.

5.3 VELOCITY AND DENSITY DEFICIT PROFILES

For steady turbulent incompressible two-dimensional non-buoyant jet flow, Gortler solved the partial differential equations of motion with the assumption of a constant eddy viscosity ε_m across a transverse section (Schlichting, 1960) to obtain the self-similar velocity profile

$$u(x,y) = u_c(x)\ \mathrm{sech}^2\eta \tag{5.6}$$

where $\eta = \sigma y/b$ (section 3.3). For a similar buoyant flow, the form of

this profile is appropriate although the centreline velocity $u_c(x)$ and the characteristic width parameter $b(x)$ (defined by $u(x, b(x))/u_c(x) = 0.5$) will vary differently with centreline distance x.

If the density variations are small the density deficit in the buoyant jet flow is analogous to the concentration of a passive tracer in a non-buoyant flow ($\rho_a - \rho \equiv c$). The form of the self-similar concentration profile (eq. 4.18) derived previously from the partial differential equation for the conservation of tracer is therefore suitable. However, as with the centreline velocity, the centreline density deficit $\rho_a - \rho_c(x)$ will behave differently from the equivalent centreline concentration $c_c(x)$ with distance x.

$$\rho_a - \rho(x,y) = \frac{4\rho_a B_o}{\pi g\, Q(x)}\ \text{sech}\eta + \frac{4\rho_a B_o}{\pi g\, Q(x)}\ \left(\frac{\rho_a-\rho_f}{\rho_a-\rho_o}\right)\ (1 - \text{sech}\eta)\ (1 - H(\eta)) + \frac{1}{2}\left[(\rho_a-\rho_f) - \frac{4\rho_a B_o}{\pi g\, Q(x)}\ \left(\frac{\rho_a-\rho_f}{\rho_a-\rho_o}\right)\right]\ (1 - \frac{2}{\pi}\tan^{-1}(\sinh\eta)) \qquad (5.7)$$

$Q(x)$, as before, is the volume flux of the jet flow. The profile defined by eq. 5.7 is illustrated in Fig. 5.2.

The forms of the velocity and concentration profiles adopted for the non-buoyant flow in the flow development region are a reasonable approximation for the buoyant situation. The width parameters $b_i(x) = y_2(x) - y_1(x)$ and $y_4(x) - y_3(x)$ defining the spread of these profiles (Fig. 5.3) will however depart from linearity with centreline distance x and the related entrainment coefficient α_i will no longer be constant. Since the buoyant flow of interest is likely to be momentum dominated near the source, the deviations of these parameters from their non-buoyant counterparts are expected to be small. The edges of the velocity and

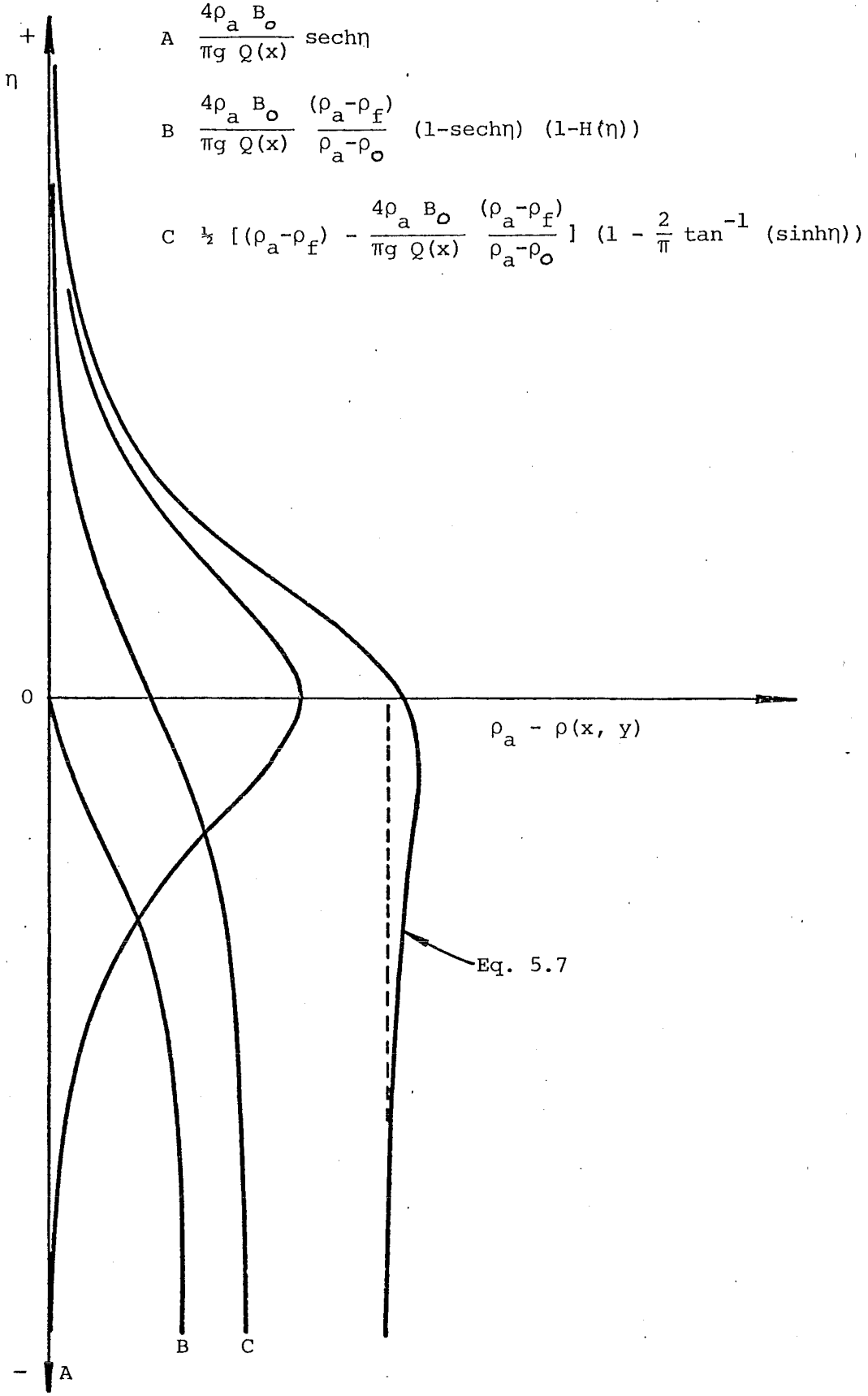

Figure 5.2 Assumed density deficit profile $\rho_a - \rho(x, y)$ for the fully developed region.

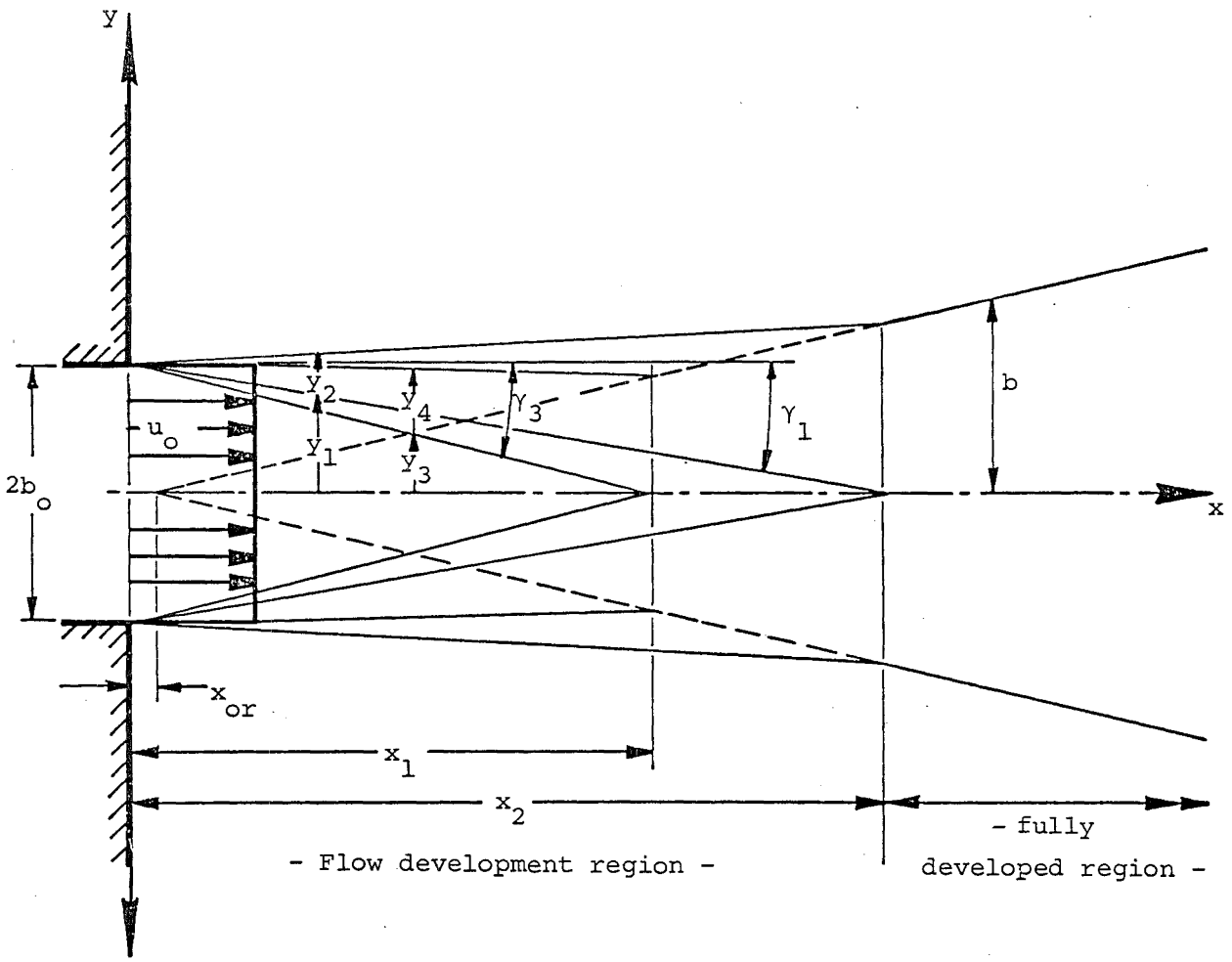

FIGURE 5.3 Geometry of the flow development region for a buoyant jet.

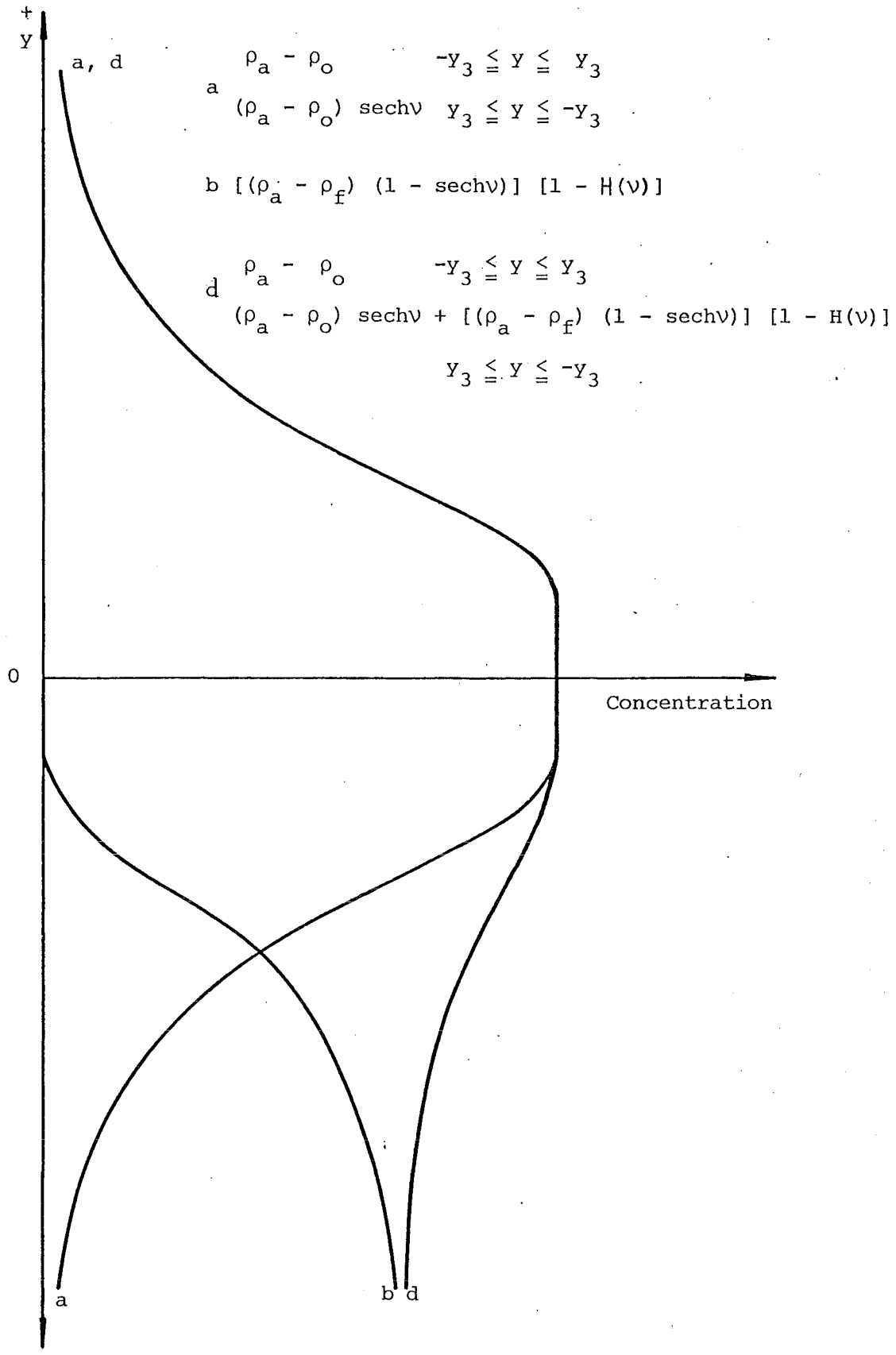

FIGURE 5.4 Assumed density deficit profile $\rho_a - \rho(x, y)$ for the flow development region.

density deficit (concentration) potential cores defined by $y_1(x)$ and $y_3(x)$ respectively (Fig. 5.3) are assumed unchanged from the pure jet case.

The velocity profile assumed then in the initial flow region is described by

$$\begin{aligned} u(x,y) &= u_o && -y_1 \leq y \leq y_1 \\ u(x,y) &= u_o \operatorname{sech}^2 \left(\frac{\sigma(y-\operatorname{sgn}(y)\, y_1)}{b_i}\right) && y_1 \leq y \leq -y_1 \end{aligned} \tag{5.8}$$

where $b_i = y_2 - y_1$. The density deficit profile assumed for $0 \leq x \leq x_1$ is

$$\begin{aligned} \rho_a - \rho(x,y) &= \rho_a - \rho_o && -y_3 \leq y \leq y_3 \\ \rho_a - \rho(x,y) &= (\rho_a-\rho_o)\ \operatorname{sech}\nu + \\ &\quad \left[(\rho_a-\rho_f)\ (1 - \operatorname{sech}\nu)\right]\left[1 - H(\nu)\right] && y_3 \leq y \leq -y_3 \end{aligned} \tag{5.9}$$

where $\nu = \sigma(y - \operatorname{sgn}(y)\ y_3)/(y_4-y_3)$. It is illustrated in Fig. 5.4.

The density profile described by eq. 5.6 is also valid for the latter part of the initial region ($x_1 \leq x \leq x_2$).

5.4 FORMULATION OF INTEGRAL EQUATIONS OF MOTION

The integral equations of motion are formulated by following the same procedure as in the development of the non-buoyant model. The self-similar distributions of mean velocity and mean density deficit defined by eqs. 5.6 to 5.9 are assumed applicable to the curved buoyant jet flow (Fig. 5.1). In these distributions, x is replaced by s, the centreline distance measured from the real source, and y by n, the distance normal to the centreline.

The Boussinesq approximation is made in the formulation of the equations of motion. The magnitude of the largest density variation in the flow will be small compared with the ambient density ρ_a. Thus there is little error in replacing a local time-averaged density $\bar{\rho}(s, n)$ with the ambient density ρ_a in all terms except the buoyancy ones where the density variation $\rho_a - \bar{\rho}(s, n)$ is important.

The integral continuity equations (3.10 and 3.27), the integral equations for the conservation of the horizontal component of momentum flux (3.11 and 3.28) and the two geometric relations derived from the coordinate system (eqs. 3.13 and 3.14) remain unchanged from the non-buoyant model. The equations for the conservation of the vertical component of momentum flux contain an additional buoyancy term and there are two further equations to describe the conservation of the density deficit flux in the flow development and fully developed regions.

5.4.1 Integral Equations of Motion for the Fully Developed Region

In the fully developed region, the conservation equation for the vertical component of momentum flux is

$$\rho_a \frac{d}{ds} \{u_c^2 \frac{b}{\sigma} \int_{-\infty}^{+\infty} \text{sech}^4 \eta \, d\eta \, \sin\theta\} = \Delta p \cos\theta + g \int_{\text{boundary}}^{+\infty} (\rho_a - \rho(s, n)) \, dn \qquad (5.10)$$

and the conservation equation for the buoyancy flux is

$$\frac{d}{ds} \{ \frac{g}{\rho_a} \int_{-\infty}^{+\infty} (\rho_a - \rho(s,n)) \, u(s,n) \, dn \} = \alpha \, u_c (\rho_a - \rho_f) \frac{g}{\rho_a} \qquad (5.11)$$

Eqs. 5.10 and 5.11 are simplified by substitution of the volume and momentum flux parameters Q and M defined in eqs. 3.15 and a buoyancy flux parameter

$$B = \int_{-\infty}^{+\infty} \frac{g}{\rho_a} (\rho_a - \rho(s, n))\, u(s, n)\, dn$$

$$= B_o \left\{ 1 + \frac{1}{2} \left(\frac{\rho_a - \rho_f}{\rho_a - \rho_o} \right) \left[\frac{Q}{Q_o} - 1 \right] \right\} \tag{5.12}$$

Then

$$\rho_a \frac{d}{ds} (M \sin\theta) = \Delta p \cos\theta + g \int_{\text{boundary}}^{+\infty} (\rho_a - \rho(s, n))\, dn \tag{5.13}$$

and

$$\frac{dB}{ds} = \alpha \frac{3M}{2Q} (\rho_a - \rho_f) \frac{g}{\rho_a} \tag{5.14}$$

Evaluation of the buoyancy term on the righthand side of eq. 5.13 poses the problem of how to deal with the lower limit of integration which has been defined as the boundary. The buoyancy term represents the net uplift on a thin slice of the curved jet. It can be considered to be composed of the two parts, one part representing the uplift pressure due to buoyancy in the jet itself and another part representing the uplift pressure due to buoyancy in the eddy. This is illustrated graphically in Fig. 5.5 where the assumed density deficit profile across the jet (defined by eq. 5.7) is shown. The different cross-hatched areas under the profile identify the different contributions to the total uplift on the thin slice of the jet. For convenience, the uplift pressure due to buoyancy in the eddy is determined by assuming that the mean density deficit field of strength $\rho_a - \rho_f$ extends to the centreline.

The first part of the buoyancy term, representing the uplift pressure due to buoyancy in the jet itself, is evaluated by ignoring the presence of the boundary and letting the lower limit of integration extent to $-\infty$.

The second part of the buoyancy term is dealt with by averaging the net uplift force due to buoyancy in the eddy over the length of the attached jet. In order for the net uplift force due to buoyancy in the eddy to be calculated, a knowledge of the eddy volume V is required.

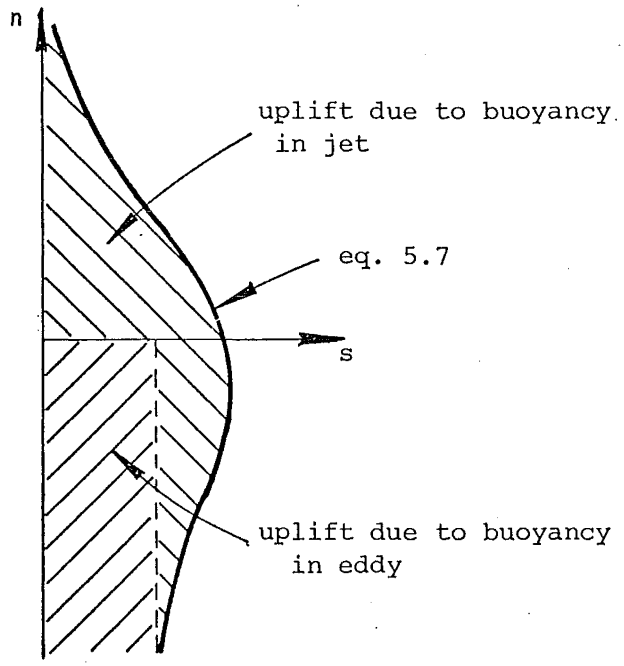

FIGURE 5.5 Composition of the net uplift due to buoyancy on a thin slice of the jet.

The eddy volume is defined as the volume ABCD in Fig. 5.1 bounded by the jet centreline, the back of the step, the horizontal boundary and a perpendicular dropped from the point $s = s_3$ along the centreline at which the jet senses the proximity of the boundary (section 3.5). It is the uplift pressure due to buoyancy in this volume that primarily determines the jet trajectory from the real source to the centreline point $s = s_3$ and which will also induce detachment of the jet from the boundary when the initial conditions are suitable. As a consequence of the definition for the eddy volume, the horizontal distance over which the net uplift force due to buoyancy in the eddy must be averaged to obtain the uplift pressure corresponds to the lower limit l_1 for the eddy length (Fig. 5.1).

Thus the buoyancy term representing the total uplift due to buoyancy on a thin slice of the jet is in expanded form

$$g \int_{-\infty}^{+\infty} (\rho_a - \rho(s, n))dn \tag{5.15}$$

$$= \frac{4\rho_a B Q}{3M} - \frac{2 (\rho_a - \rho_f) g Q^2}{3M} \quad \left\{ \begin{array}{l} \text{uplift pressure due} \\ \text{to jet buoyancy} \end{array} \right.$$

$$+ (\rho_a - \rho_f) g \frac{V}{l_1} \quad \left\{ \begin{array}{l} \text{uplift pressure due} \\ \text{to buoyancy in eddy} \end{array} \right.$$

The integral equation for the conservation of momentum in the vertical direction (eq. 5.13) becomes

$$\frac{d}{ds} (M \sin\theta) = \frac{\Delta p}{\rho_a} \cos\theta + \frac{4BQ}{3M} - \frac{2(\rho_a - \rho_f) g Q^2}{3 \rho_a M} + (\frac{\rho_a - \rho_f}{\rho_a}) g \frac{V}{l_1} \tag{5.16}$$

The same nondimensionalisation is used as in the development of the non-buoyant model (eqs. 3.21) along with the definition

$$B_* = \frac{B}{B_o} \tag{5.17}$$

in which the initial buoyancy flux B_o is known from eq. 5.2. Eqs. 5.16 and 5.14 reduce to

$$\frac{d}{d\chi}(M_* \sin\theta) = \frac{1}{2} \Delta p_* \cos\theta +$$

$$Ri_o \left\{ \frac{2 B_* Q_*}{3 M_*} + (\frac{\rho_a - \rho_f}{\rho_a - \rho_o}) \left[\frac{1}{4} \frac{V_*}{l_{1*}} - \frac{Q_*^2}{3M_*} \right] Ri_o \right\} \tag{5.18}$$

$$\frac{dB_*}{d\chi} = \alpha (\frac{\rho_a - \rho_f}{\rho_a - \rho_o}) \frac{3M_*}{4Q_*} \tag{5.19}$$

where $\Delta p_* = \Delta p \, Q_o^2 / \rho_a M_o^2$ as before. The former equation (5.18) is solved simultaneously with the dimensionless version of eq. 3.11 to eliminate either M_* or θ.

Hence the ordinary differential equations describing the motion of the attached buoyant jet in the fully developed region are

$$\frac{dQ_*}{d\chi} = \frac{3}{2}\ \alpha\ \frac{M_*}{Q_*} \tag{5.20}$$

$$\frac{dM_*}{d\chi} = \left\{ \frac{2\ B_*\ Q_*}{3M_*} + \left(\frac{\rho_a - \rho_f}{\rho_a - \rho_o}\right)\left[\frac{V_*}{4l_{1_*}} - \frac{Q_*^2}{3\ M_*}\right]\right\} Ri_o\ \sin\theta \tag{5.21}$$

$$\frac{d\theta}{d\chi} = \frac{\Delta p_*}{2M_*} + \left\{\frac{2\ B_*\ Q_*}{3\ M_*} + \left(\frac{\rho_a - \rho_f}{\rho_a - \rho_o}\right)\left[\frac{V_*}{4l_{1_*}} - \frac{Q_*^2}{3M_*}\right]\right\} \frac{Ri_o\ \cos\theta}{M_*} \tag{5.22}$$

$$\frac{dB_*}{d\chi} = \alpha\ \left(\frac{\rho_a - \rho_f}{\rho_a - \rho_o}\right)\ \frac{3M_*}{4Q_*} \tag{5.23}$$

$$\frac{dx_*}{d\chi} = \cos\theta \tag{5.24}$$

$$\frac{dy_*}{d\chi} = \sin\theta \tag{5.25}$$

The entrainment coefficient α has been shown to be variable for a buoyant jet flow (List and Imberger, 1973). However in the present case momentum effects are expected to dominate near the source and there will be little error if α is assumed to have the same constant value (0.065) as in the non-buoyant situation.

5.4.2 Integral Equations of Motion for the Flow Development Region

The flow development region must be considered in two parts (Fig. 5.3).

Integrating across the flow in the region $0 \lesssim s \lesssim s_1$, the conservation equation for the vertical component of momentum flux is

$$\rho_a \frac{d}{ds} \{2 u_o^2 \left[n_1 + \frac{b_i}{\sigma} \int_o^{\infty} \operatorname{sech}^4 \left(\frac{\sigma(n-n_1)}{b_i}\right) d \left(\frac{\sigma(n-n_1)}{b_i}\right) \right] \sin\theta \}$$

$$= \Delta p \cos\theta + g \int_{-\infty}^{+\infty} (\rho_a - \rho(s, n)) \, dn \qquad (5.26)$$

and the conservation equation for the buoyancy flux is

$$\frac{d}{ds} \left\{ \frac{g}{\rho_a} \int_{-oo}^{+oo} (\rho_a - \rho(s, n)) \, u(s, n) \, dn \right\} = \alpha_i u_o (\rho_a - \rho_f) \frac{g}{\rho_a} \qquad (5.27)$$

Simplification of eqs. 5.26 and 5.27 is achieved by substitution of the volume and momentum flux parameters Q and M (defined in eqs. 3.30 and 3.31) and the buoyancy flux parameter

$$B = \frac{g}{\rho_a} \int_{-\infty}^{+\infty} (\rho_a - \rho(s, n)) \, u(s, n) \, dn$$

The additional buoyancy term in eq. 5.24 is evaluated in a similar manner to the buoyancy term in the equivalent equation for the fully developed region

$$g \int_{-\infty}^{+\infty} (\rho_a - \rho(s, n)) \, dn = (\rho_a - \rho_o) \, g \frac{Q_o^2}{M_o^2} \left\{ \zeta + \frac{1}{2} \left(\frac{\rho_a - \rho_f}{\rho_a - \rho_o}\right) \left[\frac{V_*}{l_{l_*}} - \zeta \right] \right\} \qquad (5.28)$$

where $$\zeta = 1 - \chi \tan \gamma_3 + \frac{\pi}{\sigma} (n_4 - n_3) \frac{M_o^2}{Q_o} \qquad (5.29)$$

Nondimensionalisation is carried out as before and the two conservation equations for the components of the momentum flux are solved simultaneously to isolate M_* from θ. Hence eqs. 3.28, 5.26 and 5.27 reduce to

$$\frac{dM_*}{d\chi} = \frac{Ri_o}{2} \left\{ \zeta + \frac{1}{2} \left(\frac{\rho_a - \rho_f}{\rho_a - \rho_o}\right) \left[\frac{V_*}{l_{l_*}} - \zeta \right] \right\} \sin\theta \quad 0 \leq \chi \leq \chi_1 \qquad (5.30)$$

$$\frac{d\theta}{d\chi} = \frac{\Delta p_*}{2M_*} + \frac{Ri_o}{2} \left\{ \zeta + \frac{1}{2} \left(\frac{\rho_a - \rho_f}{\rho_a - \rho_o}\right) \left[\frac{V_*}{l_{l_*}} - \zeta \right] \right\} \frac{\cos\theta}{M_*} \quad 0 \leq \chi \leq \chi_1 \qquad (5.31)$$

$$\frac{dB_*}{d\chi} = \frac{1}{2}\,\alpha_i\,\left(\frac{\rho_a - \rho_f}{\rho_a - \rho_o}\right) \tag{5.32}$$

The conservation equation for the buoyancy flux (eq. 5.27) remains unchanged for $s_1 \lesssim s \lesssim s_2$ and therefore eq. 5.32 is valid over the entire initial flow region. The conservation equation for the vertical component of momentum is also identical to eq. 5.26 although upon evaluation the additional buoyancy term is different,

$$g\int_{-\infty}^{+\infty}(\rho_a - \rho(s,n)\,dn = (\rho_a - \rho_f)\,g\,\frac{V}{l_1} + \S\,\rho_a\,\frac{B_o\,Q_o}{M_o}\left[\frac{3}{2} - \frac{1}{2}\left(\frac{\rho_a - \rho_f}{\rho_a - \rho_o}\right)\right] \tag{5.33}$$

where

$$\S = \frac{\pi}{2\left[\tan^{-1}(\sinh\eta_1) + \int_{\eta_1}^{\infty}\operatorname{sech}\eta\,\operatorname{sech}^2\left((\eta-\eta_1)\,\frac{b}{b_i}\right)d\eta\right]} \tag{5.34}$$

Now $\eta = \sigma n/b$ and $n_1 = \sigma n_1/b$.

Following the same procedure as before then

$$\frac{dM_*}{d\chi} = \frac{Ri_o}{2}\left\{\frac{3}{2}\,\S + \frac{1}{2}\left(\frac{\rho_a - \rho_f}{\rho_a - \rho_o}\right)\left[\frac{V_*}{l_{1_*}} - \S\right]\right\}\sin\theta \tag{5.35}$$

and

$$\frac{d\theta}{d\chi} = \frac{\Delta p_*}{2M_*} + \frac{Ri_o}{2}\left\{\frac{3}{2}\,\S + \frac{1}{2}\left(\frac{\rho_a - \rho_f}{\rho_a - \rho_o}\right)\left[\frac{V_*}{l_{1_*}} - \S\right]\right\}\frac{\cos\theta}{M_*} \tag{5.36}$$

The parameters ζ and $\S$ in eqs. 5.30, 5.31, 5.35 and 5.36 are both an order of magnitude less than the ratio V_*/l_{1_*} so that they can be neglected in those equations. In other words, the contribution of the buoyancy in the jet to the net uplift is being ignored. It is logical to do this since the jet will be momentum dominated near the source.

The continuity equation derived for the non-buoyant situation

$$\frac{dQ_*}{d\chi} = \alpha_i \tag{5.37}$$

is equally valid in the buoyant situation. However the entrainment coefficient is no longer constant because of the non-constancy of the momentum flux. From the definitions of the volume and momentum flux parameters Q and M in the initial flow region (eqs. 3.30 and 3.31)

$$\alpha_i = \frac{1}{2} \tan \gamma_1 + \frac{3}{2} \frac{dM_*}{d\chi} \tag{5.38}$$

where γ_1 defines the geometry of the velocity potential core (Fig. 5.3).

The two geometric relations (eqs. 5.24 and 5.25) close the system of equations describing the buoyant jet motion in the flow development region.

5.5 THE CHARACTERISTIC EDDY PARAMETERS

The geometry of an attached jet is characterised by the step height h and the eddy length l (Fig. 5.1). The mathematical definitions of the dimensionless version of the former parameter (eq. 3.44) for the non-buoyant situation is equally appropriate for the buoyant situation. However, a mean estimate of the dimensionless eddy length is defined for the buoyant situation by extrapolating the jet to the point $\chi = \chi_4$ ($s = s_4$, Fig. 5.1) along the centreline as though the boundary was not present.

Similarly the definition of the average underpressure in dimensionless form (eq. 3.51) is valid for the buoyant situation if the Boussinesq approximation is made and the dimensionless eddy density deficit $(\rho_a - \rho_f)/(\rho_a - \rho_o)$ is given by the same equation as for the dimensionless passive tracer concentration (eq. 4.31). The assumption made that the horizontal component of momentum flux at the section FE (Fig. 3.3) is approximately equal to the momentum flux of the jet ($(M_* \cos\theta)_{FE} \simeq (M_*)_{FE}$) will be less critical than in the non-buoyant situation because the curvature of the

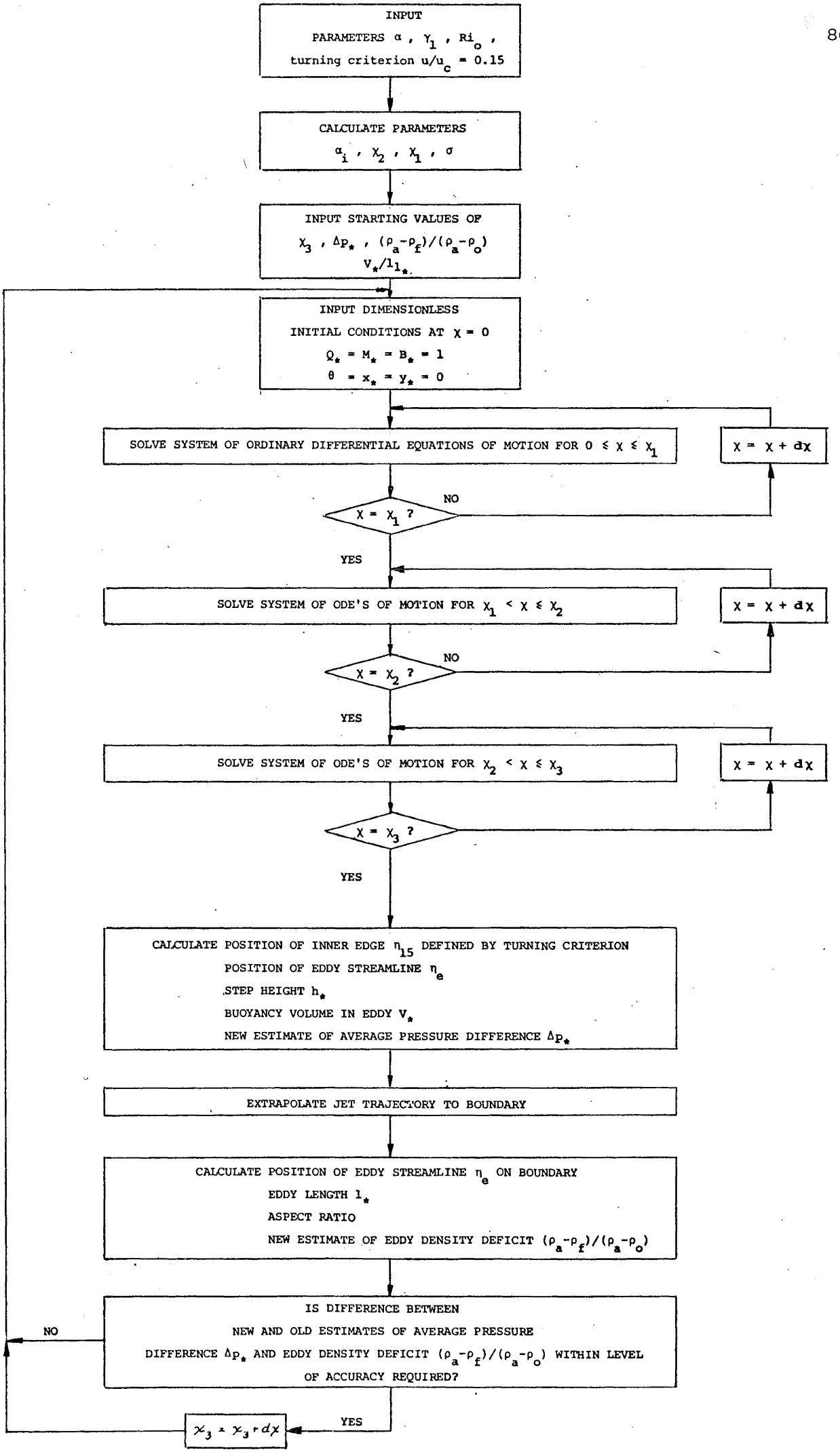

FIGURE 5.6 Solution procedure for attached buoyant jet model.

buoyant jet will not be as great. Also, the assumption that the momentum flux of the jet at the section FE approximately equals the initial momentum flux ($(M_*)_{FE} \simeq 1$) is still reasonable as the buoyant jet is expected to be momentum-dominated near the source.

5.6 SOLUTION SCHEME

The system of ordinary differential equations of motion for the attached buoyant jet is non-linear and therefore requires a numerical solution. A fourth-order Runge-Kutta method of solution was used for which a step length of $d\chi = 0.1$ gave sufficient accuracy. The solution procedure is outlined in Fig. 5.6.

Obtaining a solution became progressively more difficult as the step height increased and the initial jet Richardson number increased.

CHAPTER 6

EXPERIMENTAL INVESTIGATION

6.1 INTRODUCTION

The turbulent two-dimensional attached jet was studied experimentally to confirm the validity of the mathematical model developed in the previous chapters (3-5) and to obtain a better understanding of the attachment phenomenon.

As a preliminary check of the non-buoyant case the aspect ratio 1/h characterising the eddy geometry was determined over a range of step heights by means of a dye streak technique. In a further series of experiments a neutrally buoyant tracer was added to the jet and the concentration of tracer in the eddy measured relative to the inflow concentration with a fluorometer.

Detailed measurements of the horizontal velocity field in both the non-buoyant and buoyant cases were made using a laser Doppler anemometer. The buoyant jet was produced by increasing the temperature of the inflow relative to that of the ambient fluid and the temperature field was also measured with fast response thermistors. Data from these experiments was acquired directly by computer and stored for subsequent analysis of mean and fluctuating values.

6.2 EXPERIMENTAL SET-UP

All experiments were conducted in a glass-walled tank in the post-graduate wing of the Department of Civil Engineering. The tank measured 4.6 m x 1.5 m x 1 m deep and was filled with water from the mains supply.

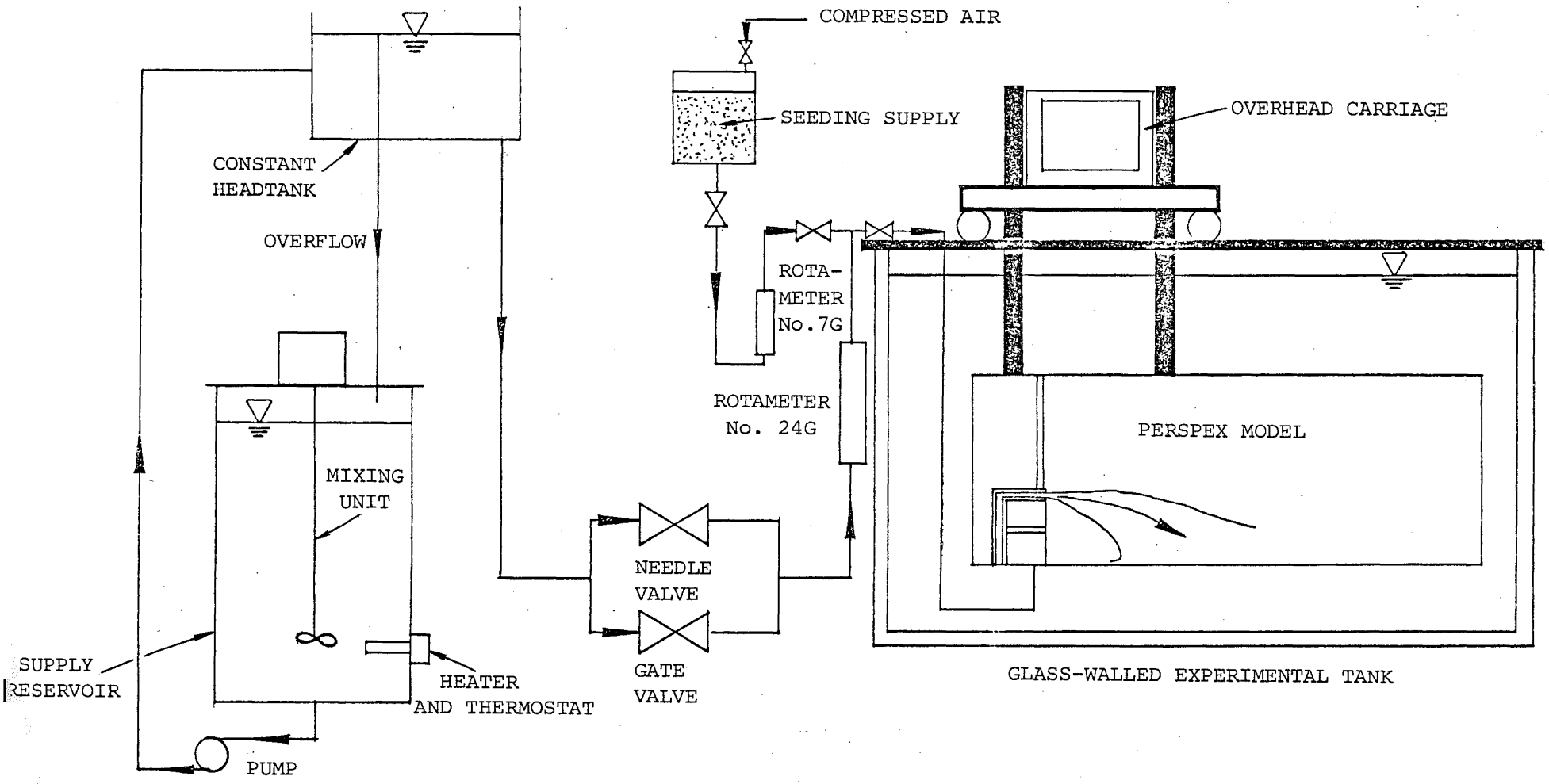

FIGURE 6.1 Diagram of experimental setup.

The water depth was controlled by an adjustable overflow weir in one corner. An overhead carriage ran on rails along the length of the tank.

The model used to generate the two-dimensional attached jet was located in one corner of the glass-walled tank (Fig. 6.1). It was suspended from the overhead carriage on a chain-drive guided by two blocks sliding on vertical shafts. A ratchet device permitted vertical movement in approximately 2 mm increments while the model moved horizontally in the longitudinal direction with the carriage. The freedom of movement in this manner allowed the laser Doppler anemometer to remain fixed in position and be aligned and focused only once for the measurement of a velocity profile across a vertical section. The relative position of the model was determined using vernier point gauges accurate to 0.2 mm.

The model consisted of a 140 mm wide channel with a box discharge unit at one end. The discharge unit incorporated an expansion chamber and a horizontal discharge slot nominally measuring 140 mm x 7 mm (Fig. 6.2). A vertical wall projected above the slot. The model was constructed entirely of perspex to facilitate measurements of the velocity field with the laser Doppler anemometer in the forward scatter differential-Doppler mode (section 6.5.1).

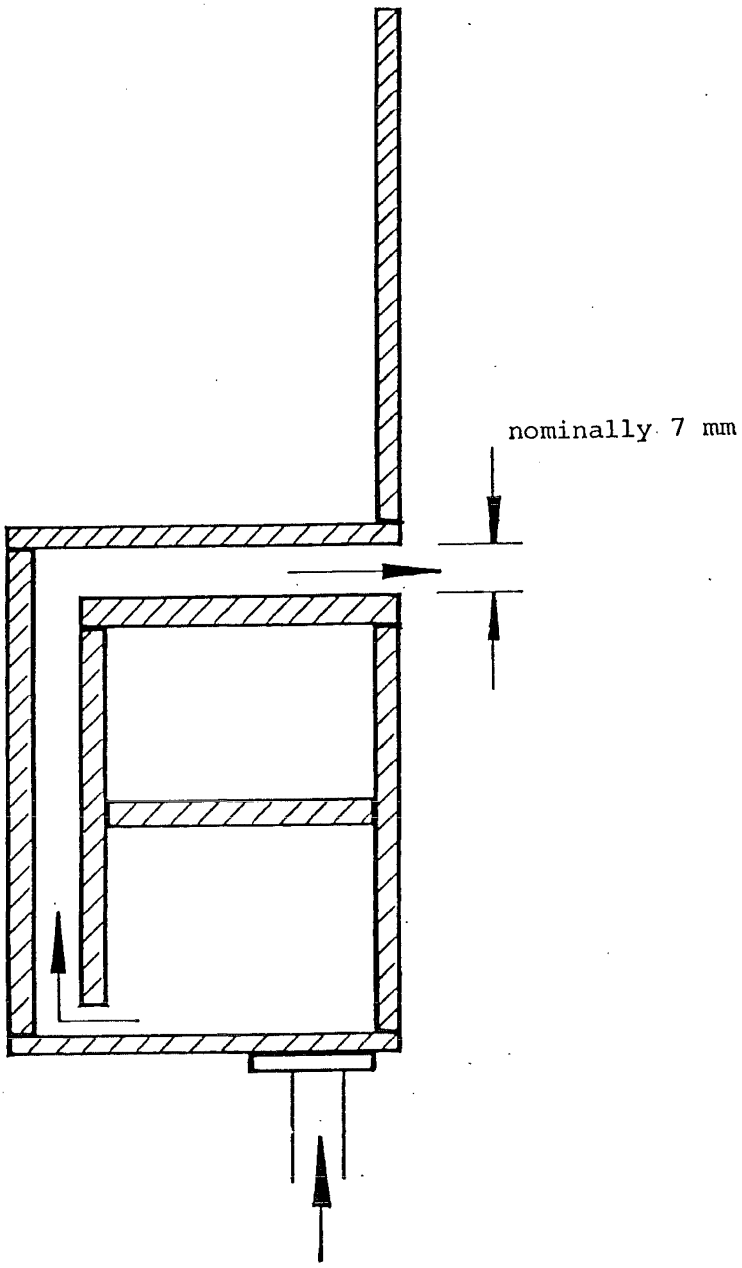

FIGURE 6.2 Sectional view of box discharge unit.

The attached jet was formed by the inflow emerging from the horizontal slot in the discharge unit and attaching to the adjacent floor of the channel. The vertical walls of the channel confined the flow to maintain two-dimensionality. The channel length was sufficiently long (2.2 m) to avoid premature detachment of the buoyant wall jet flowing downstream. The height of discharge above the channel floor was variable.

A constant head system (Fig. 6.1) supplied the inflow. Water was pumped from a 0.7 m^3 supply tank to the constant head tank and the overflow from the weir was recirculated. A mixing unit mounted over the supply tank ensured that a uniform water temperature was maintained.

The temperature of the supply reservoir relative to the ambient temperature in the tank could be adjusted appropriately using the local hot and cold water supplies. A temperature difference between the jet inflow and the ambient water of the order of 20^{o}C for the buoyant jet experiments could be maintained within $\pm$0.05^{o}C for the period of measurement.

A fine degree of control could be exercised over the flowrate from the constant head tank by a gate valve and a needle valve in a parallel combination. A rotameter (metric No. 24G made by Rotameter Mfg. Co. of England) was used to monitor the flowrate with an accuracy of $\pm$0.5%. The calibration of such a device is reasonably constant over small temperature ranges but for a 20^{o}C temperature increase of the inflow over the ambient water it will differ by as much as 2.5%. The rotameter was therefore calibrated at each average working temperature.

6.3 MEASUREMENTS OF ATTACHED JET GEOMETRY AND EDDY CONCENTRATION OF TRACER

6.3.1 Attached Jet Geometry

The aspect ratio of the eddy length to the step height describes the geometry of the attached jet. As a simple check of the pure jet model developed in Chapter 3 the mean position of the eddy streamline along the channel floor (which defines the eddy length) was determined for a range of step heights and Reynolds numbers by means of a dye streak technique. The effect of removal of the vertical wall above the jet exit was also studied.

The experiments were conducted using the model described in section 6.2 ($2 b_o$ = 6.98 mm) and a previous version ($2 b_o$ = 3.34 mm) at water depths of 500 mm and 675 mm above the channel floor respectively. In both models dye was injected through a series of tappings along the centre-line of the channel floor from a bank of small reservoirs. The head difference between the dye level in each of the reservoirs and the ambient face surface in the tank was just sufficient to cause a constant stream of dye to flow out. The flow in the attachment region is highly turbulent and the separation point along the channel floor was estimated by finding a position where the summed timelength of the forward bursts of dye approximately equalled the summed timelength of the reverse bursts over a long period. The error is likely to be of the order $\pm\frac{d}{2}$ where d is the spacing between adjacent tappings (15 mm and 7 mm respectively for the two models).

The results from the latter model were confirmed by an alternative technique of determining the separation point. A thin platinum wire forming a negative electrode was mounted on a specially constructed probe and aligned horizontally across the channel width and just above the floor. A square wave pulse was supplied and the hydrogen bubbles generated along the wire were swept away by the flow in a direction dependent on that of

the simultaneous turbulent fluctuation. The probe was traversed horizontally along the channel to find two positions on either side of the separation point for which the directions of flow were clearly opposing. A point halfway between was then examined to check that the number of forward bursts of bubbles approximately equalled the number of reverse bursts and appropriate corrections applied if necessary. The accuracy of the position of the separation point estimated in this manner is expected to be less than for the dye streak technique because of the disturbances to the flow caused by the probe and particularly the non-uniformity at any one time of the direction of the turbulent fluctuations across the channel width.

6.3.2 Eddy Concentration of Tracer

A passive tracer, Rhodamine B, was incorporated in the pure jet flow to study the concentration of tracer in the eddy without the added complication of buoyancy. The eddy concentration relative to the inflow concentration of tracer was measured by fluorometric analysis of drawn-off samples.

An L-shaped sampling tube was constructed from 3.18 mm diameter copper tubing and a short length of 1.19 mm diameter hypodermic tube formed an extension at the sampling end (Fig. 6.3). The sampling tube was mounted on a point gauge for vertical positioning. Samples were siphoned off through the tube and a rubber hose and collected in 35 ml test tubes for analysis. A draw-off rate of less than 1% of the jet efflux was used that did not measurably affect the equilibrium of the eddy. The rate was controlled by a surgical clip.

The samples were analysed in a fluorometer to determine the concentrations of fluorescent dye. For concentrations of dye less than 10^{-7} kg/m^3 the fluorometer output is linear and the sensitivity of the instrument was initially set for this range. The output appears as a scale

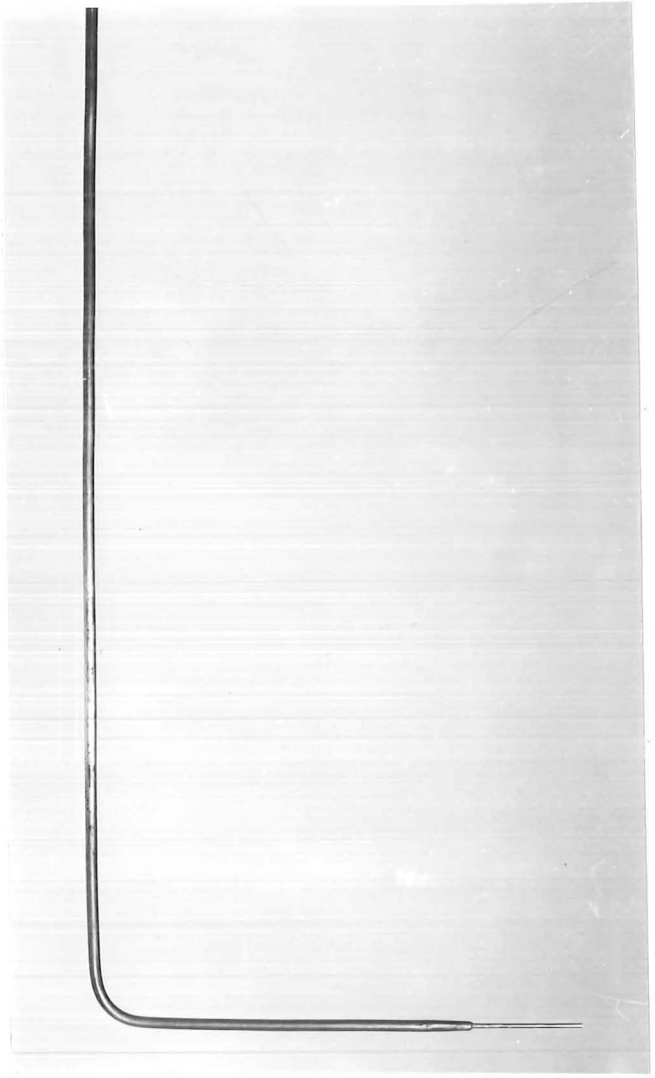

FIGURE 6.3 Sampling tube used to draw off samples from the eddy for fluorometric analysis of the tracer concentration.

reading on a meter and concentrations as low as 10^{-3} times the minimum sensitivity can be read using different overlapping scales. Correlation between scales was found necessary. Comparison of fluorometer output against a standard of known concentration was not required because relative concentrations were being measured.

For a typical experiment the fluorometer was first switched on and allowed to warm up for thirty minutes. The appropriate quantity of Rhodamine B dye was added to the constant head supply after the temperature difference between the supply and the ambient water had been corrected. The background fluorescence of the ambient water was measured. For tap water this was usually zero. After the jet flow was started time was allowed for the equilibrium flow configuration to develop and the dead volume in the sampling system to clear before the draw-off from the eddy was sampled. The sampling point was generally chosen to have the (x,y) coordinates $(\frac{1}{3}, \frac{h}{3})$ relative to the corner of the step. Several samples were taken and analysed immediately as the level of fluorescence is particularly sensitive to changes in temperature. The sampling tube was then inserted in the jet exit and the inflow concentration measured similarly. The sampling procedure was repeated for a different geometry or set of initial conditions after the ambient water had been mixed to ensure a uniform level of background fluorescence. Any experiments with a significant degree of variation between sample readings were repeated.

6.4 TEMPERATURE MEASUREMENTS

6.4.1 Thermistors

Temperature measurements were made with calibrated fast response thermistors which are thermally sensitive resistors. The particular type used were small bead thermistors of diameter 0.35 mm and nominal resistance 200 KΩ (VECO No. 52A26). The time constant which is the time taken to

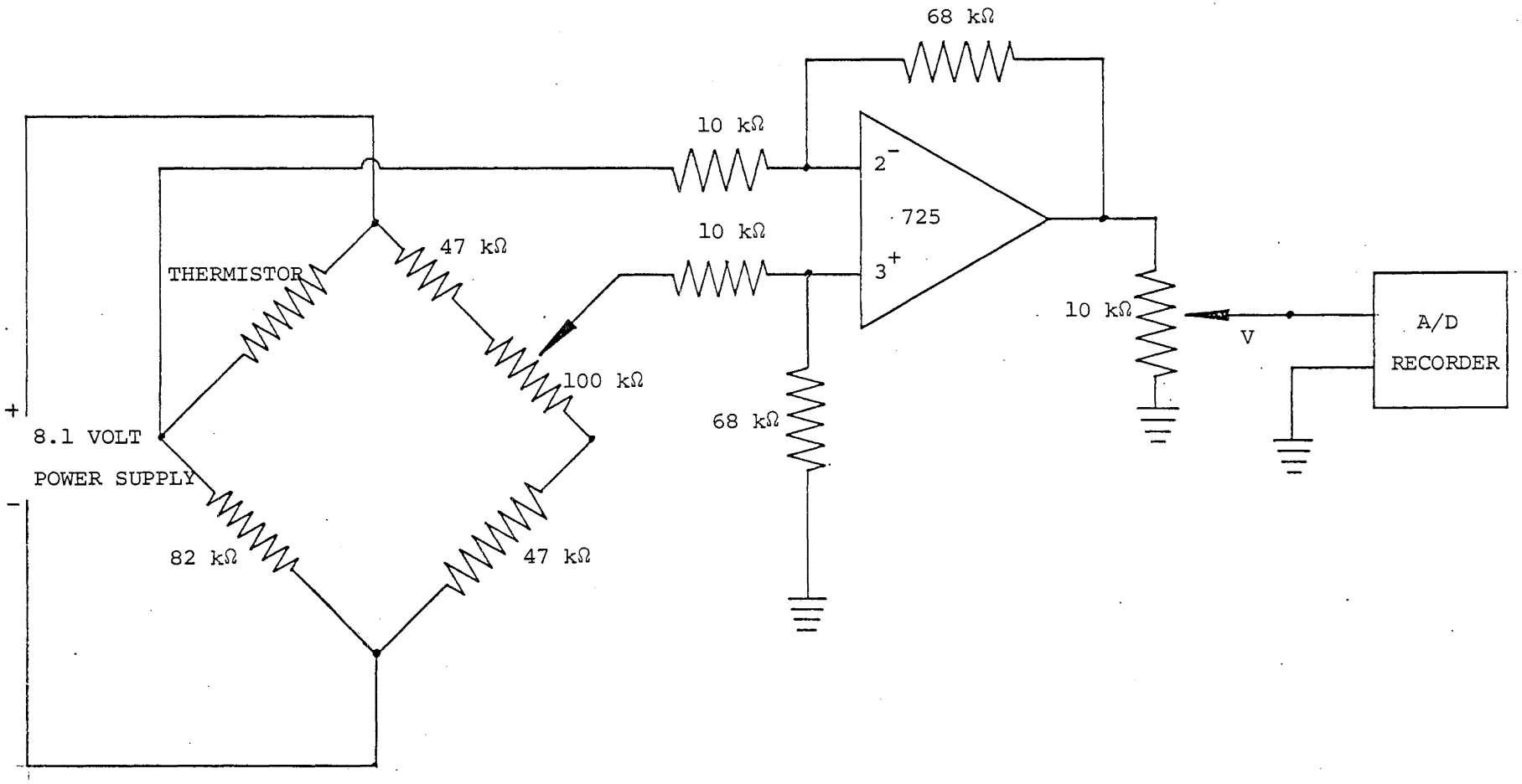

FIGURE 6.4 The bridge circuit used for measuring temperature.

respond to 63% of a step change in temperature has been quoted for these thermistors by Kotsovinos (1975) as being 45 milliseconds in moving water. The individual thermistors formed part of a bridge circuit shown in Fig. 6.4 and the thermistor response to changes in temperature was measured by the voltage output across the bridge.

Each bead thermistor was mounted in a turned nylon plug seated snugly at the tip of a length of 3.18 mm diameter stainless steel tube (Fig. 6.5). The plug was sealed with several coats of polyurethane varnish around the point of seating. The thermistor loads inside the tube had been carefully soldered to thin extension wires and insulated from each other.

Five 150 mm long probes constructed in this manner were fixed 10 mm apart on a streamlined section in the shape of an aircraft wing to form a multiprobe sensor for measuring the temperature field of an attached buoyant jet (Fig. 6.6). The extension leads from the thermistors were soldered to a terminal board inside the streamlined housing. A multicore cable threaded through the 12.7 mm diameter stainless steel tube on which the housing was mounted linked the terminal board with the thermistor bridge circuits. The mounting tube was secured to a vernier point gauge for vertical traversing of the sensor to 0.2 mm accuracy.

Two additional probes were mounted in the jet exit to monitor the exist temperature (Fig. 6.6). They were carefully sealed against water penetration where the insulated wire leads extended out of the stainless steel tube.

Each thermistor and its associated bridge circuit required individual calibration. The calibration standard was a $0.1^{o}C$ mercury thermometer on which the temperature could be estimated to $0.025^{o}C$. The voltage

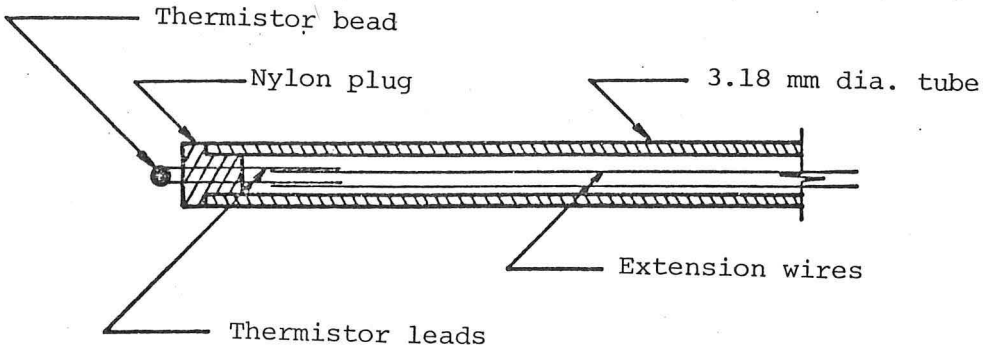

FIGURE 6.5 Enlarged sectional view of a thermistor probe.

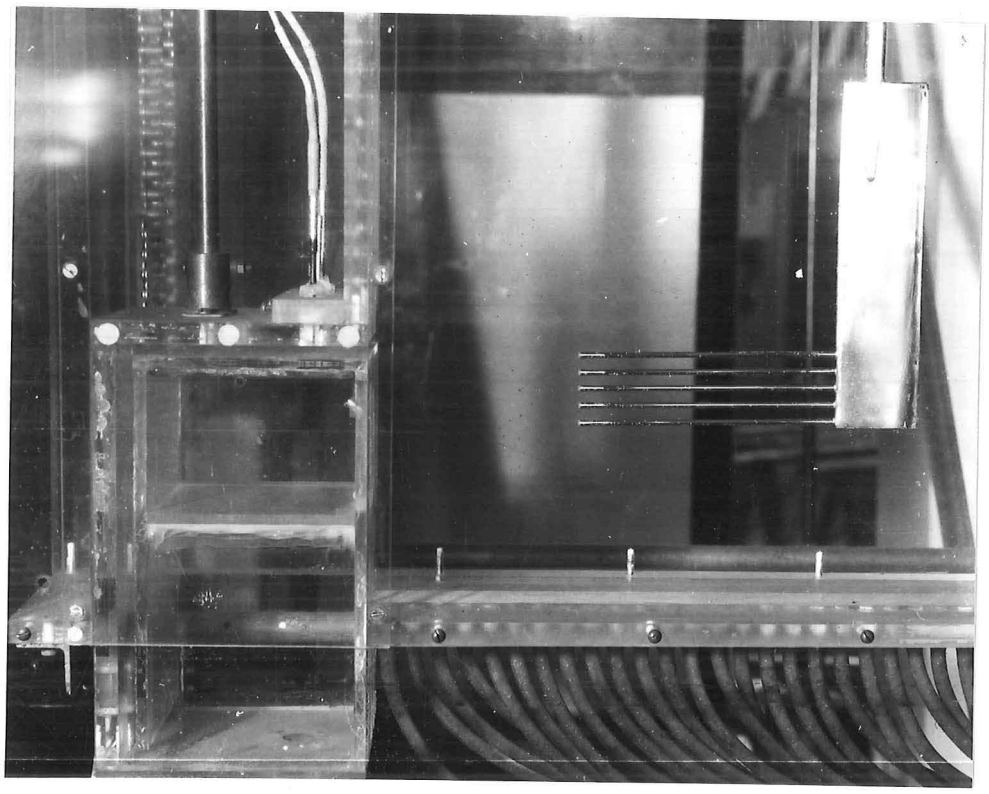

FIGURE 6.6 Location of the multiprobe and jet exit probe temperature sensors.

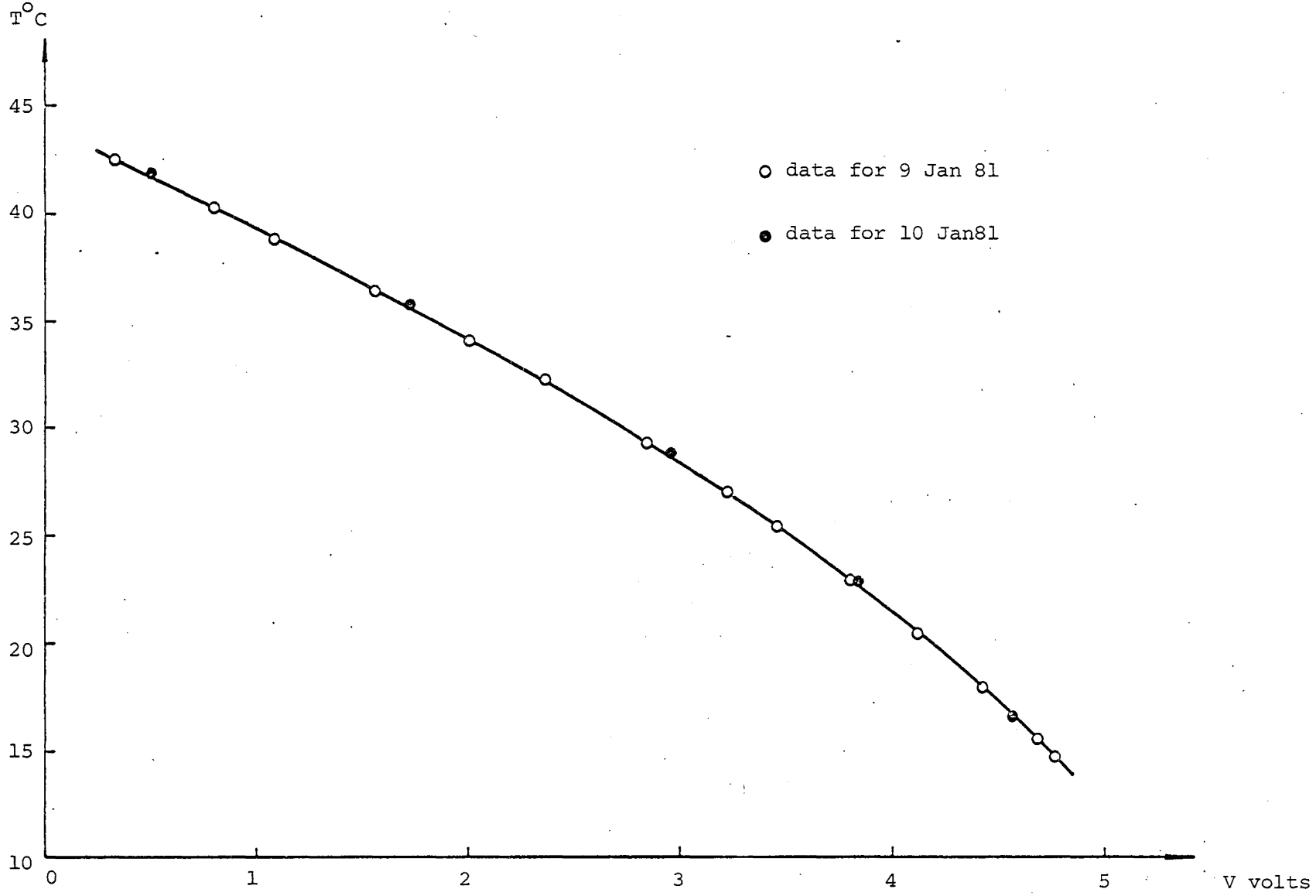

FIGURE 6.7 Typical calibration curve for a thermistor showing a daily variation.

output across the bridge was measured with a Hewlett-Packard digital voltmeter. A third order polynomial

$$T = a_o + a_1 V + a_2 V^2 + a_3 V^3 \qquad (6.1)$$

was fitted to the calibration data by a least squares technique. A typical calibration curve is shown in Fig. 6.7. The calibration of the thermistor bridge circuits changed from day to day by as much as $0.25^{o}C$ at the upper end point ($>40^{o}C$) necessitating regular recalibration.

While excellent measurements of the temperature field in an attached buoyant jet were obtained using this apparatus, the problems encountered during construction and operation were considerable. The smallness of the thermistor beads (0.35 mm diameter) and the fragility of the 0.025 mm diameter platinum-iridium wire leads demanded extreme care and patience at all phases of probe assembly, but invariably failures occurred. For unknown reasons thermistor failures were also persistently experienced throughout the experimental programme so that regular replacement was required.

6.4.2 Analogue/Digital Sampling of Temperature

The maximum sampling rate possible with the Civil Engineering Department's data acquisition system (CEDACS) was 10 samples/second (section 6.6). Kotsovinos (1975) used an identical rate for measurements of the temperature field in a plane buoyant jet and found it adequate for determining mean temperatures. However it has been suggested that his results for temperature fluctuations in the vicinity of the jet exit ($s/2\,b_o < 50$, where s is the centreline distance from the jet exit) are too low due to the poor response of thermistors at high frequencies (Chen and Rodi, 1980). In this study the recirculation region of an attached jet where the frequency of the turbulent fluctuations is likely to be smaller is of primary interest and sampling the temperature measured by the thermistors at a rate of 10 samples/second has been considered suitable.

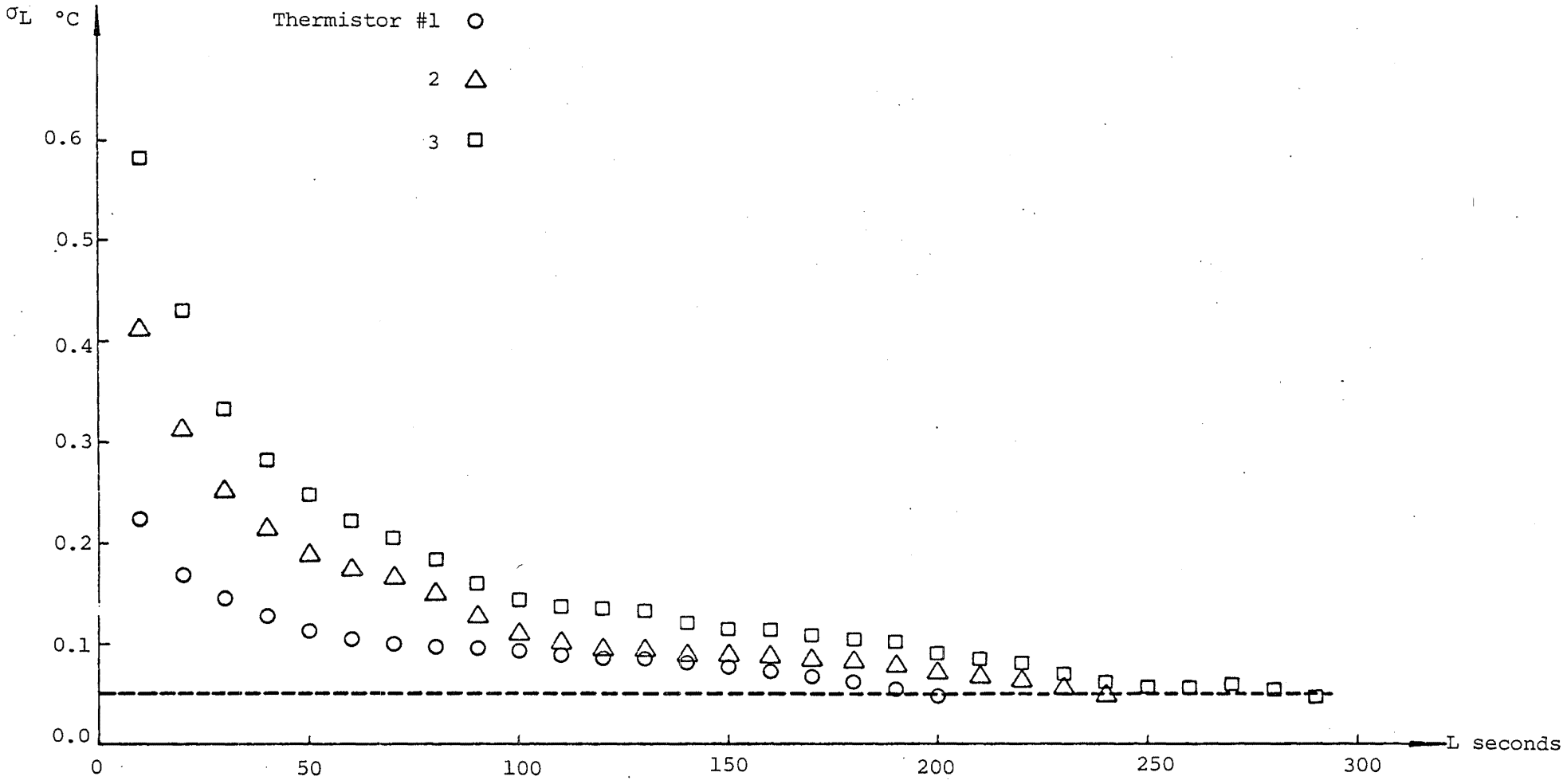

Figure 6.8 Standard deviation of the mean temperature from the 360 second mean as a function of the sampling period length.

A suitable sampling time for measuring the temperature at an arbitrary point was determined by following a similar procedure to that described by Kotsovinos (1975). A representative experiment was performed in which each of the thermistors on the multiprobe sensor was sampled at the rate of 10 samples/second for a period of 360 seconds. The samples were averaged over L = 10, 20, 30 . . . 300 seconds for a series of incremented starting positions along the length of the data record. The standard deviation σ_L from the 360 second mean $\overline{T}$ was calculated for the means of each of the sampling periods of length L seconds. If $\overline{T}_i$ is the mean of the ith L second data block and M is the total number of L second data blocks then,

$$\sigma_L = \sqrt{\frac{1}{M} \sum_{i=1}^{M} (\overline{T}_i - \overline{T})^2} \qquad (6.2)$$

σ_L is plotted against L in Fig. 6.8. For a sampling time greater than about 250 seconds the standard deviation becomes less than $0.05^{o}C$ and this period was chosen for all subsequent experiments. It is assumed implicitly that the mean $\overline{T}$ of the data record approximates closely the expected value at the arbitrary point.

6.4.3 Experimental Procedure for Temperature Measurements

The digital voltmeter and power supplies were switched on and allowed to warm up for at least thirty minutes. Calibration of the thermistors which was found necessary prior to each run was then carried out. The jet exit thermistors were calibrated *in situ* by running water of known temperature through the model. The multiprobe sensor was calibrated in a waterbath. After calibration the sensor was aligned by eye with the centreline of the channel, fixed in position and the location measured relative to the model.

While the glass-walled experimental tank was filling with water the CEDACS data acquisition system (section 6.6) was set up ready to receive data. The calibration data for each thermistor was also analysed using a programme stored in the Civil Engineering Department's PDP11/34 computer.

The temperature of the constant head supply was adjusted to the desired level relative to the ambient receiving water as the overflow recirculated. After any adjustment at least five minutes was allowed for uniformity throughout the system to be re-established. The temperature field was measured for only one value of initial jet Richardson number. For the duration of the investigation it was found that the single temperature difference between the inflow and the ambient receiving water could generally be maintained within $\pm$ 0.3^{o}C.

The jet flow was started and,before the CEDACS system was instructed to begin taking data,a period of two and a half minutes was allowed to elapse for the inflow temperature to reach a constant level and the attached jet to achieve an equilibrium configuration. The length of time for which the jet flow could be run before a backflow of warm water began being entrained by the attached jet limited the measurement of temperature to a single position of the multiprobe sensor. At the conclusion of each set of measurements therefore the inflow was stopped and the ambient receiving water mixed vigorously for five minutes. A thirty minute waiting period was sufficient to allow the restoration of a uniform temperature throughout the ambient water and the damping of any large scale motions caused by the stirring. The procedure was then repeated for further sets of measurements at different locations of the multiprobe sensor and in this manner a picture of the temperature distribution across a vertical section of the attached jet was obtained.

During the course of a set of measurements the ambient temperature in the region of the jet flow measured with a 0.1°C mercury thermometer rarely varied more than ± 0.05°C. Over the same time the drift of the reference voltage across the thermistor bridge circuits and the voltage powering the amplifiers was negligible. Both voltages were continually monitored with a digital voltmeter. Considering the daily change in calibration of the bridge circuits and the 1 in 1023 resolution of the data acquisition system (section 6.6) the absolute error of the relative temperature measurements over the working range is probably about 0.25°C.

The depth of water above the channel floor was constant in each case for which the temperature field was measured. For step heights of 50 mm and 150 mm the depths were set at 675 mm and 750 mm respectively.

6.5 VELOCITY MEASUREMENTS

6.5.1 The Laser Doppler Anemometer

The velocity fields in both an attached pure jet and an attached buoyant jet were measured for a variety of step heights with a laser Doppler anemometer (LDA). The particular unit used was a DISA type 55L LDA with a Spectra-Physics model 124A, 15 mW helium-neon laser (wavelength 632.8 nm) providing the coherent light source.

The laser Doppler anemometer was operated in the forward scattering differential-Doppler mode (Fig. 6.9).

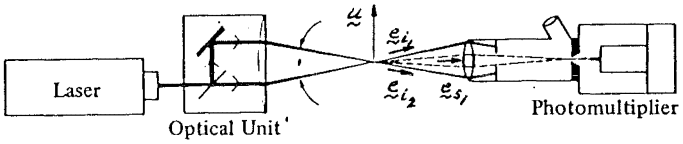

FIGURE 6.9 Forward scattering differential-Doppler mode for an LDA.

In this mode the laser light is split optically into two intersecting beams. Light is scattered by particles suspended in the fluid as they pass through the measuring volume, which is the sensing volume formed by the intersecting beams. A photosensitive device focused on the measuring volume picks up from the same direction the scattered light signals from each of the intersecting beams. It emits an alternating current with a Doppler frequency directly proportional to the scattering particle velocity (the scattering particles are assumed to be sufficiently small to have the same local velocity of the fluid). In the DISA unit a tracking device analyses the Doppler frequency of the alternating current and produces a linearly related voltage output. A more complete description of the principles of laser Doppler anemometry pertaining to the differential-Doppler mode of operation is given in Appendix B.

In this particular investigation the breadth of the glass-walled experimental tank in which the model was suspended required a slight variation on the normal configuration for the forward scattering differential-Doppler mode. A submerged mirror was used to reflect the scattered light out the adjacent side of the tank (Fig. 6.10). The length of the light

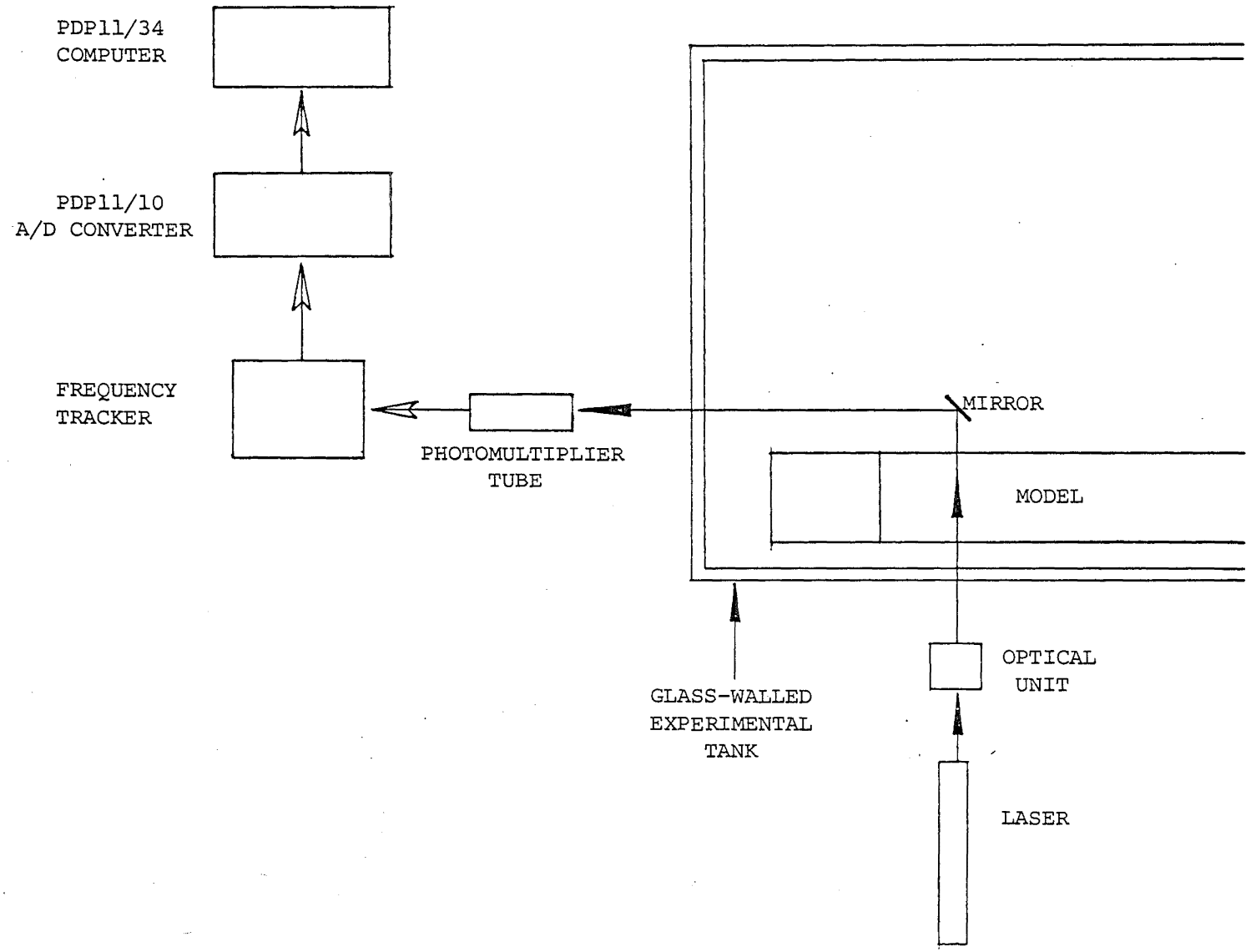

FIGURE 6.10 Plan view of LDA system setup.

path was therefore minimised and the maximum possible light intensity at the detection end ensured.

The LDA remained fixed in position for each set of measurements along a vertical section of the attached jet. The position of the measuring volume was changed simply by moving the model upwards. Thus the need for realignment and refocusing was kept to a minimum.

Some water supplies contain a sufficient number of naturally occurring scattering particles for a satisfactory Doppler signal to be obtained. For the experiments reported it was found necessary to supplement the existing particles in the water supply with artificial ones. Milk contains particles of a suitable size (0.3 - 3) and was added to the jet flow to give a concentration at the exit of 1:25000 (1:12500 in the buoyant case).

The sensitivity of the LDA to the direction of the particle velocity (and hence the fluid velocity) is important where flow reversal occurs as in an attached jet. In the DISA unit direction sensitivity is achieved by means of a pair of acousto-optic Bragg cells mounted in the optical unit (Appendix B). Each Bragg cell diffracts the laser beam passing through it and shifts the frequency of the diffracted light by a fixed amount. The directions of shift for the two cells are chosen to be opposing and thus a Doppler signal can be obtained for a scattering particle at rest. A moving particle will either increase or decrease the frequency of this signal depending on the velocity direction.

6.5.2 Analogue/Digital Sampling of Velocity

The CEDACS data acquisition system (section 6.6) was capable of a maximum sampling rate of 10 samples/second and the velocity field of the attached jet was sampled (by sampling the voltage output of the Doppler signal processer) at this rate. A suitable sampling time for measuring the mean horizontal velocity at an arbitrary point was determined in an

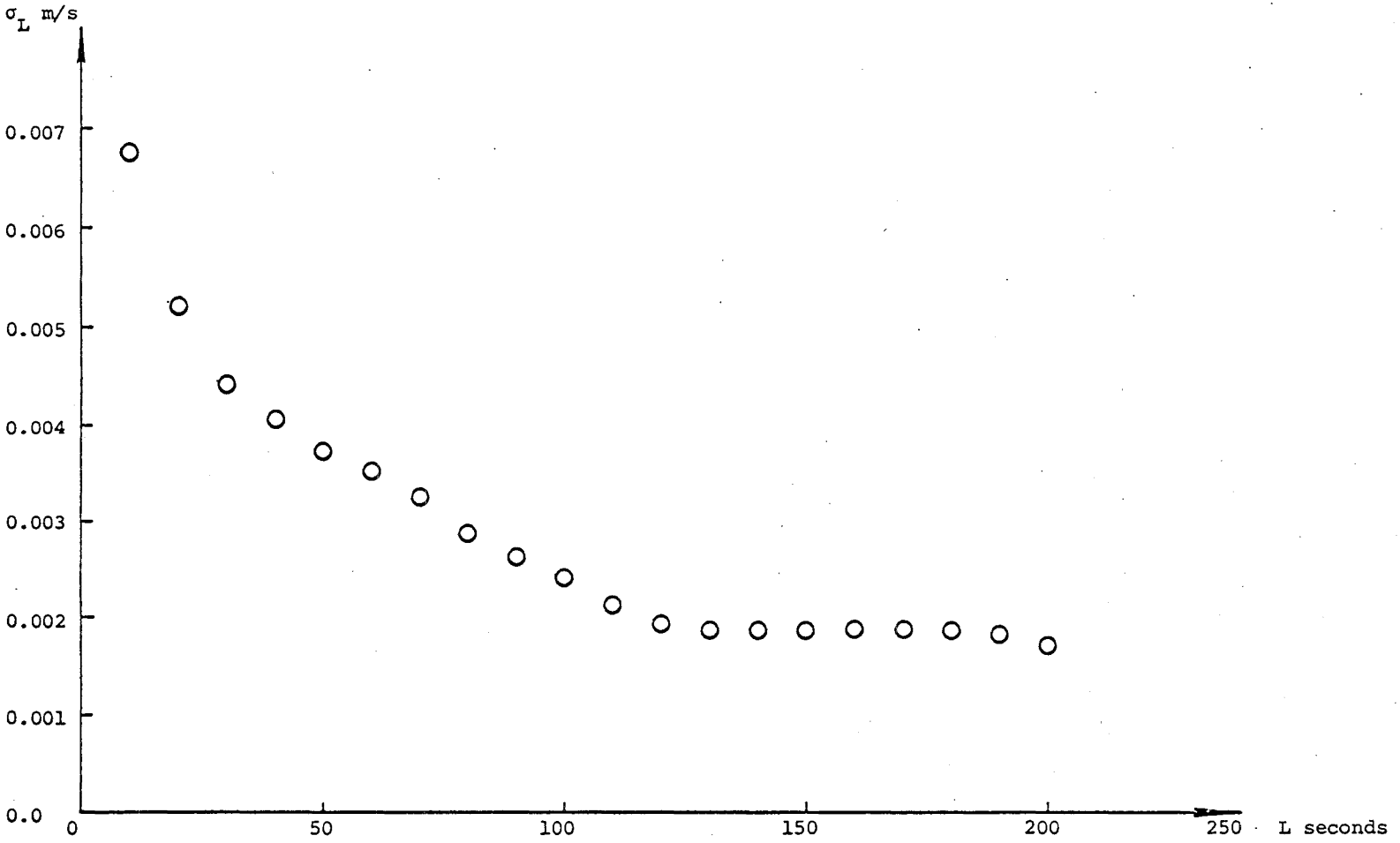

FIGURE 6.11 Standard deviation of the mean velocity from the overall mean as a function of the sampling period length.

identical fashion to the sampling time for measuring the temperature field. The data record from a representative experiment was analysed and the standard deviations σ_L from the overall mean $\bar{u}$ for the means of a series of sampling periods of length L seconds plotted against the sampling time (Fig. 6.11). At about L = 120 seconds the standard deviation becomes independent of the sampling time and this time was used for measurements of the velocity field.

6.5.3 Experimental Procedure for Velocity Measurements

The laser and the optical unit for splitting and diffracting the laser light were mounted on an optical bench aligned perpendicularly with the direction of flow. Prior to performing any measurements the Bragg cells were tuned visually for maximum diffraction and the geometry of the split beams adjusted. It was essential for the beams to lie in a horizontal plane (for measurement of horizontal velocities) and to intersect perfectly at the point of measurement (approximately midway between the two confining walls of the model when the experimental tank was filled with water). Imperfect intersection of the beams gave a poor quality Doppler signal that was difficult to track. A test objective mounted at the intersection point projected an image of the measuring volume onto a screen and the beam alignment was corrected with adjustment screws on the optical unit to obtain complete beam overlap. The original undiffracted beams remained visible when the Bragg cells were switched on and care had to be exercised continually to ensure that the appropriate adjustments were made to the diffracted beams.

The angle θ of beam intersection was determined after the laser geometry had been adjusted. A second optical bench was temporarily placed inside the empty glass-walled experimental tank and aligned with the bisector of the intersecting beams. The separation of the beams at a series

of distances from the point of intersection was measured and the tangent of the intersection angle obtained for each distance. The results were averaged and θ was calculated to an estimated accuracy of 0.1%.

A mirror was used to reflect the scattered light out the adjacent side of the experimental tank thereby reducing the light path through the water and achieving the maximum possible light intensity at the detection end (Fig. 6.10). After positioning the mirror the tank was filled with water and a quantity of homogenised milk added for the purpose of avoiding biased velocity measurements (Appendix B). During the filling process the position of the measuring volume was located relative to the model by aligning the intersection point with the channel floor and the edge of the step and reading the vertical and horizontal vernier point gauges. The tracking equipment was also switched on and allowed to warm up and the data acquisition system readied to receive data.

The photomultiplier tube was mounted on the second optical bench and aligned roughly with the bisector of the reflected laser beams. Scattered light from any direction can be collected by the photomultiplier in the differential-Doppler mode so that precise alignment was unnecessary. The image of the measuring volume was observed through the viewfinder and the photomultiplier moved along the bench until the image was focused on the pin-hole aperture. The pin-hole centre was adjusted using the screws provided to coincide with the image of the intersection point. The presence of milk in the ambient receiving water aided the alignment and focusing procedure considerably.

The photomultiplier was activated by a high voltage supply. For a scattering particle concentration corresponding to 20 ml milk/m^3 (1:50000) in the ambient receiving water, 800V applied across the photomultiplier produced the desired anode current of 50 μA. The Doppler signal

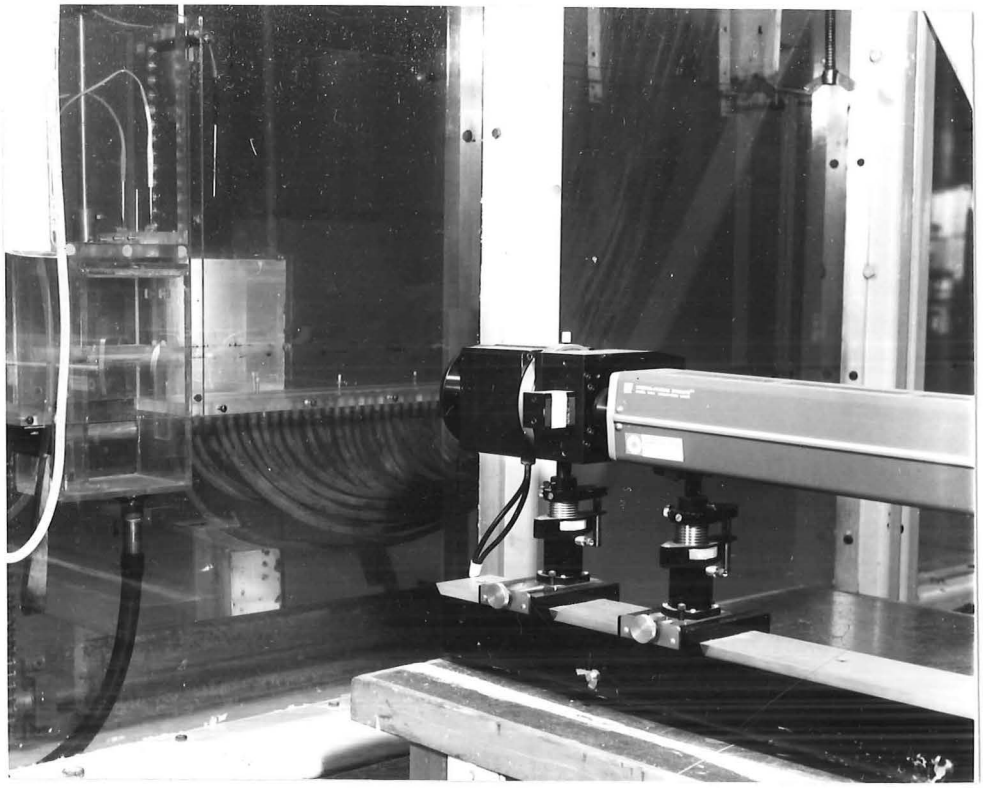

FIGURE 6.12 LDA setup viewed from the laser end

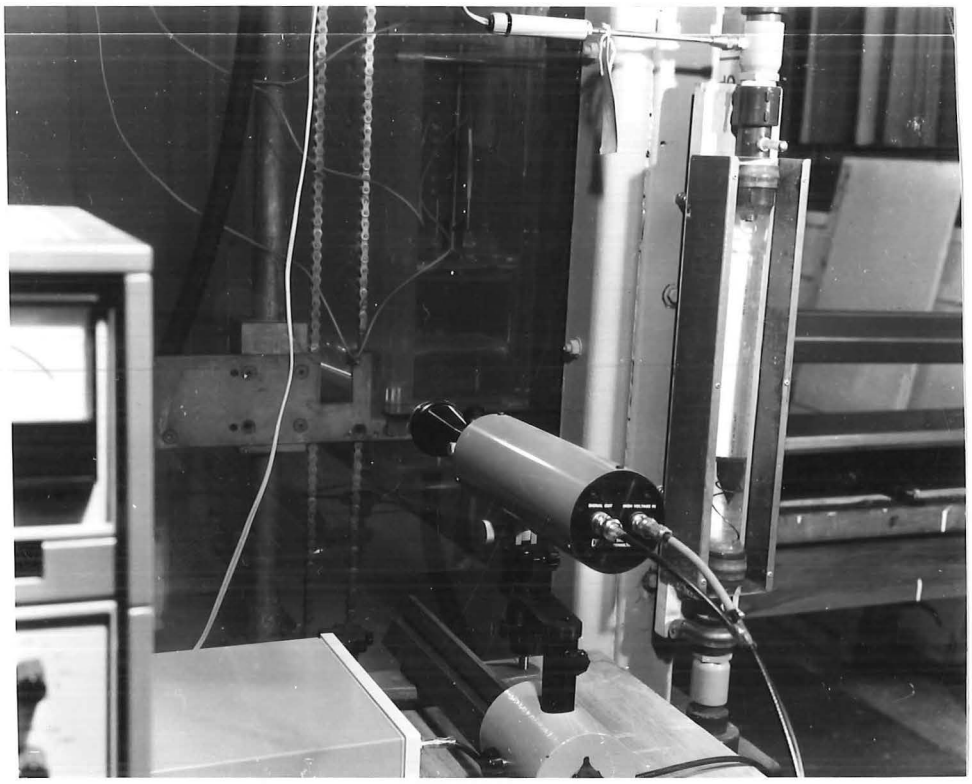

FIGURE 6.13 LDA setup viewed from the photodetection end.

due to the scattered light from the intersecting beams with pre-shifted frequencies, and which corresponded to zero velocity, was tracked and measured. A 0.5% intermediate frequency (Appendix B) bandwidth setting on the Doppler signal processer was adequate for this purpose. The Doppler frequency varied slightly each time the equipment was switched on requiring the measurement to be repeated each day.

Establishment of the Doppler frequency corresponding to a zero velocity completed the preparations for running. The jet flow was started and the rotameters measuring the constant head and seeding supplies adjusted to the correct settings. Sufficient time was allowed to elapse for the equilibrium flow configuration to be set up during which the signal processer was tuned to track the Doppler signal. The maximum intermediate frequency bandwidth setting (8%) was used as both mean velocities and turbulent intensity of velocity fluctuations were of interest. A teletype command instructed the data acquisition system to begin collecting data. At the completion of the data collection the model was moved a predetermined increment upwards. The measurement procedure was repeated for the new point after time had been allowed for disturbances due to the upward movement to cease.

The length of a run was limited by one of two factors depending on the nature of the jet. In the non-buoyant case the maximum record length capable of being stored in the PDP11/34 computer at any one time determined the run length. Entrainment of a backflow of warm water into the attached jet limited the run length more severely when the jet was buoyant.

At the end of each run the data was immediately copied into a much reduced format leaving sufficient disk storage space for further measurements. The procedure was repeated and more data collected. Eventually a picture of the horizontal velocity distribution across a vertical section of the attached jet was established.

It took a considerable amount of practice to learn how to manipulate the controls on the Doppler signal processer to obtain a smooth signal and minimise the number of dropout occurrences. Fortunately the velocity field of the pure jet was measured first, the Doppler signals in this case proving substantially easier to track. It was however virtually impossible to eliminate all traces of dropout, particularly for the buoyant situation. When the frequency tracker went momentarily out of lock for this reason during data collection that portion of the record was cut out during subsequent analysis.

At first the reason for the increased occurrence of dropout in the buoyant jet case was thought to be due to an insufficient level of scattering particle concentration. The seeding supply concentration was therefore increased and some improvement resulted. However it was later realised that dropout was caused by the laser beams failing to cross due to changes in refractive index along the light paths.

6.5.4 Errors due to Thermal-Optical Effects

Measurements of velocity with a LDA are sensitive to changes in refractive index occurring as a result of temperature gradients. The wavelength λ and the beam intersection angle θ are both functions of refractive index and will not be constant as assumed in the equation relating the fluid velocity to the Doppler frequency (Appendix B). The possible errors resulting from changes in the refractive index of water in the buoyant jet flow are therefore examined.

A mean temperature gradient in the flow causes the laser beams to refract along the full length of the light path through the water thereby changing the position of the measuring volume and the magnitude of the intersection angle. The wavelength of the laser light at the beam intersection also changes but only as a function of the refractive index at that

point. These effects are partially self-compensating (Gartrell, 1979). In any case the mean temperature gradient across the two-dimensional attached buoyant jet flow is likely to be significant only over a very short distance near the confining walls resulting in little error in the velocity measurements if homogeneity is assumed. Refraction of the beams by a mean temperature gradient also changes the component of velocity measured but the error will be within the accuracy of alignment perpendicular to the flow.

The errors due to fluctuations in the refractive index across the flow are potentially more serious. As a consequence of the fluctuations the beams are always in motion and the velocity measured is an apparent one equal to the true velocity of the water plus the relative velocity of the beam intersection. The beam "wobble" appears to be random when observed visually and is the reason for the greater occurrence of dropout (when the beams fail to intersect) than in the non-buoyant jet experiments. Gartrell (1979) in his study of mixing in density-stratified shear flows determined qualitatively the error in the velocity measurements caused by beam wobble and concluded that it was significant if the velocity fluctuations were sufficiently small and the temperature (and hence refractive index) fluctuations sufficiently large. It is difficult to compare the flow studied by Gartrell (1979) with the buoyant jet flow in the present investigation. However in the latter situation the combination of small velocity and large temperature fluctuations exists only along the upper edge of the jet where dropout due to beam wobble generally prevented satisfactory measurements from being made.

6.6 VELOCITY AND TEMPERATURE DATA COLLECTION

The Civil Engineering Department's new data acquisition system (CEDACS) was used to collect temperature and velocity data. The analogue outputs from the thermistor bridge circuits and the Doppler signal processer were fed directly to a 16 channel PDP11/10 (Digital Equipment Corporation) analogue-digital (A/D) converter. In the latter case matching of the 1.5-10V output with the 0-4.995V input of the A/D converter by suitable stepping down and amplification was required. The analogue signals were sampled discretely and converted into digital form by the A/C converter. The digital data was transmitted to a file in the Civil Engineering Department's PDP11/34 computer and stored there for subsequent processing to obtain mean and fluctuating values. The data files were later copied on the floppy disks for permanent record.

The resolution of the A/D converter was 1 part in 1023. Since the thermistors used were non-linear over the $30^{o}C$ temperature span this resolution will result in a minimum accuracy of about $0.05^{o}C$ at the lower calibration end point ($\simeq 15^{o}C$). For the laser Doppler anemometer a 1 in 1023 resolution corresponds to an accuracy of 0.001 m/s for the 500 KHz range of the signal processer, and 0.0005 m/s for the 150 KHz range.

The CEDACS data acquisition system possessed two serious disadvantages. The maximum sampling rate was limited to 10 samples/second but fortunately this rate proved adequate for measurements of both the temperature and velocity fields in the attached jet. Data acquisition however could not be performed while other users were logged on to the PDP11/34 computer. For data collection over long periods of time as in this investigation the experiments had to be conducted after normal working hours.

CHAPTER 7

RESULTS OF EXPERIMENTS TO MEASURE CHARACTERISTIC EDDY PARAMETERS AND COMPARISONS WITH THEORY

7.1 INTRODUCTION

This chapter reports the results of a series of experiments performed to provide data on the relationships between the characteristic eddy parameters that were identified by dimensional analysis for the non-buoyant attached jet. Comparisons are made with the theory developed previously and the results of other experimental and theoretical studies.

7.2 ATTACHED JET GEOMETRY

The aspect ratio, which is the ratio of the eddy length l to the step height h, characterises the geometry of the eddy in an attached jet. Assuming Reynolds number effects to be insignificant dimensional analysis predicts that the aspect ratio is a function of only the dimensionless step height. To verify the dimensional analysis prediction some experiments were conducted in which the eddy length was measured for a range of step heights. The eddy length is defined as the horizontal distance along the boundary from the step to the mean position of the eddy streamline and the latter location was found in these experiments using a dye streak technique (section 6.3.1).

Initially independence of Reynolds number (Re) was checked. The aspect ratio was determined at the upper and lower bounds of the step height range for a variety of different flowrates. The results are presented in Fig. 7.1 and confirm that the aspect ratio is indeed not a function of jet Reynolds number when Re is greater than about 800.

The aspect ratio was then measured for a number of intermediate step heights at large Reynolds numbers. The results obtained using the two versions of the model (with jet exit widths $2b_o$ = 3.34 mm and $2b_o$ = 6.98 mm respectively) appear in Fig. 7.2. The later set of measurements (for $2b_o$ = 6.98 mm) seem more consistent with the results of Sawyer (1960) and Borque and Newman (1960). The slight difference could be a function of the method of matching the frequency of the forward and reverse turbulent bursts to determine the mean position of the eddy streamline along the boundary. The mean velocity of the forward bursts may in fact exceed that of the reverse bursts thereby overestimating the separation point where the mean velocity is zero. This could also be a factor in the apparent marked difference between the results for the two jet exit widths although the method of presentation tends to accentuate the estimated error ($\pm$ d/2 where d is the spacing between adjacent dye injection points). If the later set of measurements are considered to more accurately represent the relationship between the aspect ratio and the dimensionless step height then the mathematical model developed previously predicts that relationship as well as the model proposed by Sawyer (1963), (section 2.3.1).

The effect of removal of the vertical wall above the horizontal jet discharge slot was studied using the earlier version of the physical model ($2b_o$ = 3.34 mm). The results are compared in Fig. 7.3 with those for when the wall was present. While the entrainment pattern along the upper edge of the jet in each situation was observed visually with dye to be distinctly different it appears from Fig. 7.3 that the attached jet geometry is independent of the pattern. This conclusion was confirmed by other measurements in which a hydrogen bubble technique was used to determine the separation point on the boundary (Fig. 7.4).

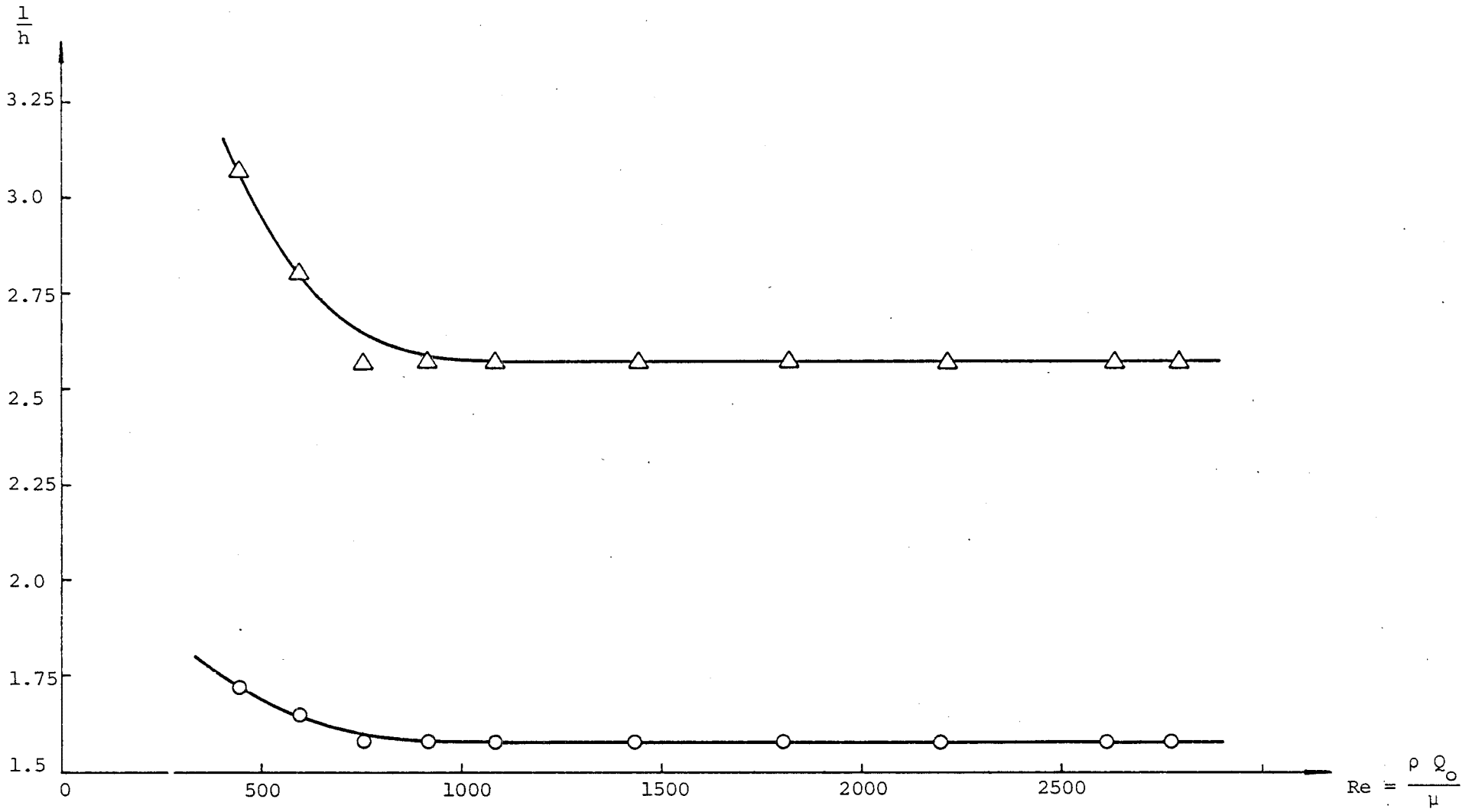

FIGURE 7.1 Independence of the eddy geometry from the jet Reynolds number.

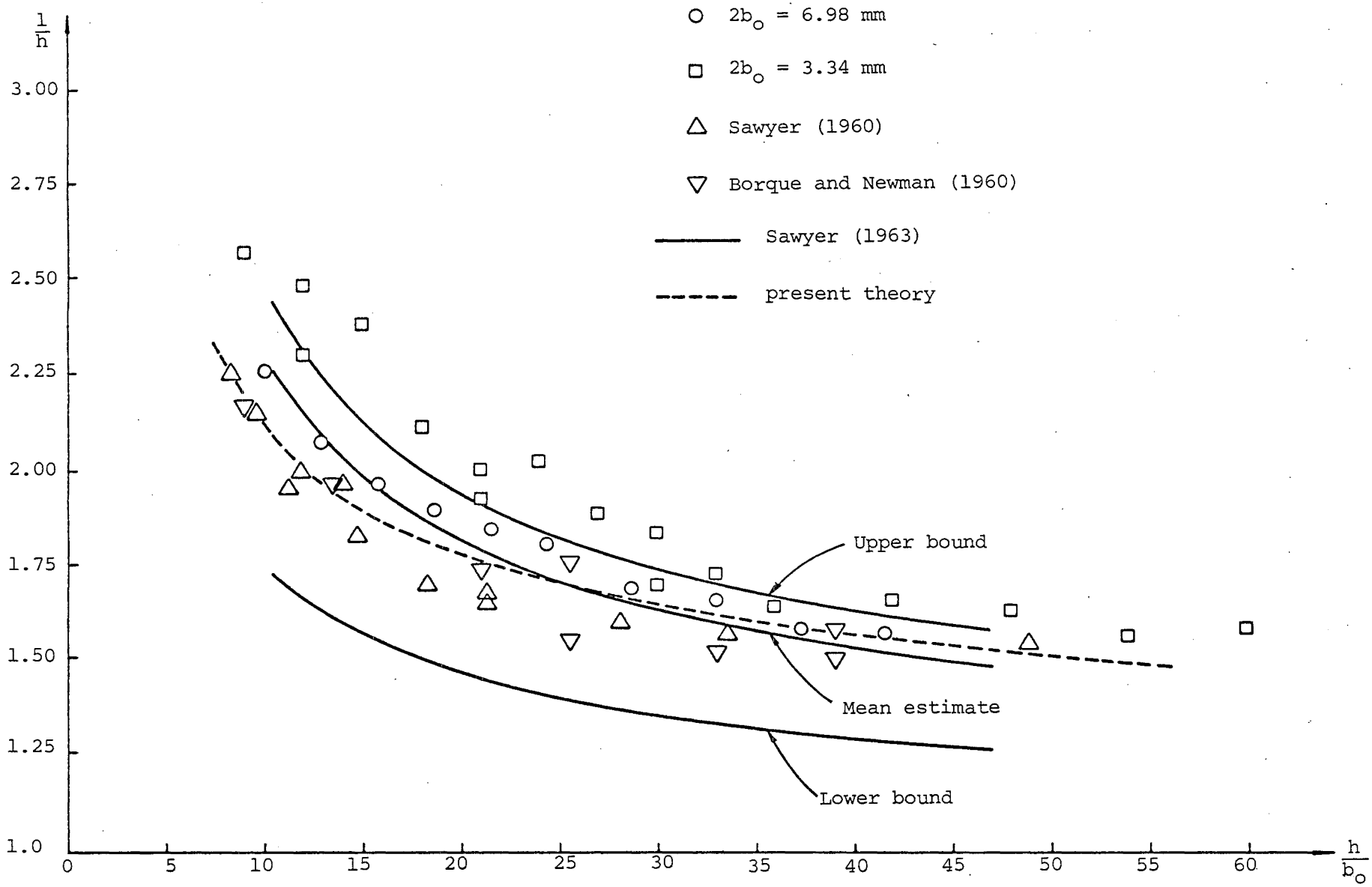

FIGURE 7.2 Comparison of experimental data with the model predictions for aspect ratio as a function of step height.

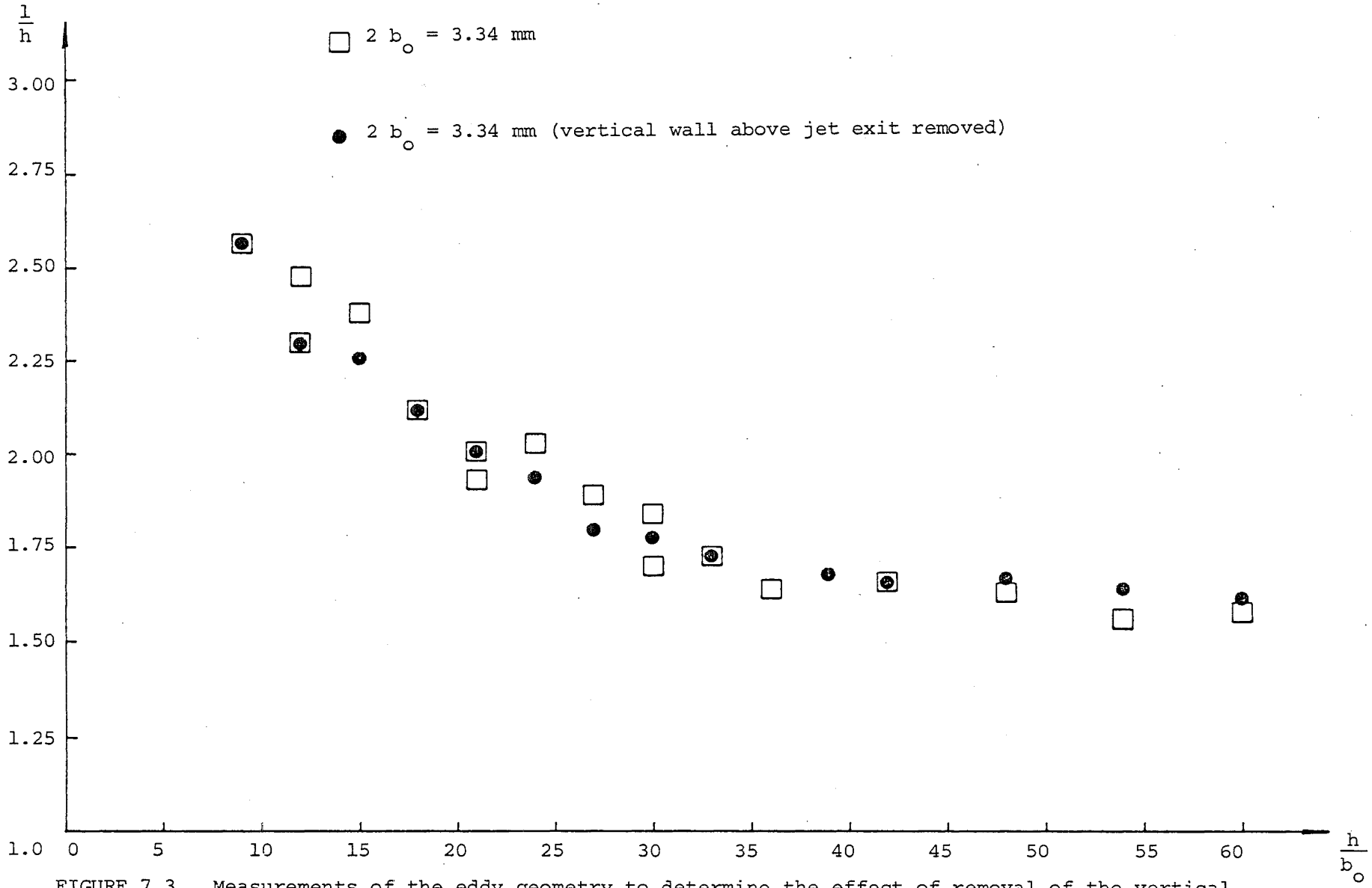

FIGURE 7.3 Measurements of the eddy geometry to determine the effect of removal of the vertical wall above the jet discharge slot.

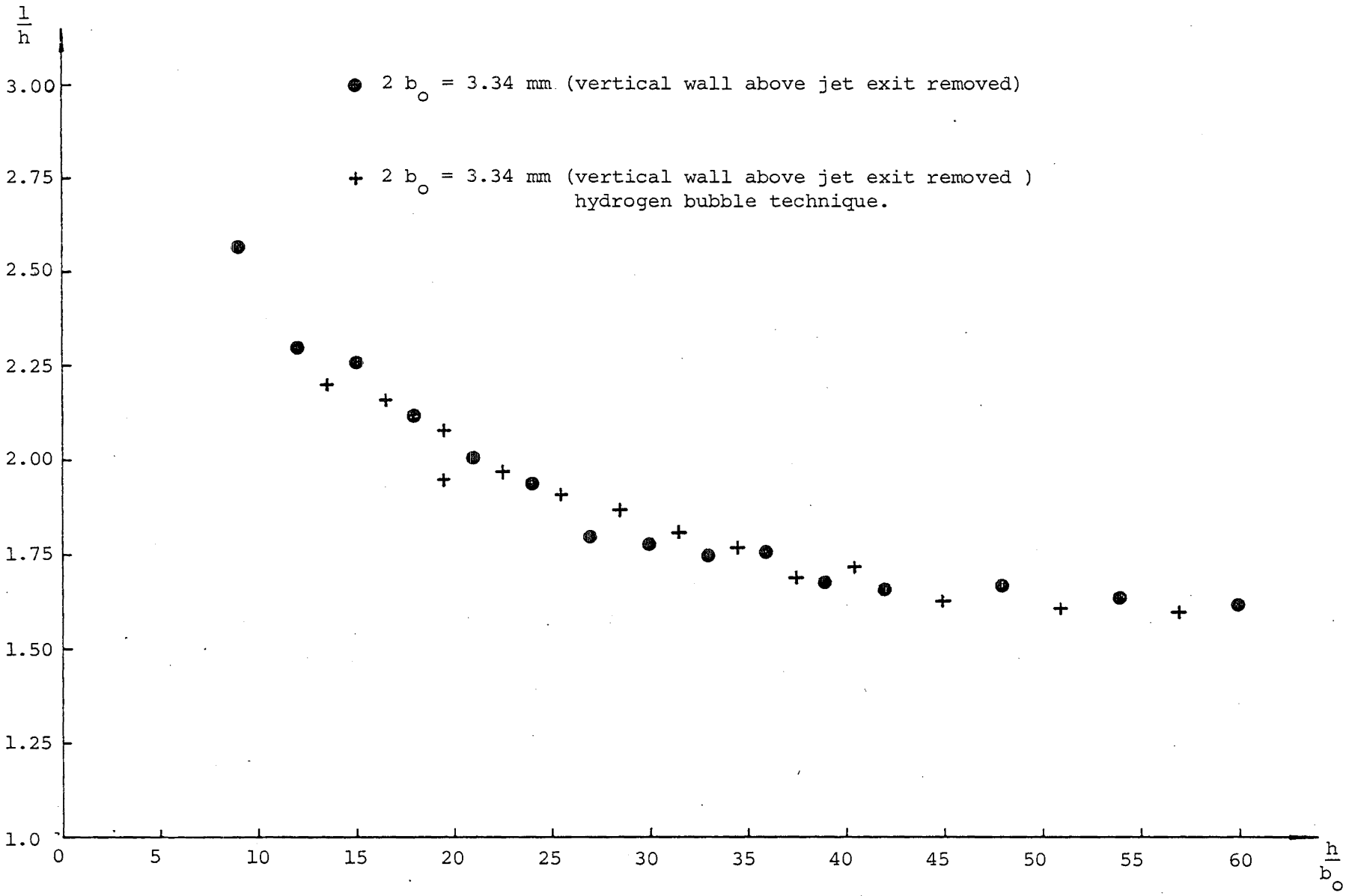

FIGURE 7.4 Comparison of eddy geometry measurements using different visual techniques.

7.3 EDDY CONCENTRATION OF TRACER

It was suspected that a passive tracer added to the inflow of an attached pure jet would result in the formation of a uniform equilibrium concentration of tracer in the eddy. If this is true and Reynolds number effects are insignificant then dimensional analysis predicts that the uniform equilibrium concentration of tracer in the eddy relative to the inflow concentration is a function of the dimensionless step height. To test the basic assumptions and confirm the dimensional analysis prediction the equilibrium concentration of a fluorescent tracer, Rhodamine B, in the eddy was measured relative to the inflow concentration using a fluorometer. Measurements were made over the range of step heights for which the attached jet geometry was determined previously.

Initially the equilibrium concentration of tracer was measured for a single large jet Reynolds number at points along a vertical section and a horizontal section through the eddy. The measured concentrations relative to the inflow concentration are plotted against x/h and y/h in Figs. 7.5 and 7.6 where the origin of the (x,y) coordinate system coincides with the step corner. The results confirm that the equilibrium concentration field in the eddy is uniform.

In a second set of experiments the eddy concentration of tracer was measured at the upper and lower bounds of the step height range for several different flowrates. The results are presented in Fig. 7.7 and show a considerable degree of scatter, the source of which cannot be traced. Despite the scatter, the results seem to indicate that the equilibrium eddy concentration is independent of the jet Reynolds number like the eddy geometry.

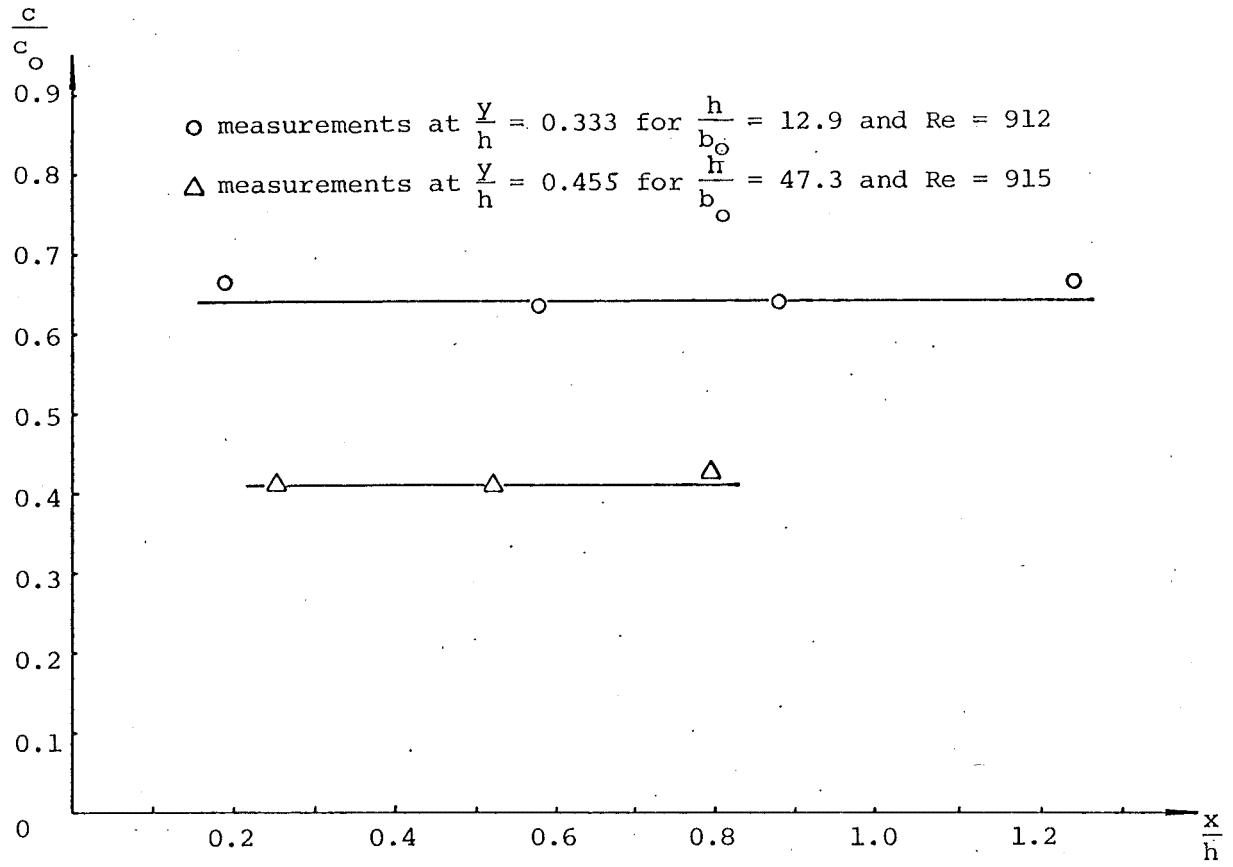

FIGURE 7.5 Uniformity of tracer concentration in the eddy-measurements along a horizontal section through the eddy.

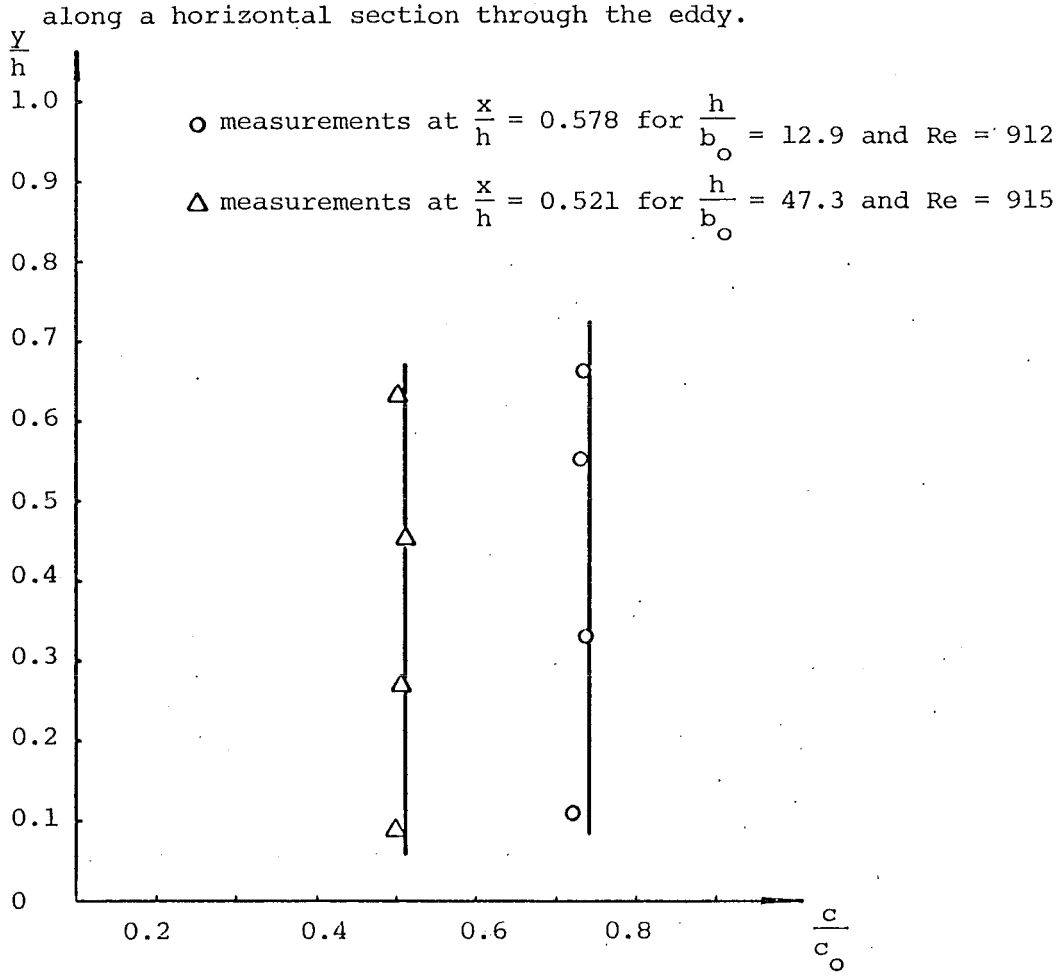

FIGURE 7.6 Uniformity of tracer concentration in the eddy-measurements along a vertical section through the eddy.

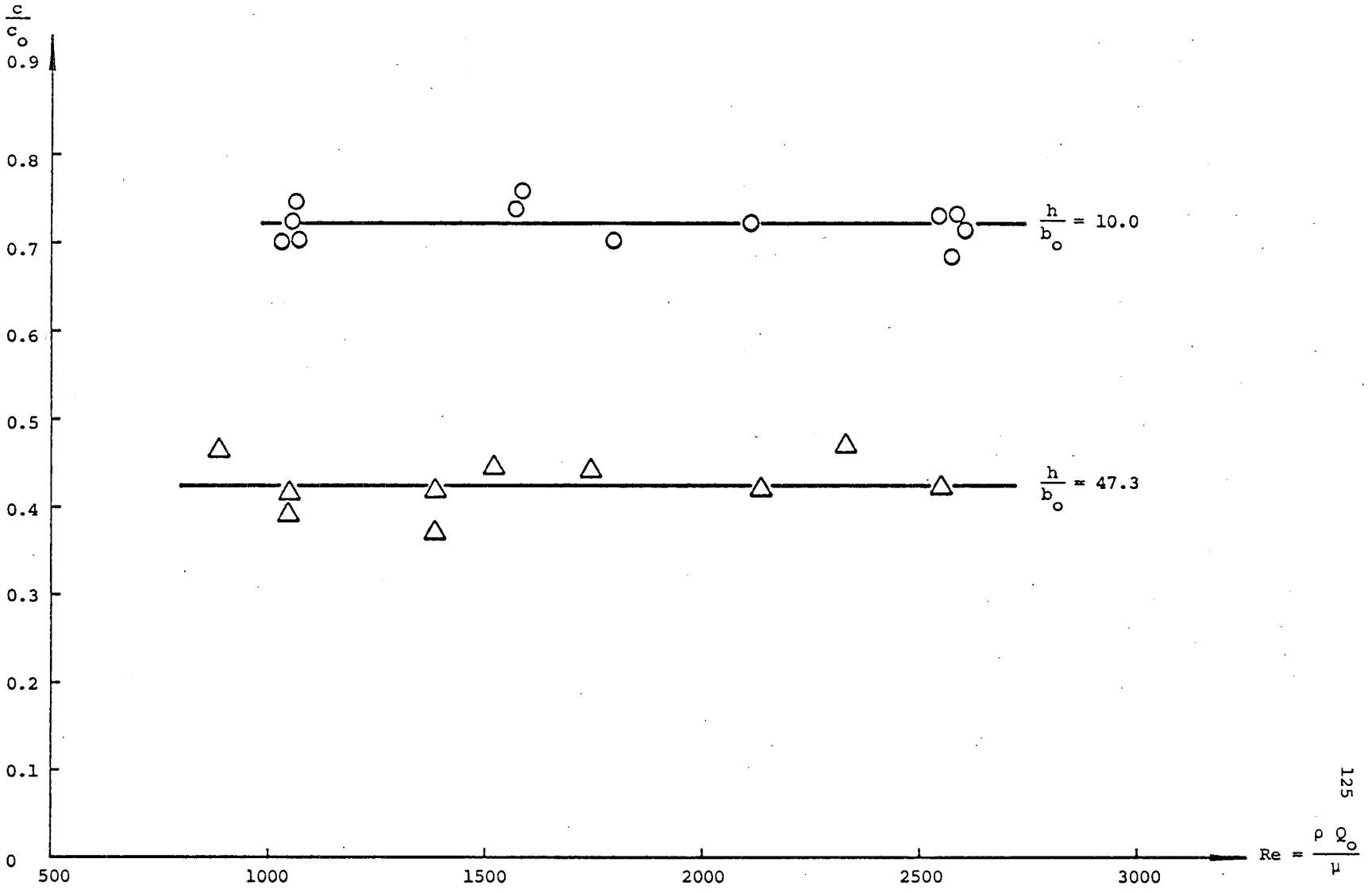

FIGURE 7.7 Independence of the eddy concentration of tracer from the jet Reynolds number.

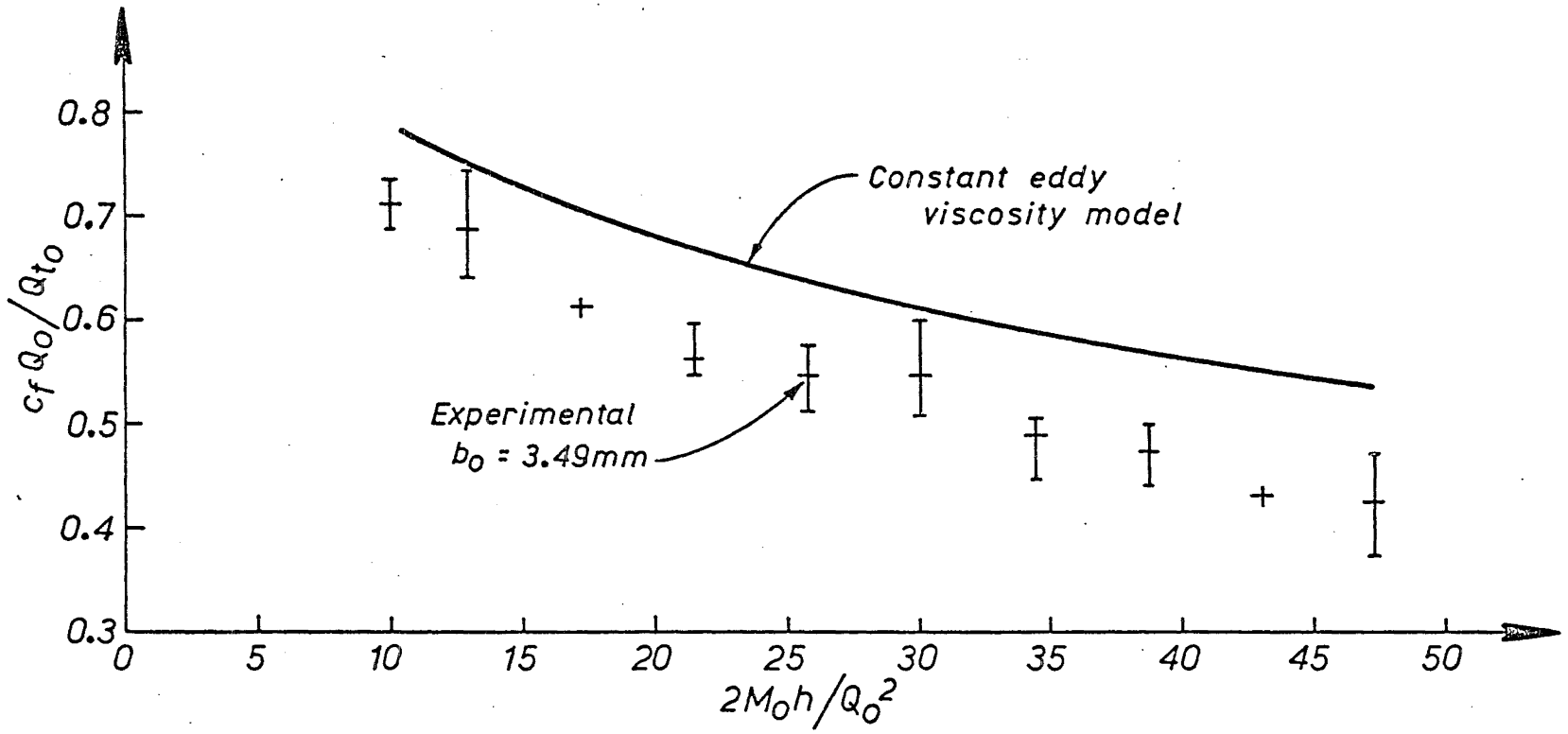

FIGURE 7.8 Comparison of experimental data with the model predictions for eddy concentration of tracer as a function of step height.

The eddy concentration of tracer was then measured relative to the inflow concentration for some intermediate step heights. Several measurements were usually made at each step height to check the repeatability and the averaged results are shown in Fig. 7.8 with error bars to indicate the scatter. The mathematical model developed previously apparently overestimates the uniform concentration of tracer in the eddy.

CHAPTER 8

RESULTS OF VELOCITY MEASUREMENTS

8.1 INTRODUCTION

The horizontal velocity field in both non-buoyant and buoyant attached jets was measured.

The basic parameters and initial conditions for the non-buoyant and buoyant jet experiments are summarised in Tables 8.1 and 8.2 respectively. For each step height and flowrate, the horizontal velocity was measured along a series of vertical sections through the attached jet. The velocity data were subsequently processed to obtain dimensionless profiles of mean horizontal velocity and the turbulent intensity of velocity fluctuations. These profiles are presented in Appendix D along with the tabulated data.

From the mean velocity profiles, streamline plots have been obtained and the turbulent intensity profiles have been used to construct contour plots. The streamline plots and contour plots of turbulent intensity are presented and discussed in this chapter.

In the instance of an attached jet, there is no clearly defined centreline. Instead the locus of maximum velocity is chosen as a reference line for the flow. By assuming a suitable velocity profile across the flow (approximately perpendicular to the streamlines), it can be shown that the locus of maximum horizontal velocity will coincide with this. The jet properties along the line of maximum velocity are reported in this chapter. Comparisons are made with the predictions of the attached jet model in which the centreline is defined as the locus of maximum velocity.

TABLE 8.1 Basic parameters and initial conditions for horizontal velocity measurements in the attached non-buoyant jet.

STEP HEIGHT h (m)	0.050		0.150	
JET EXIT WIDTH $2b_o$ (m)	0.00712	0.00712	0.00712	0.00712
FLOWRATE Q_o (m^2/s)	0.001218	0.002251	0.001218	0.002953
JET EXIT VELOCITY u_o (m/s)	0.1711	0.3161	0.1711	0.4148
JET EXIT REYNOLDS NUMBER $Re = \rho_o \frac{u_o \, 2 \, b_o}{\mu_o}$	1030 - 1070	1910 - 1940	1010 - 1060	2460 - 2620
MEASUREMENT LOCATIONS $\frac{x}{h}$	0.124, 0.390, 0.904, 1.296, 1.724, 2.102	0.124, 0.532 0.996, 1.496, 2.986	0.044, 0.367, 0.787, 1.193, 1.759	0.044, 0.583 0.916, 1.312 1.733

TABLE 8.2 Basic parameters and initial conditions for horizontal velocity measurements in the attached buoyant jet.

STEP HEIGHT h (m)	0.050	0.150
JET EXIT WIDTH $2b_o$ (m)	0.00690	0.00690
FLOWRATE Q_o (m^2/s)	0.003009	0.003009
JET EXIT VELOCITY u_o (m/s)	0.4361	0.4361
JET EXIT TEMPERATURE RELATIVE TO AMBIENT $T_o - T_a$ (^oC)	21.96 ± 0.3	22.51 ± 0.3
JET EXIT REYNOLDS NUMBER $Re = \rho_o \frac{u_o \, 2b_o}{\mu_o}$	4060 - 4610	4170 - 4760
INITIAL JET RICHARDSON NUMBER $Ri_o = \frac{(\rho_a - \rho_o) \, g \, b_o}{\rho_a \, u_o^2}$	0.00101 ± 0.00010	0.00108 ± 0.00010
MEASUREMENT LOCATIONS $\frac{x}{h}$	0.134, 0.638 1.148, 1.648, 2.150, 2.658	0.216, 0.472 0.741, 1.008 1.332, 1.600 1.832

For the attached jet model the streamlines in the fully developed region (Fig. 8.1) are defined by the equation

$$\frac{\psi}{Q_o} = \frac{1}{2}\left(1 + \int_o^{\chi_2} \alpha_i \, d\chi + \int_{\chi_2}^{\chi} \alpha\left(\frac{u_c}{u_o}\right) d\chi\right)(\tanh \eta - \tanh \eta_e) \qquad (8.1)$$

The locus of maximum velocity (u_c) is a streamline with a number $\psi/Q_o = 0.5$.

Another (x,y) coordinate system has been used to present the results in this chapter. It differs from the one assumed in the attached jet models in that the origin coincides with the corner of the step.

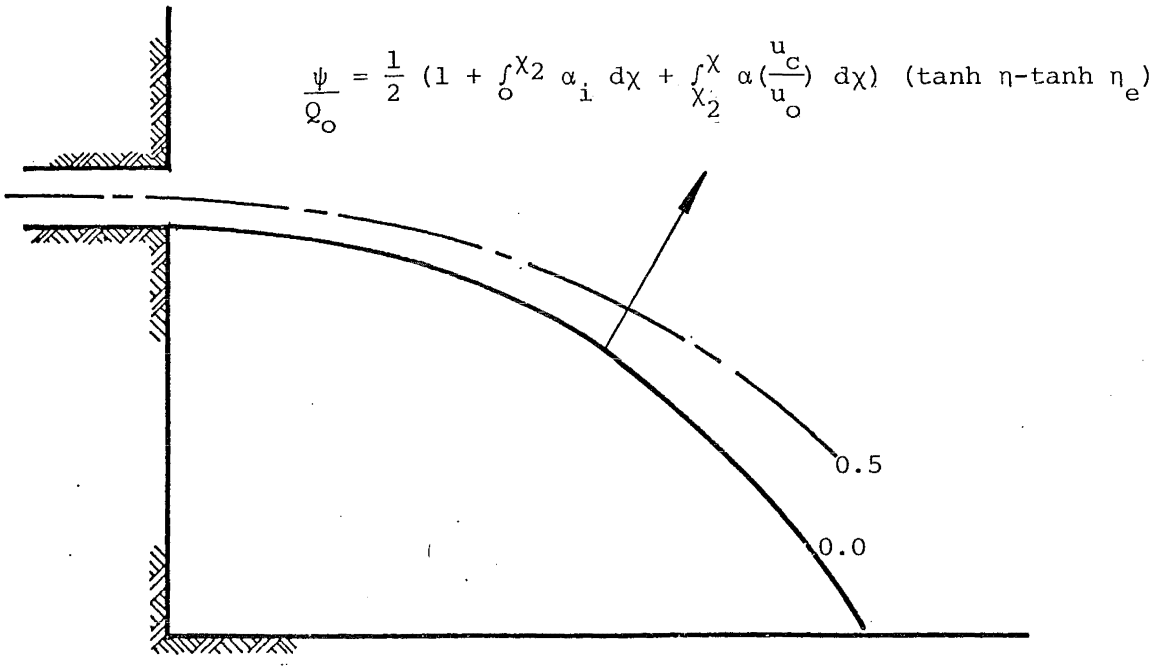

FIGURE 8.1 Streamlines for the attached jet model.

8.2 VELOCITY MEASUREMENTS IN AN ATTACHED NON-BUOYANT JET

8.2.1 Mean Velocity Field in an Attached Non-buoyant Jet

The dimensionless mean horizontal velocity profiles in Figs. D-1 to D-4 (Appendix D) have been itegrated to obtain plots of the streamlines (Figs. 8.2 to 8.5 respectively). Although no great accuracy is claimed for these plots, they do portray the essential features of the flow. For example, the recirculating fluid in the eddy is indicated by the streamlines forming closed loops.

A comparison between the two streamline plots for each step height shows that there is no marked difference even though the Reynolds numbers are different. The streamline plots for the smaller step height appear to be simply longitudinally stretched versions of those for the larger step height.

The positions of maximum horizontal velocity obtained from the mean velocity profiles are indicated on the streamline plots. It is apparent that the locus of maximum velocity follows a streamline $\psi/Q_o \simeq 0.4$ for a considerable distance before diverging. Sawyer (1960) made the same observation for a step height $h/b_o = 11.2$, except that he gave the value of the streamline number as $\psi/Q_o \simeq 0.5$.

Sawyer's value of ψ/Q_o is consistent with that of the line of maximum velocity in the attached jet model (Fig. 8.1). A value of streamline number $\psi/Q_o < 0.5$ for the locus of maximum velocity implies an asymmetric velocity profile across the jet (approximately perpendicular to the streamlines). However, the mean velocity data were too widely spaced for any noticeable asymmetry to be detected in the velocity profiles near the jet exit where jet curvature is small. The chances of error in the streamline plots are increased by the stages that must be gone through

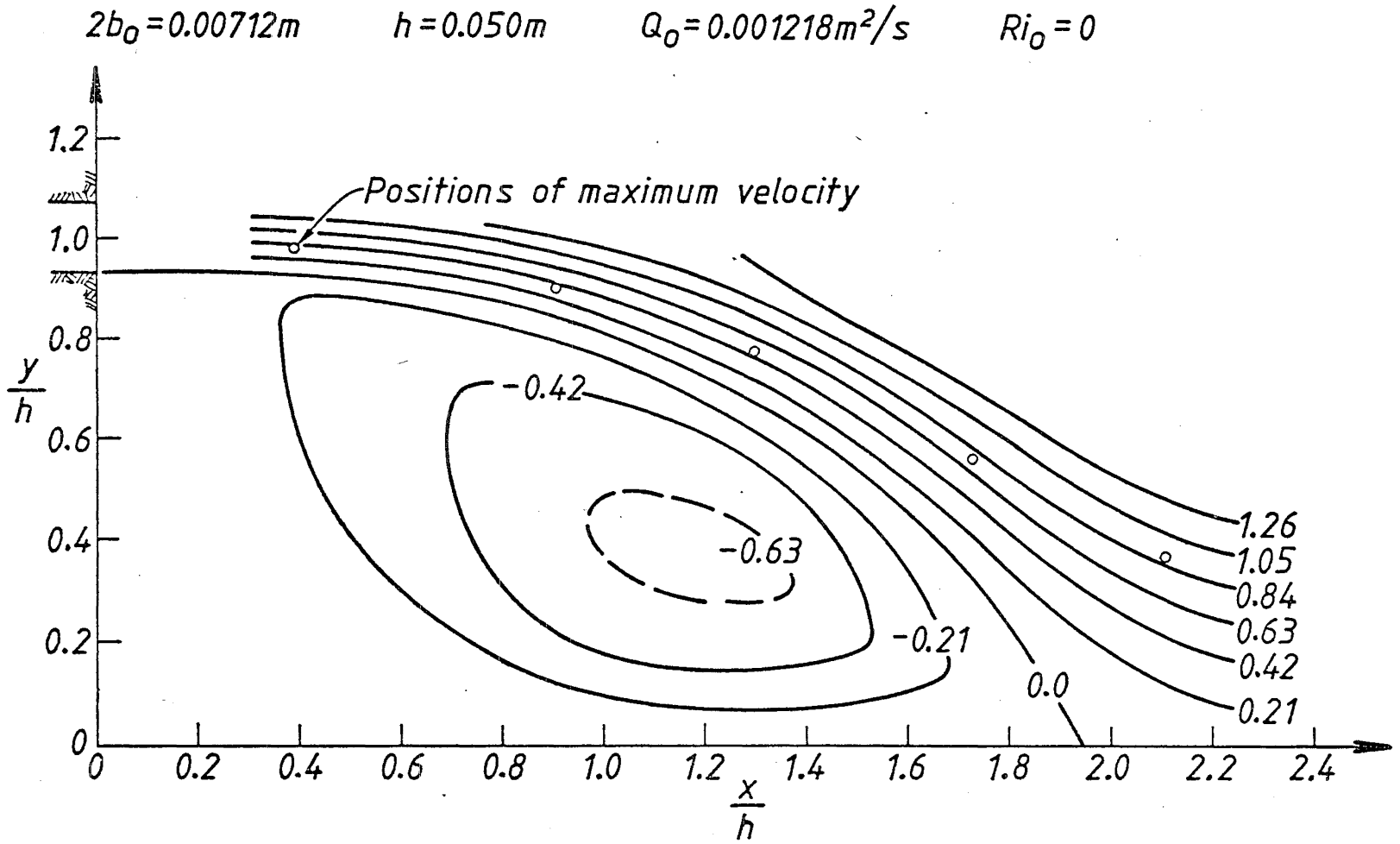

FIGURE 8.2 Streamlines for an attached non-buoyant jet. h/b_o = 14.0 and Re ≃ 1050.

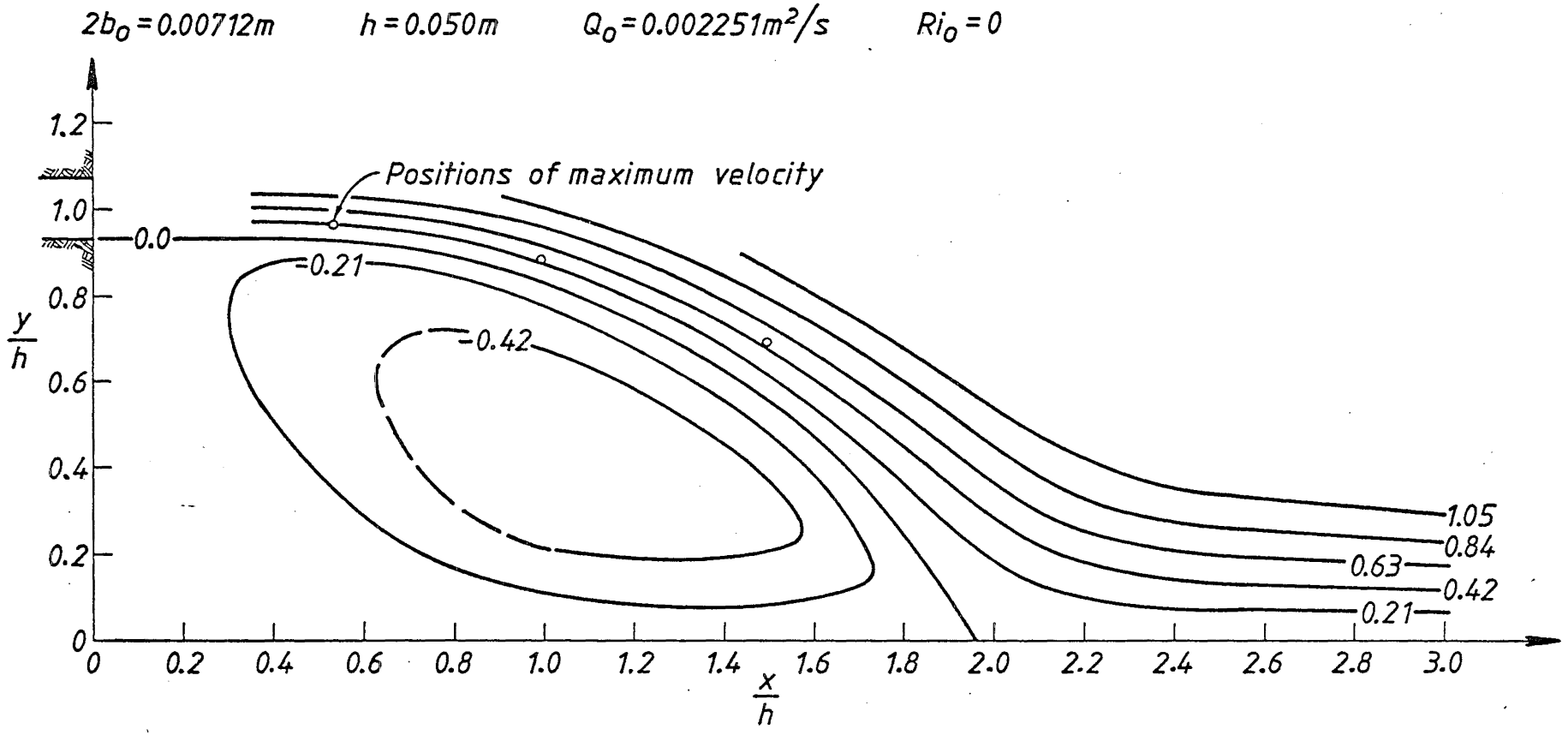

FIGURE 8.3 Streamlines for an attached non-buoyant jet. $h/b_o = 14.0$ and $Re \approx 1925$.

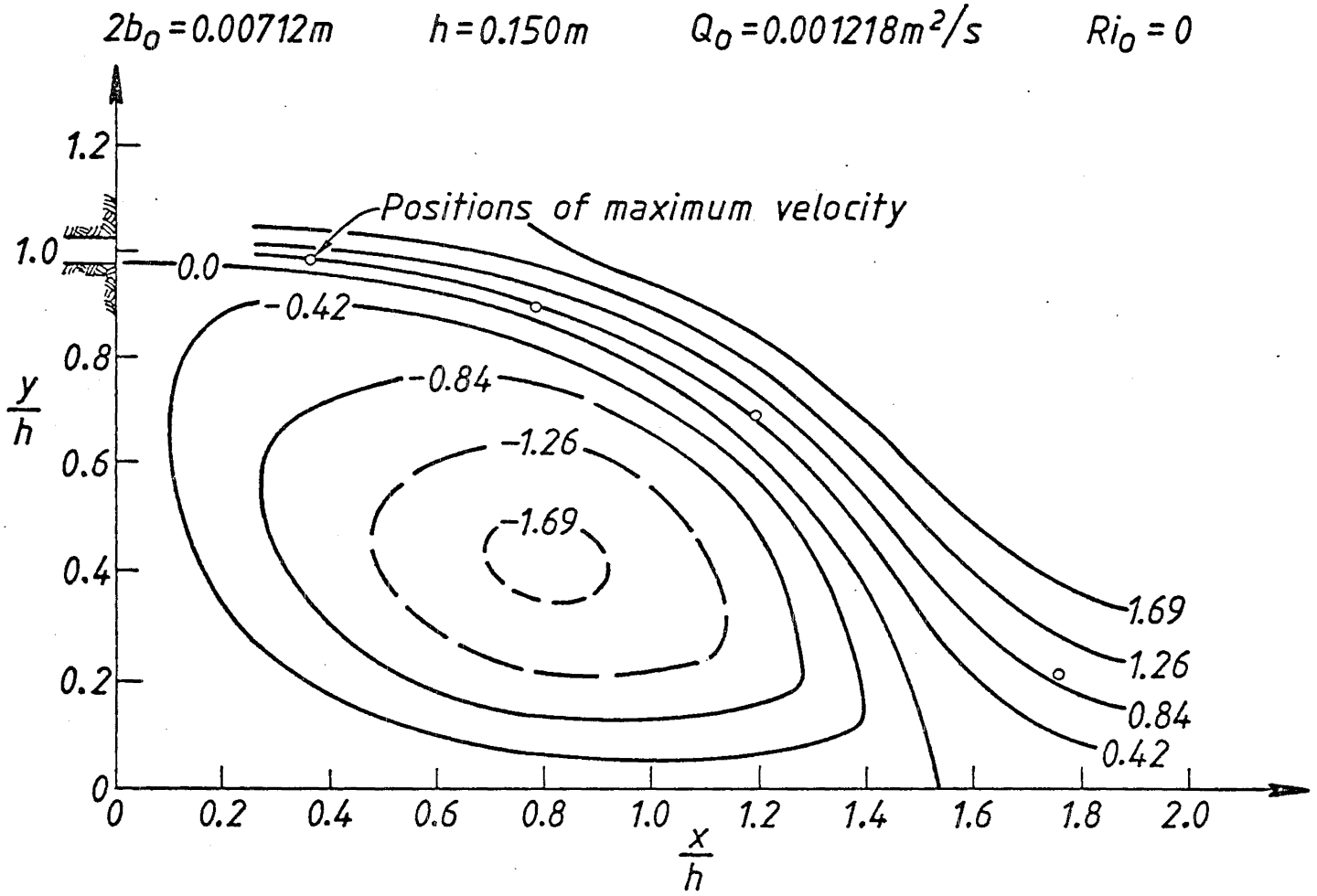

FIGURE 8.4 Streamlines for an attached non-buoyant jet. h/b_o = 42.1 and Re ≈ 1035.

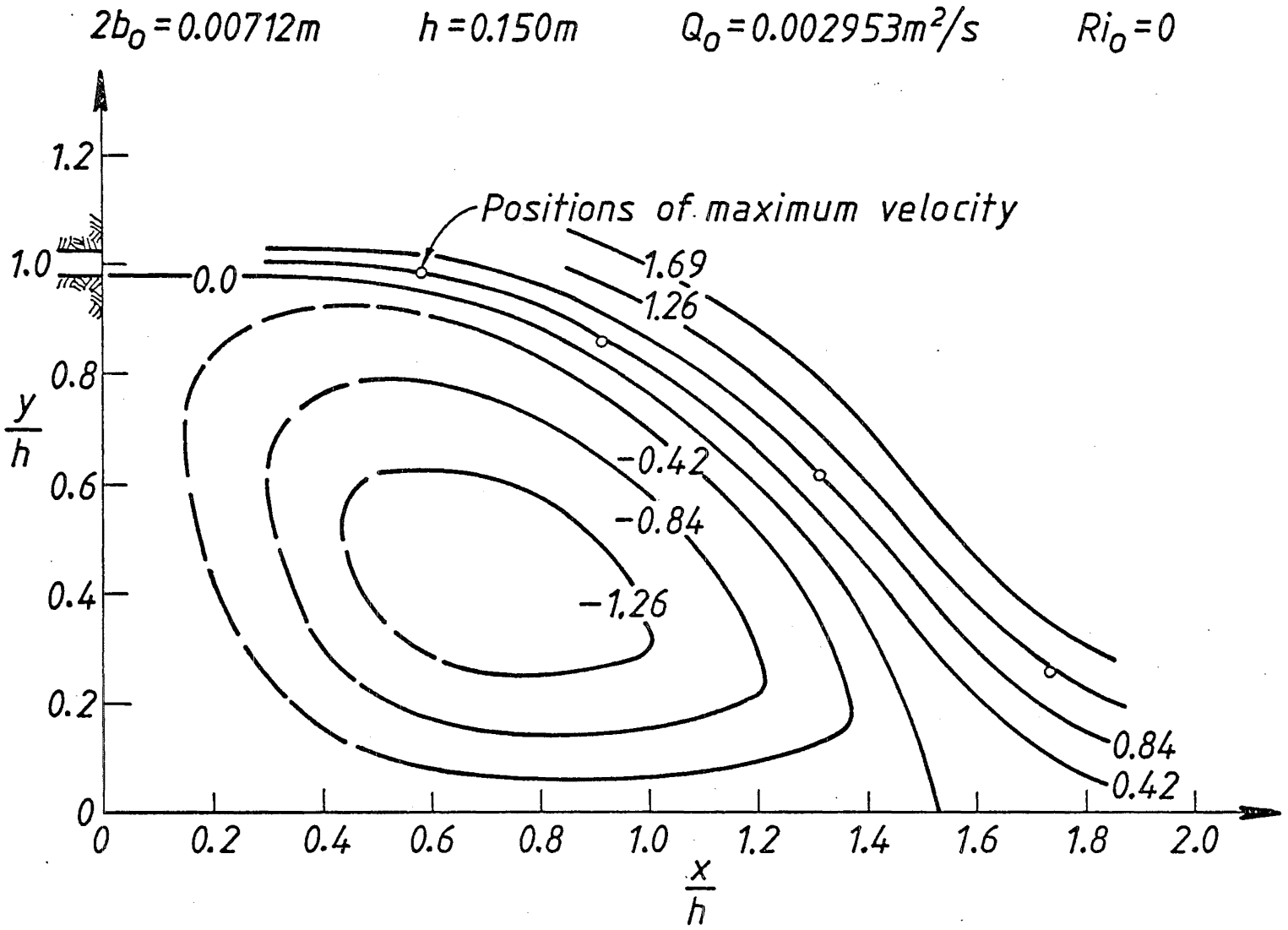

FIGURE 8.5 Streamlines for an attached non-buoyant jet. h/b_o = 42.1 and Re ≈ 2540.

to produce them: interpolation of the mean profiles from the velocity data, integration of the profiles to obtain the streamline positions and interpolation of a streamline plot from all the streamline positions. Since the position of maximum velocity on the mean velocity profiles is quite distinct, this is a more likely explanation of the discrepancy between Sawyer's (1960) result and the present ones.

The points along the locus of maximum velocity and the points along the eddy streamline have been plotted again in Figs. 8.6 and 8.7 for comparison with the predictions of the non-buoyant jet model (Chapter 3). The model predicts a much greater curvature of the jet than is observed experimentally. However the curvature of the measured eddy streamline (ψ/Q_o = 0.0) appears to increase more rapidly than that of the predicted one as the jet approaches the attachment point. This explains why the model satisfactorily describes the position of the eddy streamline on the boundary (section 7.2). The experimental results also indicate that jet curvature in the flow development region becomes less significant as the step height increases and the average pressure difference across the jet decreases. At a sufficiently large step height, jet curvature in the initial region is negligible.

Although the predicted locus of maximum velocity is not coincident with the observed one, the distances along each are similar for a given x/h value. Thus it is still possible to compare the maximum velocities obtained from the mean velocity profiles with the horizontal component of the maximum velocity predicted by the model. Both velocities are plotted in Figs. 8.8 and 8.9 where the solid line represents the predicted decay of maximum velocity (proportional to $s^{-\frac{1}{2}}$ in the fully developed region). The results are good for the larger step height (h/b_o = 42.1, Fig. 8.9). The discrepancy in those for the smaller step height (h/b_o = 14.0, Fig. 8.8)

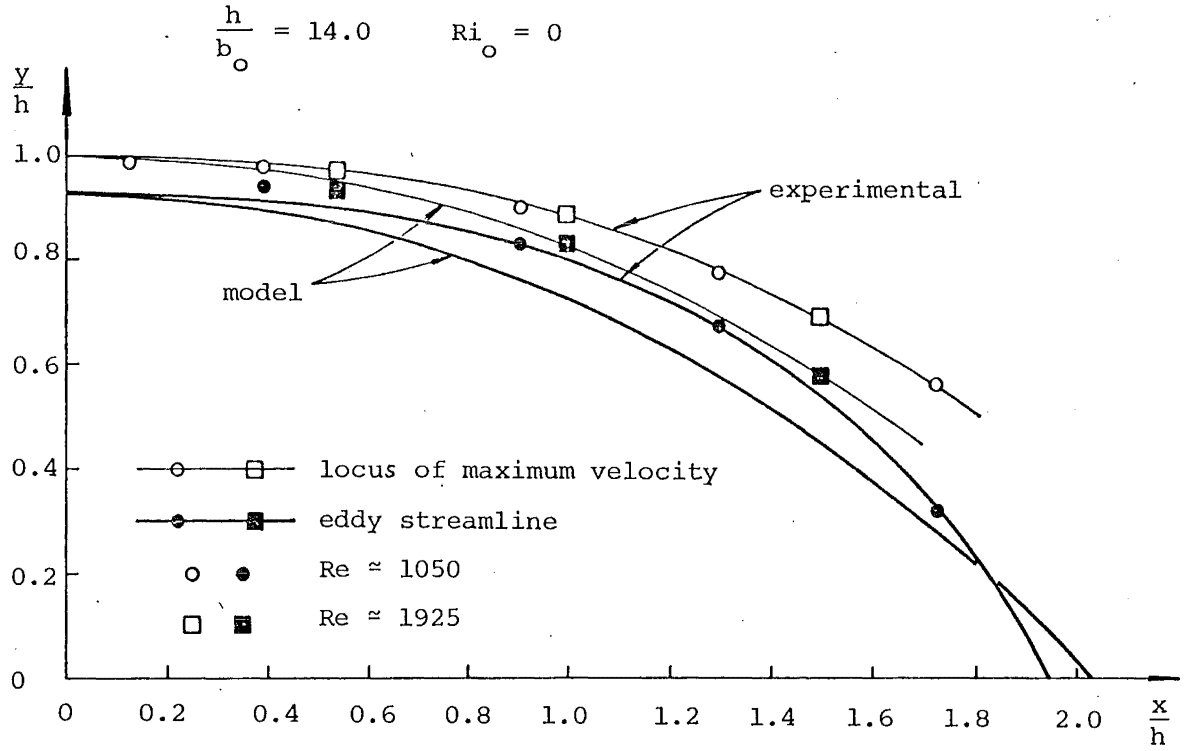

FIGURE 8.6 Locus of maximum mean velocity and eddy streamline position for an attached non-buoyant jet. $h/b_o = 14.0$

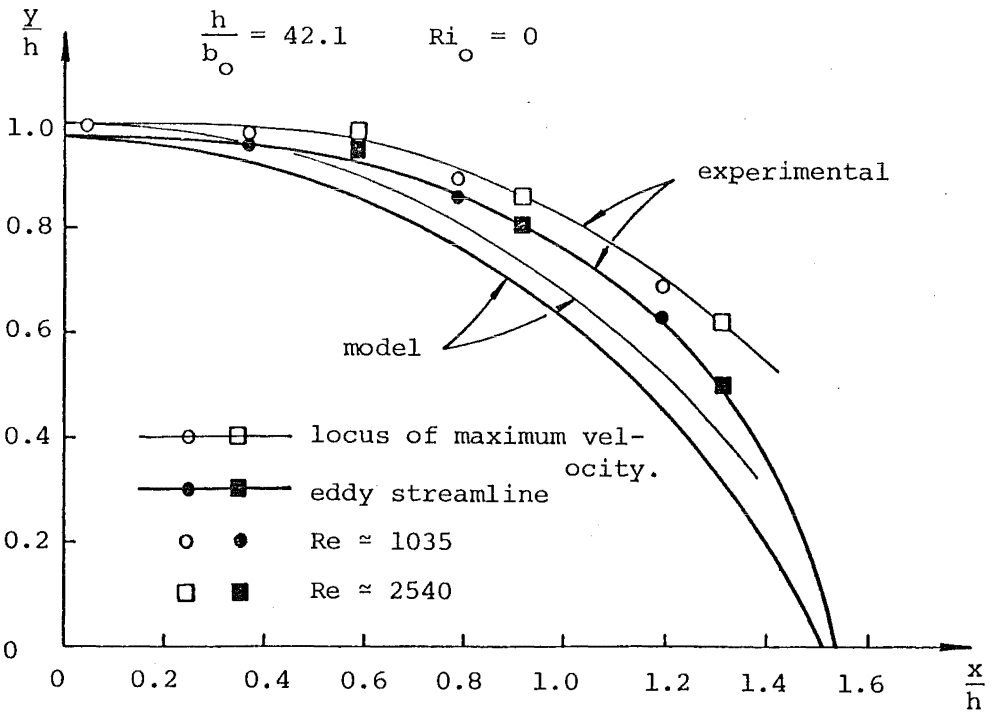

FIGURE 8.7 Locus of maximum mean velocity and eddy streamline position for an attached non-buoyant jet. $h/b_o = 42.1$

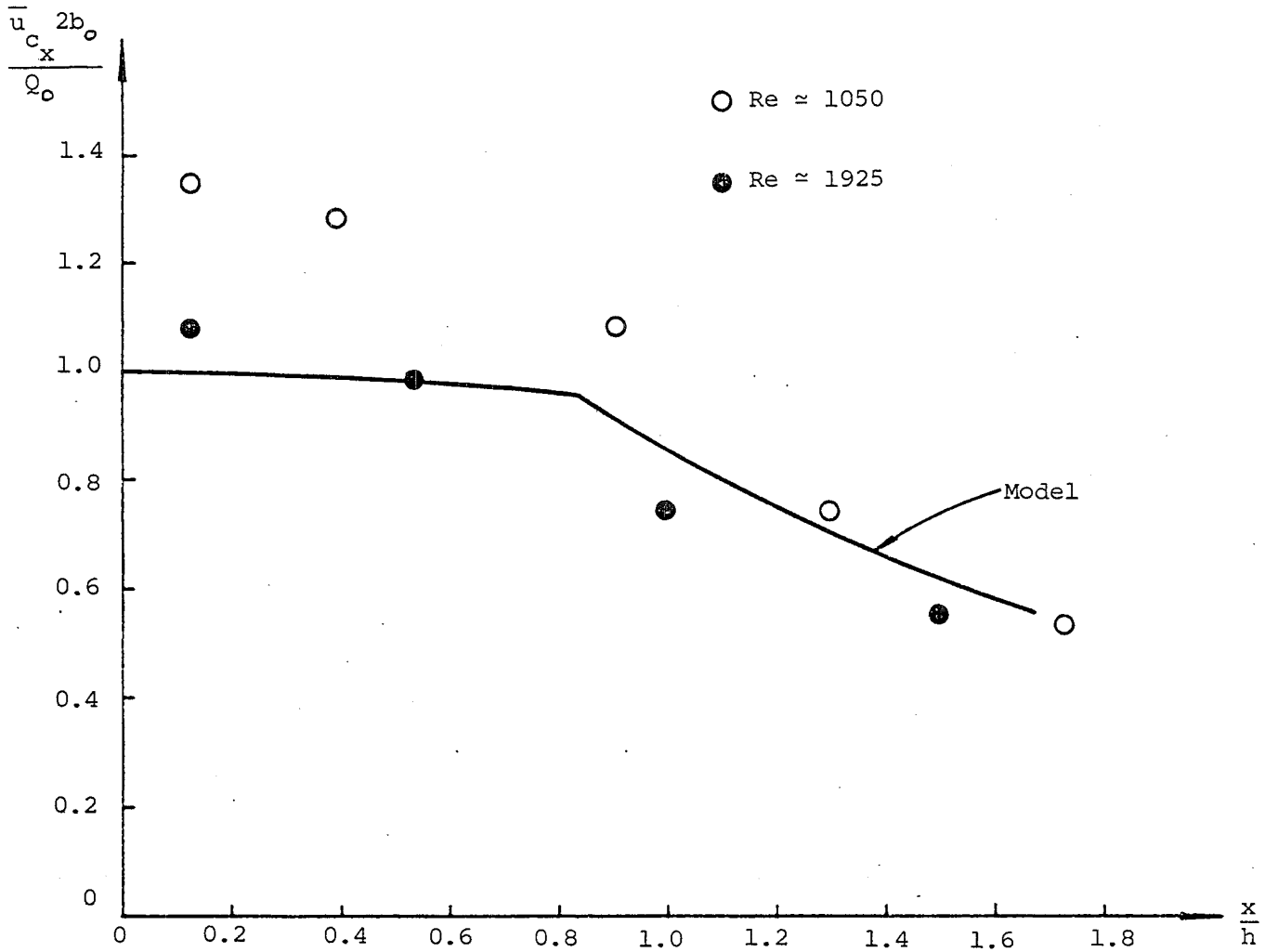

Figure 8.8 Decay of maximum mean horizontal velocity $\bar{u}_{c_x} 2b_o/Q_o$ in an attached non-buoyant jet $h/b_o = 14.0$.

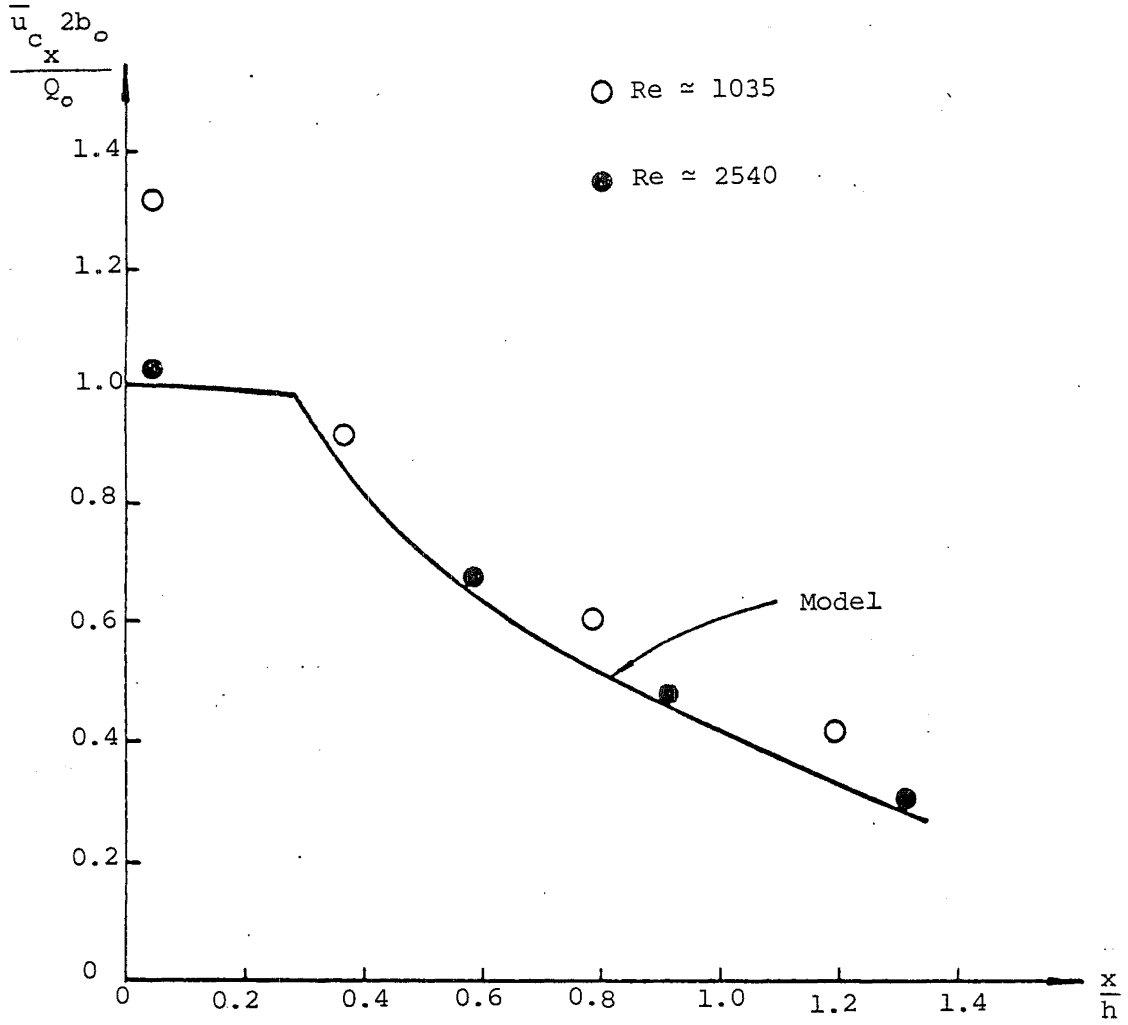

Figure 8.9 Decay of maximum mean horizontal velocity $\bar{u}_{c_x} 2b_o/Q_o$ in an attached non-buoyant jet $h/b_o = 42.1$.

could be due to an overestimate of the potential core length in the model (visual observations indicated the potential core in the buoyant case to be about $10b_o$ long compared with the assumed value of approximately $12b_o$). The velocity measurements in the initial flow region (particularly those at the lower flowrates) indicate that the assumed jet exit velocity profile in the attached jet model differs markedly from the actual one (Fig. 8.10). Beyond the initial region though, the measured velocities follow the predicted decay rate or else rapidly approach it as x/h increases.

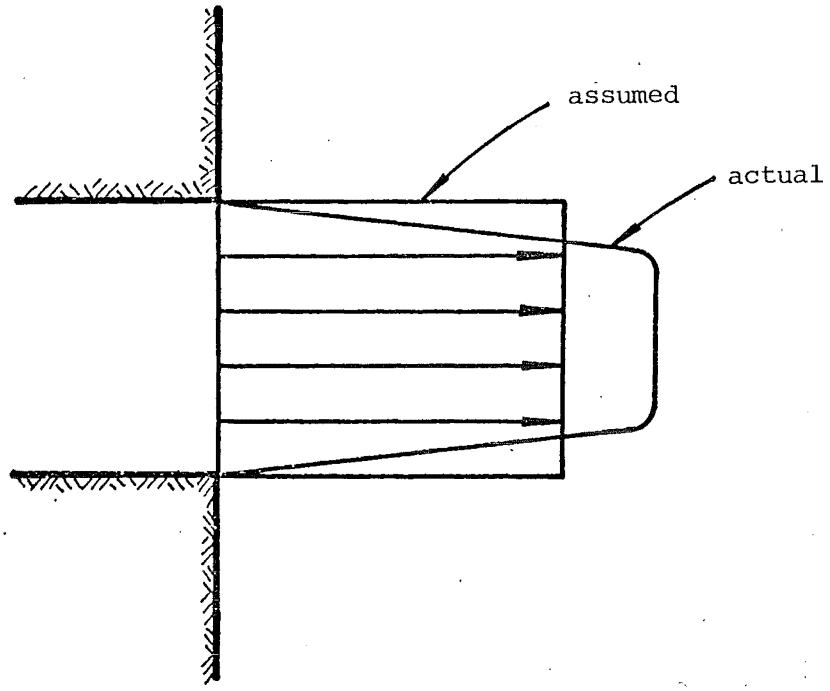

Figure 8.10 Velocity profiles at the jet exit.

8.2.2 Turbulent Intensity of Velocity Fluctuations in an Attached Non-buoyant Jet

The dimensionless profiles of the turbulent intensity of velocity fluctuations in Figs. D-5 and D-8 (Appendix D) have been used to construct percentage contour plots of dimensionless turbulent intensity $\sqrt{u'^2_x}\ 2b_o/Q_o$ (Figs. 8.11 and 8.12 respectively). It is expected that the turbulent intensity of the horizontal velocity fluctuations up to the point of

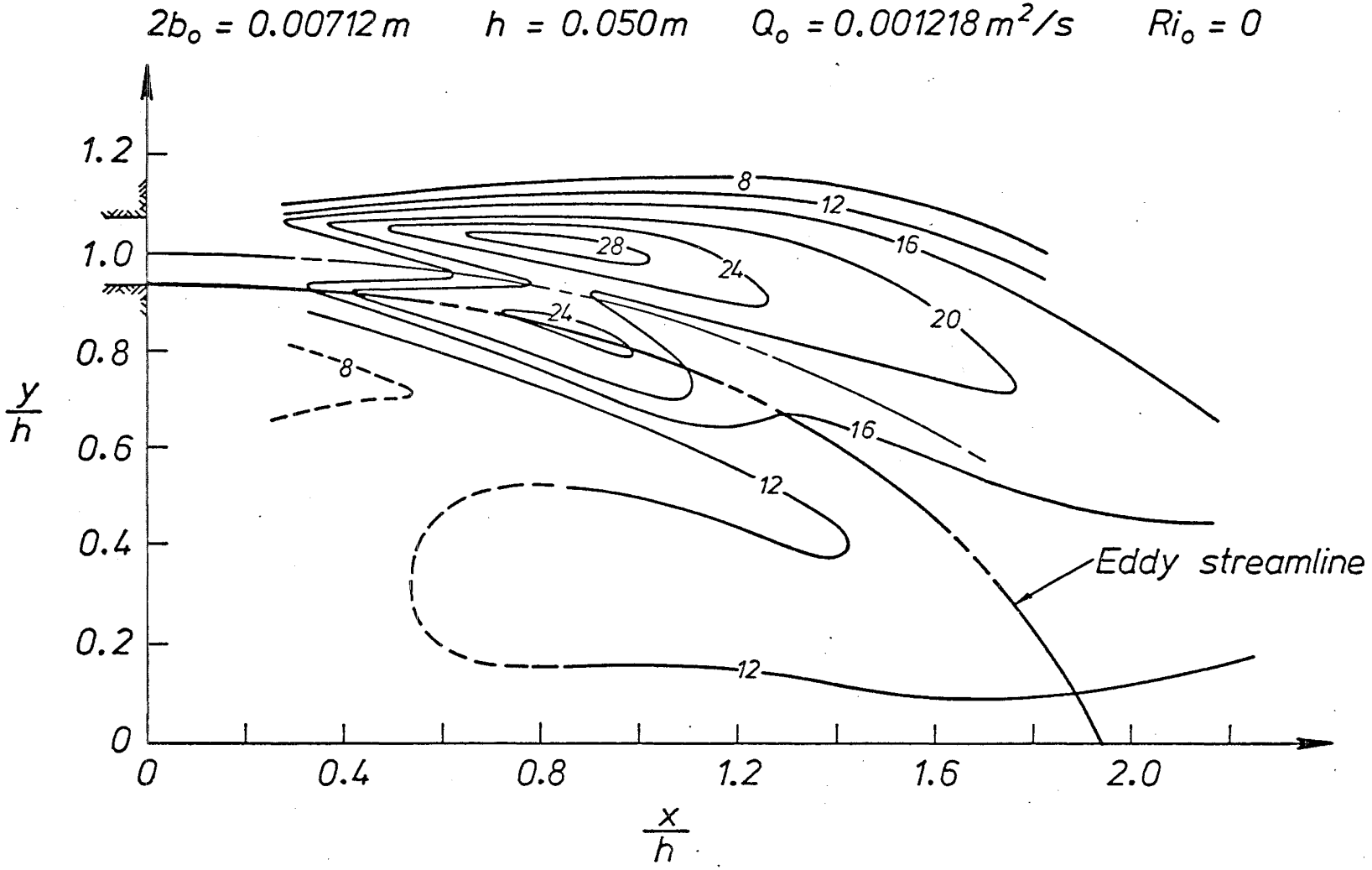

FIGURE 8.11 Percentage contours of dimensionless turbulent intensity of horizontal velocity fluctuations $\sqrt{\overline{u'^2_{c_x}}}\ 2b_o/Q_o$, h/b_o = 14.0 and Re ≃ 1050.

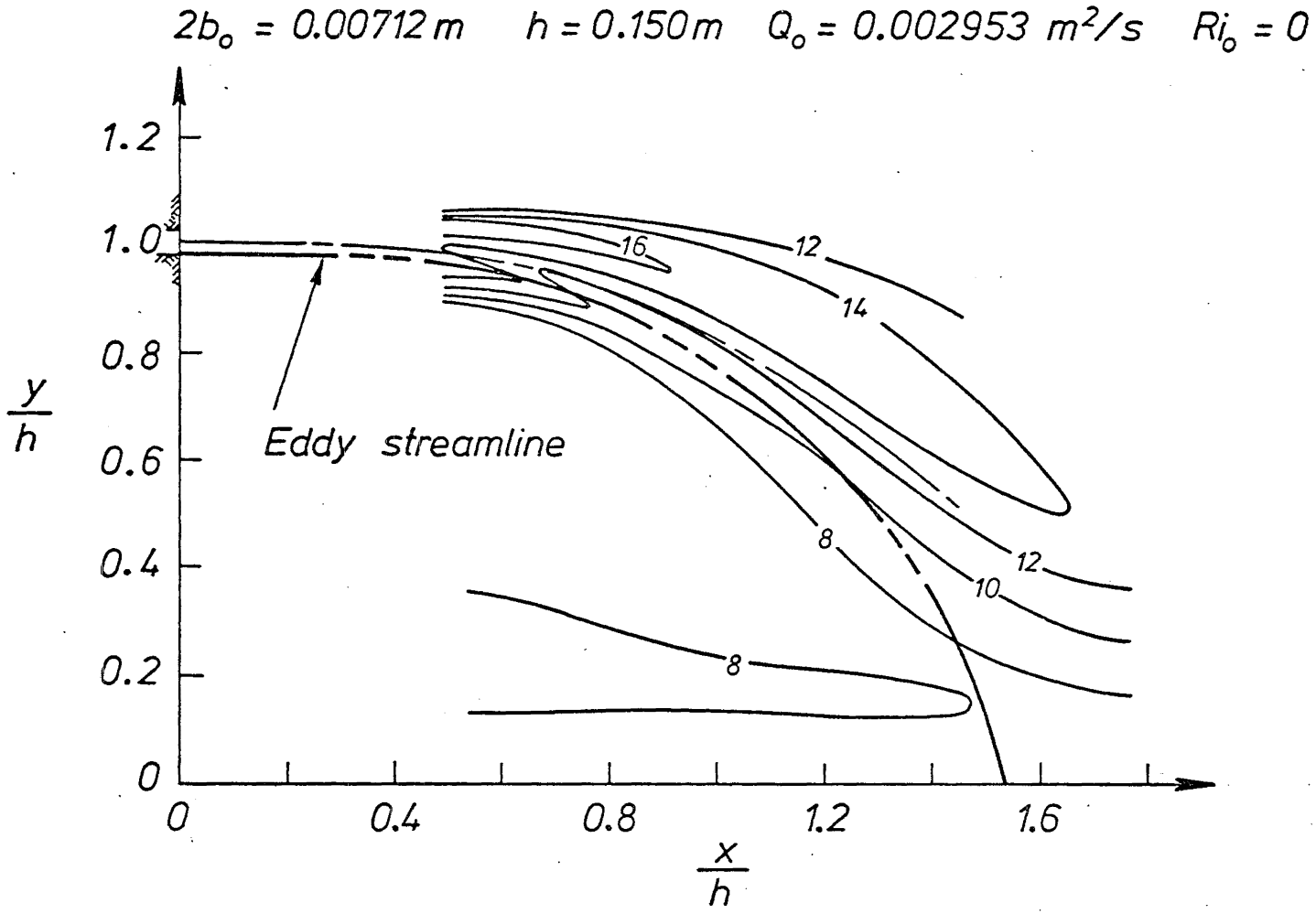

FIGURE 8.12 Percentage contours of dimensionless turbulent intensity of horizontal velocity fluctuations $\sqrt{\overline{u'^2_{c_x}}}\ 2b_o/Q_o$. $h/b_o = 42.1$ and Re ≃ 2540.

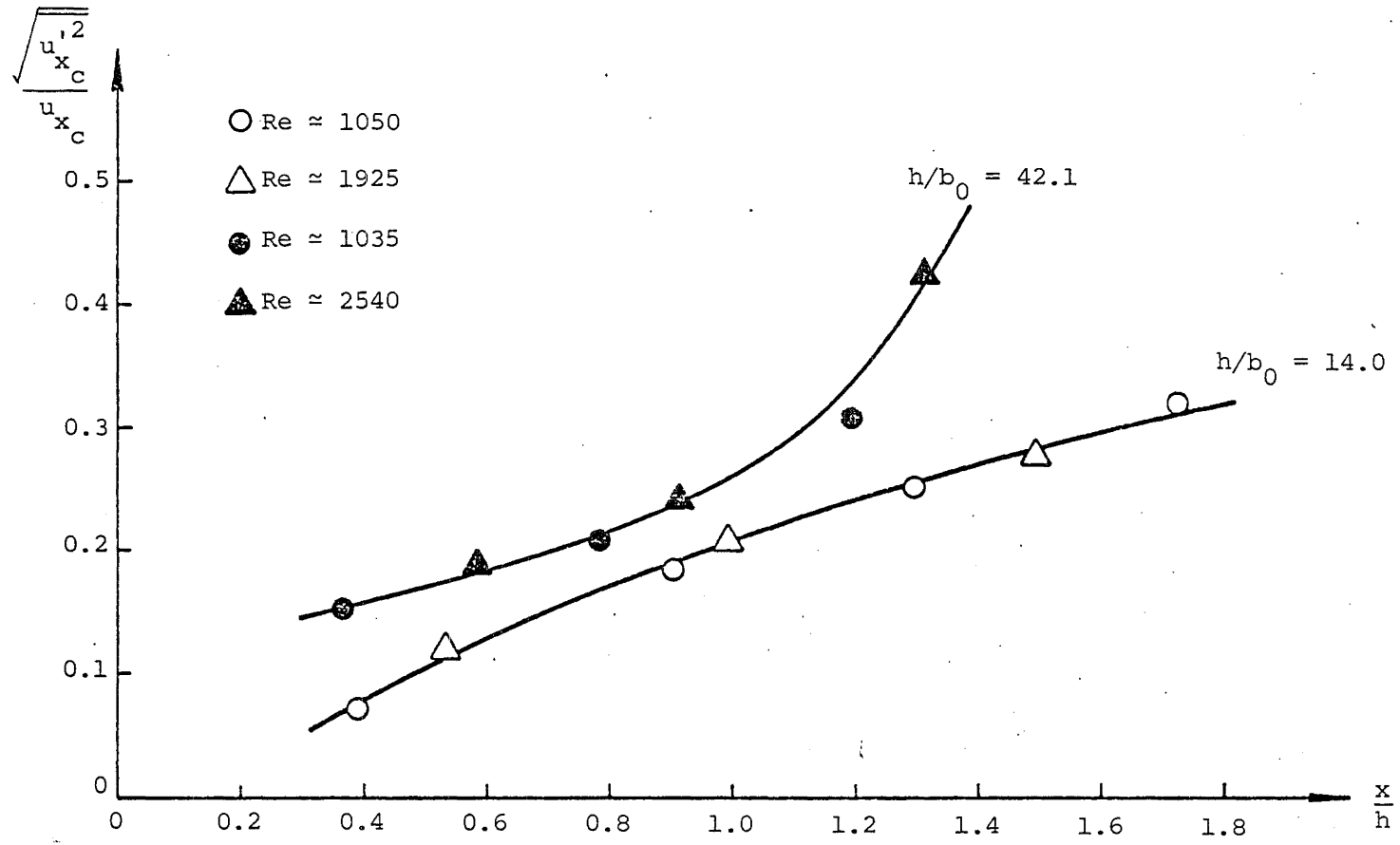

Figure 8.13 : Relative turbulent intensity of horizontal velocity fluctuations $\sqrt{\overline{u'^2_{c_x}}}/\overline{u}_{c_x}$ along the locus of maximum velocity in an attached non-buoyant jet.

attachment will reflect to some extent the turbulent intensity of the fluctuations of velocity in the direction of the streamlines. Therefore qualified comparisons can be made with plane jet data.

The contour plots clearly show twin peaks of turbulent intensity with a trough between them. The trough follows the line of maximum velocity until the inner turbulent intensity peak disappears. The appearance of twin peaks of turbulent intensity astride the line of maximum velocity is consistent with observations in plane non-buoyant jets (Chen and Rodi, 1980). However, in the case of the attached jet, the peak along the outer edge has a greater magnitude. This is probably indicative of the enhanced mixing caused by centrifugal effects. The turbulent intensity in the eddy is relatively low and varies little throughout.

The relative turbulent intensity along the locus of maximum velocity, $\sqrt{\overline{u'^2_{c_x}}} \; / \; \bar{u}_{c_x}$, has been plotted against x/h in Fig. 8.13. Although the relative turbulent intensity is observed to increase with distance as in a plane non-buoyant jet (Chen and Rodi, 1980), in the case of the larger step height it shows a sharp increase as the jet approaches the attachment point and is deflected by the boundary. The buoyant jet data are consistent with this latter trend (section 8.3) and a possible explanation is postulated later.

8.3 VELOCITY MEASUREMENTS IN AN ATTACHED BUOYANT JET

8.3.1 Mean Velocity Field in an Attached Buoyant Jet

The velocity data obtained for the attached buoyant jet ($Ri_o \simeq 0.001$) have been analysed in an identical fashion to the non-buoyant data.

The streamline plots constructed from the dimensionless profiles of mean horizontal velocity in Figs. D-9 and D-10 (Appendix D) appear as

Figs. 8.14 and 8.15. A comparison of these streamline plots with those for the non-buoyant case (Figs. 8.2 to 8.5) shows little apparent difference except that the former are more stretched out in the longitudinal direction due to the buoyancy of the eddy volume. The spread of the buoyant jet appears virtually identical to that of the non-buoyant one which is not surprising since it is momentum dominated ($Ri_o \simeq 0.001$). The positions of maximum velocity on the mean velocity profiles have also been located in Figs. 8.14 and 8.15 and again they indicate that, beyond the potential core, the line of maximum velocity follows a streamline before diverging. However there is an inconsistency in the value of the streamline for the two step heights ($\psi/Q_o \simeq 0.4$ for $h/b_o = 14.5$ and $\psi/Q_o \simeq 0.5$ for $h/b_o = 43.5$). The reason is again probably that given in the previous section for the non-buoyant jet results.

The positions of maximum velocity and the points along the eddy streamline obtained from the mean velocity profiles are compared in Figs. 8.16 and 8.17 with the predictions of the attached buoyant jet model. As in the non-buoyant case, the model overestimates the curvature of the jet. Jet curvature is again observed to become less significant as the step height increases and the average difference across the jet decreases. A comparison of the observed loci of maximum velocity in the buoyant and non-buoyant cases shows, as expected, that the curvature of the jet is less in the former. The difference is more pronounced as the step height increases and as the relative importance of the uplift due to the buoyancy of the eddy volume compared to the opposing force due to the negative pressure difference across the jet becomes greater.

The maximum mean horizontal velocities are shown in Fig. 8.18 for comparison with the model predictions. The results are good for both step heights although, in the case of the lower one, the length of the

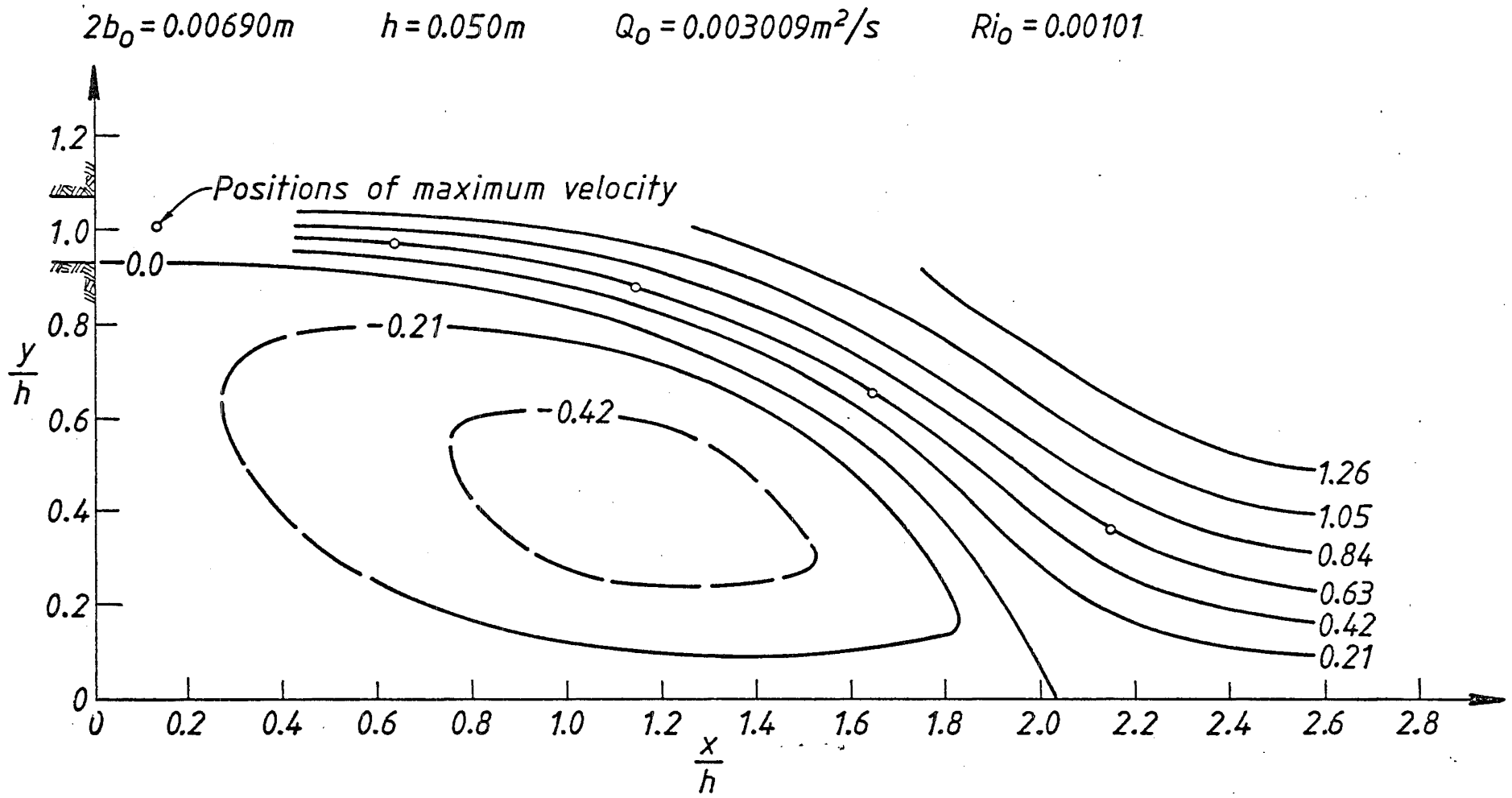

FIGURE 8.14 Streamlines for an attached buoyant jet. h/b_o = 14.5, Re ≃ 4335 and Ri_o = 0.00101.

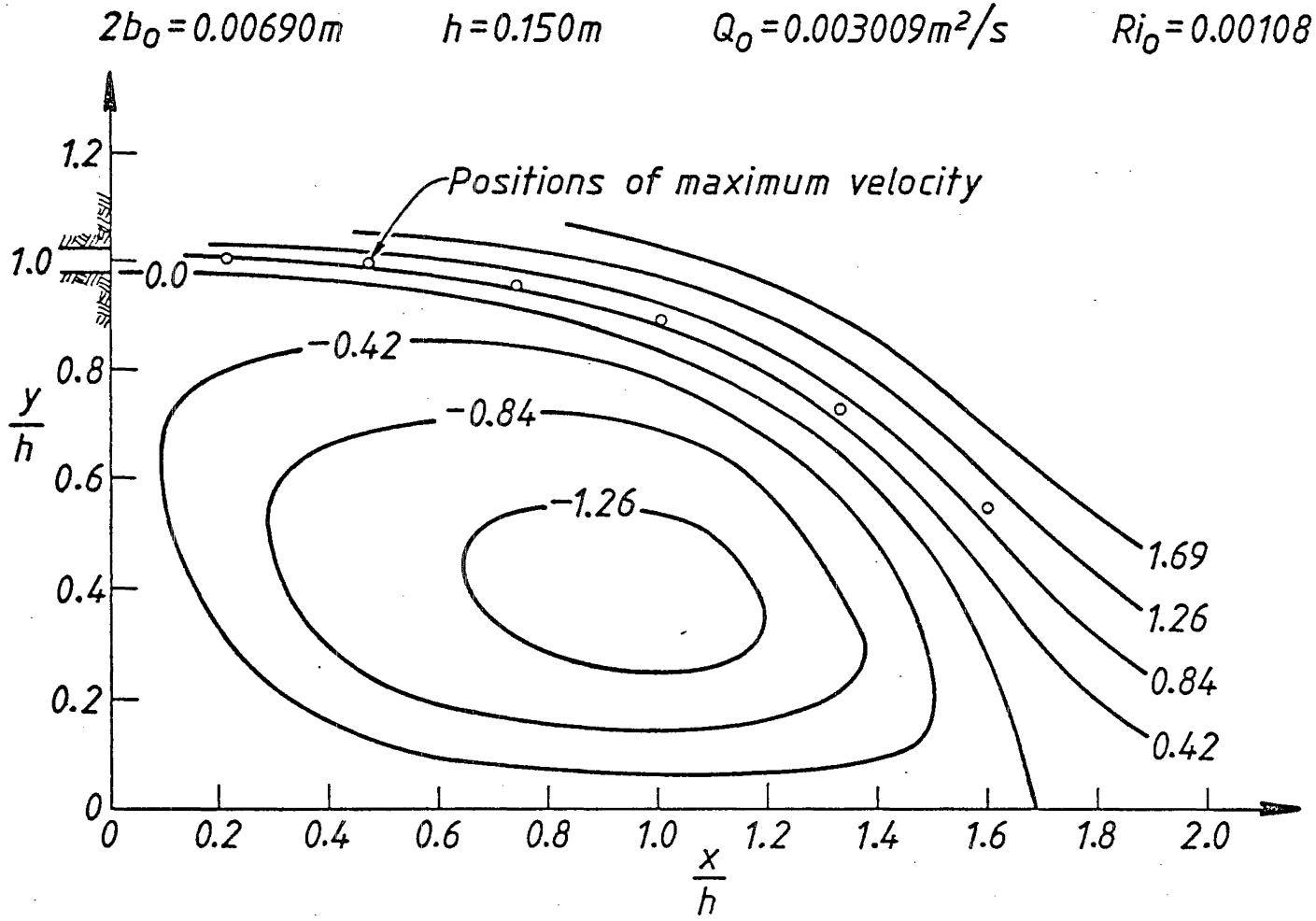

FIGURE 8.15 Streamlines for an attached buoyant jet. h/b_o = 43.5, Re ≈ 4465 and Ri_o = 0.00108.

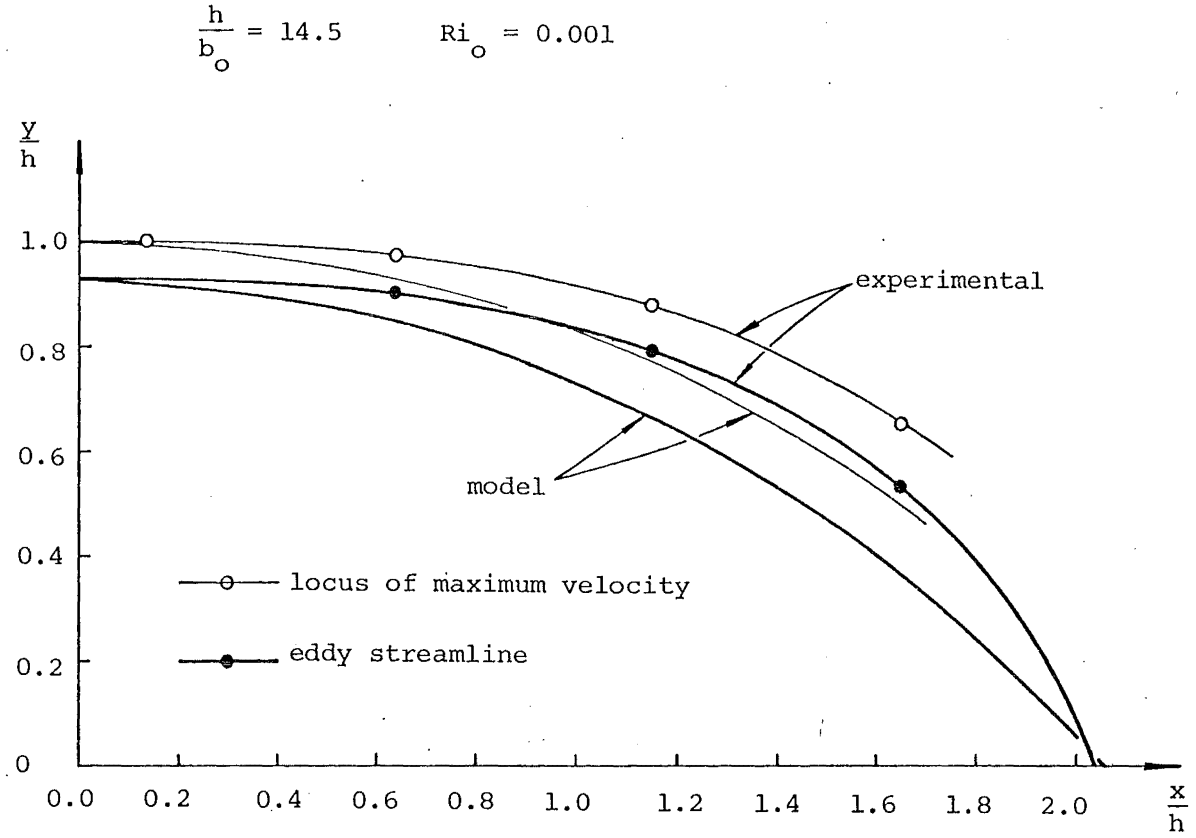

FIGURE 8.16 Locus of maximum velocity and eddy streamline position for an attached buoyant jet. $h/b_o = 14.5$ and $Ri_o \simeq 0.001$.

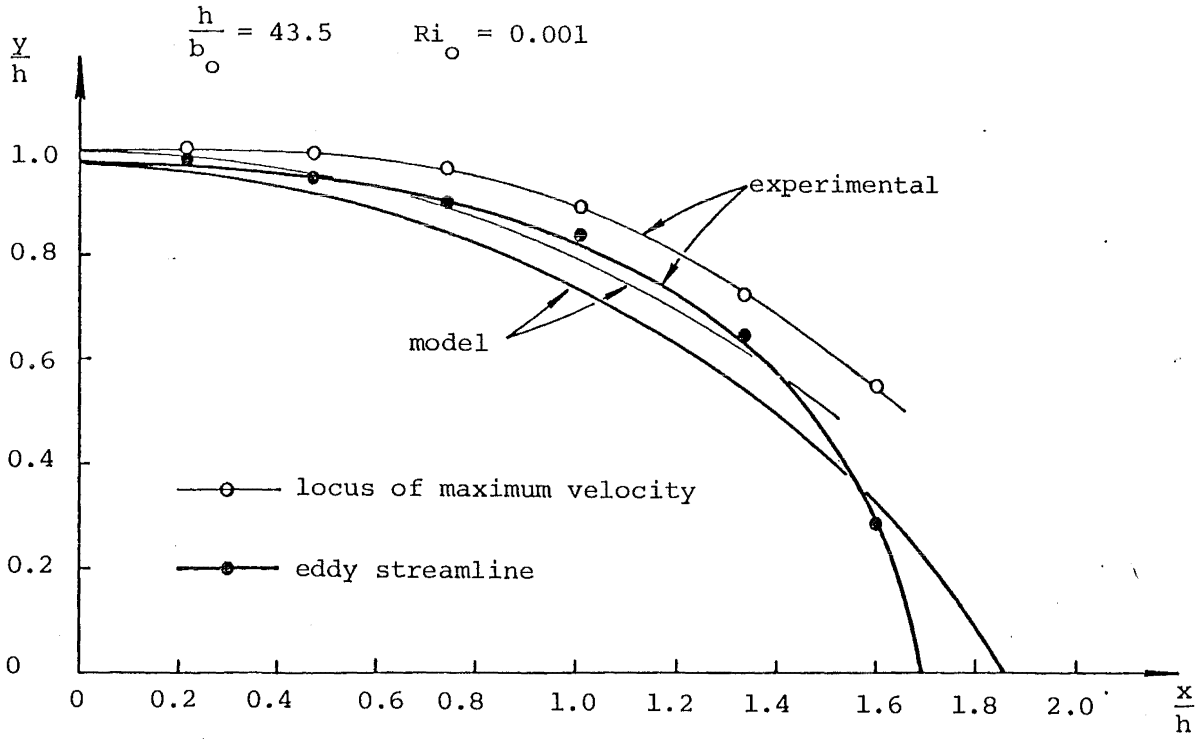

FIGURE 8.17 Locus of maximum velocity and eddy streamline position for an attached buoyant jet. $h/b_o = 43.5$ and $Ri_o \simeq 0.001$.

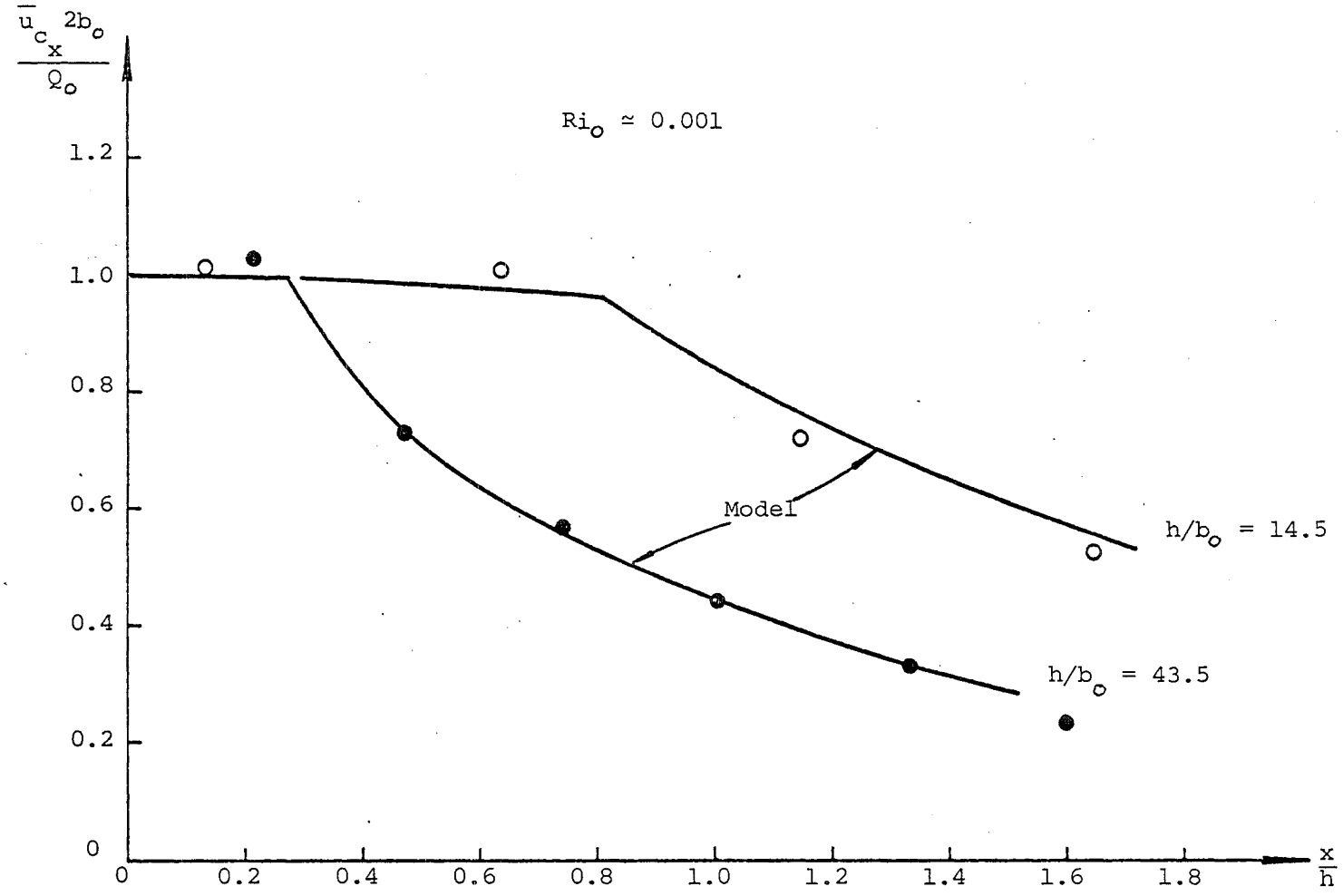

Figure 8.18 Decay of maximum horizontal velocity $\bar{u}_{c_x} 2b_o/Q_o$ in an attached buoyant jet.

potential core is probably overestimated by the model. The model assumes a potential core length of about 6 slot widths ($12b_o$) compared to the estimated length 5 slot widths ($10b_o$) that was observed visually. A potential core length of $10b_o$ would make the results for the lower step height more consistent.

A comparison of the non-buoyant and buoyant data indicates little difference in the decay rate of the maximum mean horizontal velocity. This means that in the buoyant case the jet is still momentum dominated when it is deflected by the boundary.

8.3.2 Turbulent Intensity of Velocity Fluctuations in an Attached Buoyant Jet

Percentage contour plots of dimensionless turbulent intensity of horizontal velocity fluctuations $\sqrt{\overline{u'^2_x}}\ 2b_o/Q_o$ (Figs. 8.19 and 8.20) have been constructed from the dimensionless profiles in Figs. D-11 and D-12 (Appendix D). These plots are consistent with those for the attached non-buoyant jet (Figs. 8.9 and 8.10). Twin peaks of turbulent intensity are observed with a trough between which initially follows the line of maximum velocity. The magnitudes of the peaks in the non-buoyant and buoyant cases are similar suggesting again that, prior to attachment, the buoyant jet is still very much momentum dominated. However, the turbulent intensity along the outer jet edge is greater for the buoyant jet. This is indicative of an unstable interface where a layer of fluid flows underneath another layer of greater density.

The relative turbulent intensity of horizontal velocity fluctuations along the line of maximum velocity, $\sqrt{\overline{u'^2_{c_x}}} / \bar{u}_{c_x}$, is illustrated in Fig. 8.21. It is observed to generally increase with distance as in a plane jet. In the case of the larger step height, the data shows a dramatic

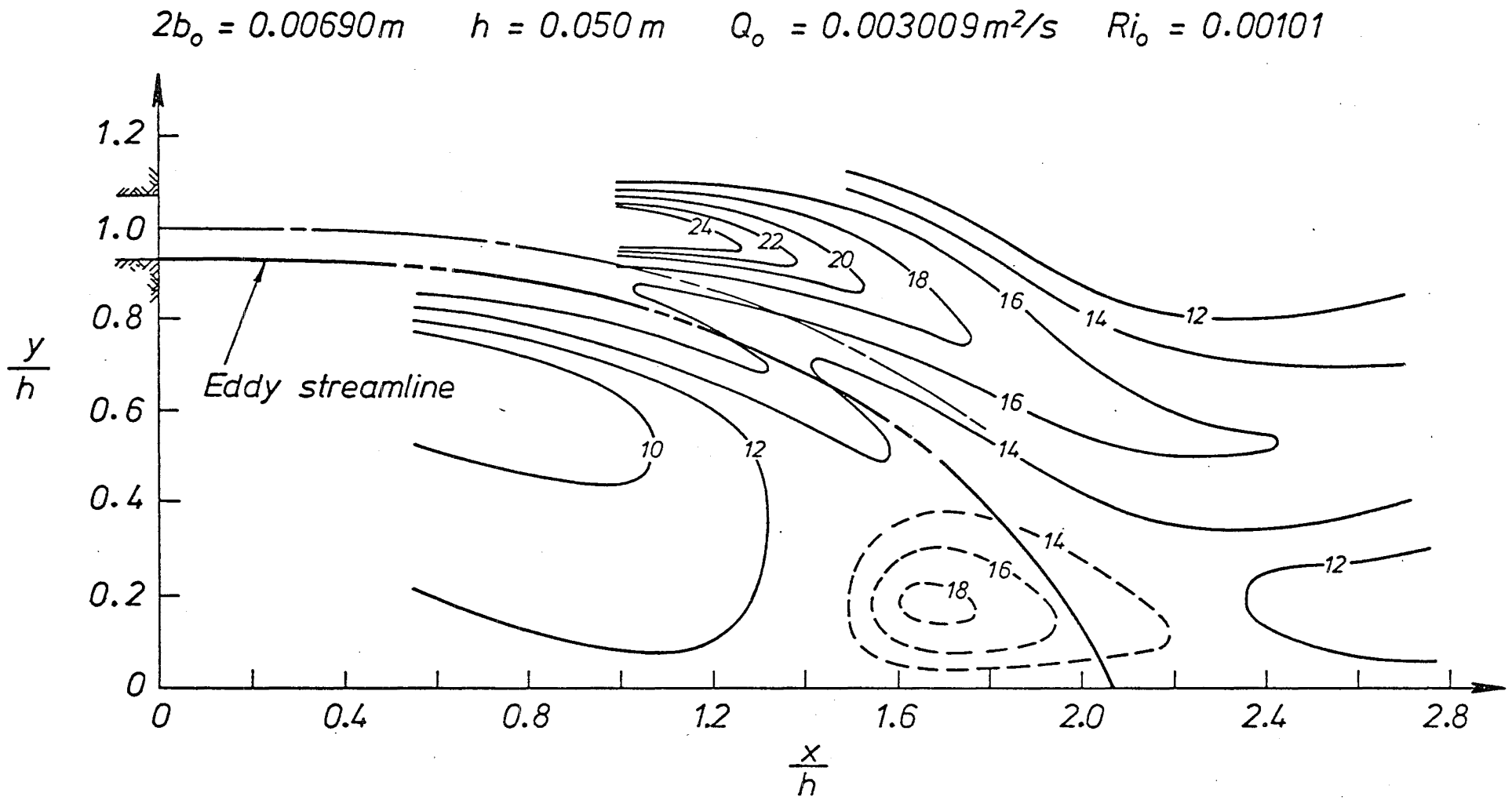

FIGURE 8.19 Percentage contours of dimensionless turbulent intensity of horizontal velocity fluctuations $\sqrt{\overline{u'^2_{c_x}}}\, 2b_o/Q_o$ in an attached buoyant jet. $h/b_o = 14.5$, $Re \simeq 4335$ and $Ri_o = 0.00101$.

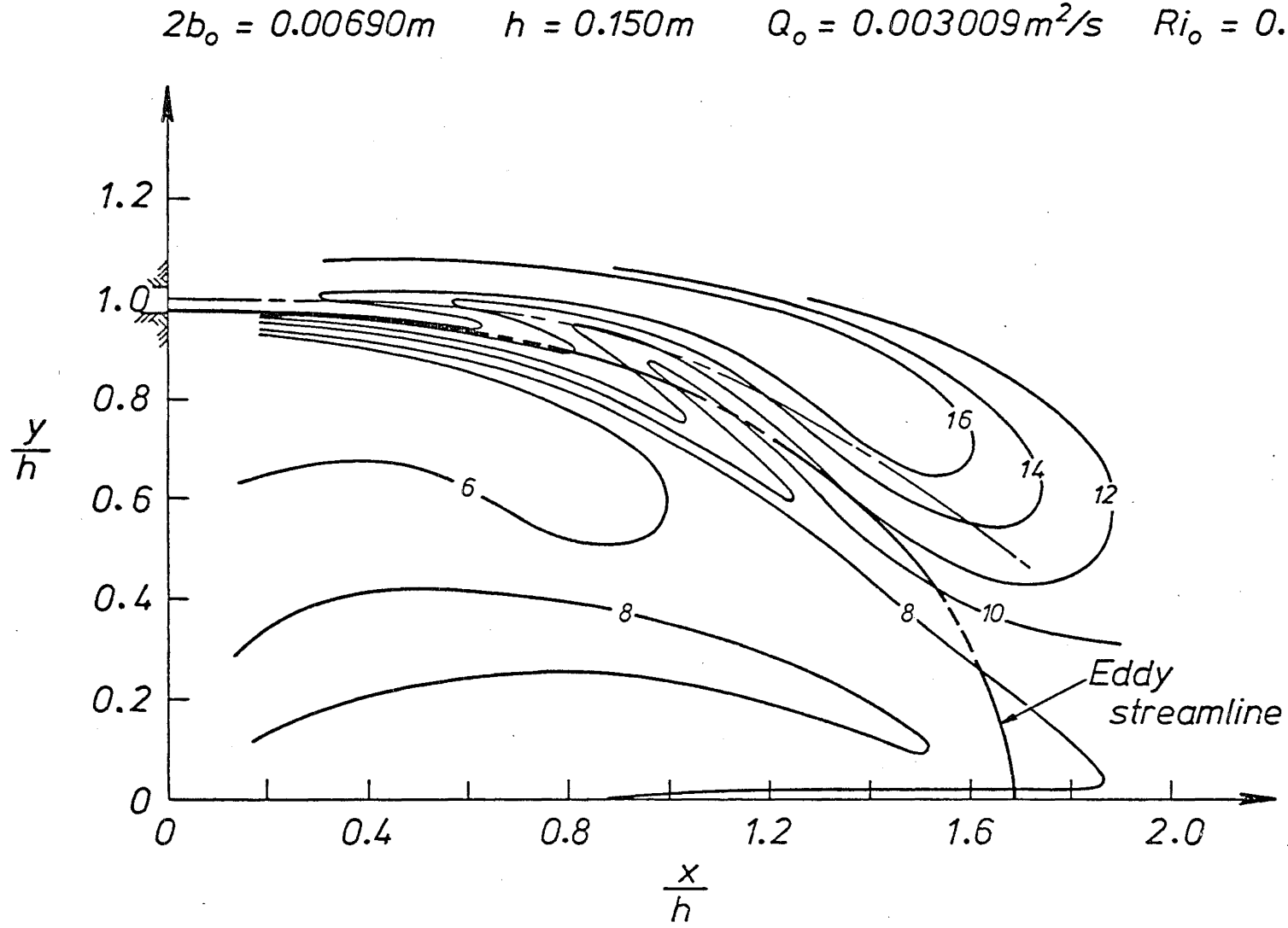

FIGURE 8.20 Percentage contours of dimensionless turbulent intensity of horizontal velocity fluctuations $\sqrt{\overline{u'^2}}\, 2b_o/Q_o$ in an attached buoyant jet. $h/b_o = 43.5$, $Re \simeq 4465$ and $Ri_o = 0.00108$.

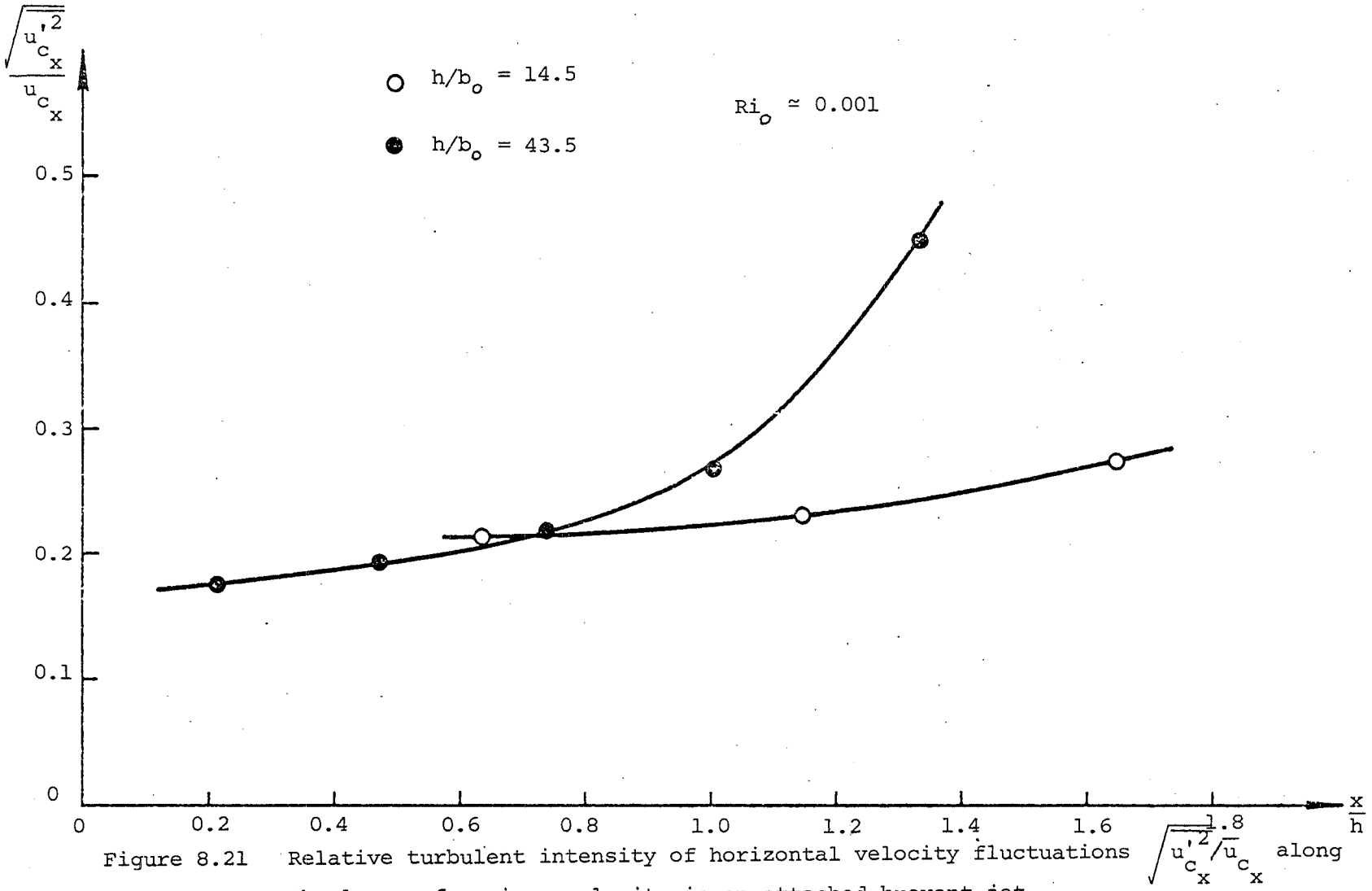

Figure 8.21 Relative turbulent intensity of horizontal velocity fluctuations $\sqrt{\overline{u'^2_{c_x}}}/u_{c_x}$ along the locus of maximum velocity in an attached buoyant jet.

increase as the jet approaches the attachment point. This is not due to the method of plotting the data against x/h rather than s/h. Instead it is probably caused by the jet sensing the impending impact on the boundary and subsequent deflection. The greater change of direction downstream experienced by the jet at the larger step height is the reason why the sharp increase in relative turbulent intensity along the line of maximum velocity is only noticed in that case.

CHAPTER 9

RESULTS OF TEMPERATURE MEASUREMENTS

9.1 INTRODUCTION

The temperature field in an attached buoyant jet ($Ri_o \simeq 0.001$) was measured. The basic parameters and initial conditions for all the

TABLE 9.1 Basic parameters and initial conditions for temperature measurements.

STEP HEIGHT h (m)	0.050	0.150
JET EXIT WIDTH $2b_o$ (m)	0.00690	0.00690
FLOWRATE Q_o (m^2/s)	0.003003	0.003003
JET EXIT VELOCITY u_o (m/s)	0.4352	0.4352
AVERAGE EXCESS TEMPERATURE AT EXIT $T_o - T_a$ (^oC)	23.40 ± 0.3	23.27 ± 0.3
EXIT REYNOLDS NUMBER $Re = \frac{\rho_o u_o 2b_o}{\mu_o}$	4500 - 4800	4500 - 4800
AVERAGE INITIAL JET RICHARDSON NUMBER $Ri_o = \frac{(\rho_a - \rho_o)\, g\, b_o}{\rho_a u_o^2}$	0.00126 ± 0.00010	0.00121 ± 0.0001
MEASUREMENT LOCATIONS $\frac{x}{h}$	0.150, 0.550, 0.944, 1.336, 1.738, 2.360 2.956	0.180, 0.493, 0.880 1.170, 1.378, 1.735 2.295

experiments conducted are summarised in Table 9.1. The data was analysed to obtain a series of vertical profiles of the mean temperature relative to ambient and the intensity of turbulent fluctuations of temperature. From the mean profiles for each step height case, isotherm plots and contour plots of the turbulent intensity of temperature fluctuations have been constructed. These are presented and discussed in this chapter.

In presenting the results, the same (x,y) coordinate system has been used as for the velocity data. This differs from the coordinate system assumed for mathematical modelling purposes in that the origin has been chosen to coincide with the corner of the step.

9.2 MEAN TEMPERATURE MEASUREMENTS

The profiles of mean temperature relative to ambient (mean excess temperature) are presented in dimensionless form in Appendix E (Figs. E-1 and E-2). From these profiles, contours of dimensionless mean excess temperature (isotherms) have been plotted for easier interpretation of the data. The contour plots appear as Figs. 9.1 and 9.2.

Figs. 9.1 and 9.2 show clearly that the mean excess temperature is approximately constant throughout the eddy. The mean temperature profiles in Figs. E-1 and E-2 suggest a very slight gradient in the eddy but the fact that there is no correlation between the gradient signs for the two step height cases makes this observation inconclusive. Since density deficit is approximately linearly related to excess temperature for small temperature variations (section 5.2), it can be concluded that the assumption in the buoyant jet model of a uniform distribution of mean density deficit (relative to ambient) in the eddy is a reasonable one.

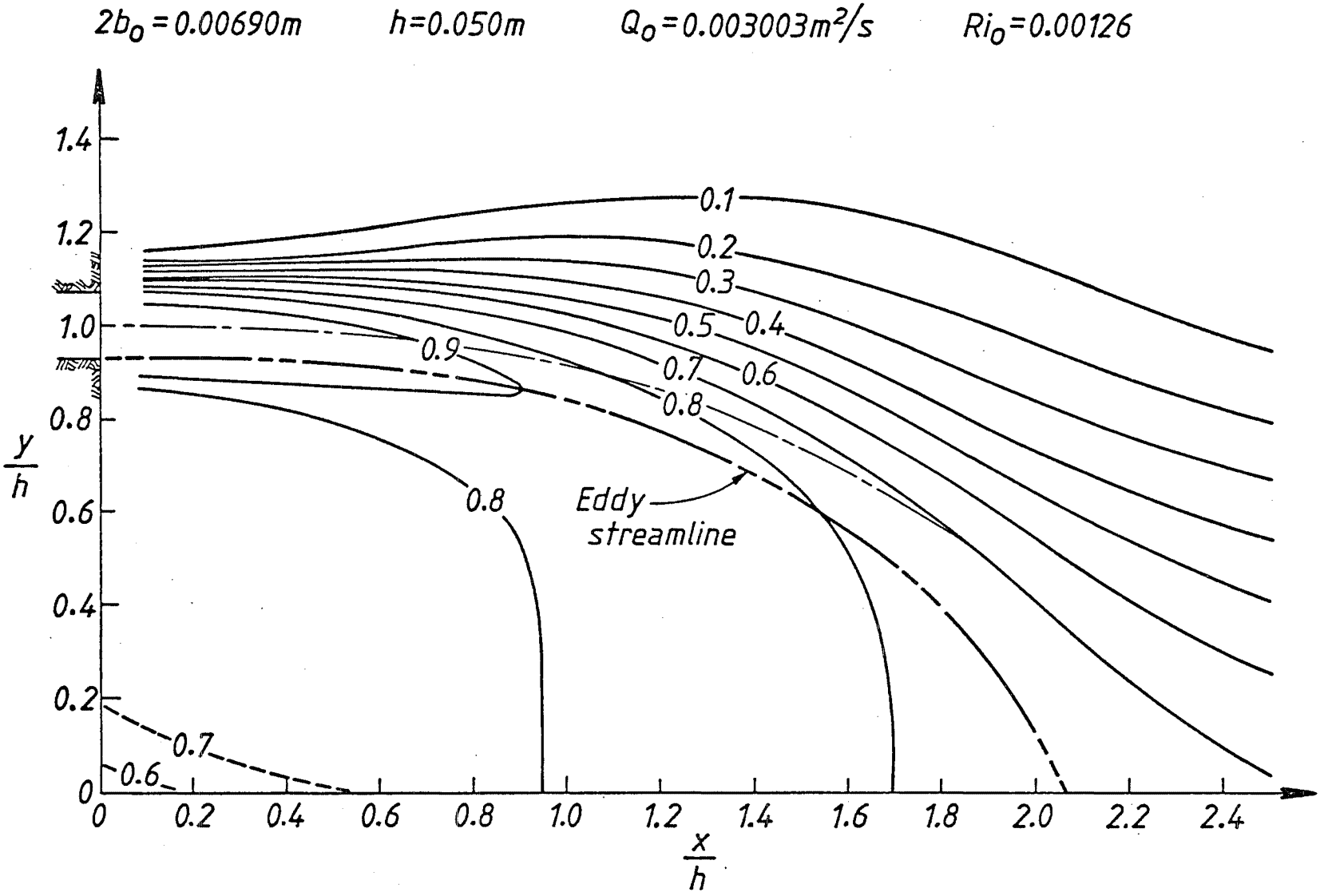

FIGURE 9.1 Contours of constant dimensionless mean excess temperature $(\bar{T}-T_a)/(T_o-T_a)$ for $h/b_o = 14.5$, $Re \simeq 4650$ and $Ri_o = 0.00126$.

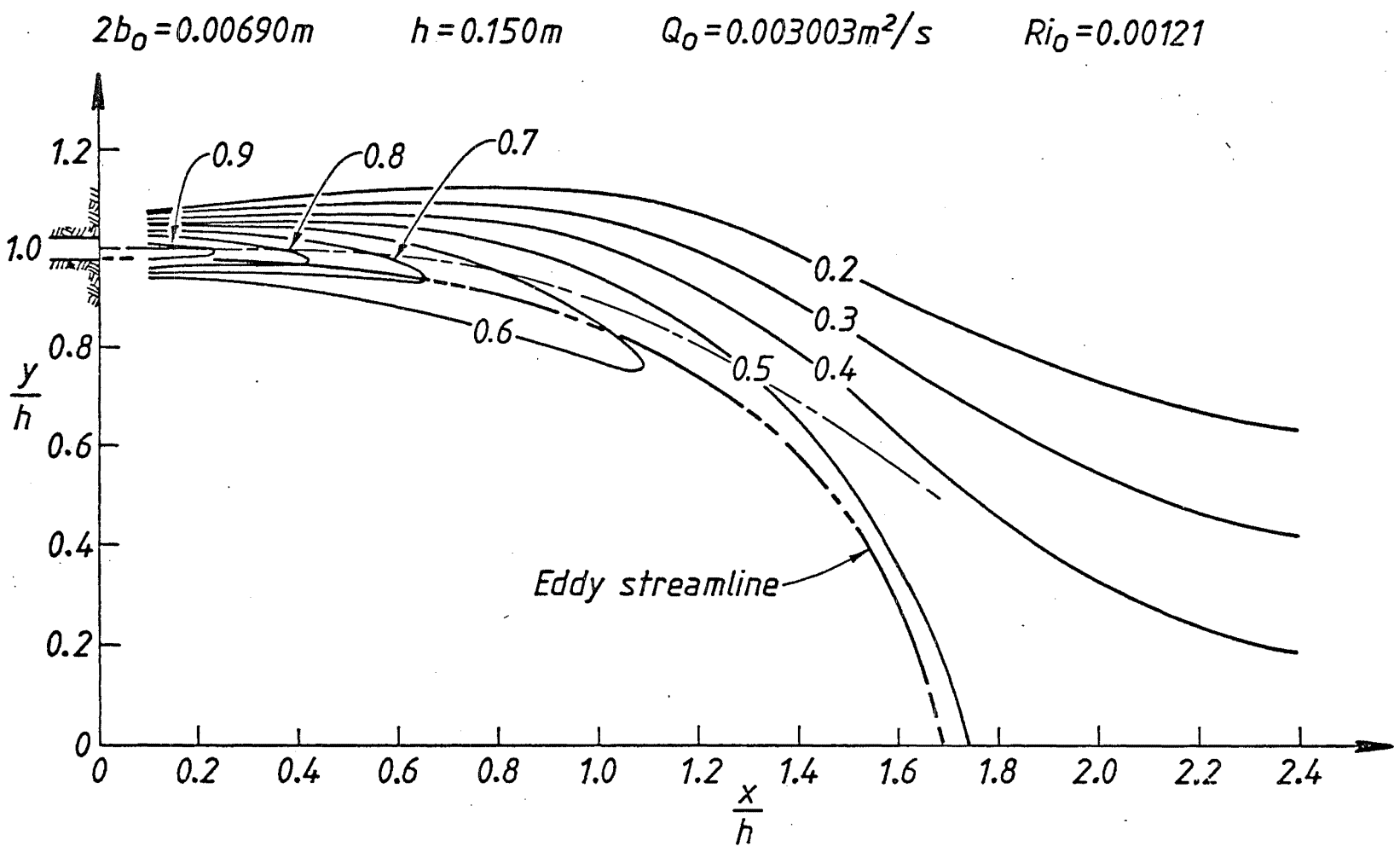

FIGURE 9.2 Contours of constant dimensionless mean excess temperature $(\bar{T}-T_a)/(T_o-T_a)$ for h/b_o = 43.5, Re ≃ 4650 and Ri_o = 0.00121.

A comparison of Figs. 9.1 and 9.2 indicates that the effect of the initial region is more significant for the smaller step height than for the larger step height. Consequently the mean excess temperature in the eddy is greater.

Fig. 9.1 also shows the existence of a pocket of lower temperature fluid in the corner of the step. This could be indicative of a smaller eddy within the body of the main one. Apart from the corresponding results for the intensity of turbulent fluctuations of temperature, there is no other corroboratory evidence for such an eddy. The mean streamlines in this region are sparsely distributed (Fig. 8.14) and the presence of a small eddy in the step corner could be speculated. In the higher step height case the temperature profiles were not measured close enough to the step for the same observation to be made.

The lines of maximum velocity obtained for the corresponding cases in which the velocity field was measured (Chapter 8) have been shown in Figs. 9.1 and 9.2. It is apparent that the locus of maximum mean excess temperature deviates from the line of maximum velocity with increasing distance. This is consistent with the locus of the peak mean density deficit in the buoyant jet model (eq. 5.7). While there is a zero net transfer of heat across the eddy streamline, this observation is indicative of the greater level of excess heat in the jet compared to the eddy.

From the dimensionless mean excess temperature profiles in Figs. E-1 and E-2 (Appendix E), the mean excess temperature $(\bar{T}_c - T_o)/(T_o - T_a)$ along the line of maximum velocity was determined. The values obtained are compared in Fig. 9.3 with the decay of mean density deficit predicted by the buoyant jet model. The slight difference between the results is probably due to an overestimate of the length of the density deficit potential core in the model. The predicted decay of density deficit along

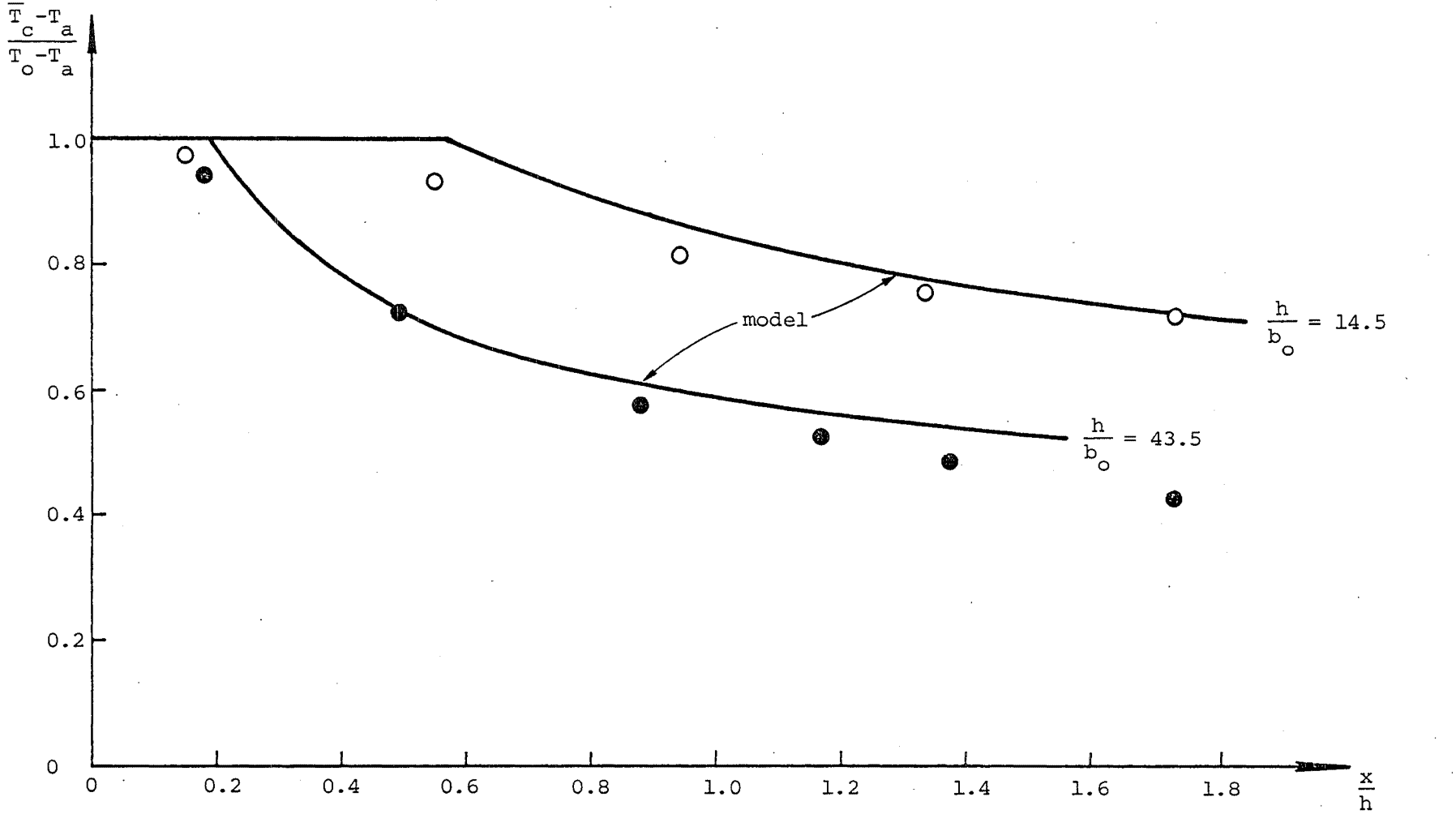

FIGURE 9.3 Dimensionless mean excess temperature (density deficit) along the locus of maximum velocity $(\overline{T}_c - T_o)/(T_o - T_a)$. $Ri_o \simeq 0.001$.

the line of maximum velocity is defined by the equation

$$\frac{\rho_a - \bar{\rho}_c}{\rho_a - \rho_o} = \frac{4}{\pi}\,\frac{1}{Q_*(\chi)} + \frac{1}{2}\left(\frac{\rho_a - \overline{\rho_f}}{\rho_a - \rho_o}\right)\left(1 - \frac{4}{\pi}\,\frac{1}{Q_*(\chi)}\right) \qquad (9.1)$$

where $Q_*(\chi)$ is the volume flux at distance χ.

A qualitative comparison of Figs. D-9 and D-10 with Figs. E-1 and E-2 confirms the general observation that the lateral spread of heat is faster than the lateral spread of momentum.

9.3 MEASUREMENTS OF THE TURBULENT INTENSITY OF TEMPERATURE FLUCTUATIONS

The distributions of the turbulent intensity of temperature fluctuations are contained in Appendix E (Figs. E-3 and E-4). Again these data are more easily interpreted in an alternative form and contours of turbulent intensity $\sqrt{\overline{T'^2}}/(T_o - T_a)$ have been plotted in Figs. 9.4 and 9.5.

For both step heights (h/b_o = 14.5 and h/b_o = 43.5) the turbulent intensity is observed to be very low in the eddy and is approximately constant. In the lower step height case the turbulent intensity increases in the step corner and it has been suggested previously that this is indicative of a smaller eddy there within the main one.

The general turbulent structure in the body of the jet is more clearly seen in the case of the larger step height (Fig. 9.5). As for the velocity data (Chapter 8), twin peaks of turbulent intensity are observed astride the locus of maximum velocity except that for the temperature data the peaks are further apart. This is additional evidence of the faster lateral spread of heat compared to that of momentum. The magnitude of the outer peak of turbulent intensity is greater than that of the inner one (which eventually disappears) and again this is probably due to the enhanced mixing along the outer edge caused by centrifugal effects.

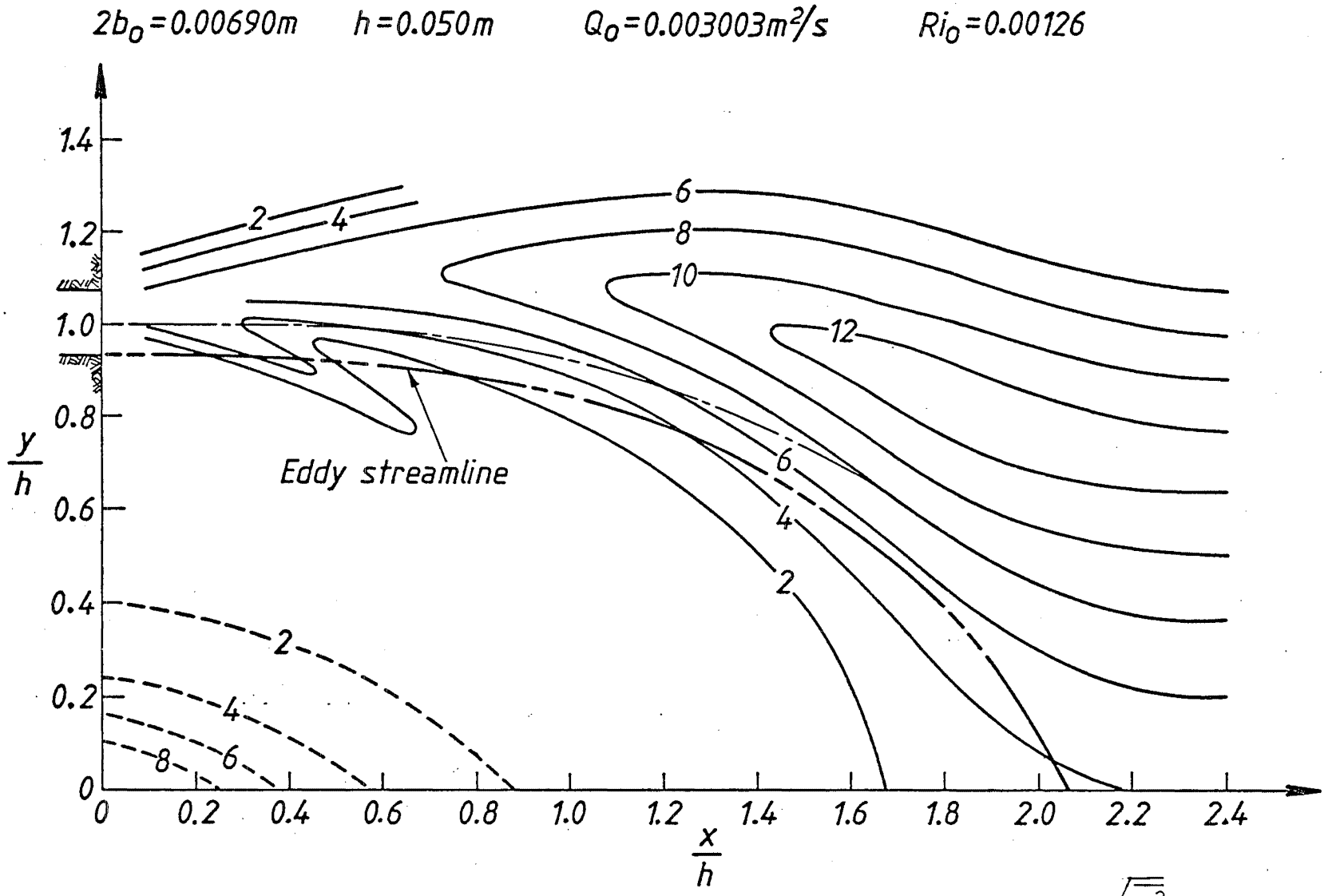

FIGURE 9.4 Percentage contours of constant dimensionless turbulent intensity $\sqrt{\overline{T'^2}}/(T_o - T_a)$ for $h/b_o = 14.5$, $Re \simeq 4650$ and $Ri_o = 0.00126$.

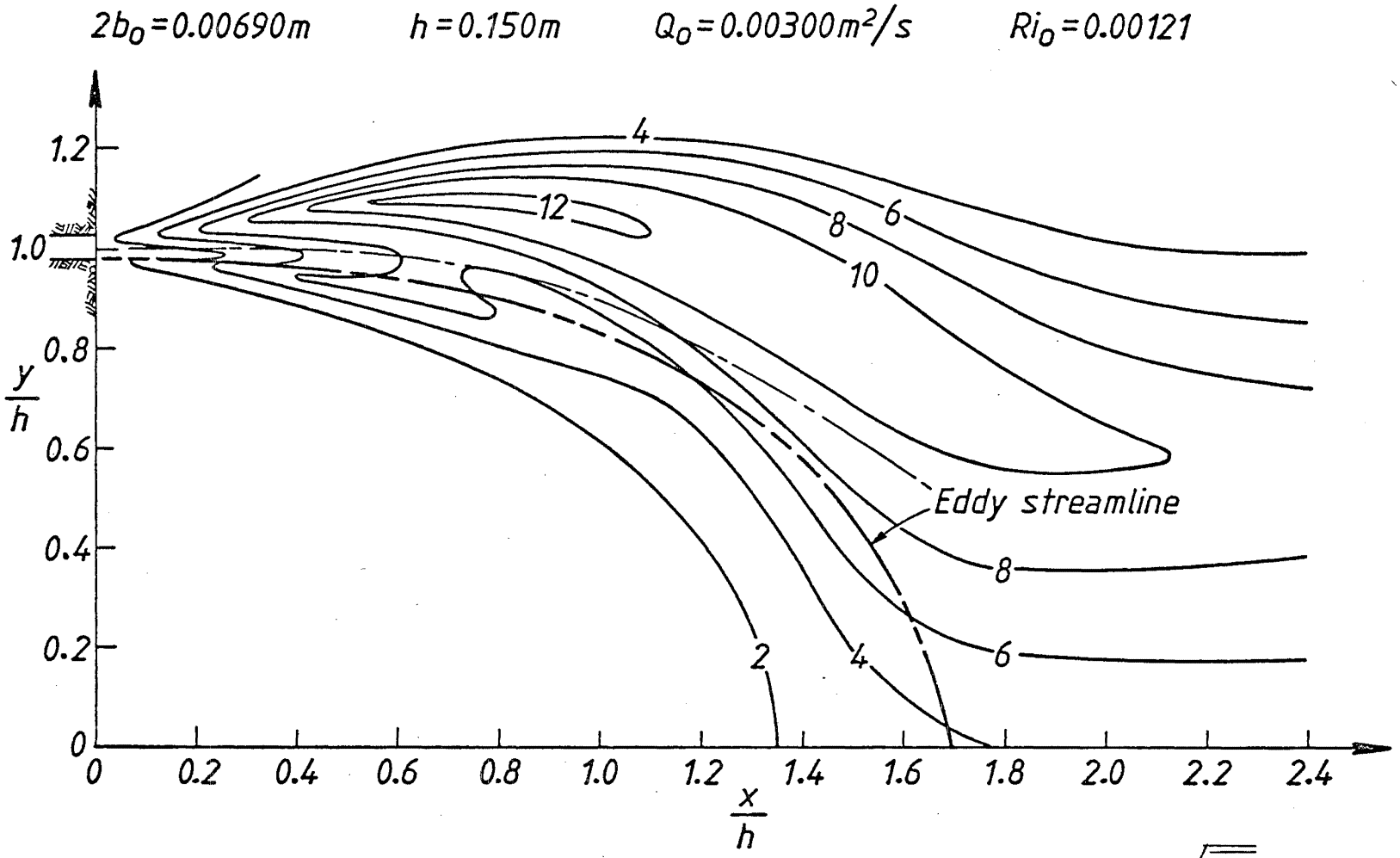

FIGURE 9.5 Percentage contours of constant dimensionless turbulent intensity $\sqrt{\overline{T'^2}}/(T_o - T_a)$ for $h/b_o = 43.5$, $Re \simeq 4650$ and $Ri_o = 0.00121$.

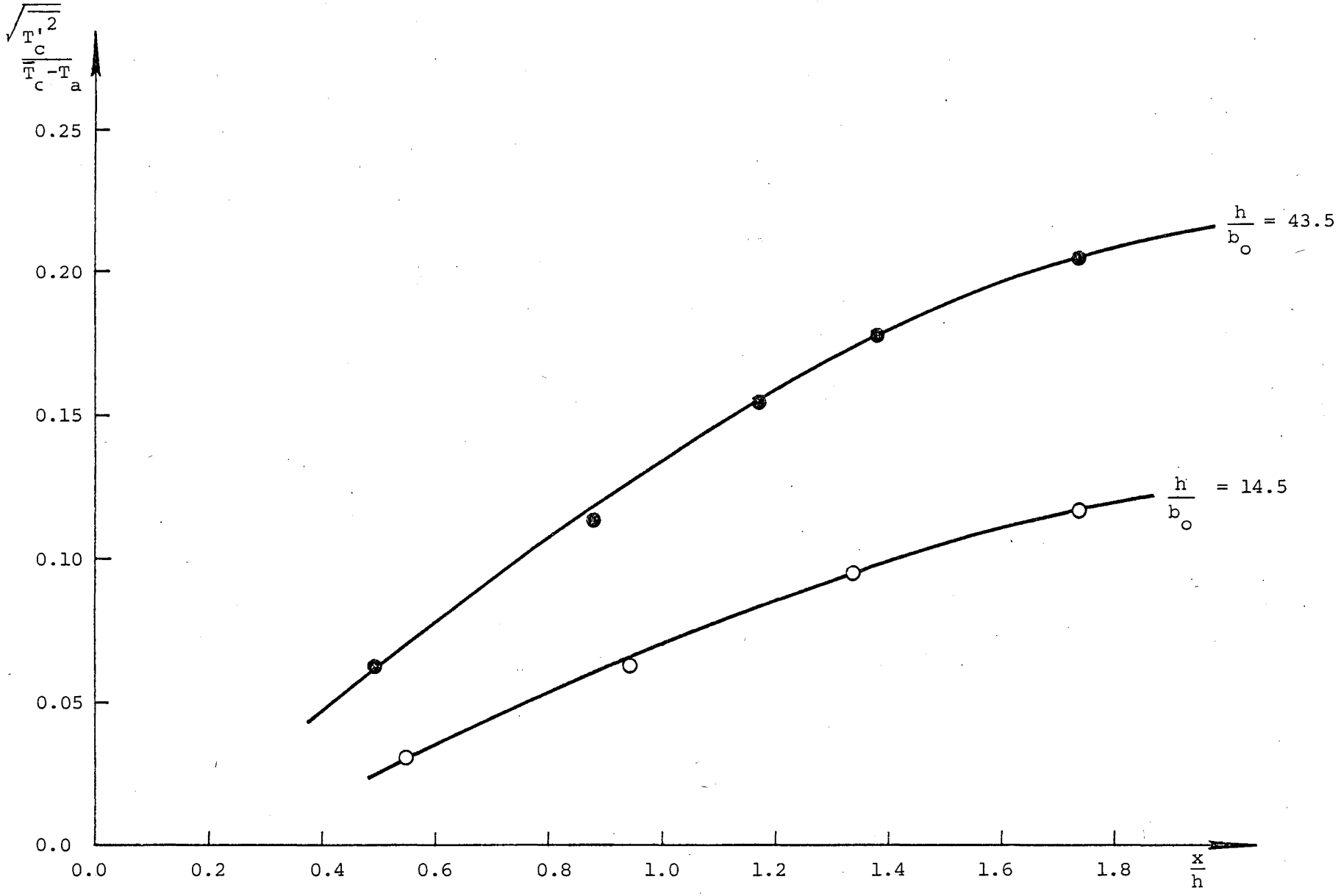

FIGURE 9.6 Relative turbulent intensity of temperature fluctuations along the locus of maximum velocity $\sqrt{\overline{T_c'^2}}/(\overline{T}_c - T_a)$. $Ri_c \simeq 0.001$.

Formula cut off in original as well as copy

From the profiles of turbulent intensity in Figs. E-2 and E-4, the turbulent intensity of temperature fluctuations along the line of maximum velocity $\sqrt{\overline{T'^2_c}}/(T_o-T_a)$ was obtained. The relative values of turbulent intensity $\sqrt{\overline{T'^2_c}}/(T_o-T_a)$ are shown in Fig. 9.6. They follow an increasing trend with distance and are consistent with some data reported by Kotsovinos (1975) for a plane buoyant jet.

Some criticism has been made of temperature measurements with thermistors in buoyant jet flows due to the poor response of thermistors at high frequencies of temperature fluctuations (Chen and Rodi, 1980). However, in the present investigation the turbulent intensity in the eddy has been found to be low so that the data reported is considered reliable.

CHAPTER 10

EVALUATION OF ATTACHED BUOYANT JET MODEL

10.1 INTRODUCTION

The attached buoyant jet model predicts the characteristic eddy parameters as functions of the dimensionless step height, h/b_o, and the initial jet Richardson number, Ri_o (Chapter 5). The model predictions of eddy length, l/b_o, and eddy density deficit, $(\rho_a-\rho_f)/(\rho_a-\rho_o)$, are evaluated by comparison with data obtained from the results of the velocity and temperature measurements (Chapters 8 and 9). Although the static pressure distribution through the attached jet was not measured in this investigation, some non-buoyant jet data reported in the literature are compared with the predicted average negative pressure differences across the jet.

10.2 PREDICTIONS OF CHARACTERISTIC EDDY PARAMETERS BY ATTACHED BUOYANT JET MODEL

10.2.1 Eddy Length

The dimensionless profiles of mean horizontal velocity in Appendix D were integrated to obtain streamline plots (Figs. 8.2 to 8.5, 8.14 and 8.15) for the attached non-buoyant and buoyant jets. The position of the eddy streamline on the boundary has been estimated in these plots and the corresponding x/h value denotes the aspect ratio, l/h. The aspect ratio has previously been plotted for convenience against the dimensionless step height. However, since the step height h is an independent variable and the eddy length is a dependent one, it is more correct to plot the eddy length alone as a function of the step height. The experimental

data obtained from the streamline diagrams are plotted accordingly in Fig. 10.1 for comparison with the predictions of the attached non-buoyant and buoyant jet models. The attached non-buoyant jet data measured using the visual technique of dye injection (section 7.2) are also shown.

The eddy length data from the streamline plots for the non-buoyant jet cases (Figs. 8.2 to 8.5) are consistent with the data measured directly by the dye injection technique. The results correlate well with the predictions of the attached non-buoyant jet model ($Ri_o = 0$)

The agreement between the predictions of the attached buoyant jet model and the eddy length data obtained from the streamline plots for the buoyant jet cases (Figs. 8.14 and 8.15) is satisfactory. However, for large step heights, it is apparent that the model overestimates the eddy length. This means that, whereas the model overestimates the curvature of the jet initially (section 8.3.1), it underestimates the curvature of the eddy streamline in extrapolating the eddy streamline to the boundary. It seems that the error increases for increasing values of initial jet Richardson number.

Despite this criticism, it is useful to interpret the predictions of the attached buoyant jet model. For each initial jet Richardson number, the eddy length is predicted to tend assymptotically to infinity at some constant step height (Fig. 10.1). The value of the step height decreases as the initial jet Richardson number increases. Thus under certain boundary and initial conditions there is no solution for an attached buoyant jet. This means that for these conditions a buoyant jet will not attach to the boundary. Progressively greater difficulty was experienced in obtaining a solution with the model as these conditions were approached.

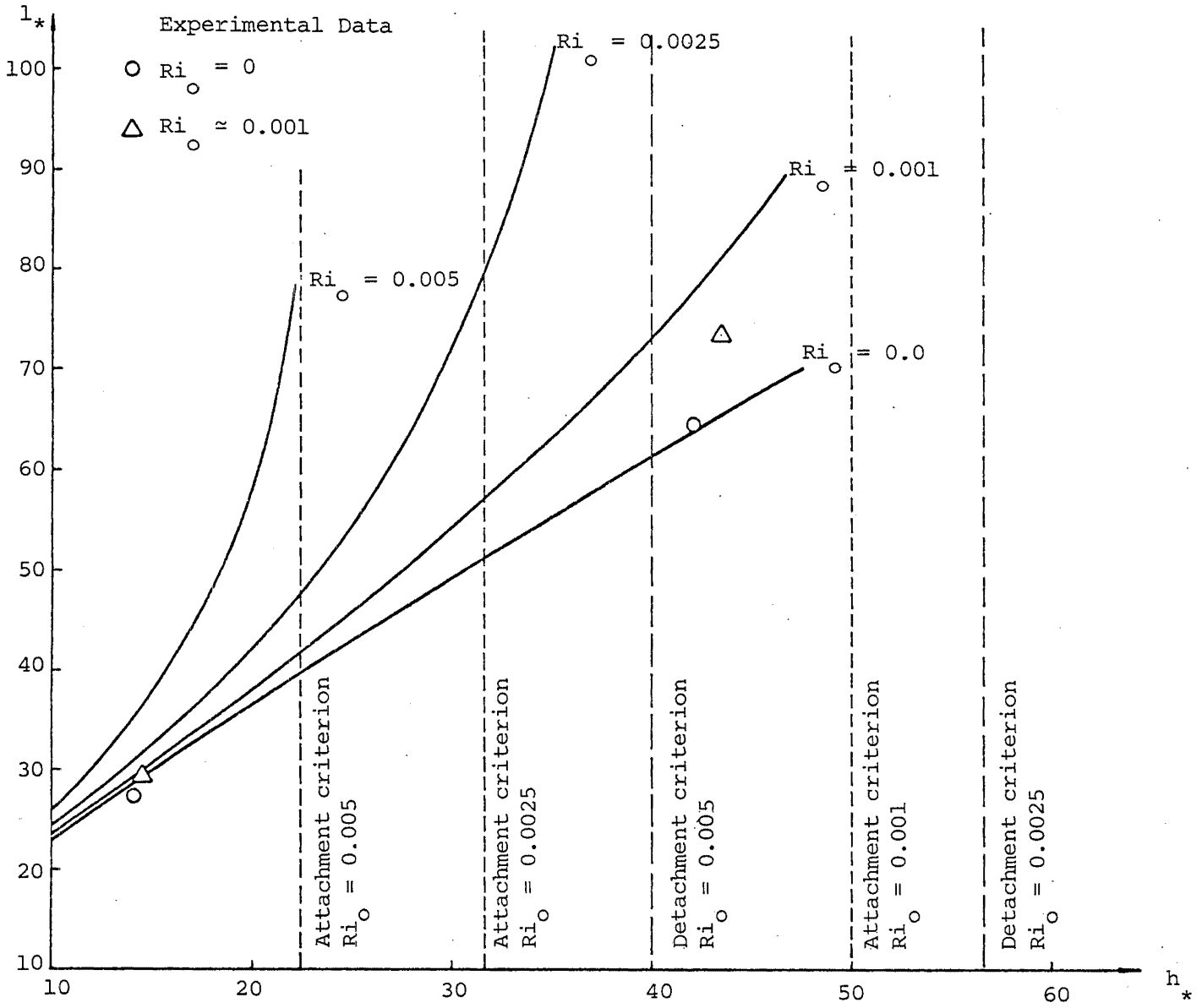

Figure 10.1 Eddy length as a function of step height for an attached jet.

It is unclear how the conditions for non-attachment are related to the two criteria postulated by Bates (1977). These criteria represent the limiting conditions for a free buoyant jet to spontaneously attach to the boundary (eq. 2.4) and for an attached buoyant jet to spontaneously detach from the boundary (eq. 2.5). The critical step height values have been calculated on the basis of these criteria for several initial jet Richardson numbers. They are tabulated in Table 10.1 and are also shown in Fig. 10.1.

TABLE 10.1 Critical step height values based on Bates' (1977) criteria.

Ri_o	h/b_o	
	Attachment (eq. 2.4)	Detachment (eq. 2.5)
0.001	50.0	89.4
0.0025	31.6	56.6
0.005	22.4	40.0

The critical step height values calculated for the spontaneous attachment of a free buoyant jet to the boundary appear to correlate well with the assymptotic values of step height for the model predictions. Not too much significance can be attached to this coincidence for two reasons. The amount of scatter in the experimental data that provided the basis for the attachment criterion (eq. 2.4) was large and the experimental data in the present study has indicated that the model overestimates the eddy length in the upper step height range (as the conditions for non-attachment are approached).

It can be concluded that the attached buoyant jet model provides a conservative estimate of the eddy length. Furthermore, the model shows that only momentum dominated buoyant jets (with $Ri_o < 0.005$) will attach to the boundary in the step height range $h/b_o > 10$.

It is unclear from the experimental data or the model predictions how the eddy length varies in the non-buoyant case as the step height becomes very large. It is suspected that at a sufficiently large step height, attachment of a buoyant jet will not occur ($l \to \infty$). In practice the critical factor will be the ratio of the step height to the depth of submergence. The attached jet model implicitly assumes that the depth of submergence is large compared to the step height.

The assumption of a thin jet ($h/2b_o >> 1$) has been made in formulating the attached jet model. Thus it is invalid for $0 < h/b_o < 10$. Some non-buoyant data are reported in the literature for this step height range (Rajaratnam and Subramanya, 1968), which indicates that as the step height tends to zero, the eddy length behaves likewise.

10.2.2 Eddy Density Deficit

The temperature field measurements in the attached buoyant jet indicated that the distribution of mean temperature relative to ambient was almost uniform in the eddy (Figs. 9.1 and 9.2). This is equivalent to saying that the density deficit throughout the eddy is approximately constant if a linear relationship between mean excess temperature and density difference is assumed (eq. 5.5). Therefore the assumption of a constant eddy density deficit in the attached buoyant jet model is a reasonable one.

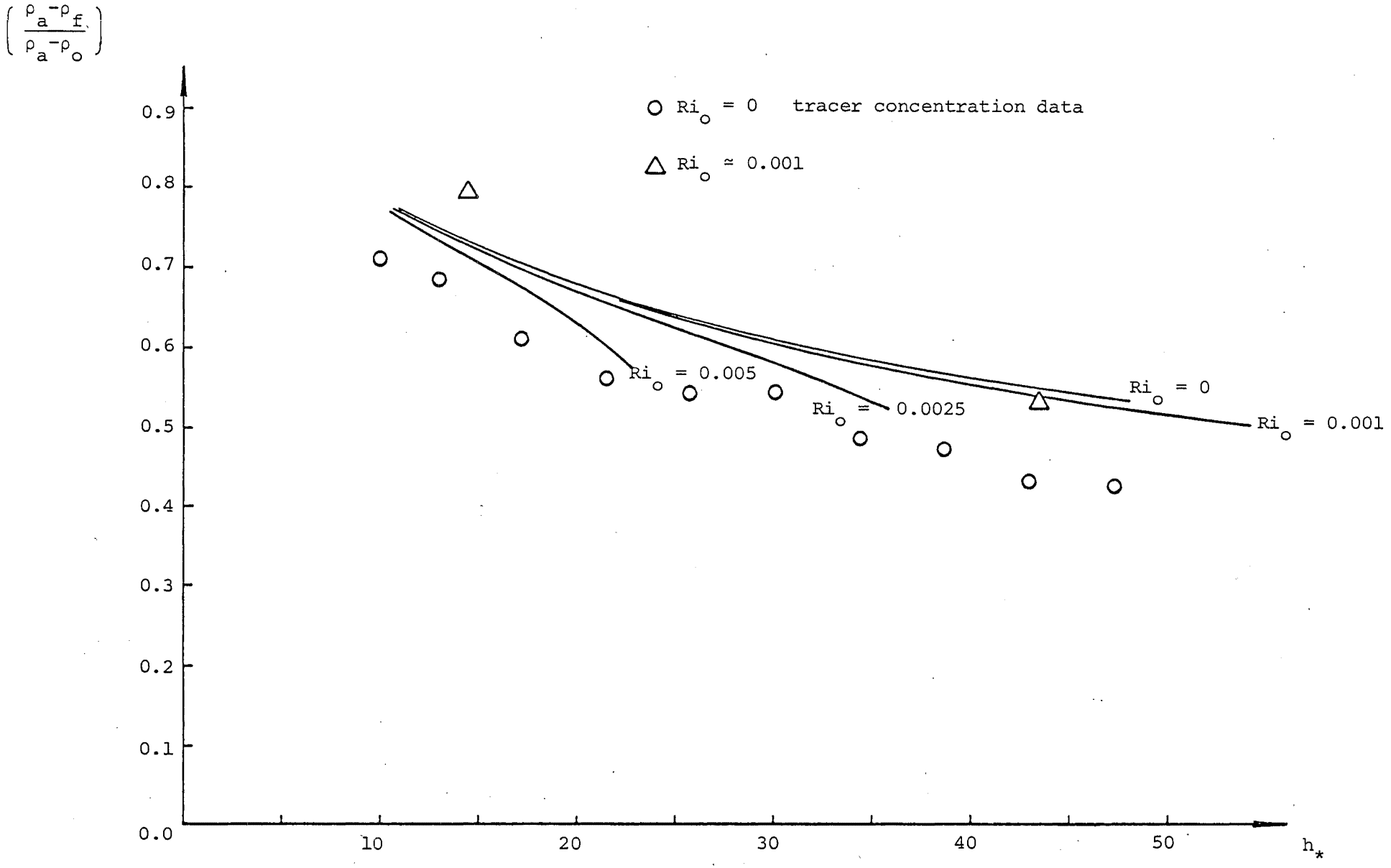

FIGURE 10.2 Eddy density deficit as a function of step height for an attached buoyant jet.

The dimensionless mean excess temperature (or density deficit) measured in the eddy is compared with that predicted by the attached buoyant jet model in Fig. 10.2. Again, the agreement is satisfactory, particularly for the higher step height. For the lower step height, the excess temperature in the eddy is underestimated slightly which could be an effect of the initial region of jet flow. The measurements of the dimensionless eddy concentration of tracer in the non-buoyant situation are also shown in Fig. 10.2.

If the rates of turbulent diffusion of heat and tracer are similar, it seems logical to expect the eddy concentration of tracer in the non-buoyant jet to be greater than the eddy density deficit in the buoyant jet for a given step height. The reason is the increased eddy length (and hence volume) in the latter case. The experimental data are not consistent with this expectation and it is unclear why this is so. In contrast, the eddy density deficit predicted by the attached buoyant jet model behaves as expected, decreasing for a given step height as the initial jet Richardson number increases. However, the magnitude of the decrease is very small except where the conditions for non-attachment are approached. In other words, the eddy density deficit is predicted to be almost independent of initial jet Richardson number. This means that, for a given step height, the same line of constant tracer flux is approximately coincident with the eddy streamline at the attachment point for all values of initial jet Richardson number.

10.2.3 Average Underpressure

The static pressure distribution through the eddy is complex but can be approximated as a uniform one. Sawyer (1960) remarks how the static pressure distribution along the boundary closely reflects that in the eddy. He defines the average pressure in the eddy as the negative

mean of the pressure on the boundary between x/h = 0 and 0.95 times the value of x/h at which $p - p_a = 0$ (Fig. 2.6). Thus it is possible to compare some experimentally determined values of the average pressure difference across the jet (underpressure) obtained using this definition with the model predictions. Sawyer's (1960) data for the attached non-buoyant jet are plotted in Fig. 10.3 along with Borque and Newman's (1960) data as recalculated by Sawyer (1960). A comparison shows the average underpressure prediction of the attached buoyant jet model for a non-buoyant jet ($Ri_o = 0$) to be good. Consequently the underpressure prediction of the model can be viewed with some degree of confidence.

For a particular step height, the model predicts that the average underpressure in the eddy increases as the initial jet Richardson number increases. In other words, the increasing uplift due to buoyancy in the eddy is countered by an increasing average negative pressure difference across the jet. At some stage the uplift will balance the opposing effect of the underpressure and the attached jet will be capable of detachment.

The estimation of the average underpressure by the attached buoyant jet model is dependent on a number of assumptions. To obtain from a control volume analysis the average negative pressure difference across a vertical section FE (Fig. 3.3) through the attached jet, it is assumed that the horizontal component of the momentum flux at that section is approximately equal to the momentum flux of the jet.

$$(M_* \cos \theta)_{FE} \simeq (M_*)_{FE}$$

Further, it is assumed that the momentum flux of the jet at the section, FE, is approximately equal to the initial momentum flux of the jet since the exact position of the section is not known. $((M_*)_{FE} \simeq 1$. The experimental results indicate that the attached buoyant jet is momentum dominated

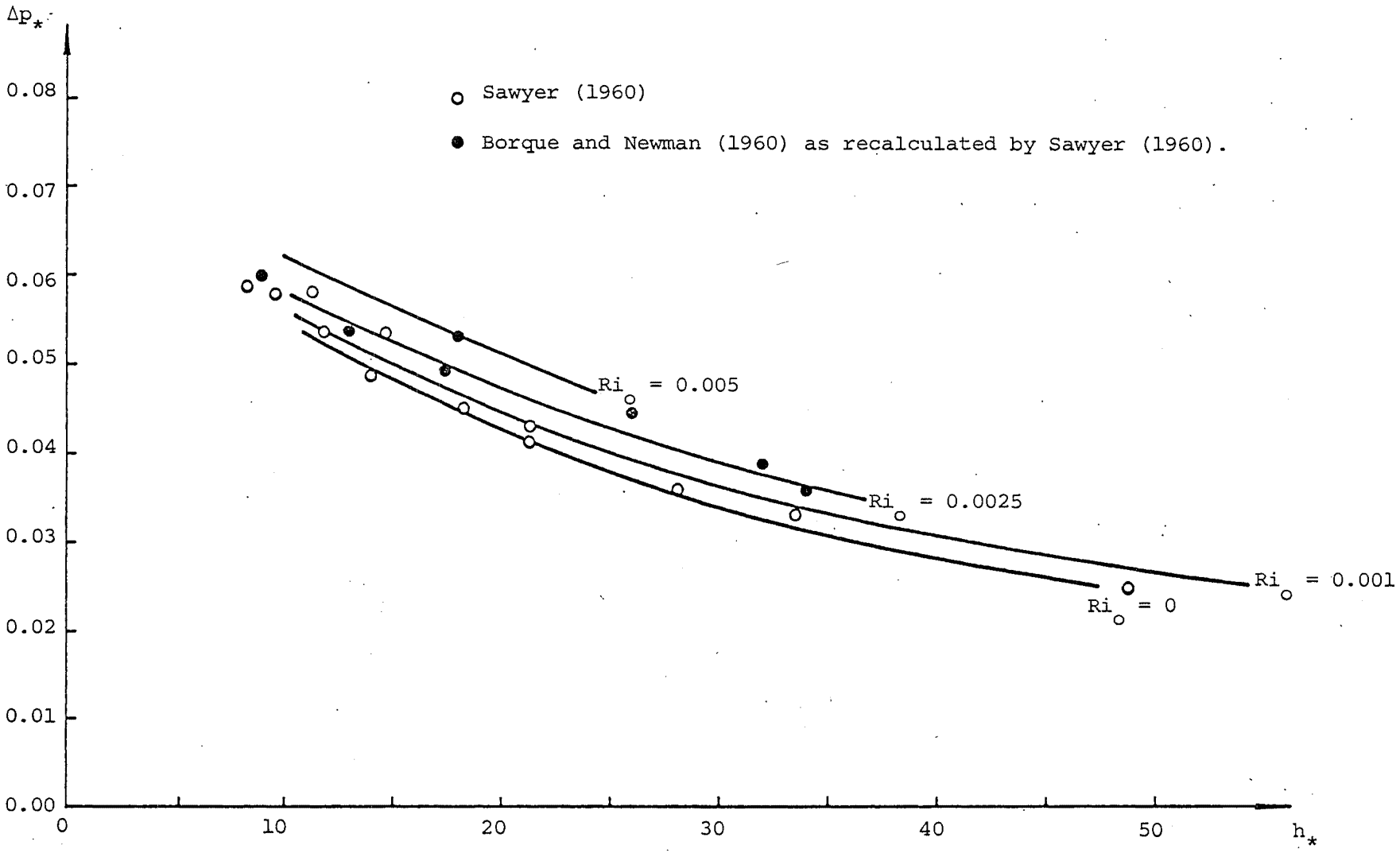

FIGURE 10.3 Average underpressure as a function of step height for an attached buoyant jet.

at least up to the point of attachment and that the initial curvature of the centreline is small. Thus the assumptions made are very reasonable on the basis of the experimental evidence.

The fact that the attached jet models overestimate the curvature of the jet initially is probably due to the assumption of an average pressure difference across the jet. Measurements of the static pressure distribution through the eddy by Sawyer (1960) indicate a more complete distribution than the assumed uniform one with an off-centred negative peak. The pressure difference across the initial jet region is somewhat less than the average underpressure.

10.3 ON THE PHYSICAL SIGNIFICANCE OF BATES' (1977) CRITERIA

The physical significance of Bates' (1977) criteria for attachment and detachment and the way in which they are related to the conditions for non-attachment predicted by the model have not been explored. It is suspected that the limiting criterion for detachment from the boundary of an attached buoyant jet (eq. 2.5) is connected with the condition where the uplift force due to buoyancy balances the opposing force due to the underpressure.

CHAPTER 11

CONCLUSIONS

An entrainment model of a two-dimensional attached buoyant jet has been developed. The model satisfactorily predicts the basic parameters that characterise the flow configuration. However, it overestimates the curvature of the jet initially. This is probably due to the approximation of the complex pressure distribution by a uniform one and the assumption that the average underpressure thus defined acts over the entire jet. The magnitude of the pressure difference across the jet in the initial flow region is lower than the average underpressure. Jet curvature in this region was observed to be small accordingly and became even less significant as the average underpressure decreased.

The introduction of buoyancy produces an uplift pressure in the eddy. For a given step height the average underpressure increases with the initial jet Richardson number to counter this uplift pressure. It is suspected that detachment of the jet from the boundary will occur when the forces due to these opposing effects balance. The model indicates that, for certain boundary and initial conditions, no solution is possible and attachment of a free buoyant jet will not occur. Only momentum dominated buoyant jets ($Ri_o < 0.005$) will attach for the boundary conditions considered ($h/b_o > 10$).

Measurements of the horizontal velocity field and temperature field indicate that an attached buoyant jet develops similarly to a plane buoyant jet. The attached buoyant jet remains momentum dominated at least up to the point of attachment. The turbulent structure is similar

to that of a plane buoyant jet. However in the present case the peak along the outer jet edge is of greater magnitude than the one along the inner edge. This is probably due to the enhanced mixing caused by centrifugal effects. The eddy is confirmed as a region of approximately uniform temperature or density deficit (tracer concentration) and of low turbulent intensity.

The fact that only momentum dominated buoyant jets will attach to an adjacent boundary means that this configuration is somewhat restricted in prototype situations. It appears more suitable for application to thermal discharges rather than to the discharge of sewage effluent. Before it is applied in such a context, an investigation of shear effects along the lateral edges of the more realistic three dimensional situation needs to be conducted.

The method of linearly superimposing solutions of the tracer (density deficit) conservation equation for different concentration boundary and initial conditions is of potentially wider application.

REFERENCES

ABRAMOVICH, G. N. (1963) The Theory of Turbulent Jets. Cambridge, Massachusetts Institute of Technology Press. p 17-25.

ALBERTSON, M. L., DAI, Y. B., JENSEN, R. A. AND ROUSE, H. (1950) Diffusion of submerged jets. *Transactions, A.S.C.E.*, 115, p 639-664.

ANWAR, H. O. (1973) Two-dimensional buoyant jet in a current. *Journal of Engineering Mathematics*, 7, p 297-311.

BATCHELOR, G. K. (1950) Note on free turbulent flows, with special reference to the two-dimensional wake. *Journal of the Aeronautical Sciences*, 17, p 441-445.

BATES, J. H. T. (1977) A study of buoyant wall jets with respect to certain physical parameters. Unpublished report, Department of Physics, University of Canterbury. 30p.

BORQUE, C. and NEWMAN, B. G. (1960) Reattachment of a two-dimensional incompressible jet to an adjacent flat plate. *The Aeronautical Quarterly*, 11, p 201-232.

CHEN, C. J. and RODI, W. (1980) Vertical Turbulent Buoyant Jets - A Review of Experimental Data. Oxford, Pergamon Press. 83p.

DANIEL, R. J. and WOOD, I. R. (1976) The mixing caused by the discharge of a buoyant plume down a slope. National Conference Publication, Institution of Engineers, Australia, 76/12.

DURST, F., MELLING, A. and WHITELAW, J. H. (1976) Principles and Practice of Laser-Doppler Anemometry. London, Academic Press. 405p.

FORSTALL, W. and GAYLORD, E. W. (1955) Momentum and mass transfer in a submerged water jet. *A.S.M.E. Journal of Applied Mechanics*, 22, p 161-164.

GARTRELL, G. (1979) Studies on the Mixing in a Density-Stratified Shear Flow. Ph.D. thesis, California Institute of Technology report No. KH-R-39, 447p.

HESTRONI, G., HALL, C. W. and DHANAK, A. M. (1965) Momentum transfer in thermally asymmetric turbulent jets. *A.S.M.E. Journal of Heat Transfer*, 87, p 429-435.

KOTSOVINOS, N. E. (1975) A Study of the Entrainment and Turbulence in a Plane Buoyant Jet. Ph.D. thesis, California Institute of Technology report No. KH-R-32, 306p.

LAUNDER, B. E. and SPALDING, D. B. (1972) Mathematical Models of Turbulence. London, Academic Press. 169 p.

LIST, E. J. and IMBERGER, J. (1973) Turbulent entrainment in buoyant jets and plumes. *A.S.C.E. Journal of Hydraulics Division*, 99, No. HY9, p 1461-1474.

MORTON, B. R. (1959) Forced plumes. *Journal of Fluid Mechanics*, 5, p 151-163.

MORTON, B. R. (1961) On a momentum-mass flux diagram for turbulent jets, plumes and wakes. *Journal of Fluid Mechanics*, 10, p 101-112.

MORTON, B. R. (1968) Non-similar turbulent plumes. Clayton, Victoria, Monash University. 50p. (Geophysical Fluid Dynamics Laboratory Paper 7).

MORTON, B. R., TAYLOR, G. I. and TURNER, J. S. (1956) Turbulent gravitational convection from maintained and instantaneous sources. *Proceedings, Royal Society of London*, A234, p 1-23.

PRANDTL, L. (1960) Essentials of Fluid Dynamics. Glasgow, Blackie and Son Ltd. p 119.

RAJARATNAM, N. (1976) Turbulent Jets. Amsterdam, Elsevier Scientific Publishing Company. p 99-102.

RAJARATNAM, N. and SUBRAMANYA, K. (1968) Plane turbulent reattached wall jets. *A.S.C.E. Journal of the Hydraulics Division*, 94, No. HY1, p 95-112.

RAUDKIVI, A. J. and CALLANDER, R. A. (1975) Advanced Fluid Mechanics: An Introduction. London, Edward Arnold. 325p.

SAWYER, R. A. (1960) The flow due to a two-dimensional jet issuing parallel to a flat plate. *Journal of Fluid Mechanics*, 9, p 543-560.

SAWYER, R. A. (1963) Two-dimensional reattaching jet flows including the effects of curvature on entrainment. *Journal of Fluid Mechanics*, 17, p 481-498.

SCHLICHTING, H. (1960) Boundary Layer Theory. 4th ed. New York, McGraw-Hill. 647p.

SQUIRE, H. B. (1950) Jet flow and its effects on aircraft. *Aircraft Engineering*, 22, p 62-67.

SHARP, J. J. (1975) The use of a buoyant wall jet to improve the dilution of a submerged outfall. *Proceedings, Institution of Civil Engineers*, 59, p 527-534.

STROUD, A. H. and SECREST, D. (1966) Gaussian Quadrature Formulas. Englewood Cliffs, N.J., Prentice-Hall. 374p.

TAYLOR, G. I. (1958) Flow induced by jets. *Journal of the Aeronautical Sciences*, 25, p464-465.

TURNER, J. S. (1973) Buoyancy Effects in Fluids. Cambridge, Cambridge University Press. 367p.

WATTENDORF, F. L. (1935) A study of the effect of curvature on fully developed turbulent flow. *Proceedings, Royal Society of London*, A148, p 565-598.

YOSHIDA, J. and NAGATA, Y. (1979) The behaviour of the two dimensional forced plume ejected near the vertical wall. *Coastal Engineering in Japan*, 22, p 111-122.

APPENDIX A

DERIVATION OF VELOCITY AND CONCENTRATION PROFILES FOR STEADY TWO-DIMENSIONAL TURBULENT INCOMPRESSIBLE JET FLOW

A.1 DERIVATION OF VELOCITY PROFILE

For a steady two-dimensional turbulent incompressible non-buoyant flow, the time averaged equations of motion are

$$\frac{\partial u}{\partial x} + \frac{\partial v}{\partial y} = 0 \tag{A.1}$$

$$u \frac{\partial u}{\partial x} + v \frac{\partial u}{\partial y} = - \frac{1}{\rho} \frac{\partial p}{\partial x} - \frac{\partial \overline{u'^2}}{\partial x} - \frac{\partial \overline{u'v'}}{\partial y} \tag{A.2}$$

$$u \frac{\partial v}{\partial x} + v \frac{\partial v}{\partial y} = - \frac{1}{\rho} \frac{\partial p}{\partial y} - \frac{\partial \overline{u'v'}}{\partial x} - \frac{\partial \overline{v'^2}}{\partial y} \tag{A.3}$$

The overbars indicating mean quantities are neglected where they are not essential in these equations.

Now it is reasonable to assume (Kotsovinos, 1975) that

$$u^2 >> \frac{p}{\rho} + \overline{u'^2}$$

Furthermore, Prandtl has postulated a relationship between the Reynolds stress and the local mean velocity field

$$- \overline{u'v} = \varepsilon_m \frac{\partial u}{\partial y}$$

where $\varepsilon_m = kbu_c$ is an apparent eddy viscosity.

Thus eq. A.2 reduces to

$$u \frac{\partial u}{\partial x} + v \frac{\partial u}{\partial y} - \varepsilon_m \frac{\partial^2 u}{\partial y^2} = 0 \tag{A.4}$$

For a two-dimensional jet, eqs. A.1 and A.4 can be solved assuming self-similarity and a constant eddy viscosity across the flow. To facilitate the solution it is helpful to construct a stream function ψ from which the transverse stream velocity v can be found. Now it is known that

$$u = -\frac{\partial \psi}{\partial y} \tag{A.5}$$

$$= u_c \phi_1 (\eta)$$

where $\eta = \sigma y/b$.

Thus $$\psi = -u_c b \frac{1}{\sigma} \int_o^\eta \phi_1 (\eta) d\eta \tag{A.6}$$

$$= -u_c b \frac{1}{\sigma} \Phi (\eta)$$

if $\psi = 0$ at $y = 0$ and

$$\Phi (\eta) = \int_o^\eta \phi_1(\eta)\, d(\eta) \tag{A.7}$$

The transverse velocity is related to the stream function by the equation

$$v = \frac{\partial \psi}{\partial x} \tag{A.8}$$

Hence $$v = -\frac{du_c}{dx} b \frac{1}{\sigma} \Phi (\eta) - u_c \frac{db}{dx} \frac{1}{\sigma} \Phi (\eta)$$

$$+ u_c \frac{db}{dx} \frac{1}{\sigma} \eta \phi_1 (\eta) \tag{A.9}$$

The integral equations of continuity and momentum in the x direction are

$$\frac{d}{dx} \left\{ \frac{k_1}{\sigma} u_c b \right\} = 2 \alpha u_c \tag{A.10}$$

$$\frac{d}{dx} \left\{ \frac{k_2}{\sigma} u_c^2 b \right\} = 0 \tag{A.11}$$

where $$k_1 = \int_{-\infty}^{+\infty} \phi_1 (\eta)\, d\eta \tag{A.12}$$

and $$k_2 = \int_{-\infty}^{+\infty} \phi_1^2 (\eta)\, d\eta \tag{A.13}$$

Differentiating eqs. A.10 and A.11, expressions for du_c/dx and db/dx can be obtained and substituted into eq. A.9. Thus

$$v = \frac{4}{k_1} \alpha u_c \left(- \frac{1}{2} \Phi (\eta) + \eta \phi_1 (\eta)\right) \tag{A.14}$$

The basic assumption of the entrainment coefficient approach to the solution of the equations of motion is that

$$\lim_{y \to \pm\infty} v(x,y) = \mp \alpha u_c$$

For eq. A.14 to be consistent with this assumption, then

$$\lim_{y \to \pm\infty} \frac{d}{d\eta} \left[\frac{1}{\phi_1 (\eta)} \right] \to \pm \infty \tag{A.15}$$

Substitution of the assumed expression for the mean stream velocity u and the implied expression for the transverse velocity v into eq. A.4 gives

$$\frac{d}{d\eta} (\Phi (\eta) \phi_1 (\eta)) + \frac{2k}{\frac{db}{dx}} \sigma^2 \phi_1'' (\eta) = 0 \tag{A.16}$$

The boundary conditions for this differential equation are

$$\Phi (0) = 0 \qquad \Phi (\pm\infty) = \pm \frac{k_1}{2}$$

$$\phi_1(0) = \Phi' (0) = 1 \qquad \Phi'(\pm\infty) = 0$$

$$\phi_1'(0) = \Phi'' (0) = 0$$

Integrating eq. A.16 twice and applying the given boundary conditions, it is found that

$$\left[\Phi (\eta)\right]^2 + \left(\frac{k_1}{2}\right)^2 \Phi' (\eta) = \left(\frac{k_1}{2}\right)^2 \tag{A.17}$$

where

$$\left(\frac{k_1}{2}\right)^2 = \frac{4k\sigma^2}{\frac{db}{dx}}$$

This has a solution

$$\Phi(\eta) = \tanh \eta \tag{A.18}$$

and

$$\phi_1(\eta) = \Phi'(\eta) = \operatorname{sech}^2 \eta \tag{A.19}$$

since

$$k_1 = \int_{-\infty}^{+\infty} \operatorname{sech}^2 \eta \, d\eta$$

$$= 2$$

A.2 DERIVATION OF CONCENTRATION PROFILES

The time-averaged partial differential equation for the conservation of tracer has previously been reduced to

$$u \frac{\partial c}{\partial x} + v \frac{\partial c}{\partial y} - \varepsilon_D \frac{\partial^2 c}{\partial y^2} = 0 \tag{4.5}$$

in which the overbars denoting mean quantities are again not essential. ε_D is the eddy mass diffusivity defined in eq. 4.4. The ratio of the eddy mass diffusivity to the apparent eddy viscosity, $\varepsilon_D/\varepsilon_m = \lambda^2$, is a measure of the relative rate of spread of mass and momentum. λ^2 is assumed constant and a value of 2 has been chosen in this study. It is also useful to obtain solutions to eq. 4.5 for $\lambda^2 = 1$.

Self-similarity has been assumed so that the concentration profiles are of the form

$$c = c_c \, \phi_2 \left(\frac{\eta}{\lambda}\right) \tag{A.20}$$

Substitution of eqs. A.5 and A.9 and the appropriate derivatives of eq. A.20 into eq. 4.5 then gives

$$-\frac{\frac{2}{c_c}\frac{dc_c}{dx}}{\frac{1}{b}\frac{db}{dx}} \Phi'(\eta) \, \phi_2 \left(\frac{\eta}{\lambda}\right) + \frac{1}{\lambda} \Phi(\eta) \, \phi_2'\left(\frac{\eta}{\lambda}\right) + \frac{1}{2} \phi_2''\left(\frac{\eta}{\lambda}\right) = 0 \tag{A.21}$$

For a flux of tracer incorporated with the jet, the integral conservation equation is

$$\frac{d}{dx} (k_3 \, c_c \, u_c \, b) = 0 \tag{A.22}$$

where $$k_3 = \int_{-\infty}^{+\infty} \phi_2 \left(\frac{\eta}{\lambda}\right) \phi_1(\eta) \, d\eta \tag{A.23}$$

Differentiating eqs. A.11 and A.22 produces the result that

$$\frac{-2 \, \dfrac{dc_c}{dx}}{\dfrac{c_c}{1} \quad \dfrac{db}{dx}} = 1$$

Thus for this case, eq. A.21 reduces to

$$\Phi'(\eta) \, \phi_2\left(\frac{\eta}{\lambda}\right) + \frac{1}{\lambda} \Phi(\eta) \, \phi_2'\left(\frac{\eta}{\lambda}\right) + \frac{1}{2} \phi_2''\left(\frac{\eta}{\lambda}\right) = 0 \tag{A.24}$$

Since $\Phi(\eta)$ is known, this differential equation can be integrated twice. Using the boundary conditions

$$\phi_2(0) = 1$$

$$\phi_2'(0) = 0$$

it is found that

$$\phi_2\left(\frac{\eta}{\lambda}\right) = (\operatorname{sech} \eta)^{\lambda^2} \tag{A.25}$$

In the case of a jet with a uniform concentration field of tracer on one side of the flow, the integral tracer conservation equation is

$$\frac{d}{dx} (k_3' \, c_c \, u_c \, b) = \alpha \, u_c \, c_f \tag{A.26}$$

where c_f is the field concentration. Differentiating eq. A.25 and substituting eq. A.11 suggests that

$$\frac{dc_c}{dx} = 0$$

Thus eq. A.21 reduces to

$$\frac{1}{\lambda}\,\Phi(\eta)\;\phi_2'\left(\frac{\eta}{\lambda}\right) + \frac{1}{2}\,\phi_2''\left(\frac{\eta}{\lambda}\right) \;=\; 0 \qquad \text{(A.27)}$$

This differential equation has the boundary conditions

$$\phi_2(0) \;=\; 1$$

$$\lim_{\eta\to+\infty}\;\phi_2\left(\frac{\eta}{\lambda}\right) \;=\; 0$$

$$\lim_{\eta\to-\infty}\;\phi_2\left(\frac{\eta}{\lambda}\right) \;=\; \frac{c_f}{c_c}$$

It can only be integrated when particular values are assigned to λ^2.

Evaluating eq. A.27 for $\lambda^2 = 1$ and $\lambda^2 = 2$ gives

$$\phi_2\left(\frac{\eta}{\lambda}\right) \;=\; 1 \;-\; \tanh\,\eta \qquad \lambda^2 = 1 \qquad \text{(A.28)}$$

$$\phi_2\left(\frac{\eta}{\lambda}\right) \;=\; 1 \;-\; \frac{2}{\pi}\tan^{-1}\left(\sinh\,\eta\right) \qquad \lambda^2 = 2 \qquad \text{(A.29)}$$

Both solutions imply that $c_c = \frac{1}{2}\,c_f$.

APPENDIX B

A SUMMARY OF THE PRINCIPLES OF LASER DOPPLER ANEMOMETRY

The principles of laser Doppler anemometry are well documented (Durst et al, 1976) and only a brief summary relevant to the forward scattering differential-Doppler mode of operation is given in this appendix.

The laser light is split optically into two intersecting beams (Fig. 6.9). The sensing volume formed by the intersection of the two beams is known as the measuring volume and light is scattered by particles suspended in the fluid as they pass through it. A photosensitive device focused on the measuring volume picks up the scattered light signals from each of the two intersecting beams and emits an alternating current with a Doppler frequency proportional to the scattering particle velocity.

The frequency f_s of the scattered light is shifted relative to the frequency f_i of the incident light that it originates from according to the equation

$$f_s = f_i + \frac{1}{\lambda} \underset{\sim}{u}. \ (\underset{\sim}{e}_s - \underset{\sim}{e}_i) \qquad \text{(B-1)}$$

where λ is the wavelength of the incident light, $\underset{\sim}{u}$ is the velocity vector of the particle and $\underset{\sim}{e}_s$ and $\underset{\sim}{e}_i$ are unit vectors in the scattered and incident directions respectively (Fig. 6.9). Hence if the incident beams are denoted by subscripts 1 and 2

$$f_{s_1} = f_{i_1} + \frac{1}{\lambda} \underset{\sim}{u} \ (\underset{\sim}{e}_{s_1} - \underset{\sim}{e}_{i_1})$$

$$\text{and} \qquad f_{s_2} = f_{i_2} + \frac{1}{\lambda} \underset{\sim}{u} \ (\underset{\sim}{e}_{s_1} - \underset{\sim}{e}_{i_2}) \qquad \text{(B-2)}$$

The photosensitive device receiving these signals emits an alternating current with a Doppler frequency

$$f_D = f_{s_2} - f_{s_1}$$
$$= \frac{1}{\lambda} \underset{\sim}{u} \cdot (\underset{\sim}{e}_{i_1} - \underset{\sim}{e}_{i_2}) \tag{B-3}$$

since $f_{i_1} = f_{i_2}$ and $\underset{\sim}{e}_{s_1} = \underset{\sim}{e}_{s_2}$. It is apparent that the Doppler frequency in the differential mode is independent of the angle from which the scattered light is viewed and that the measured velocity component is perpendicular to the bisector of the beam intersection angle θ and in the same plane as the incident beams. Eq. B-3 can be rearranged and expressed in the more familiar form,

$$|\underset{\sim}{u}| = \frac{\lambda f_D}{2 \sin \frac{\theta}{2}} \tag{B-4}$$

Eq. B-4 is valid for measurements in air. Most fluid flows (particularly liquid ones) are constrained by physical boundaries and the effect on this equation of refraction at the interfaces of several parallel layers of different media must be examined. For refraction at a liquid-air interface (Fig. B-1)

$$n_1 \lambda_1 = n \lambda$$

and

$$n_1 \sin \frac{\theta_1}{2} = n \sin \frac{\theta}{2} \tag{B-5}$$

where n is the refractive index, λ is the wavelength, θ is the angle between the two intersecting beams and thesubscript "1" denotes the liquid medium. Substitution of these laws into eq. B-4 indicates that the form remains unchanged

$$|\underset{\sim}{u}| = \frac{\lambda f_D}{2 \sin \frac{\theta}{2}} = \frac{\lambda_1 f_D}{2 \sin \frac{\theta_1}{2}}$$

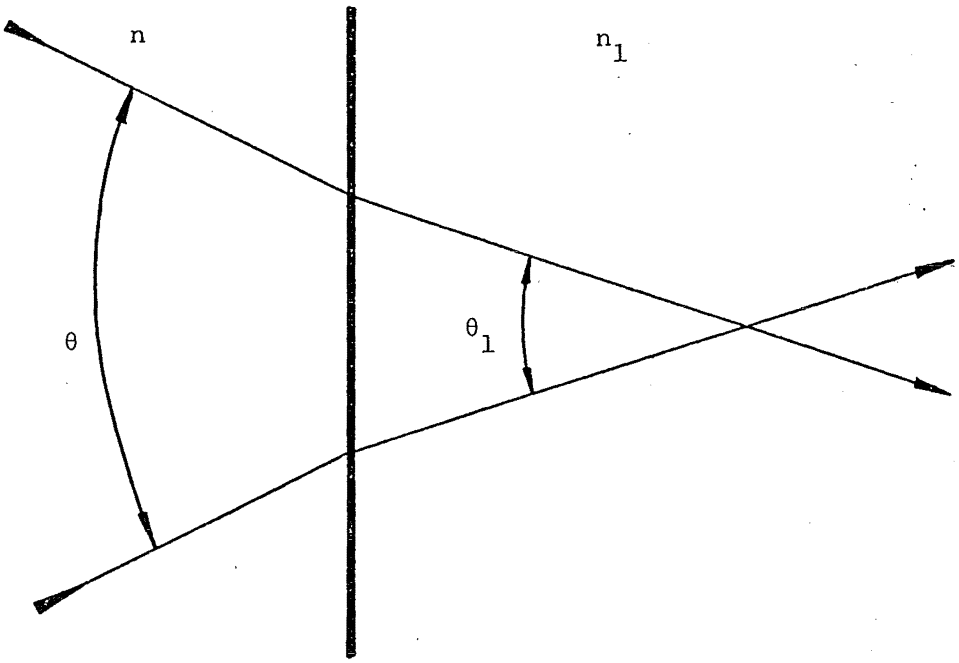

FIGURE B-1 Refraction at a plane liquid-air interface.

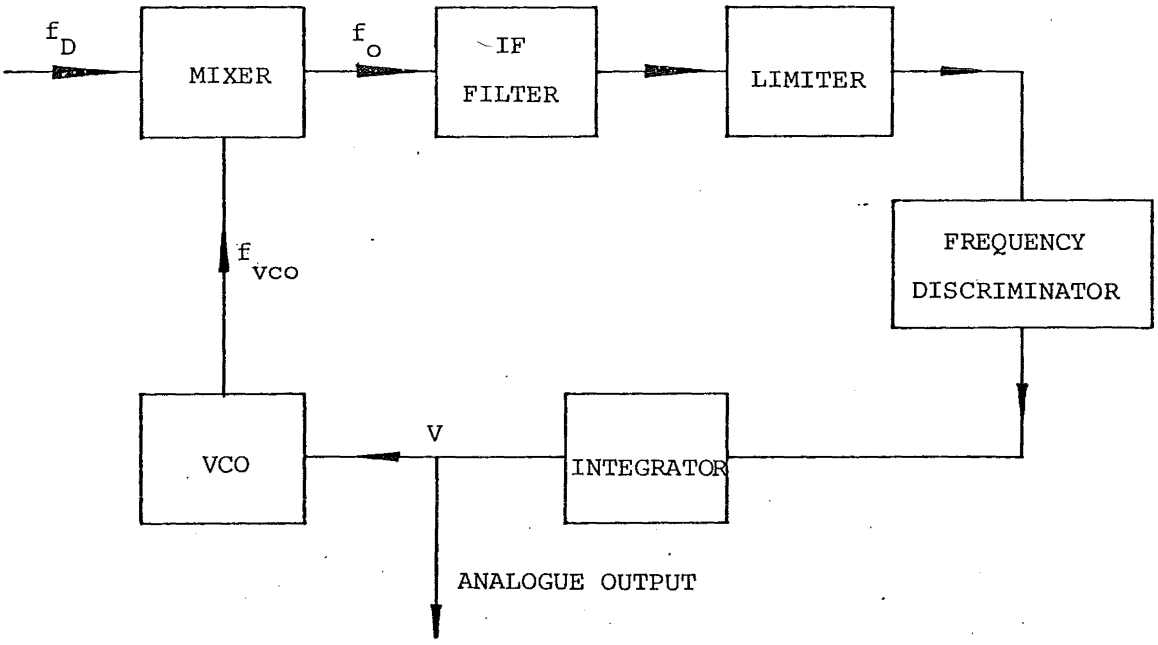

FIGURE B-2 Block diagram of frequency tracker.

The same conclusion applies when the two intersection beams pass through several parallel layers of different refractive indices. The location of the measuring volume will however differ from the original position in air.

There are several methods for analysing the Doppler frequency of the alternating photoelectric current. The DISA type 55L LDA employs a frequency tracking technique (Fig. B-2). Initially the Doppler signal $A(t) \cos\left[2\pi f_D t + \phi\right]$ is mixed with the output $\cos 2\pi f_{vco} t$ of a voltage controlled oscillator (vco) to give a signal $\frac{A(t)}{2} \cos\left[2\pi(f_{vco} - f_D)t - \phi\right]$ with an intermediate frequency (IF) $f_o = f_{vco} - f_D$. The IF signal is passed through a narrow band filter centred on the IF f_o to remove as much noise as possible, then through a limiter to eliminate the amplitude variations $A(t)/2$, and on to a frequency discriminator. The frequency discriminator produces a voltage to drive the vco in a feedback loop such that the difference between the instantaneous IF $f_i = f_{vco} - f_D$ and the constant centre IF f_o as the Doppler frequency f_D subsequently changes is corrected. Slight deviation of f_i from f_o can occur due to the finite response time necessary for stability of the feedback loop (regulated by the integrator). In this manner the vco frequency f_{vco} tracks the Doppler frequency f_D with a nearly constant difference equal to the centre IF f_o (Fig. B-3). The tracker output is obtained from the voltage driving the vco which is linearly proportional to the Doppler frequency and hence the flow velocity (eq. B-4).

Frequency tracking normally requires a near-continuous input signal but this is avoided by incorporating a mechanism which, if the input signal is lost, holds the last known signal until a new one is received. Signal loss is termed "dropout" and is generally due to either small scattering particle concentrations, an inherent inability of the tracker to follow

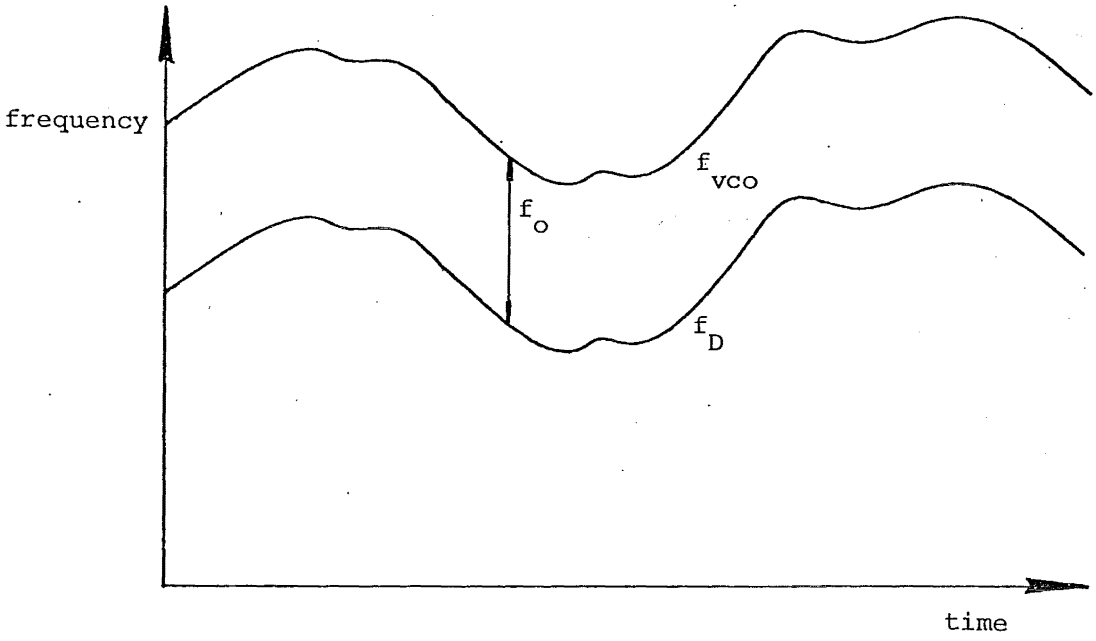

FIGURE B-3 VCO frequency tracking Doppler frequency.

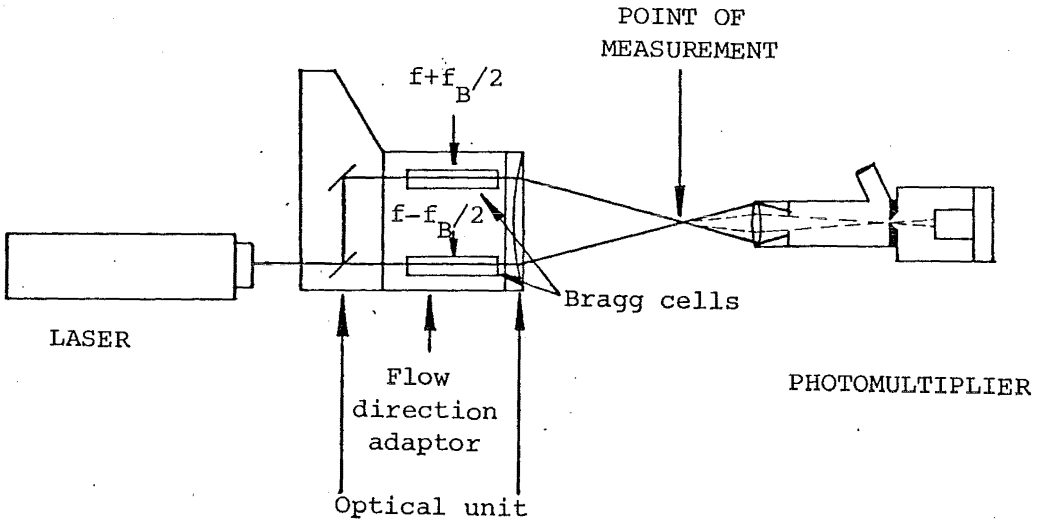

FIGURE B-4 Direction sensitive LDA system.

rapidly varying frequencies, or the rejection of a signal by validation circuitry (Durst et al. 1978).

Dropout occurring as a consequence of low scattering particle concentrations can be minimised by artificial "seeding" of the flow. The particles must be small enough to accurately follow the turbulent motion of the fluid and yet sufficiently large to produce detectable scattering of the laser light. The level of particle concentration needs to be high enough to ensure a near-continuous Doppler signal but not so high that the laser beams become diffuse. It is desirable also that the seeding particles are cheap, harmless and convenient to use.

When artificial seeding is employed in jet flow experiments a bias in the velocity probability density function for a point in the intermittent region of the jet may arise due to entrainment. Near the edge of the jet parcels of seeded fluid will mix with parcels of unseeded ambient fluid but only the former will yield a Doppler signal as they pass through the measuring volume resulting in a biased measurement. The possibility of bias from this source is countered simply by seeding the ambient fluid as well as the inflow. However diffusion of the laser light becomes a problem if the required concentration is too high and a compromise must be made.

In highly turbulent flows the sign of the velocity becomes important. The LDA as it has been described so far is insensitive to the velocity direction and will yield erroneous measurements, particularly if a recirculation zone exists as in the attached jet. Direction sensitivity in the DISA type 55L LDA is achieved by preshifting up and down the frequency of the split laser beams with acousto-optic Bragg cells. The cells are mounted between the beam splitter and lens sections of the optical unit (Fig. B-4).

In a Bragg cell a train of plane ultrasonic waves is generated across an acousto-optic medium. The wave fronts effectively form a moving diffraction grating and for a particular angle of incidence with respect to the wave motion (the Bragg angle) the diffracted beam is a first order one. The frequency of the diffracted light is shifted by the frequency of the ultrasonic waves. The alternating current emitted by the photosensitive device at the detection end of the LDA will therefore have the Doppler frequency

$$f_D = f_{i_2} - f_{i_1} + \frac{1}{\lambda} \underset{\sim}{u}. (\underset{\sim}{e}_{s_1} - \underset{\sim}{e}_{s_2}) \qquad \text{(B-6)}$$

where $f_{i_2} - f_{i_1} = f_B$

and $f_B/2$ is the frequency shift created by each of the Bragg cells (Fig. B-4).

APPENDIX C

CALIBRATION OF THE DOPPLER SIGNAL PROCESSER

The calibration of the Doppler signal processer for each of the frequency ranges used in the velocity field measurements was determined by supplying a series of known frequencies to the input of the preamplifier and measuring the voltage output. The linear relationship between frequency input and voltage output is shown in Figs. C-1, C-2 for the 150 and 500 KHz ranges respectively.

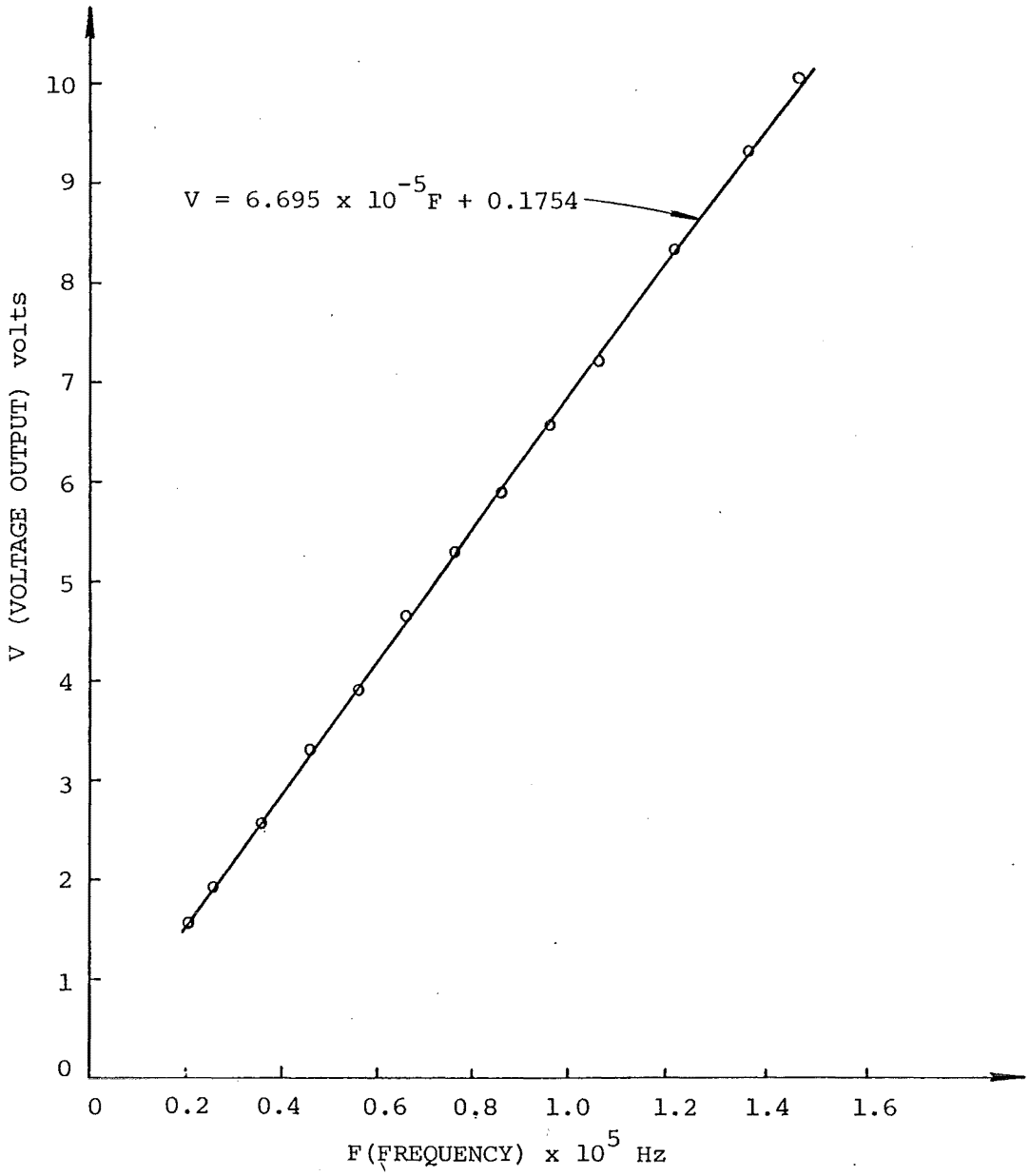

FIGURE C-1 Calibration of frequency tracker for 150 kHz range.

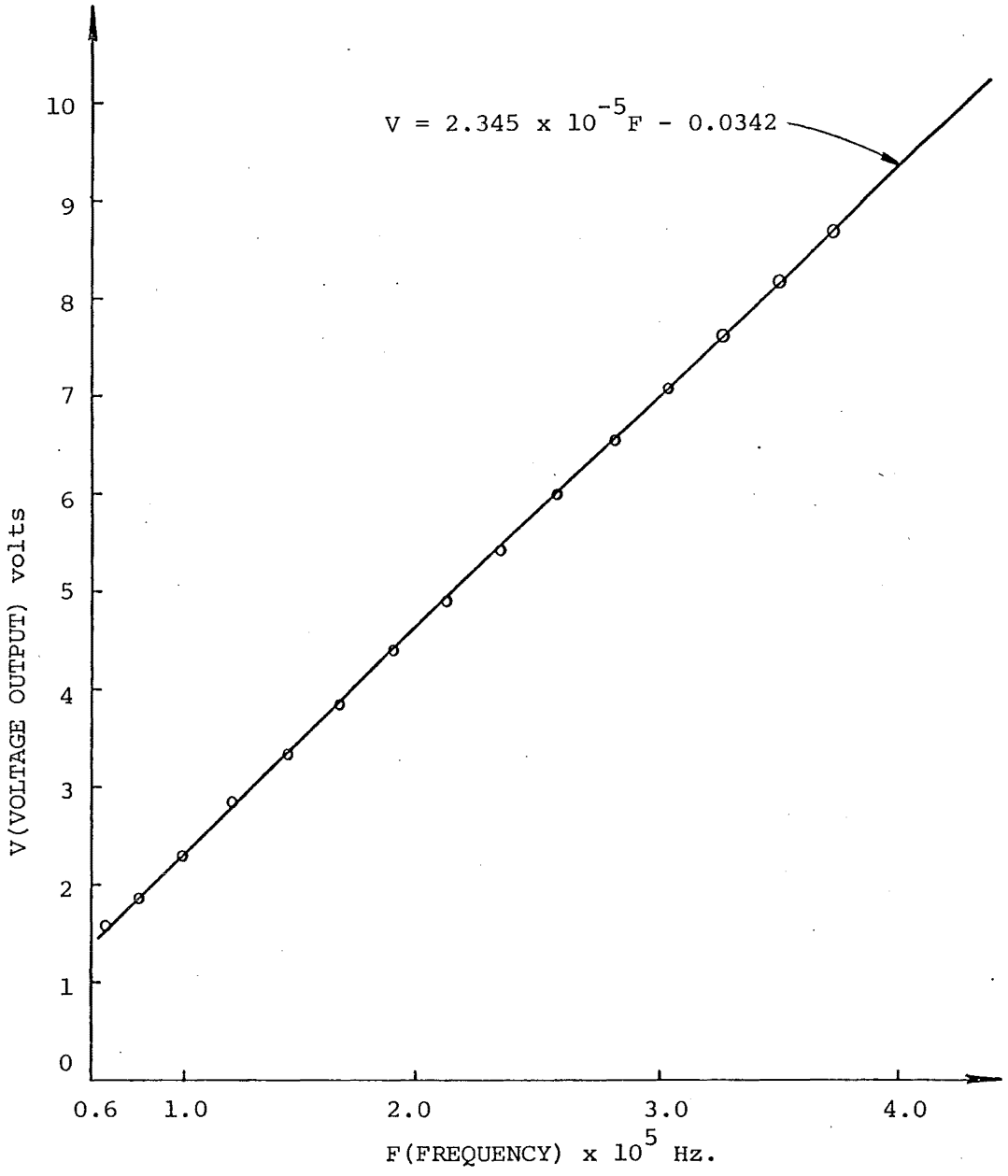

FIGURE C-2 Calibration of frequency tracker for 500 kHz range.

APPENDIX D

EXPERIMENTAL DATA-VELOCITY MEASUREMENTS

The horizontal velocity was measured along a series of vertical sections in both attached non-buoyant and buoyant jets. The data obtained have been processed to give dimensionless profiles of mean horizontal velocity and turbulent intensity of velocity fluctuations. The profiles are presented in this appendix. The data is also tabulated.

For convenience, horizontal velocity is denoted by the symbol u rather than u_x as in the text.

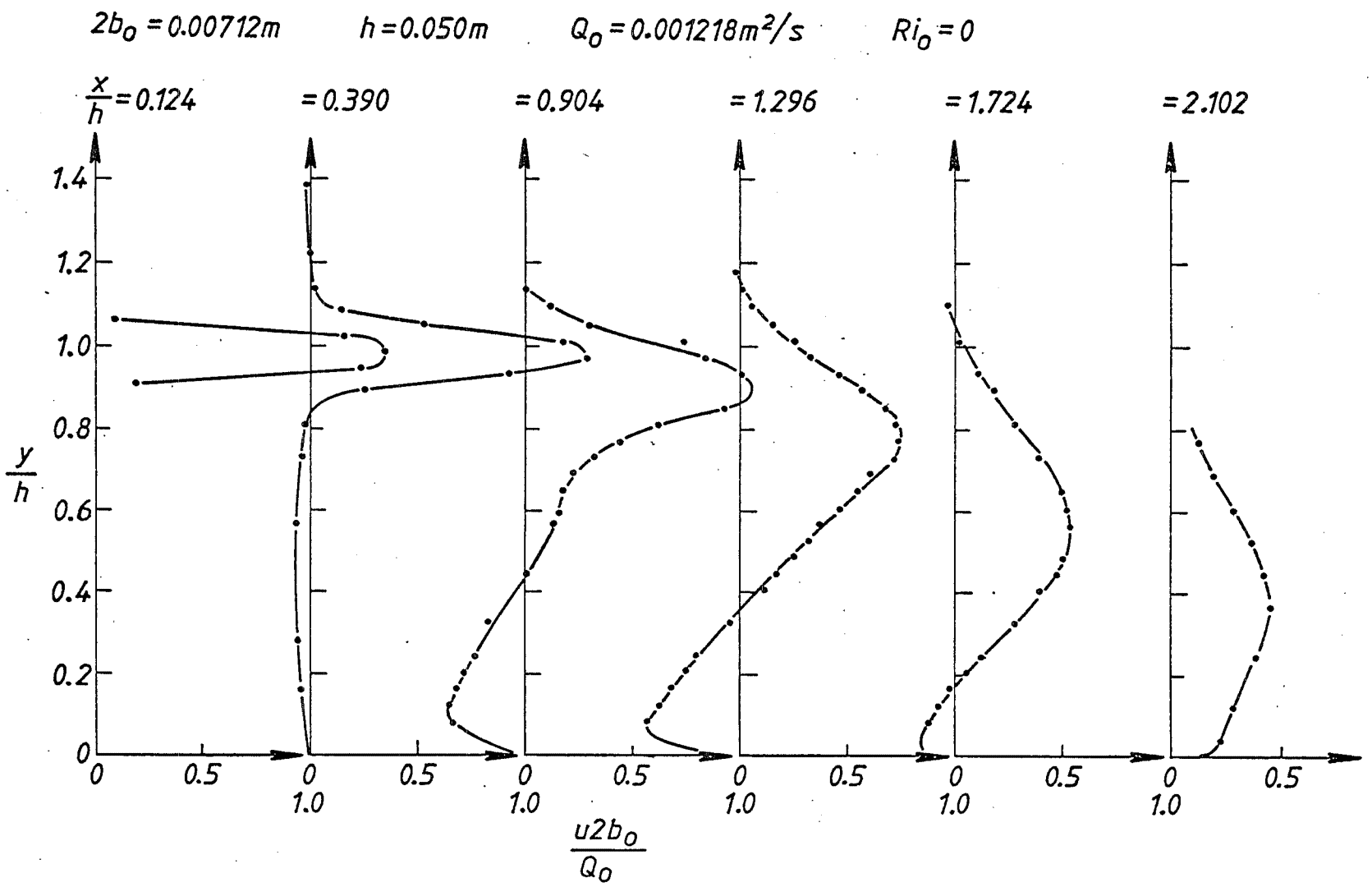

FIGURE D-1 Dimensionless mean horizontal velocity data from an attached non-buoyant jet. h/b_o = 14.0 and Re ≃ 1050.

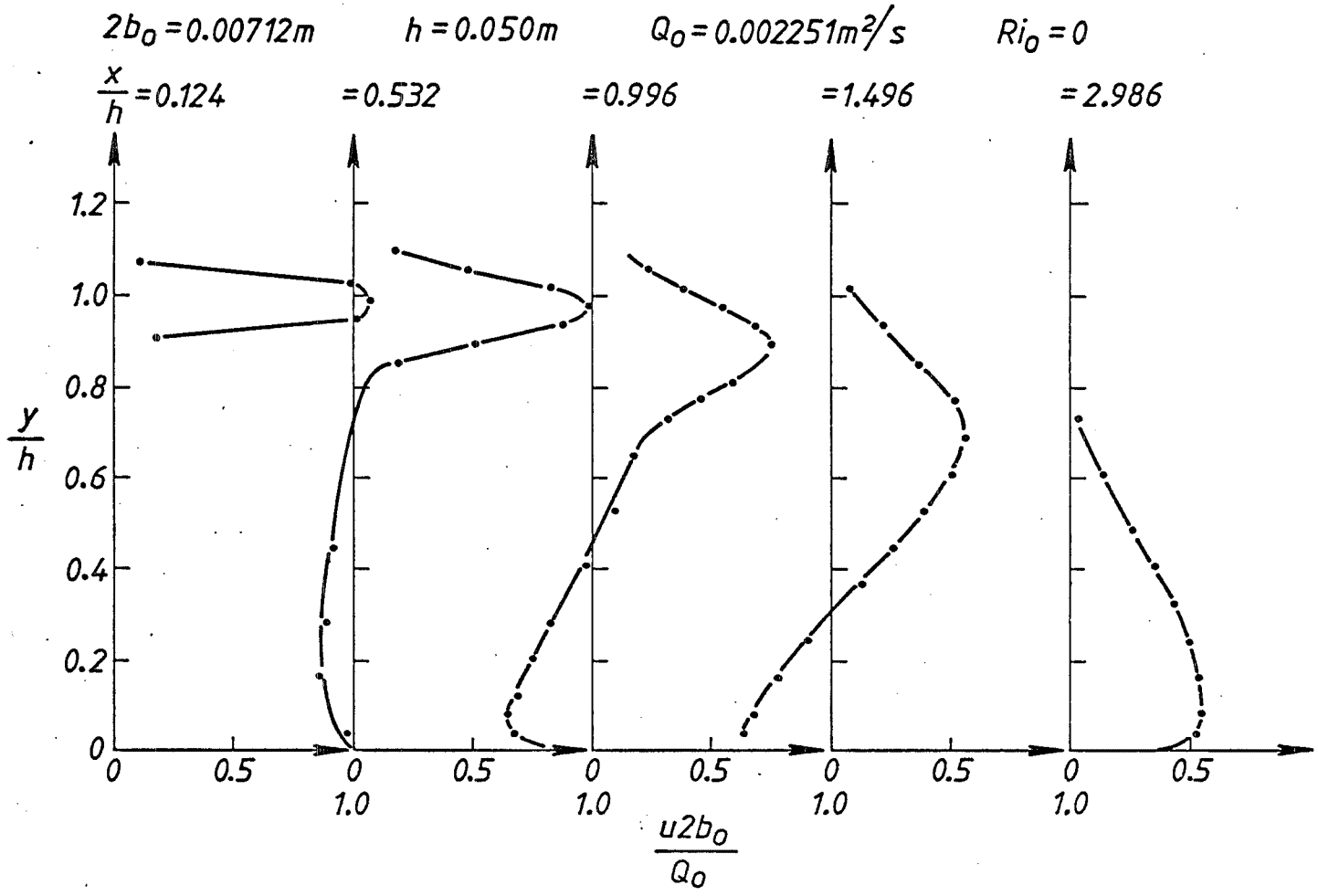

FIGURE D-2 Dimensionless mean horizontal velocity data from an attached non-buoyant jet. h/b_o = 14.0 and Re ≃ 1925.

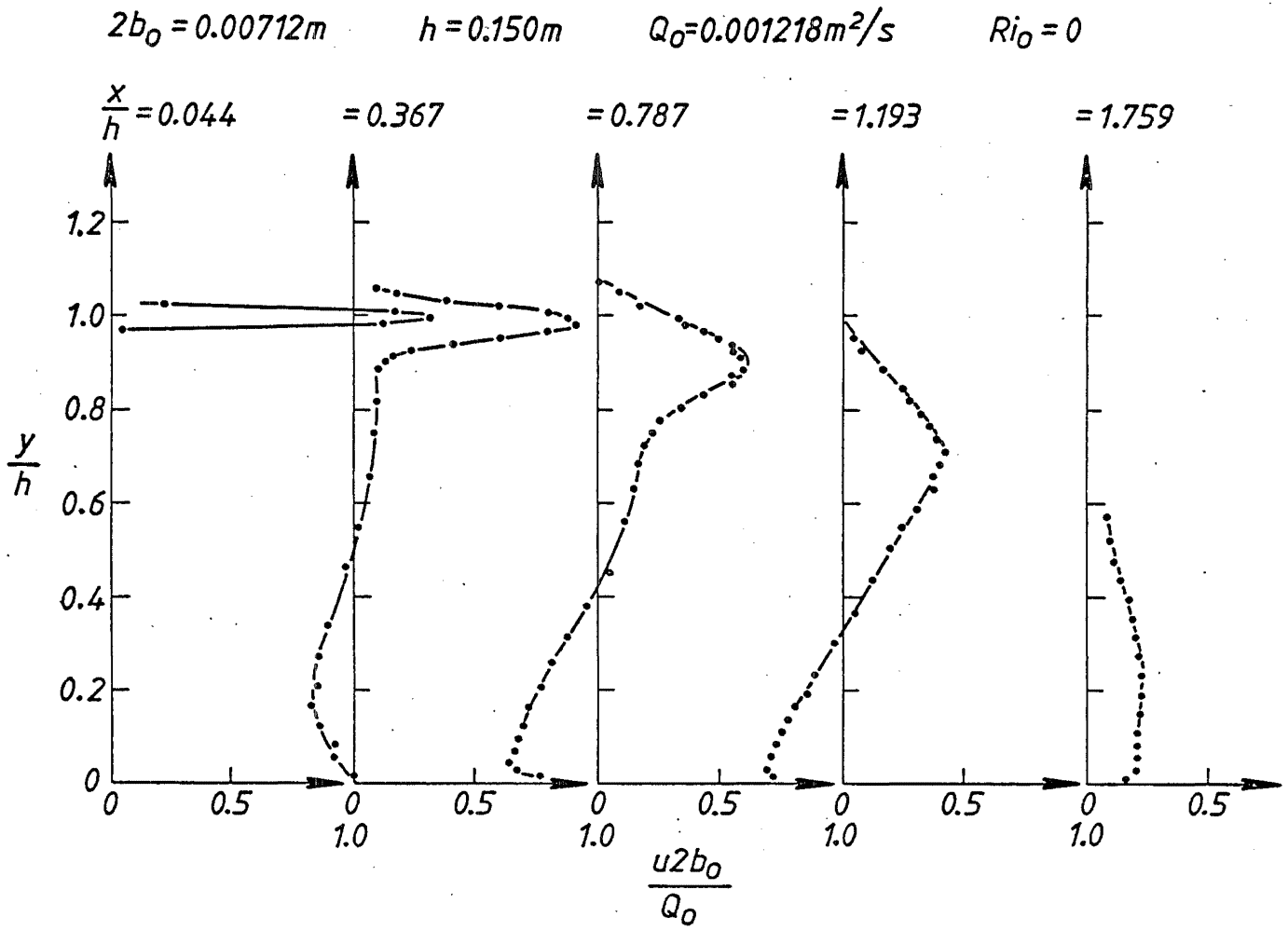

FIGURE D-3 Dimensionless mean horizontal velocity data from an attached non-buoyant jet. h/b_o = 42.1 and Re ≃ 1035.

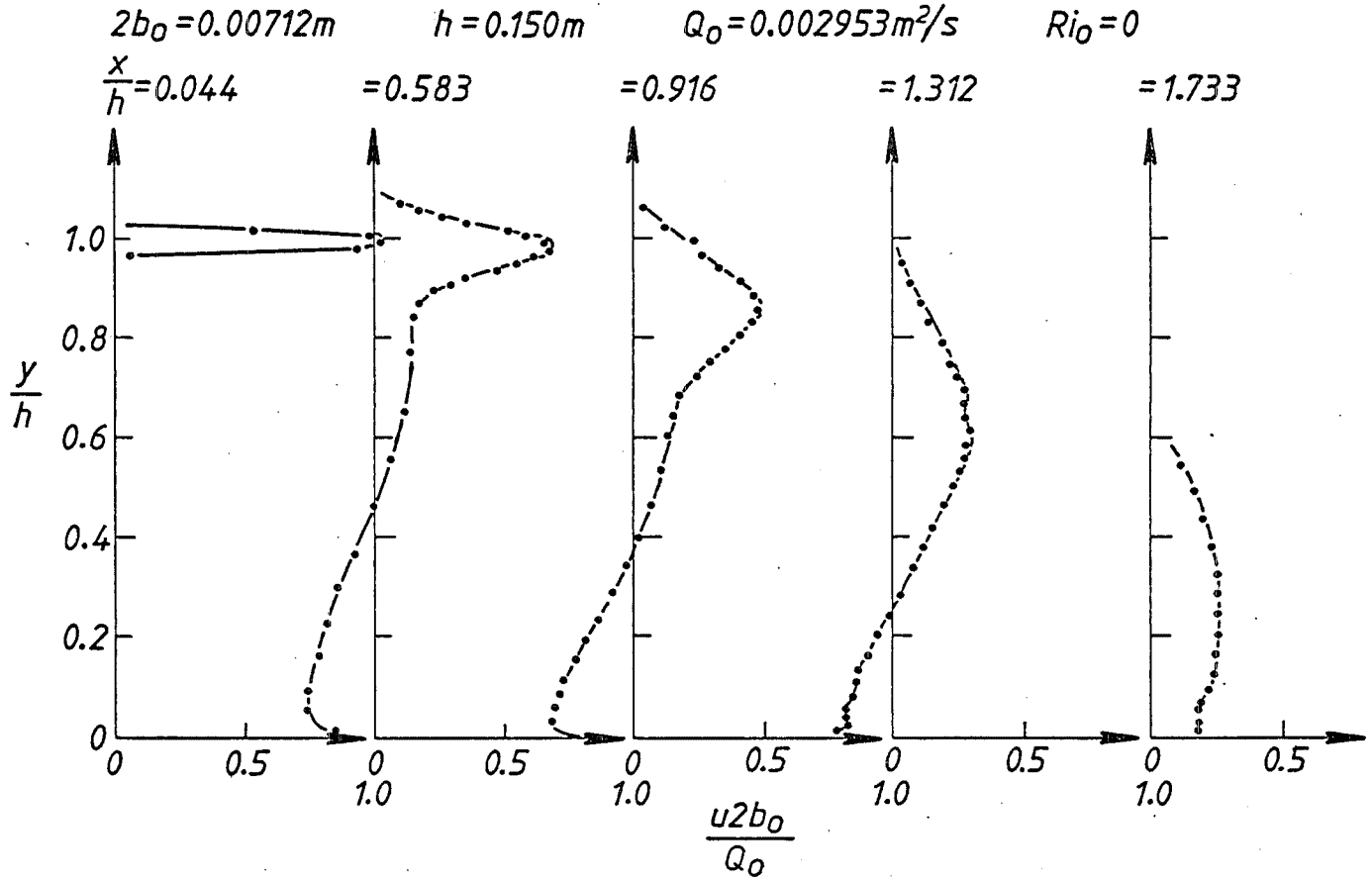

FIGURE D-4 Dimensionless mean horizontal velocity data from an attached non-buoyant jet. h/b_o = 42.1 and Re ≈ 2540.

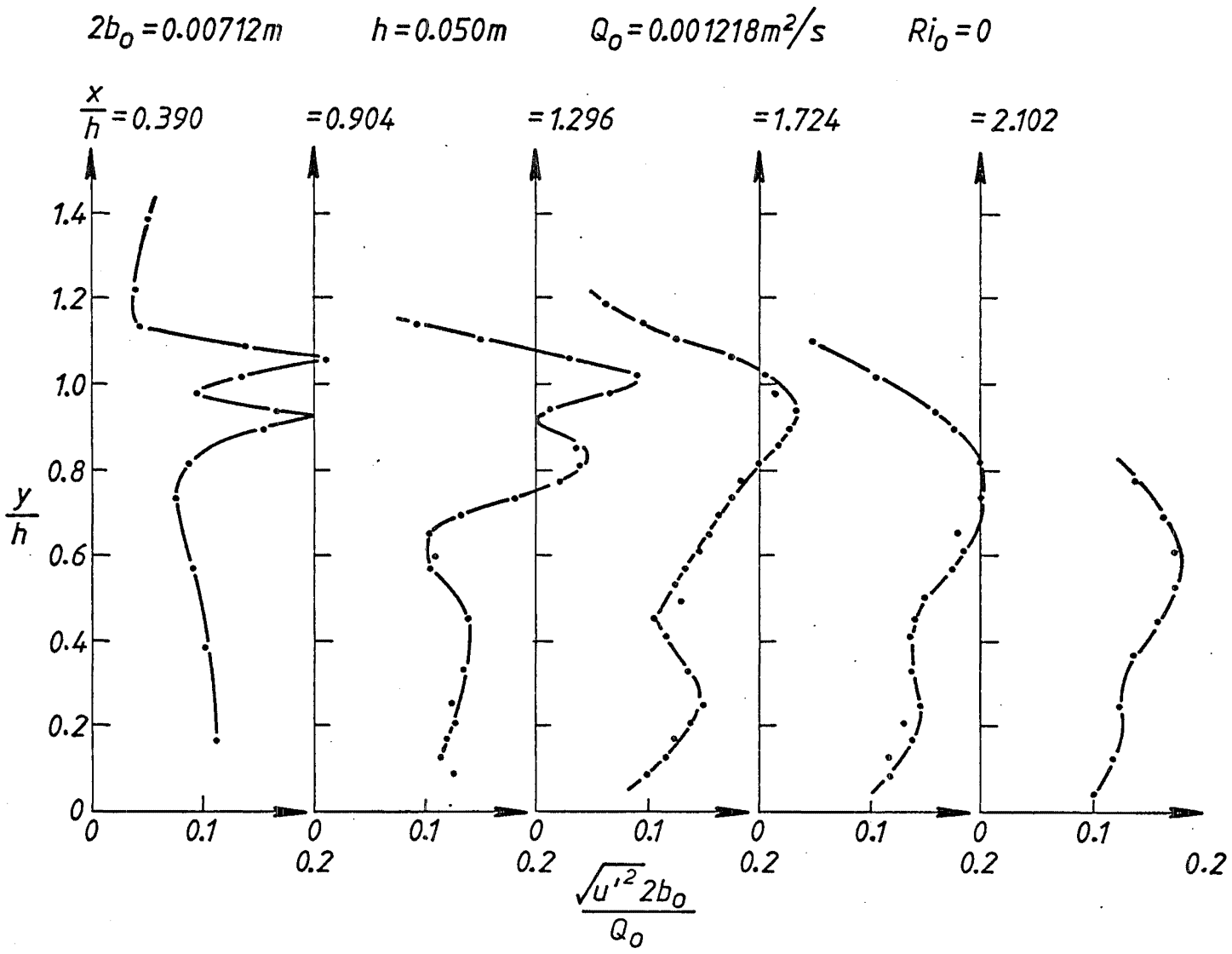

FIGURE D-5 Dimensionless turbulent intensity of horizontal velocity fluctuations in an attached non-buoyant jet. h/b_o = 14.0 and Re ≃ 1050.

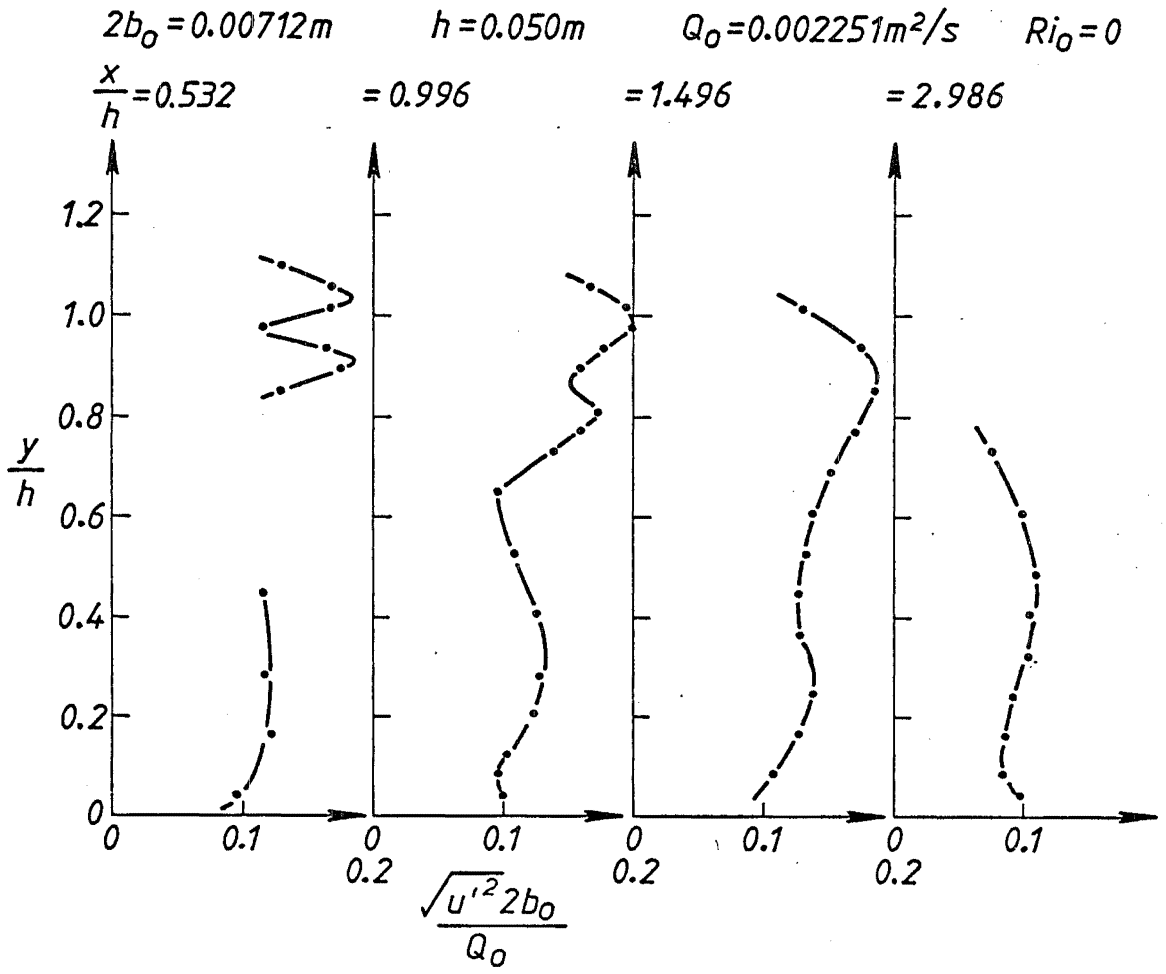

FIGURE D-6 Dimensionless turbulent intensity of horizontal velocity fluctuations in an attached non-buoyant jet. h/b_o = 14.0 and Re ≈ 1925.

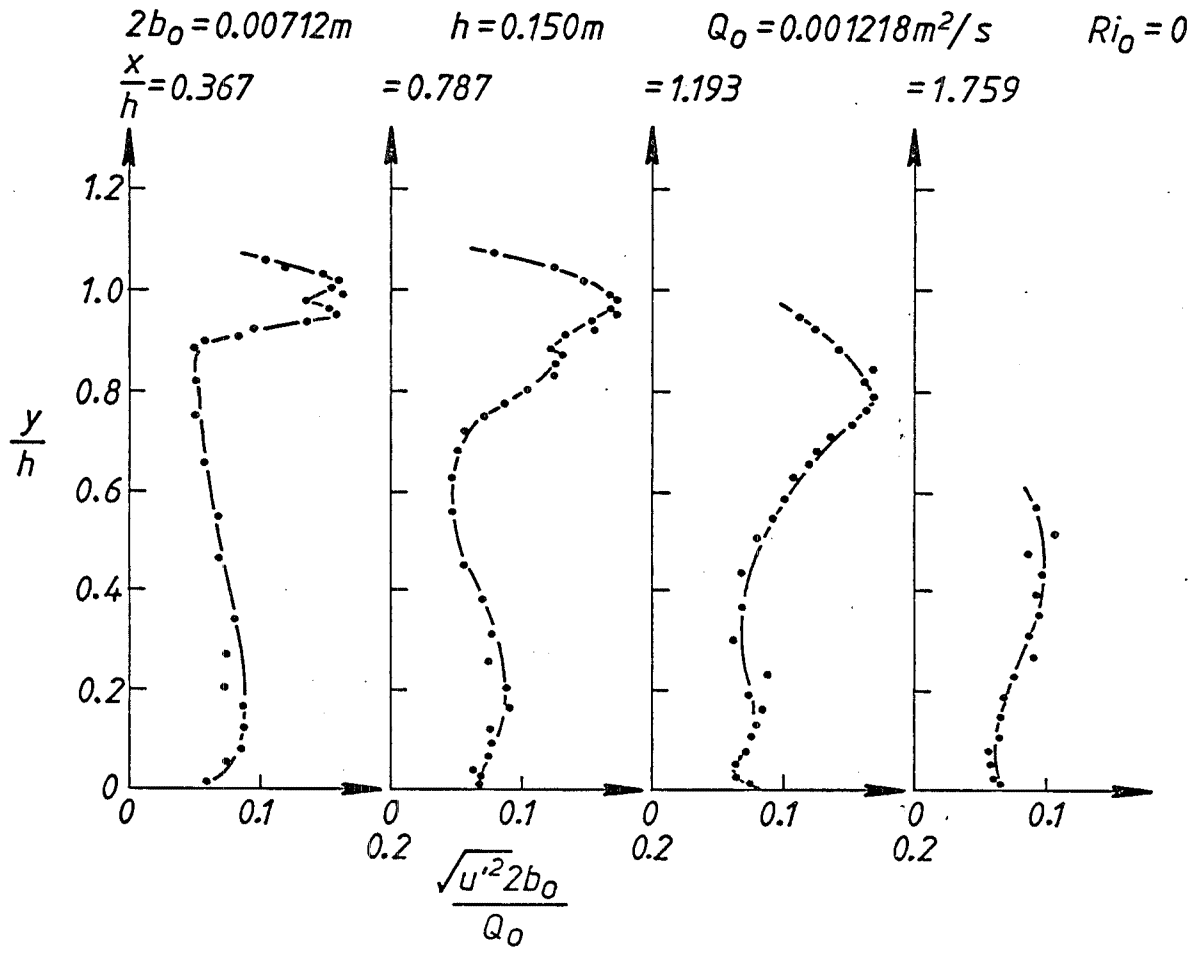

FIGURE D-7 Dimensionless turbulent intensity of horizontal velocity fluctuations in an attached non-buoyant jet. h/b_o = 42.1 and Re ≃ 1035.

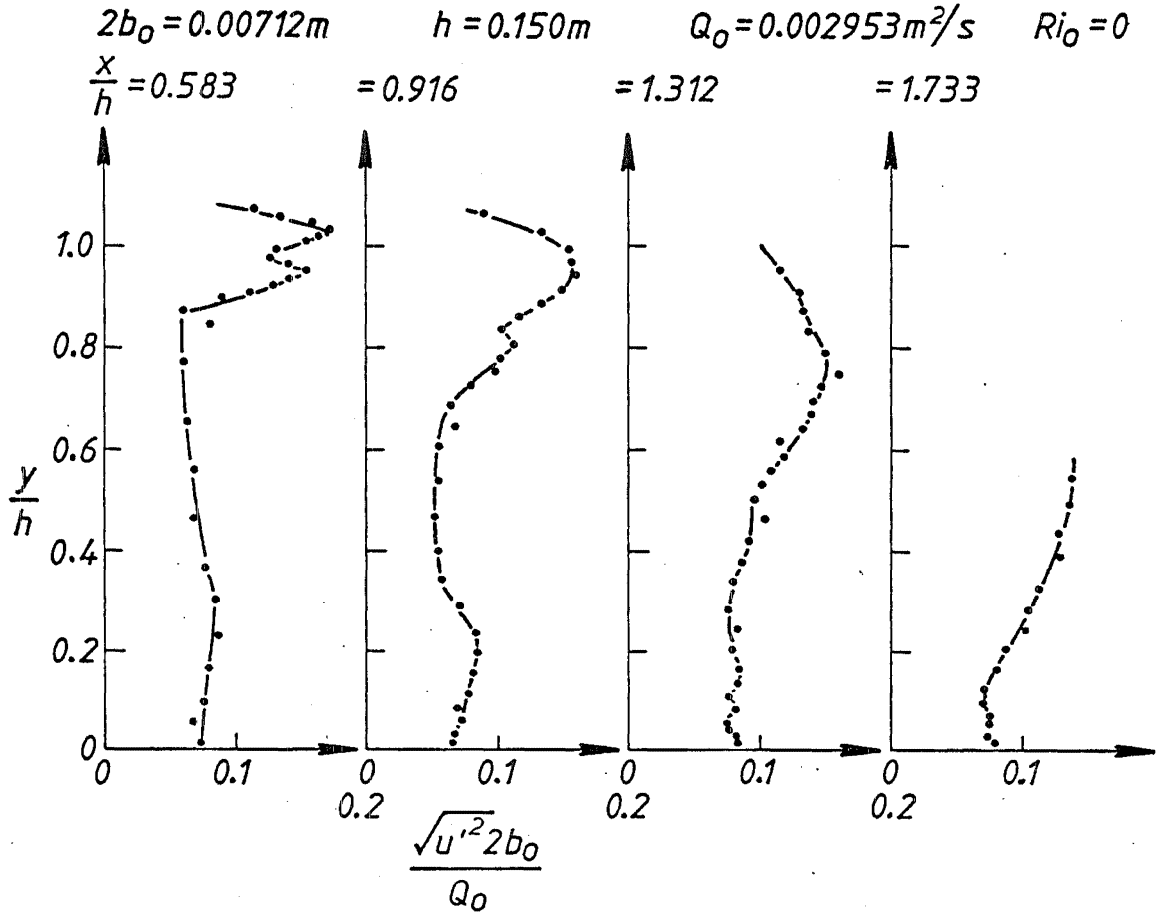

FIGURE D-8 Dimensionless turbulent intensity of horizontal velocity fluctuations in an attached non-buoyant jet. h/b_o = 42.1 and Re ≃ 2540.

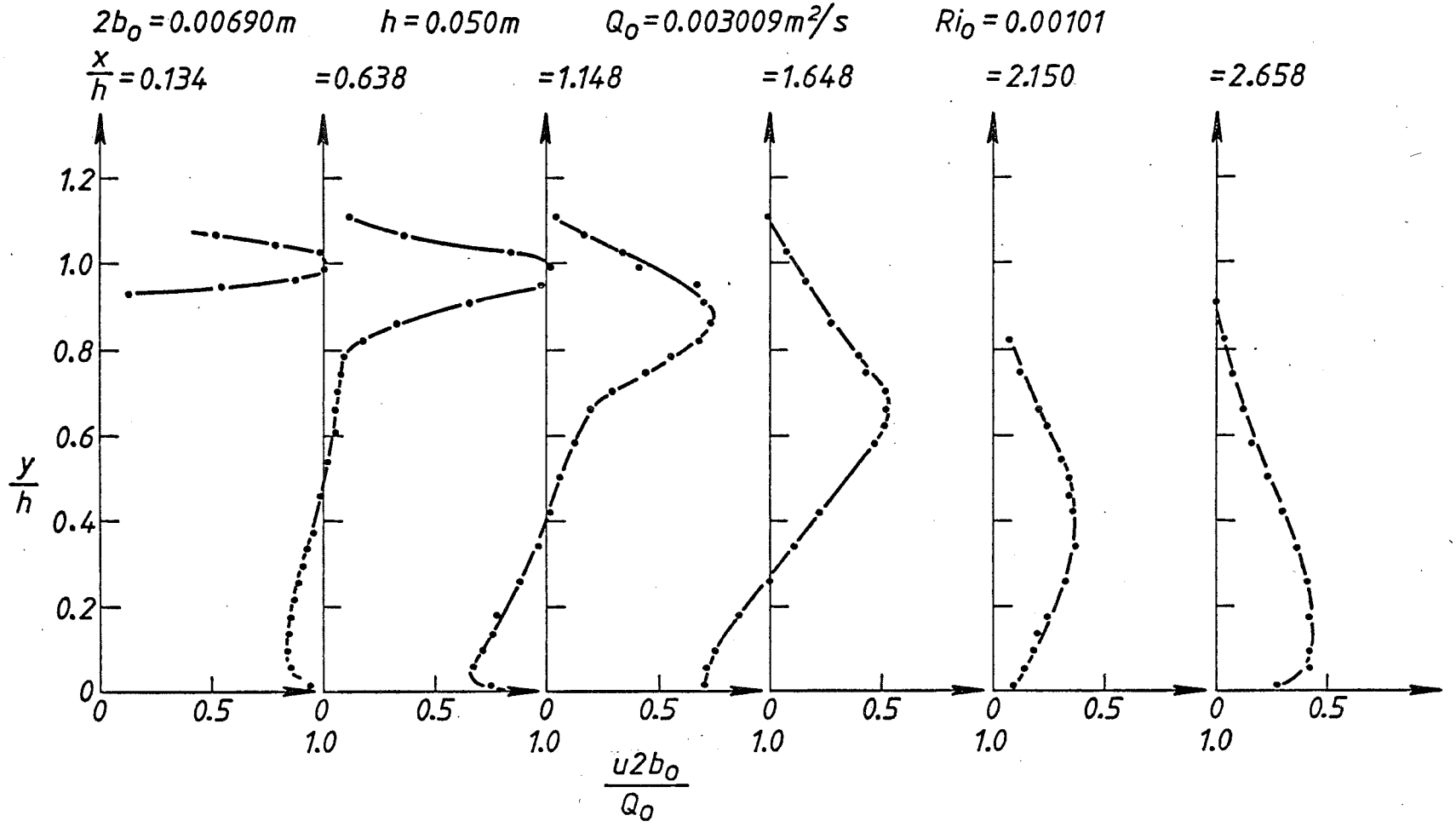

FIGURE D-9 Dimensionless mean horizontal velocity data from an attached buoyant jet. $h/b_o = 14.5$, $Re \simeq 4335$ and $Ri_o = 0.00101$.

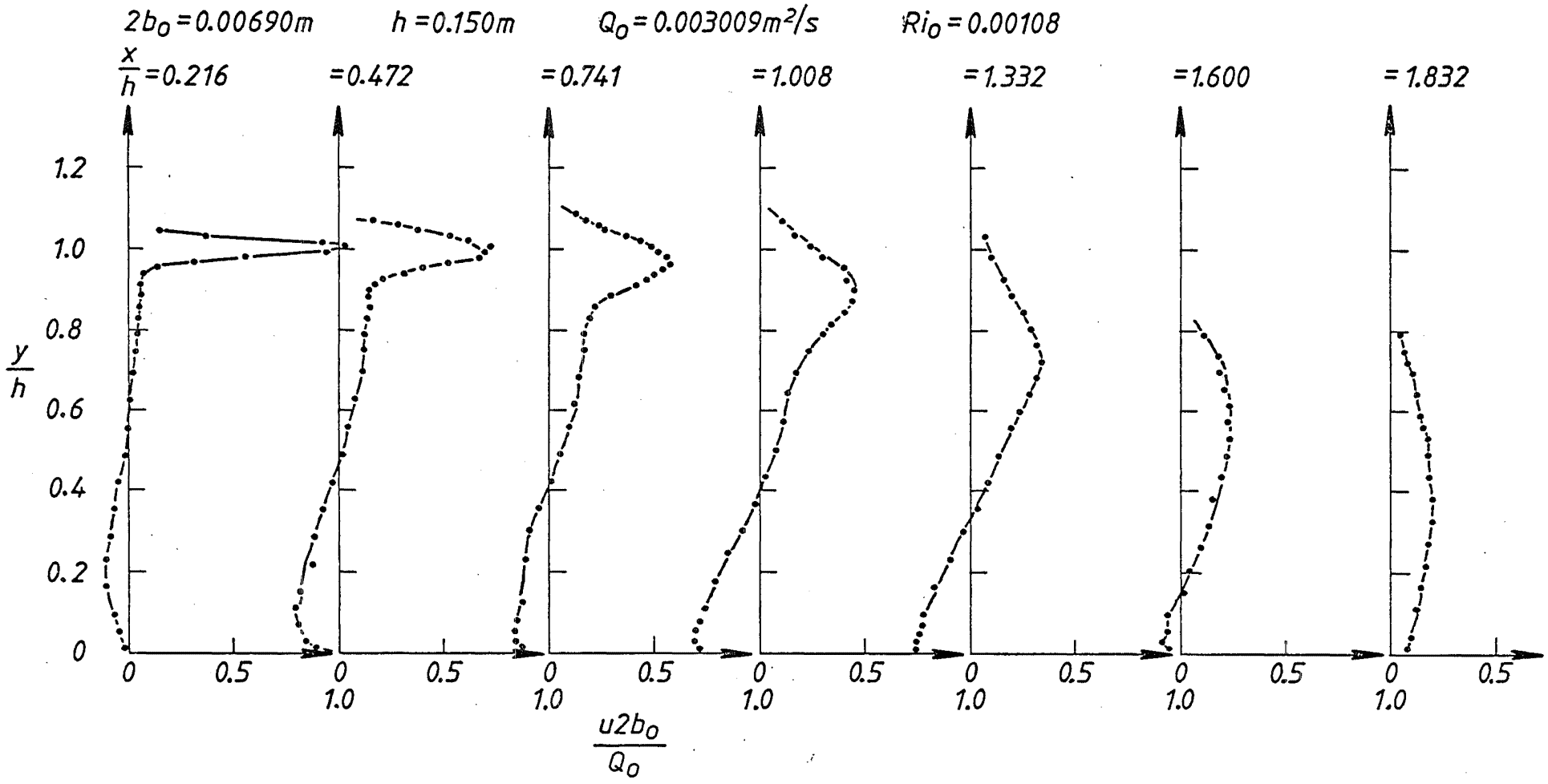

FIGURE D-10 Dimensionless mean horizontal velocity data from an attached buoyant jet. h/b_o = 43.5, Re ≃ 4465 and Ri_o = 0.00108.

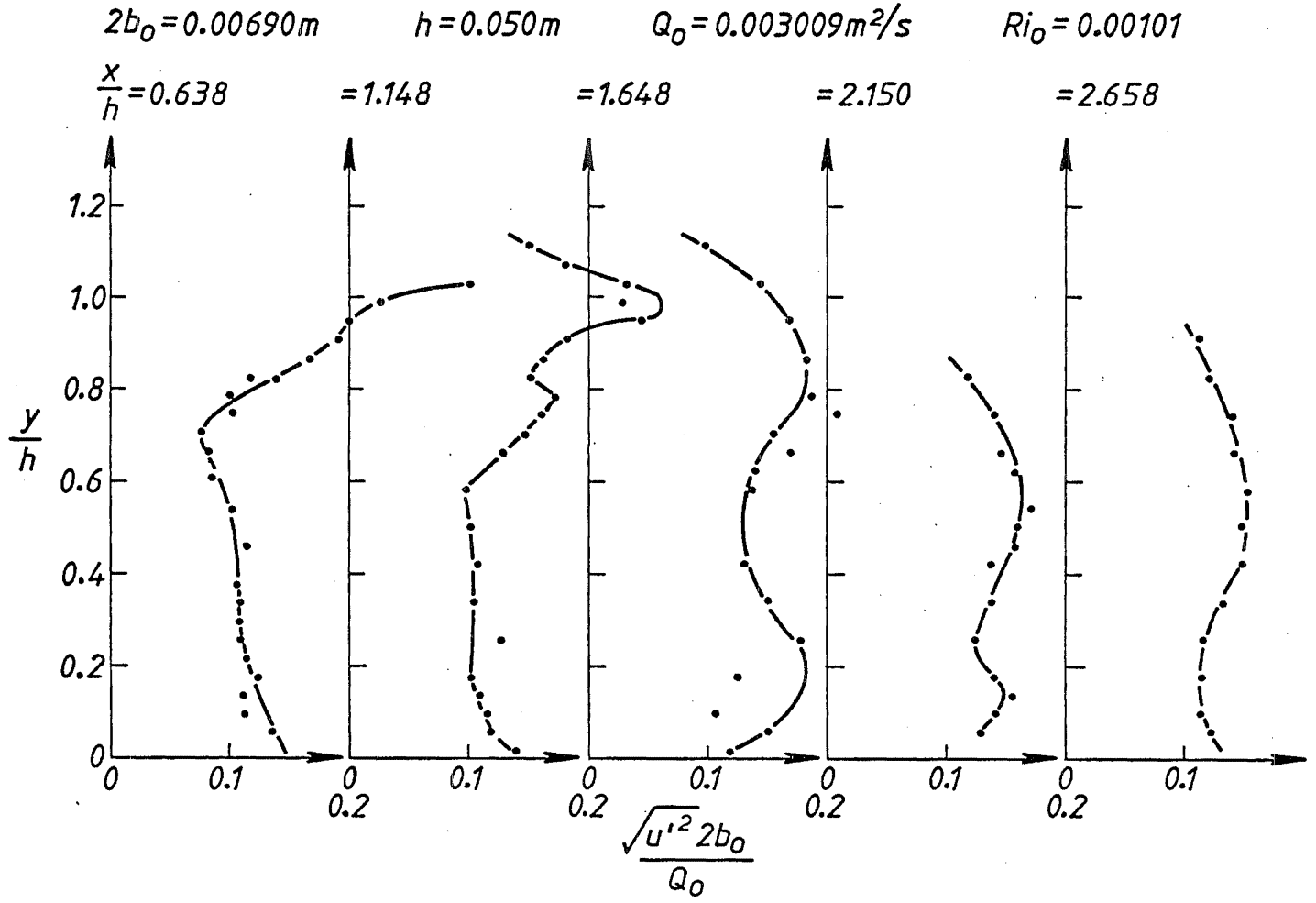

FIGURE D-11 Dimensionless turbulent intensity of horizontal velocity fluctuations in an attached buoyant jet. $h/b_o = 14.5$, $Re \simeq 4335$ and $Ri_o = 0.00101$.

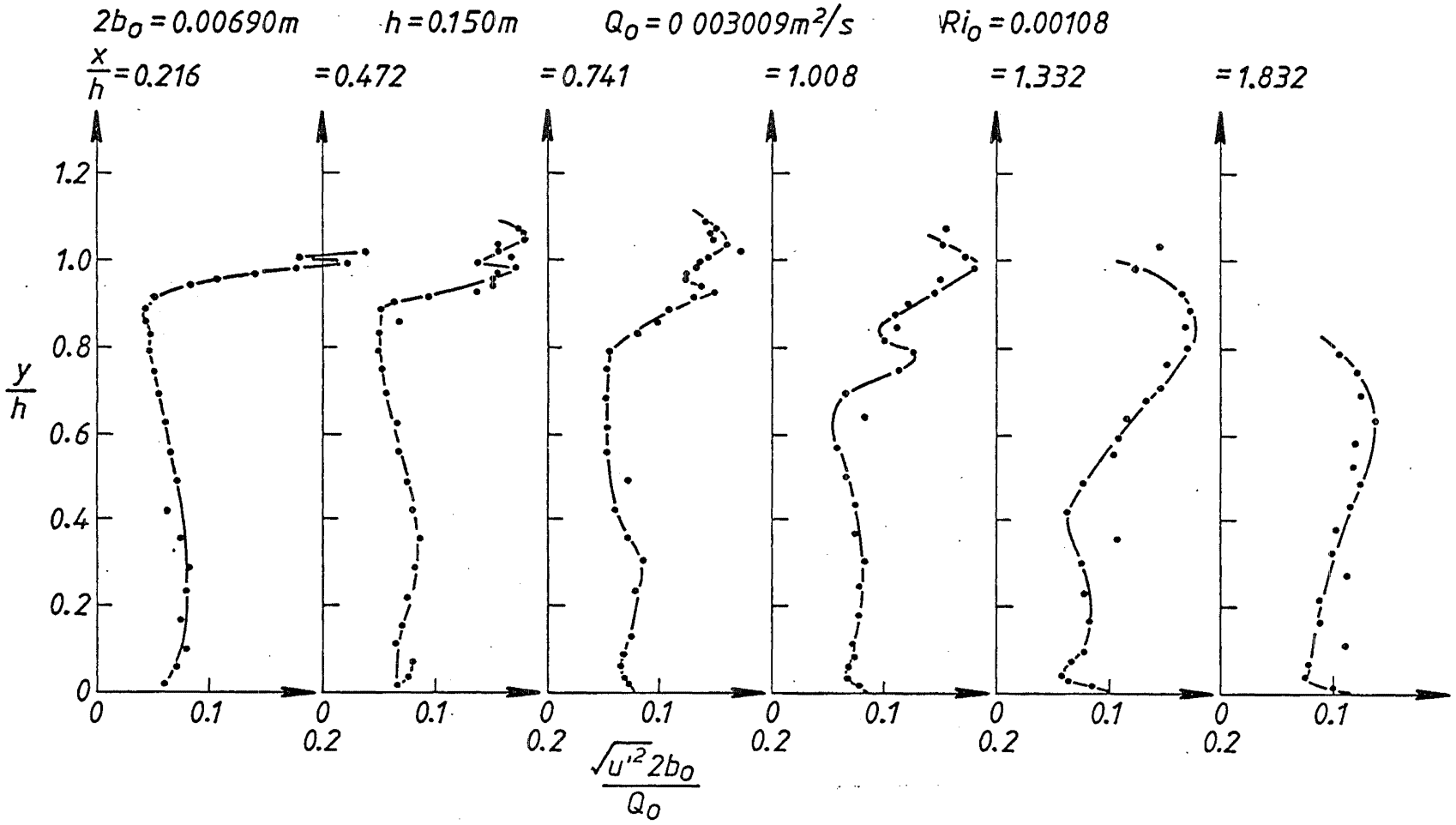

FIGURE D-12 Dimensionless turbulent intensity of horizontal velocity fluctuations in an attached buoyant jet. $h/b_o = 43.5$, $Re \simeq 4465$ and $Ri_o = 0.00108$.

$h = 0.050$ m

$2b_o = 0.00712$ m

$Q_o = 0.001218$ m^2/s

$Ri_o = 0$

x	y	$\bar{u}$	$\sqrt{\overline{u'^2}}$	$\frac{y}{h}$	$\frac{\bar{u}2b_o}{Q_o}$	$\frac{\sqrt{\overline{u'^2}}2b_o}{Q_o}$
mm	mm	m/s	m/s			
6.2	53.3	0.0151		1.066	0.088	
	51.3	0.1981	0.0202	1.026	1.158	0.118
	49.4	0.2311	0.0122	0.988	1.351	0.071
	49.4	0.2294	0.0128	0.988	1.341	0.075
	47.4	0.2117	0.0176	0.948	1.238	0.103
	45.4	0.0321	0.0119	0.908	0.188	0.069
19.5	69.2	-0.0022	0.0088	1.384	-0.013	0.052
	61.0	0.0009	0.0068	1.220	0.005	0.040
	56.8	0.0038	0.0077	1.136	0.022	0.045
	54.3	0.0255	0.0201	1.086	0.149	0.118
	52.7	0.0912	0.0364	1.054	0.533	0.213
	50.7	0.2010	0.0234	1.014	1.175	0.137
	48.8	0.2199	0.0162	0.976	1.286	0.095
	46.8	0.1592	0.0288	0.936	0.931	0.168
	44.8	0.0441	0.0267	0.896	0.258	0.156
	40.6	-0.0028	0.0149	0.812	-0.016	0.087
	36.6	-0.0056	0.0132	0.732	-0.033	0.077
	28.4	-0.0102	0.0158	0.568	-0.060	0.092
	14.1	-0.0088	0.0175	0.282	-0.051	0.102
	8.2	-0.0067	0.0194	0.164	0.040	0.113
45.2	56.9	0.0007	0.0161	1.138	0.004	0.094
	55.0	0.0199	0.0258	1.100	0.116	0.151
	52.7	0.0518	0.0393	1.054	0.303	0.230
	50.8	0.1265	0.0500	1.016	0.740	0.292
	48.8	0.1438	0.0458	0.976	0.841	0.268
	46.9	0.1792	0.0365	0.938	1.048	0.214
	42.6	0.1588	0.0405	0.852	0.928	0.237

x	y	$\bar{u}$	$\sqrt{\overline{u'^2}}$	$\frac{y}{h}$	$\frac{\bar{u}2b_o}{Q_o}$	$\frac{\sqrt{\overline{u'^2}}2b_o}{Q_o}$
mm	mm	m/s	m/s			
45.2	40.6	0.1065	0.0410	0.812	0.623	0.240
	38.6	0.0751	0.0380	0.772	0.439	0.222
	36.6	0.0560	0.0309	0.732	0.327	0.181
	34.6	0.0396	0.0228	0.692	0.231	0.133
	32.4	0.0304	0.0179	0.648	0.178	0.105
	29.8	0.0278	0.0189	0.596	0.163	0.110
	28.4	0.0223	0.0180	0.568	0.130	0.105
	22.4	0.0019	0.0238	0.448	0.011	0.139
	16.4	-0.0275	0.0232	0.328	-0.161	0.135
	12.3	-0.0386	0.0214	0.246	-0.226	0.125
	10.2	-0.0469	0.0218	0.204	-0.274	0.128
	8.2	-0.0532	0.0204	0.164	-0.311	0.120
	6.2	-0.0580	0.0195	0.124	-0.339	0.114
	4.2	-0.0556	0.0213	0.084	-0.325	0.125
64.8	59.0	-0.0037	0.0108	1.180	-0.021	0.063
	56.9	0.0021	0.0163	1.138	0.012	0.095
	54.9	0.0093	0.0215	1.098	0.055	0.126
	52.8	0.0259	0.0303	1.056	0.151	0.177
	50.8	0.0449	0.0353	1.016	0.262	0.206
	48.8	0.0561	0.0370	0.976	0.328	0.216
	46.8	0.0793	0.0400	0.936	0.464	0.234
	44.8	0.0978	0.0389	0.896	0.572	0.227
	42.6	0.1169	0.0372	0.852	0.684	0.218
	40.6	0.1254	0.0342	0.812	0.733	0.200
	38.6	0.1263	0.0317	0.772	0.738	0.185
	36.6	0.1232	0.0304	0.732	0.720	0.178
	34.6	0.1055	0.0281	0.692	0.617	0.164
	32.5	0.0941	0.0267	0.650	0.550	0.156
	30.4	0.0793	0.0253	0.608	0.464	0.148
	28.4	0.0640	0.0232	0.568	0.374	0.135
	26.4	0.0555	0.0216	0.528	0.324	0.126
	24.4	0.0437	0.0223	0.488	0.255	0.130
	22.4	0.0306	0.0183	0.448	0.179	0.107
	20.4	0.0208	0.0201	0.408	0.121	0.118
	16.4	-0.0073	0.0232	0.328	-0.043	0.136
	12.3	-0.0337	0.0257	0.246	-0.197	0.150
	10.2	-0.0424	0.0238	0.204	-0.248	0.139

x mm	y mm	$\overline{u}$ m/s	$\sqrt{\overline{u'^2}}$ m/s	$\frac{y}{h}$	$\frac{\overline{u} 2b_o}{\varrho_o}$	$\frac{\sqrt{\overline{u'^2}}\ 2b_o}{\varrho_o}$
64.8	8.3	-0.0543	0.0212	0.166	-0.317	0.124
	6.3	-0.0624	0.0200	0.126	-0.365	0.117
	4.2	-0.0729	0.0172	0.084	-0.426	0.100
86.2	54.9	-0.0043	0.0084	1.098	-0.025	0.049
	50.8	0.0035	0.0180	1.016	0.021	0.105
	46.8	0.0187	0.0271	0.936	0.109	0.159
	44.8	0.0308	0.0300	0.896	0.180	0.176
	40.6	0.0481	0.0342	0.812	0.281	0.200
	36.6	0.0665	0.0344	0.732	0.389	0.201
	32.5	0.0855	0.0306	0.650	0.500	0.179
	30.4	0.0899	0.0316	0.608	0.526	0.185
	28.4	0.0915	0.0300	0.568	0.535	0.176
	24.4	0.0866	0.0254	0.488	0.506	0.148
	22.4	0.0814	0.0240	0.448	0.476	0.141
	20.4	0.0689	0.0233	0.408	0.403	0.137
	16.4	0.0476	0.0236	0.328	0.279	0.138
	12.3	0.0213	0.0251	0.246	0.125	0.147
	10.2	0.0090	0.0225	0.204	0.053	0.131
	8.3	-0.0032	0.0237	0.166	-0.019	0.139
	6.2	-0.0129	0.0202	0.124	-0.076	0.118
	4.2	-0.0205	0.0202	0.084	-0.120	0.118
105.1	38.6	0.0221	0.0240	0.772	0.129	0.140
	34.5	0.0349	0.0282	0.690	0.204	0.165
	30.4	0.0511	0.0298	0.608	0.299	0.174
	26.4	0.0658	0.0300	0.528	0.385	0.176
	22.4	0.0755	0.0275	0.448	0.442	0.160
	18.4	0.0804	0.0238	0.368	0.470	0.139
	12.3	0.0696	0.0219	0.246	0.407	0.128
	6.2	0.0505	0.0206	0.124	0.295	0.120
	2.1	0.0418	0.0177	0.042	0.244	0.103

$h = 0.050$ m

$2b_o = 0.00712$ m

$Q_o = 0.00225 m^2/s$

$Ri_Q = 0$

x	y	$\bar{u}$	$\sqrt{\overline{u'^2}}$	$\frac{y}{h}$	$\frac{\bar{u} 2b_o}{Q_o}$	$\frac{\sqrt{\overline{u'^2}}\ 2b_o}{Q_o}$
mm	mm	m/s	m/s			
6.2	53.4	0.0341	0.0251	1.068	0.108	0.079
	51.3	0.3129	0.0291	1.026	0.990	0.092
	49.4	0.3398	0.0225	0.988	1.075	0.071
	49.4	0.3383	0.0222	0.988	1.070	0.070
	47.4	0.3216	0.0280	0.948	1.017	0.089
	45.4	0.0571	0.0359	0.908	0.181	0.114
26.6	54.9	0.0560	0.0412	1.098	0.177	0.130
	52.7	0.1509	0.0530	1.054	0.477	0.168
	50.7	0.2609	0.0529	1.014	0.825	0.168
	48.8	0.3107	0.0363	0.976	0.983	0.115
	46.8	0.2762	0.0518	0.936	0.874	0.164
	44.8	0.1615	0.0553	0.896	0.511	0.175
	42.6	0.0592	0.0407	0.852	0.187	0.129
	22.4	-0.0255	0.0368	0.448	-0.081	0.116
	14.2	-0.0352	0.0370	0.284	-0.111	0.117
	8.3	-0.0433	0.0386	0.166	-0.137	0.122
	2.1	-0.0076	0.0307	0.042	-0.024	0.097
49.8	52.7	0.0741	0.0529	1.054	0.234	0.167
	50.7	0.1197	0.0613	1.014	0.379	0.194
	48.8	0.1731	0.0626	0.976	0.547	0.198
	46.8	0.2152	0.0559	0.936	0.681	0.177
	44.8	0.2342	0.0503	0.896	0.741	0.159
	40.5	0.1847	0.0548	0.810	0.584	0.173
	38.6	0.1410	0.0507	0.772	0.446	0.160
	36.6	0.0996	0.0441	0.732	0.315	0.139

x	y	$\bar{u}$	$\sqrt{\overline{u'^2}}$	$\frac{y}{h}$	$\frac{\bar{u} 2b_o}{Q_o}$	$\frac{\sqrt{\overline{u'^2}}\ 2b_o}{Q_o}$
mm	mm	m/s	m/s			
49.8	32.5	0.0552	0.0304	0.650	0.175	0.096
	26.4	0.0306	0.0341	0.528	0.097	0.108
	20.4	-0.0064	0.0399	0.408	-0.020	0.126
	14.1	-0.0530	0.0405	0.282	-0.168	0.128
	10.2	-0.0769	0.0393	0.204	-0.243	0.124
	6.2	-0.0987	0.0326	0.124	-0.312	0.103
	4.2	-0.1091	0.0303	0.084	-0.345	0.096
	2.1	-0.1014	0.0319	0.042	-0.321	0.101
74.8	50.7	0.0245	0.0407	1.014	0.077	0.129
	46.8	0.0680	0.0551	0.936	0.215	0.174
	42.6	0.1142	0.0585	0.852	0.361	0.185
	38.6	0.1605	0.0539	0.772	0.508	0.171
	34.5	0.1760	0.0476	0.690	0.557	0.151
	30.4	0.1581	0.0432	0.608	0.500	0.137
	26.4	0.1214	0.0417	0.528	0.384	0.132
	22.4	0.0823	0.0397	0.448	0.260	0.126
	18.4	0.0391	0.0404	0.368	0.124	0.128
	12.2	-0.0304	0.0435	0.244	-0.096	0.138
	8.3	-0.0687	0.0402	0.166	-0.217	0.127
	4.2	-0.1007	0.0337	0.084	-0.319	0.107
	2.1	-0.1134	0.0294	0.042	-0.359	0.093
149.3	36.6	0.0103	0.0232	0.732	0.032	0.074
	30.4	0.0440	0.0308	0.608	0.139	0.097
	24.4	0.0813	0.0338	0.488	0.257	0.107
	20.4	0.1115	0.0324	0.408	0.353	0.103
	16.3	0.1370	0.0322	0.326	0.434	0.102
	12.1	0.1571	0.0287	0.242	0.497	0.091
	8.3	0.1688	0.0268	0.166	0.534	0.085
	4.2	0.1731	0.0261	0.084	0.548	0.083
	2.1	0.1662	0.0302	0.042	0.526	0.096

$h = 0.150$ m

$2b_o = 0.00712$ m

$Q_o = 0.001218$ m^2/s

$Ri_o = 0$

x	y	$\bar{u}$	$\sqrt{\overline{u'^2}}$	$\frac{y}{h}$	$\frac{\bar{u}2b_o}{Q_o}$	$\frac{\sqrt{\overline{u'^2}}\,2b_o}{Q_o}$
mm	mm	m/s	m/s			
6.6	153.5	0.0395	0.0113	1.023	0.231	0.066
	151.5	0.2014	0.0185	1.010	1.177	0.108
	149.4	0.2255	0.0128	0.996	1.318	0.075
	149.4	0.2260	0.0124	0.996	1.321	0.073
	147.4	0.1940	0.0200	0.984	1.134	0.117
	145.5	0.0099	0.0076	0.970	0.058	0.044
55.0	159.0	0.0162	0.0179	1.060	0.095	0.105
	157.0	0.0312	0.0205	1.047	0.182	0.120
	155.0	0.0656	0.0254	1.033	0.383	0.149
	153.0	0.1022	0.0274	1.020	0.598	0.160
	151.0	0.1379	0.0265	1.007	0.806	0.155
	148.8	0.1513	0.0280	0.992	0.885	0.164
	147.0	0.1571	0.0233	0.980	0.919	0.136
	144.9	0.1368	0.0264	0.966	0.800	0.154
	142.8	0.1038	0.0270	0.952	0.607	0.158
	140.8	0.0703	0.0229	0.939	0.411	0.134
	138.4	0.0416	0.0164	0.923	0.243	0.096
	136.6	0.0286	0.0144	0.911	0.167	0.084
	134.8	0.0221	0.0101	0.899	0.129	0.059
	132.6	0.0177	0.0087	0.884	0.103	0.051
	122.7	0.0176	0.0090	0.818	0.103	0.052
	112.5	0.0148	0.0088	0.750	0.087	0.051
	98.3	0.0126	0.0100	0.655	0.074	0.058
	82.0	0.0044	0.0117	0.547	0.026	0.069
	69.3	-0.0047	0.0120	0.462	-0.027	0.070
	50.8	-0.0170	0.0140	0.339	-0.100	0.082
	40.5	-0.0243	0.0129	0.270	-0.142	0.076

x	y	$\bar{u}$	$\sqrt{\overline{u'^2}}$	$\frac{y}{h}$	$\frac{\bar{u} 2b_o}{\varrho_o}$	$\frac{\sqrt{\overline{u'^2}}\ 2b_o}{\varrho_o}$
mm	mm	m/s	m/s			
55.0	30.5	-0.0246	0.0126	0.203	-0.144	0.074
	24.4	-0.0285	0.0152	0.163	-0.167	0.089
	18.4	-0.0233	0.0153	0.123	-0.136	0.089
	12.3	-0.0122	0.0149	0.082	-0.071	0.087
	8.2	-0.0129	0.0128	0.055	-0.075	0.075
	2.1	0.0017	0.0104	0.014	0.010	0.061
118.1	161.0	0.0025	0.0136	1.073	0.015	0.080
	157.0	0.0159	0.0214	1.047	0.093	0.125
	153.0	0.0305	0.0252	1.020	0.178	0.148
	148.8	0.0583	0.0288	0.992	0.341	0.168
	147.0	0.0622	0.0297	0.980	0.363	0.174
	144.9	0.0757	0.0288	0.966	0.443	0.169
	142.8	0.0857	0.0296	0.952	0.501	0.173
	140.8	0.0936	0.0263	0.939	0.547	0.154
	138.4	0.0966	0.0267	0.923	0.565	0.156
	136.5	0.1009	0.0229	0.910	0.590	0.134
	134.8	0.1030	0.0222	0.899	0.602	0.130
	132.6	0.1027	0.0210	0.884	0.600	0.123
	130.8	0.0953	0.0223	0.872	0.557	0.131
	128.6	0.0951	0.0215	0.857	0.556	0.126
	124.7	0.0753	0.0216	0.831	0.440	0.126
	120.6	0.0600	0.0180	0.804	0.351	0.105
	116.4	0.0446	0.0148	0.776	0.261	0.087
	112.5	0.0393	0.0123	0.750	0.230	0.072
	108.5	0.0331	0.0097	0.723	0.194	0.057
	102.3	0.0293	0.0089	0.682	0.171	0.052
	94.2	0.0275	0.0083	0.628	0.161	0.048
	84.0	0.0195	0.0082	0.560	0.114	0.048
	67.4	0.0092	0.0097	0.449	0.054	0.057
	57.0	-0.0067	0.0121	0.380	-0.039	0.071
	47.0	-0.0200	0.0134	0.313	-0.117	0.078
	38.7	-0.0304	0.0128	0.258	-0.178	0.075
	30.5	-0.0381	0.0154	0.203	-0.223	0.090
	24.5	-0.0470	0.0155	0.163	-0.275	0.091
	18.4	-0.0501	0.0131	0.123	-0.293	0.077

x	y	$\overline{u}$	$\sqrt{\overline{u'^2}}$	$\frac{y}{h}$	$\frac{\overline{u} 2b_o}{Q_o}$	$\frac{\sqrt{\overline{u'^2}}\ 2b_o}{Q_o}$
mm	mm	m/s	m/s			
118.1	14.2	-0.0536	0.0133	0.095	-0.313	0.078
	10.3	-0.0565	0.0129	0.069	-0.331	0.076
	6.3	-0.0605	0.0110	0.042	-0.354	0.064
	4.2	-0.0566	0.0118	0.028	-0.331	0.069
	2.1	-0.0387	0.0120	0.014	-0.226	0.070
179.0	142.7	0.0089	0.0191	0.951	0.052	0.112
	138.4	0.0143	0.0212	0.923	0.084	0.124
	132.6	0.0302	0.0242	0.884	0.177	0.142
	126.6	0.0422	0.0287	0.844	0.247	0.168
	122.7	0.0483	0.0278	0.818	0.283	0.162
	118.5	0.0563	0.0289	0.790	0.329	0.169
	114.5	0.0626	0.0278	0.763	0.366	0.163
	110.6	0.0666	0.0262	0.737	0.389	0.153
	106.4	0.0725	0.0232	0.709	0.424	0.136
	102.2	0.0690	0.0215	0.681	0.404	0.125
	98.3	0.0661	0.0204	0.655	0.386	0.119
	94.2	0.0654	0.0184	0.628	0.383	0.107
	87.9	0.0542	0.0173	0.586	0.317	0.101
	82.0	0.0431	0.0158	0.547	0.252	0.092
	75.6	0.0350	0.0138	0.504	0.205	0.080
	65.2	0.0224	0.0115	0.435	0.131	0.068
	55.1	0.0105	0.0117	0.367	0.062	0.069
	44.9	-0.0033	0.0107	0.299	-0.019	0.062
	34.8	-0.0176	0.0150	0.232	-0.103	0.088
	28.5	-0.0232	0.0126	0.190	-0.135	0.074
	24.5	-0.0312	0.0142	0.163	-0.183	0.083
	20.4	-0.0364	0.0135	0.136	-0.213	0.079
	16.4	-0.0407	0.0128	0.109	-0.238	0.075
	12.3	-0.0449	0.0123	0.082	-0.262	0.072
	8.3	-0.0486	0.0109	0.055	-0.284	0.064
	4.2	-0.0522	0.0113	0.028	-0.305	0.066
	2.1	-0.0488	0.0127	0.014	-0.286	0.074

x	y	$\bar{u}$	$\sqrt{\overline{u'^2}}$	$\frac{y}{h}$	$\frac{\bar{u} 2b_o}{Q_o}$	$\frac{\sqrt{\overline{u'^2}}\ 2b_o}{Q_o}$
mm	mm	m/s	m/s			
263.9	85.7	0.0147	0.0159	0.571	0.086	0.093
	77.5	0.0169	0.0182	0.517	0.099	0.107
	71.3	0.0187	0.0151	0.475	0.109	0.088
	65.1	0.0246	0.0167	0.434	0.144	0.098
	59.0	0.0311	0.0161	0.393	0.182	0.094
	52.8	0.0329	0.0163	0.352	0.193	0.096
	46.9	0.0349	0.0153	0.313	0.204	0.089
	40.6	0.0360	0.0156	0.271	0.211	0.091
	34.6	0.0396	0.0131	0.231	0.232	0.077
	28.4	0.0397	0.0118	0.189	0.232	0.069
	22.4	0.0382	0.0114	0.149	0.223	0.066
	16.4	0.0356	0.0111	0.109	0.208	0.065
	12.3	0.0356	0.0100	0.082	0.208	0.058
	8.3	0.0366	0.0101	0.055	0.214	0.059
	4.2	0.0355	0.0105	0.028	0.207	0.061
	2.1	0.0291	0.0113	0.014	0.170	0.066

h = 0.150 m

$2b_o$ = 0.00712 m

Q_o = 0.002953 m^2/s

Ri_o = 0

x	y	$\bar{u}$	$\sqrt{\overline{u'^2}}$	$\frac{y}{h}$	$\frac{\bar{u}2b_o}{Q_o}$	$\frac{\sqrt{\overline{u'^2}}\,2b_o}{Q_o}$
mm	mm	m/s	m/s			
6.6	153.0	0.2224	0.0549	1.020	0.536	0.132
	151.4	0.4082	0.0304	1.009	0.984	0.073
	149.4	0.4259	0.0268	0.996	1.027	0.065
	149.4	0.4253	0.0276	0.996	1.025	0.067
	147.5	0.3901	0.0366	0.983	0.941	0.088
	145.4	0.0250	0.0292	0.969	0.060	0.070
87.5	161.0	0.0417	0.0477	1.073	0.101	0.115
	159.0	0.0721	0.0556	1.060	0.174	0.134
	157.0	0.1106	0.0661	1.047	0.267	0.159
	154.9	0.1500	0.0715	1.033	0.362	0.172
	153.0	0.2154	0.0679	1.020	0.519	0.164
	151.0	0.2424	0.0639	1.007	0.584	0.154
	148.8	0.2731	0.0545	0.992	0.658	0.131
	147.0	0.2809	0.0525	0.980	0.677	0.127
	144.9	0.2581	0.0579	0.966	0.622	0.140
	142.8	0.2312	0.0638	0.952	0.557	0.154
	140.8	0.1982	0.0584	0.939	0.478	0.141
	138.4	0.1456	0.0534	0.923	0.351	0.129
	136.6	0.1232	0.0462	0.911	0.297	0.111
	134.8	0.0953	0.0372	0.899	0.230	0.090
	130.8	0.0717	0.0250	0.872	0.173	0.060
	126.6	0.0640	0.0333	0.844	0.154	0.080
	116.4	0.0571	0.0259	0.776	0.138	0.062
	98.4	0.0493	0.0264	0.656	0.119	0.064
	84.0	0.0288	0.0284	0.560	0.069	0.069
	69.4	-0.0004	0.0287	0.463	-0.001	0.069
	55.0	-0.0288	0.0325	0.367	-0.069	0.078
	44.8	-0.0571	0.0352	0.299	-0.138	0.085
	34.6	-0.0748	0.0361	0.231	-0.180	0.087

x mm	y mm	$\bar{u}$ m/s	$\sqrt{\overline{u'^2}}$ m/s	$\frac{y}{h}$	$\frac{\bar{u} 2b_o}{Q_2}$	$\frac{\sqrt{\overline{u'^2}}\ 2b_o}{Q_o}$
87.5	24.4	-0.0882	0.0331	0.163	-0.213	0.080
	14.2	-0.1049	0.0318	0.095	-0.253	0.077
	8.2	-0.1071	0.0283	0.055	-0.258	0.068
	2.1	-0.0642	0.0305	0.014	-0.155	0.074
137.4	159.6	0.0175	0.0374	1.064	0.042	0.090
	153.6	0.0523	0.0554	1.024	0.126	0.134
	149.5	0.0975	0.0640	0.997	0.235	0.154
	145.5	0.1119	0.0645	0.970	0.270	0.156
	141.4	0.1397	0.0663	0.943	0.337	0.160
	137.2	0.1719	0.0622	0.915	0.414	0.150
	133.2	0.1931	0.0557	0.888	0.465	0.134
	129.1	0.1992	0.0486	0.861	0.480	0.117
	125.2	0.1917	0.0432	0.835	0.462	0.104
	121.2	0.1723	0.0469	0.808	0.415	0.113
	117.0	0.1468	0.0427	0.780	0.354	0.103
	113.1	0.1240	0.0406	0.754	0.299	0.098
	109.1	0.1023	0.0330	0.727	0.247	0.079
	102.8	0.0743	0.0266	0.685	0.179	0.064
	96.9	0.0648	0.0284	0.646	0.156	0.069
	90.6	0.0557	0.0227	0.604	0.134	0.055
	80.5	0.0442	0.0228	0.537	0.107	0.055
	70.0	0.0288	0.0221	0.467	0.069	0.053
	59.7	0.0085	0.0224	0.398	0.020	0.054
	51.4	-0.0092	0.0240	0.343	-0.022	0.058
	43.3	-0.0312	0.0296	0.289	-0.075	0.071
	35.2	-0.0551	0.0342	0.235	-0.133	0.082
	29.1	-0.0744	0.0349	0.194	-0.179	0.084
	23.0	-0.0905	0.0336	0.153	-0.218	0.081
	17.0	-0.1091	0.0328	0.113	-0.263	0.079
	12.9	-0.1152	0.0287	0.086	-0.278	0.069
	8.8	-0.1230	0.0303	0.059	-0.297	0.073
	4.8	-0.1293	0.0280	0.032	-0.312	0.067
	2.7	-0.1254	0.0273	0.018	-0.302	0.066
	0.6	-0.0853	0.0305	0.004	-0.206	0.074

x	y	$\bar{u}$	$\sqrt{\overline{u'^2}}$	$\frac{y}{h}$	$\frac{\bar{u}2b_o}{Q_o}$	$\frac{\sqrt{\overline{u'^2}}\,2b_o}{Q_o}$
mm	mm	m/s	m/s			
196.8	142.8	0.0145	0.0476	0.952	0.035	0.115
	136.6	0.0299	0.0537	0.911	0.072	0.130
	130.8	0.0448	0.0555	0.872	0.108	0.134
	124.8	0.0557	0.0574	0.832	0.134	0.138
	118.6	0.0805	0.0620	0.791	0.194	0.150
	112.6	0.0912	0.0661	0.751	0.220	0.160
	108.6	0.1046	0.0610	0.724	0.252	0.147
	104.5	0.1137	0.0585	0.697	0.274	0.141
	100.3	0.1142	0.0581	0.669	0.275	0.140
	96.3	0.1168	0.0551	0.642	0.281	0.133
	92.3	0.1255	0.0475	0.615	0.303	0.115
	88.0	0.1221	0.0494	0.587	0.294	0.119
	84.0	0.1149	0.0448	0.560	0.277	0.108
	79.9	0.1109	0.0423	0.533	0.267	0.102
	75.6	0.0965	0.0399	0.504	0.233	0.096
	69.4	0.0827	0.0422	0.463	0.199	0.102
	63.1	0.0639	0.0382	0.421	0.154	0.092
	57.0	0.0501	0.0355	0.380	0.121	0.086
	50.8	0.0339	0.0331	0.339	0.082	0.080
	42.7	0.0114	0.0319	0.285	0.027	0.077
	36.7	-0.0059	0.0345	0.245	-0.014	0.083
	30.5	-0.0222	0.0329	0.203	-0.054	0.079
	24.5	-0.0387	0.0349	0.163	-0.093	0.084
	20.4	-0.0532	0.0342	0.136	-0.128	0.082
	16.4	-0.0581	0.0317	0.109	-0.140	0.076
	12.3	-0.0620	0.0338	0.082	-0.149	0.081
	8.3	-0.0751	0.0311	0.055	-0.181	0.075
	6.3	-0.0715	0.0320	0.042	-0.172	0.077
	4.2	-0.0735	0.0341	0.028	-0.177	0.082
	2.1	-0.0776	0.0344	0.014	-0.187	0.083
260.0	81.8	0.0465	0.0571	0.545	0.112	0.138
	73.4	0.0703	0.0563	0.489	0.169	0.136
	65.1	0.0816	0.0529	0.434	0.197	0.128
	57.0	0.0958	0.0535	0.380	0.231	0.129

x	y	$\overline{u}$	$\sqrt{\overline{u'^2}}$	$\frac{y}{h}$	$\frac{\overline{u} 2b_o}{Q_o}$	$\frac{\sqrt{\overline{u'^2}}\ 2b_o}{Q_o}$
mm	mm	m/s	m/s			
260.0	48.9	0.1046	0.0468	0.326	0.252	0.113
	42.6	0.1065	0.0434	0.284	0.257	0.105
	36.7	0.1060	0.0423	0.245	0.255	0.102
	30.5	0.1063	0.0363	0.203	0.256	0.088
	24.4	0.1022	0.0336	0.163	0.246	0.081
	18.4	0.0997	0.0300	0.123	0.240	0.072
	14.1	0.0892	0.0290	0.094	0.215	0.070
	10.2	0.0789	0.0312	0.068	0.190	0.075
	8.2	0.0772	0.0313	0.055	0.186	0.075
	4.2	0.0748	0.0307	0.028	0.180	0.074
	2.1	0.0748	0.0328	0.014	0.180	0.079

$h = 0.050$ m

$2b_o = 0.00690$ m

$Q_o = 0.003009$ m^2/s

$Ri_o = 0.00101$

x	$T_o - T_a$	y	$\bar{u}$	$\sqrt{\overline{u'^2}}$	$\frac{y}{h}$	$\frac{\bar{u} 2b_o}{Q_o}$	$\frac{\sqrt{\overline{u'^2}}\ 2b_o}{Q_o}$
mm	°C	mm	m/s	m/s			
6.7	22.06	53.3	0.2277		1.066	0.522	
	21.79	52.1	0.3400		1.042	0.779	
	21.98	51.2	0.4274		1.024	0.980	
	21.88	49.3	0.4359		0.986	0.999	
	22.29	48.1	0.3778		0.962	0.866	
	21.83	47.3	0.2382		0.946	0.546	
	21.84	46.4	0.0566		0.928	0.130	
31.9	22.00	55.4	0.0508		1.108	0.116	
	22.07	53.3	0.1571		1.066	0.359	
	22.01	51.3	0.3654	0.1317	1.026	0.834	0.301
	21.97	49.4	0.4427	0.0989	0.988	1.010	0.226
	22.04	47.3	0.4248	0.0871	0.946	0.970	0.199
	22.01	45.3	0.2877	0.0837	0.906	0.657	0.191
	22.30	43.1	0.1416	0.0729	0.862	0.323	0.167
	21.84	41.1	0.0866	0.0512	0.822	0.199	0.117
	22.24	41.0	0.0755	0.0605	0.820	0.172	0.138
	21.99	39.2	0.0380	0.0440	0.784	0.087	0.101
	22.02	37.2	0.0340	0.0444	0.744	0.078	0.102
	22.12	35.1	0.0271	0.0334	0.702	0.062	0.077
	21.98	33.0	0.0239	0.0357	0.660	0.055	0.082
	21.89	30.3	0.0217	0.0376	0.606	0.050	0.086
	21.76	26.9	0.0094	0.0446	0.538	0.022	0.102
	21.86	23.0	-0.0060	0.0503	0.460	-0.014	0.115
	21.94	18.8	-0.0206	0.0468	0.376	-0.047	0.107
	21.67	16.8	-0.0311	0.0480	0.336	-0.071	0.110
	21.76	14.7	-0.0386	0.0477	0.294	-0.088	0.109
	21.81	12.8	-0.0486	0.0481	0.256	-0.111	0.110
		10.8	-0.0562	0.0499	0.216	-0.129	0.115
		8.8	-0.0623	0.0543	0.176	-0.143	0.124

x mm	$T_o - T_a$ °C	y mm	$\bar{u}$ m/s	$\sqrt{\overline{u'^2}}$ m/s	$\frac{y}{h}$	$\frac{\bar{u} 2b_o}{Q_o}$	$\frac{\sqrt{\overline{u'^2}}\ 2b_o}{Q_o}$
31.9	21.62	6.8	-0.0681	0.0482	0.136	-0.156	0.111
	21.54	4.8	-0.0695	0.0487	0.096	-0.159	0.112
	21.74	2.7	-0.0659	0.0591	0.054	-0.151	0.136
	21.82	0.6	-0.0256	0.0653	0.012	-0.059	0.150
57.4	21.58	55.4	0.0153	0.0659	1.108	0.035	0.151
	21.43	53.3	0.0716	0.0789	1.066	0.164	0.181
	21.80	51.3	0.1480	0.1007	1.026	0.339	0.231
	21.71	49.4	0.1796	0.0994	0.988	0.412	0.228
	21.85	47.4	0.2932	0.1066	0.948	0.672	0.244
	21.80	45.4	0.3052	0.0795	0.908	0.700	0.182
	22.08	43.1	0.3176	0.0711	0.862	0.728	0.163
	22.00	41.1	0.2976	0.0665	0.822	0.682	0.153
	22.08	39.1	0.2386	0.0750	0.782	0.547	0.172
	22.03	37.2	0.1914	0.0701	0.744	0.439	0.161
	21.96	35.0	0.1241	0.0646	0.700	0.284	0.148
	21.92	33.0	0.0843	0.0567	0.660	0.193	0.130
	21.90	29.0	0.0527	0.0425	0.580	0.121	0.098
	21.84	25.0	0.0238	0.0443	0.500	0.055	0.102
	21.77	21.0	0.0046	0.0472	0.420	0.011	0.108
	21.74	16.9	-0.0178	0.0459	0.338	-0.041	0.105
	21.90	12.8	-0.0531	0.0552	0.256	-0.122	0.127
	21.87	8.8	-0.1000	0.0449	0.176	-0.229	0.103
	21.87	6.8	-0.1077	0.0478	0.136	-0.247	0.110
	21.79	4.8	-0.1265	0.0507	0.096	-0.290	0.116
	21.94	2.7	-0.1451	0.0520	0.054	-0.333	0.119
	21.83	0.6	-0.1089	0.0611	0.012	-0.250	0.140
82.4	21.98	55.4	-0.0029	0.0428	1.108	-0.007	0.098
	21.89	51.3	0.0299	0.0626	1.026	0.069	0.144
	22.29	47.4	0.0693	0.0734	0.948	0.159	0.168
	22.14	43.1	0.1186	0.0797	0.862	0.272	0.183
	21.99	39.1	0.1715	0.0817	0.782	0.393	0.187
	21.84	37.2	0.1864	0.0913	0.744	0.427	0.209
	21.97	35.0	0.2228	0.0685	0.700	0.511	0.157

x	$T_o - T_a$	y	$\bar{u}$	$\sqrt{\overline{u'^2}}$	$\frac{y}{h}$	$\frac{\bar{u} 2b_o}{Q_o}$	$\frac{\sqrt{\overline{u'^2}}\ 2b_o}{Q_o}$
mm	°C	mm	m/s	m/s			
82.4	21.96	33.0	0.2253	0.0740	0.660	0.517	0.170
	21.97	31.0	0.2250	0.0610	0.620	0.516	0.140
	21.87	29.0	0.2042	0.0596	0.580	0.468	0.137
	22.28	21.0	0.0954	0.0572	0.420	0.219	0.131
	22.17	17.0	0.0465	0.0658	0.340	0.107	0.151
	22.18	12.8	0.0006	0.0776	0.256	0.001	0.178
	22.05	8.8	-0.0630	0.0547	0.176	-0.144	0.125
	22.89	4.7	-0.1064	0.0470	0.094	-0.244	0.108
	22.94	2.7	-0.1233	0.0657	0.054	-0.283	0.151
	22.05	0.6	-0.1269	0.0520	0.012	-0.290	0.119
107.5	22.27	41.1	0.0316	0.0506	0.822	0.073	0.116
	22.23	37.1	0.0533	0.0604	0.742	0.122	0.139
	22.01	33.1	0.0894	0.0638	0.660	0.205	0.146
	21.95	31.0	0.1039	0.0685	0.620	0.238	0.157
	22.06	27.0	0.1332	0.0746	0.540	0.306	0.171
	22.15	25.0	0.1473	0.0698	0.500	0.338	0.160
	22.01	23.0	0.1468	0.0689	0.460	0.337	0.158
	22.05	21.0	0.1545	0.0600	0.420	0.354	0.138
	22.13	16.9	0.1601	0.0602	0.338	0.367	0.138
	22.04	12.8	0.1417	0.0543	0.256	0.325	0.125
	22.11	8.8	0.1079	0.0609	0.176	0.247	0.140
	22.20	6.8	0.0879	0.0677	0.136	0.202	0.155
	22.27	4.7	0.0784	0.0620	0.094	0.179	0.142
	22.28	2.6	0.0628	0.0565	0.052	0.143	0.129
	22.24	0.6	0.0379	0.0550	0.012	0.087	0.126
132.9	21.86	45.4	0.0015	0.0485	0.908	0.003	0.111
	21.86	41.1	0.0141	0.0521	0.822	0.032	0.119
	21.97	37.1	0.0301	0.0605	0.742	0.069	0.139
	21.86	33.0	0.0506	0.0614	0.660	0.116	0.141
	21.77	28.9	0.0704	0.0664	0.578	0.161	0.152
	21.93	25.0	0.1009	0.0639	0.500	0.231	0.147
	21.89	21.0	0.1280	0.0647	0.420	0.293	0.148
	21.86	16.8	0.1556	0.0570	0.336	0.357	0.131

x	T_o-T_a	y	$\bar{u}$	$\sqrt{\overline{u'^2}}$	$\frac{y}{h}$	$\frac{\bar{u}2b_o}{Q_o}$	$\frac{\sqrt{\overline{u'^2}}\ 2b_o}{Q_o}$
mm	°C	mm	m/s	m/s			
132.9	22.00	12.8	0.1785	0.0500	0.256	0.409	0.115
	22.05	8.8	0.1867	0.0495	0.176	0.428	0.114
	22.31	4.7	0.1829	0.0491	0.094	0.419	0.113
	22.07	2.7	0.1838	0.0533	0.054	0.421	0.122
	22.08	0.6	0.1189		0.012	0.273	

h = 0.150 m

$2b_o$ = 0.00690 m

Q_o = 0.003009 m^2/s

Ri_o = 0.00108

x	T_o-T_a	y	$\bar{u}$	$\sqrt{\overline{u'^2}}$	$\frac{y}{h}$	$\frac{\bar{u}2b_o}{Q_o}$	$\frac{\sqrt{\overline{u'^2}}\,2b_o}{Q_o}$
mm	°C	mm	m/s	m/s			
32.4	22.61	156.8	0.0685		1.045	0.157	
	22.69	154.8	0.1633		1.032	0.374	
	22.38	152.2	0.4035	0.1036	1.015	0.925	0.238
	22.40	150.6	0.4496	0.0790	1.004	1.031	0.181
	22.24	148.8	0.4130	0.0973	0.992	0.947	0.223
	22.33	147.0	0.2455	0.0775	0.980	0.563	0.178
	22.68	145.0	0.1401	0.0628	0.967	0.320	0.143
	22.75	143.0	0.0634	0.0471	0.953	0.145	0.108
	22.37	140.9	0.0370	0.0362	0.939	0.085	0.083
	22.56	136.8	0.0311	0.0230	0.912	0.071	0.053
	22.55	132.9	0.0313	0.0195	0.886	0.072	0.045
	22.69	128.5	0.0293	0.0195	0.857	0.067	0.045
	22.55	124.4	0.0267	0.0214	0.829	0.061	0.049
	22.56	118.5	0.0230	0.0207	0.790	0.053	0.048
	22.78	111.6	0.0199	0.0225	0.744	0.046	0.052
	22.48	103.5	0.0146	0.0245	0.690	0.034	0.056
	22.48	93.7	0.0089	0.0271	0.625	0.020	0.062
	22.49	83.4	0.0049	0.0290	0.556	0.011	0.066
	22.66	73.1	-0.0029	0.0314	0.487	-0.007	0.072
	22.63	62.9	-0.0151	0.0283	0.419	-0.034	0.065
	22.62	52.9	-0.0248	0.0333	0.353	-0.057	0.076
	22.31	42.8	-0.0324	0.0364	0.285	-0.074	0.083
	22.55	34.6	-0.0411	0.0349	0.231	-0.094	0.080
	22.02	24.4	-0.0408	0.0329	0.163	-0.094	0.076
	22.23	14.3	-0.0230	0.0347	0.095	-0.053	0.080
	22.51	8.2	-0.0132	0.0314	0.055	-0.030	0.072
	22.63	2.1	-0.0025	0.0268	0.014	-0.006	0.061

x	T_o-T_a	y	$\bar{u}$	$\sqrt{\overline{u'^2}}$	$\frac{y}{h}$	$\frac{\bar{u}2b_o}{\nu_o}$	$\frac{\sqrt{\overline{u'^2}}\,2b_o}{\nu_o}$
mm	°C	mm	m/s	m/s			
70.8	22.50	160.5	0.0714	0.0764	1.070	0.164	0.175
	22.33	158.8	0.1238	0.0779	1.059	0.284	0.179
	22.55	157.0	0.1633	0.0784	1.047	0.374	0.180
	22.53	154.8	0.2307	0.0685	1.032	0.529	0.157
	22.65	152.8	0.2691	0.0685	1.019	0.617	0.157
	22.74	150.8	0.3164	0.0732	1.005	0.725	0.168
		148.8	0.3051	0.0607	0.992	0.696	0.139
		147.0	0.2945	0.0757	0.980	0.672	0.173
		145.0	0.2305	0.0689	0.967	0.526	0.157
		143.0	0.1786	0.0669	0.953	0.408	0.153
		140.8	0.1353	0.0665	0.939	0.309	0.152
		138.6	0.0912	0.0602	0.924	0.208	0.138
		136.8	0.0773	0.0422	0.912	0.176	0.096
		134.8	0.0665	0.0283	0.899	0.152	0.065
	22.41	132.8	0.0642	0.0232	0.885	0.147	0.053
	22.71	128.5	0.0666	0.0301	0.857	0.153	0.069
	22.45	124.5	0.0602	0.0222	0.830	0.138	0.051
	22.74	118.6	0.0550	0.0220	0.791	0.126	0.050
	22.55	112.3	0.0541	0.0236	0.749	0.124	0.054
	22.80	104.2	0.0508	0.0247	0.695	0.116	0.057
	22.72	93.8	0.0359	0.0294	0.625	0.082	0.067
	22.79	83.6	0.0217	0.0291	0.557	0.050	0.067
	22.34	73.1	0.0098	0.0331	0.487	0.022	0.076
	22.45	63.0	-0.0078	0.0354	0.420	-0.018	0.081
	22.35	53.0	-0.0311	0.0379	0.353	-0.071	0.087
	22.43	42.8	-0.0472	0.0365	0.285	-0.108	0.083
	22.59	32.6	-0.0529	0.0331	0.217	-0.121	0.076
	22.80	22.5	-0.0769	0.0314	0.150	-0.176	0.072
	22.56	16.4	-0.0861	0.0287	0.109	-0.197	0.066
	22.64	10.4	-0.0805	0.0355	0.069	-0.184	0.081
	22.63	4.4	-0.0650	0.0337	0.029	-0.148	0.077
	22.71	2.3	-0.0462	0.0294	0.015	-0.106	0.067

x	T_o-T_a	y	$\bar{u}$	$\sqrt{u'^2}$	$\frac{y}{h}$	$\frac{\bar{u}2b_o}{\nu_o}$	$\frac{\sqrt{u'^2}\,2b_o}{\nu_o}$
mm	°C	mm	m/s	m/s			
111.2	22.43	163.0	0.0559	0.6165	1.087	0.128	0.141
	22.47	160.6	0.0793	0.0659	1.071	0.182	0.151
	22.43	158.8	0.1044	0.0642	1.059	0.239	0.147
	22.33	157.0	0.1157	0.0643	1.047	0.265	0.148
	22.45	154.8	0.1611	0.6957	1.032	0.369	0.160
	22.55	152.8	0.1908	0.7526	1.019	0.438	0.173
	22.50	150.8	0.2127	0.0632	1.005	0.488	0.145
	22.38	148.8	0.2275	0.0593	0.992	0.522	0.136
	22.47	147.0	0.2432	0.0580	0.980	0.558	0.133
	22.37	145.0	0.2501	0.0543	0.967	0.573	0.125
	22.42	143.0	0.2403	0.0538	0.953	0.548	0.123
	22.36	140.9	0.2207	0.0606	0.939	0.507	0.138
	22.47	138.7	0.2053	0.0650	0.925	0.469	0.149
	22.48	136.8	0.1831	0.0576	0.912	0.418	0.132
	22.76	132.8	0.1314	0.0475	0.885	0.300	0.109
	22.72	128.6	0.0992	0.0433	0.857	0.226	0.099
	22.65	124.5	0.0844	0.0355	0.830	0.193	0.081
	22.60	118.6	0.0717	0.0244	0.791	0.164	0.056
	22.65	112.2	0.0718	0.0238	0.748	0.164	0.054
	22.66	102.2	0.0626	0.0233	0.681	0.143	0.053
	22.45	91.9	0.0545	0.0245	0.613	0.125	0.056
	22.55	83.6	0.0436	0.0236	0.557	0.100	0.054
	22.33	73.2	0.0235	0.0318	0.488	0.054	0.073
	22.28	63.0	0.0047	0.0264	0.420	0.011	0.061
	22.56	53.0	-0.0196	0.0315	0.353	-0.045	0.072
	22.43	44.8	-0.0402	0.0373	0.299	-0.092	0.086
	22.29	34.6	-0.0910	0.0345	0.231	-0.209	0.079
	22.38	18.6	-0.0978	0.0332	0.124	-0.224	0.076
	22.52	12.3	-0.1085	0.0299	0.082	-0.249	0.069
	22.53	8.4	-0.1155	0.0288	0.056	-0.265	0.066
	22.52	4.4	-0.1124	0.0307	0.029	-0.257	0.070
	22.65	2.3	-0.1081	0.0321	0.015	-0.247	0.073

x	T_o-T_a	y	$\bar{u}$	$\sqrt{\overline{u'^2}}$	$\frac{y}{h}$	$\frac{\bar{u}2b_o}{Q_o}$	$\frac{\sqrt{\overline{u'^2}}\,2b_o}{Q_o}$
mm	°C	mm	m/s	m/s			
151.2	22.25	160.6	0.0485	0.0677	1.071	0.111	0.155
	22.24	155.0	0.0709	0.0661	1.033	0.163	0.152
	22.28	151.0	0.1072	0.0749	1.007	0.246	0.172
	22.26	147.1	0.1319	0.0786	0.981	0.302	0.180
	22.42	143.1	0.1656	0.0655	0.954	0.399	0.150
	22.40	138.8	0.1817	0.0633	0.925	0.417	0.145
	22.40	134.9	0.1950	0.0527	0.899	0.447	0.121
	22.39	130.8	0.1945	0.0480	0.872	0.446	0.110
	22.44	126.8	0.1767	0.0485	0.845	0.405	0.111
	22.47	122.6	0.1508	0.0437	0.817	0.346	0.100
	22.28	118.7	0.1335	0.0549	0.791	0.306	0.126
	22.26	112.4	0.1041	0.0494	0.749	0.239	0.113
	22.35	104.2	0.0757	0.0289	0.695	0.174	0.066
	22.32	96.0	0.0597	0.0360	0.640	0.137	0.083
	22.47	85.5	0.0501	0.0254	0.570	0.115	0.058
	22.57	75.3	0.0345	0.0287	0.502	0.079	0.066
	22.43	65.2	0.0131	0.0321	0.435	0.030	0.074
	22.43	55.1	-0.0098	0.0324	0.367	-0.022	0.074
	22.65	44.8	-0.0357	0.0361	0.299	-0.082	0.083
	22.63	36.6	-0.0633	0.0340	0.244	-0.145	0.078
	22.57	26.6	-0.0907	0.0341	0.177	-0.207	0.078
	22.64	16.5	-0.1122	0.0314	0.110	-0.256	0.072
	22.77	12.2	-0.1211	0.0325	0.081	-0.276	0.074
	22.73	8.4	-0.1291	0.0306	0.056	-0.295	0.070
	22.65	4.4	-0.1330	0.0301	0.029	-0.303	0.069
	22.59	2.3	-0.1292	0.0344	0.015	-0.295	0.078
199.8	22.27	154.8	0.0295	0.0630	1.032	0.068	0.145
	22.18	147.0	0.0454	0.0540	0.980	0.104	0.124
	22.52	138.6	0.0694	0.0716	0.924	0.159	0.164
	22.51	132.8	0.0872	0.0753	0.885	0.200	0.173
	22.52	126.7	0.1114	0.0729	0.845	0.255	0.167
	22.50	120.5	0.1270	0.0739	0.803	0.291	0.170
	22.61	114.4	0.1401	0.0664	0.763	0.321	0.152
	22.47	108.2	0.1476	0.0637	0.721	0.338	0.146
	22.59	102.0	0.1418	0.0583	0.680	0.324	0.133
	22.56	95.8	0.1264	0.0509	0.639	0.289	0.116

x	$T_o - T_a$	y	$\bar{u}$	$\sqrt{\overline{u'^2}}$	$\frac{y}{h}$	$\frac{\bar{u} 2b_o}{\nu_o}$	$\frac{\sqrt{\overline{u'^2}}\ 2b_o}{\nu_o}$
mm	°C	mm	m/s	m/s			
199.8	22.75	89.6	0.1078	0.0475	0.597	0.246	0.109
	22.66	83.5	0.0869	0.0461	0.557	0.198	0.105
	22.67	73.1	0.0603	0.0342	0.487	0.138	0.078
	22.61	63.0	0.0384	0.0279	0.420	0.088	0.064
	22.67	52.9	0.0172	0.0475	0.353	0.039	0.108
	22.60	44.8	-0.0114	0.0334	0.299	-0.026	0.076
	22.54	34.6	-0.0382	0.0341	0.231	-0.087	0.078
	22.95	24.5	-0.0730	0.0363	0.163	-0.167	0.083
	22.88	14.4	-0.0945	0.0343	0.096	-0.216	0.078
	22.21	10.4	-0.0951	0.0292	0.069	-0.218	0.067
	22.49	6.2	-0.1027	0.0255	0.041	-0.236	0.059
	22.42	4.4	-0.1064	0.0285	0.029	-0.244	0.065
	22.49	2.2	-0.1068	0.0377	0.015	-0.250	0.086
240.0	22.68	118.5	0.0502		0.790	0.115	
	22.59	110.2	0.0810		0.735	0.186	
	22.70	104.1	0.0819		0.694	0.187	
	22.63	97.8	0.0925		0.652	0.211	
	22.81	91.7	0.1032		0.611	0.236	
	22.78	85.4	0.1002		0.569	0.229	
	22.75	79.3	0.1023		0.529	0.234	
	22.70	73.1	0.0982		0.487	0.224	
	22.92	65.1	0.0876		0.434	0.200	
	22.82	57.0	0.0687		0.380	0.157	
	22.67	46.9	0.0587		0.313	0.134	
	22.66	38.8	0.0450		0.259	0.103	
	22.62	30.6	0.0192		0.204	0.044	
	22.51	22.5	0.0093		0.150	0.021	
	22.62	14.4	-0.0231		0.096	-0.053	
	22.54	8.4	-0.0239		0.056	-0.055	
	22.69	4.4	-0.0349		0.029	-0.080	
	22.66	2.3	-0.0219		0.015	-0.050	

x	T_o-T_a	y	$\bar{u}$	$\sqrt{\overline{u'^2}}$	$\frac{y}{h}$	$\frac{\bar{u}2b_o}{\nu_o}$	$\frac{\sqrt{\overline{u'^2}}\,2b_o}{\nu_o}$
mm	°C	mm	m/s	m/s			
274.8	22.38	118.4	0.0193	0.0460	0.789	0.044	0.105
	22.33	112.2	0.0266	0.0530	0.748	0.061	0.121
	22.43	108.1	0.0317		0.721	0.073	
	22.47	104.1	0.0465	0.0544	0.694	0.106	0.124
	22.38	95.8	0.0526	0.0599	0.639	0.120	0.137
	22.26	87.6	0.0578	0.0520	0.584	0.133	0.119
	22.41	83.5	0.0648		0.557	0.149	
	22.26	79.4	0.0741	0.0516	0.529	0.170	0.118
	22.19	73.2	0.0744	0.0540	0.488	0.171	0.124
	22.41	65.2	0.0784	0.0502	0.435	0.180	0.115
	22.34	57.1	0.0850	0.0448	0.381	0.195	0.103
	22.33	48.8	0.0856	0.0430	0.325	0.196	0.099
	22.26	40.8	0.0791	0.0486	0.272	0.181	0.112
	22.43	32.6	0.0714	0.0385	0.217	0.164	0.088
	22.40	24.6	0.0632	0.0388	0.164	0.145	0.089
	22.20	16.4	0.0542	0.0481	0.109	0.124	0.110
	22.19	10.4	0.0561	0.0342	0.069	0.129	0.078
	22.55	6.2	0.0431	0.0331	0.041	0.099	0.076
	22.51	2.3	0.0359	0.0426	0.015	0.082	0.098

APPENDIX E

EXPERIMENTAL DATA - TEMPERATURE MEASUREMENTS

The temperature was measured along a series of vertical sections in an attached buoyant jet. Dimensionless values of mean temperature and the turbulent intensity of temperature fluctuations have been extracted from the data obtained. Profiles of these parameters have been drawn. They are presented in this appendix along with the tabulated data.

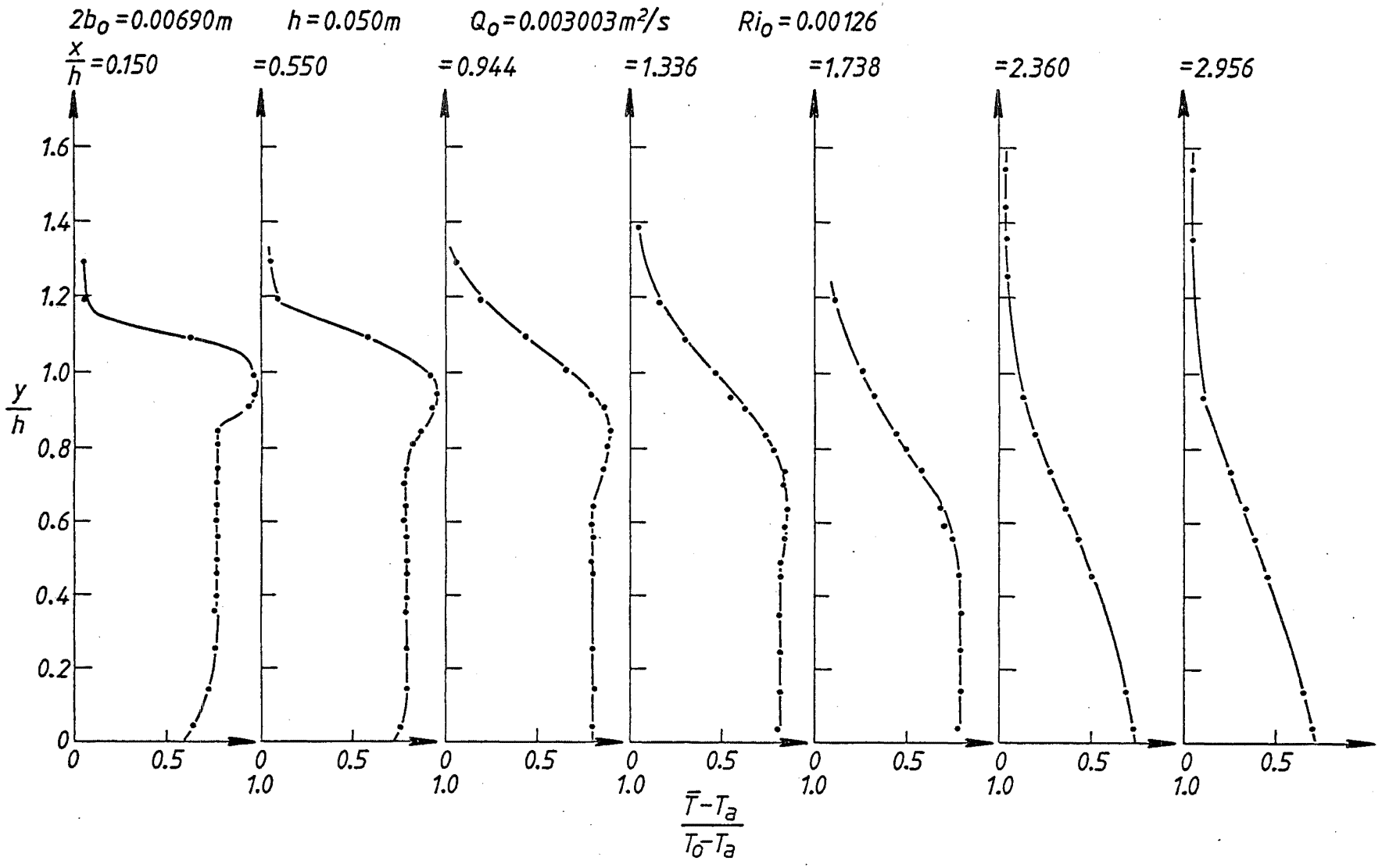

FIGURE E-1 Dimensionless mean temperature data from an attached buoyant jet. h/b_o = 14.5, Re ≃ 4650 and Ri_o = 0.00126.

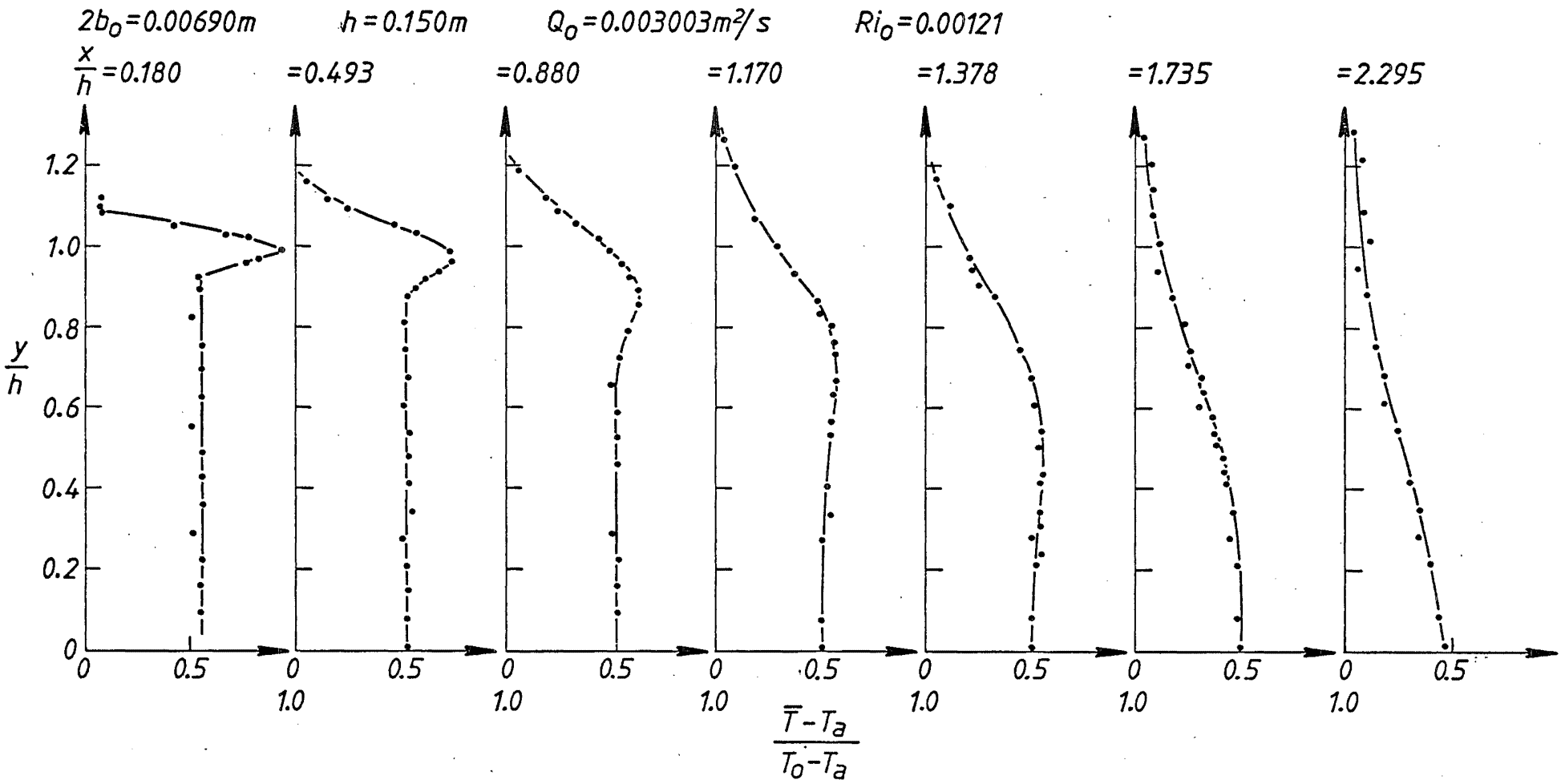

FIGURE E-2 Dimensionless mean temperature data from an attached buoyant jet, $h/b_o = 43.5$, $Re \simeq 4650$ and $Ri_o = 0.00121$.

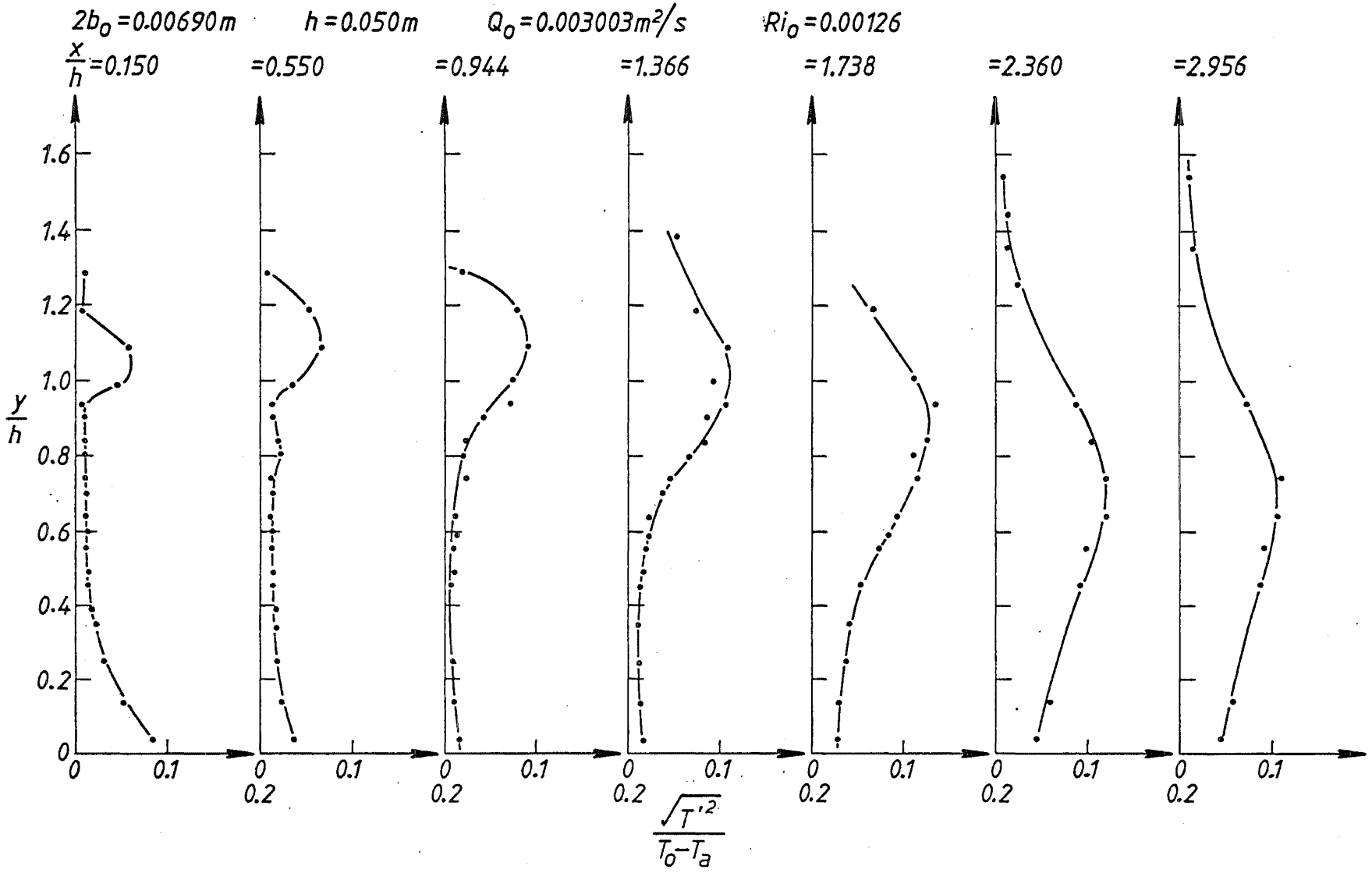

FIGURE E-3 Dimensionless turbulent intensity of temperature fluctuations in an attached buoyant jet. $h/b_o = 14.5$, $Re \simeq 4650$ and $Ri_o = 0.00126$

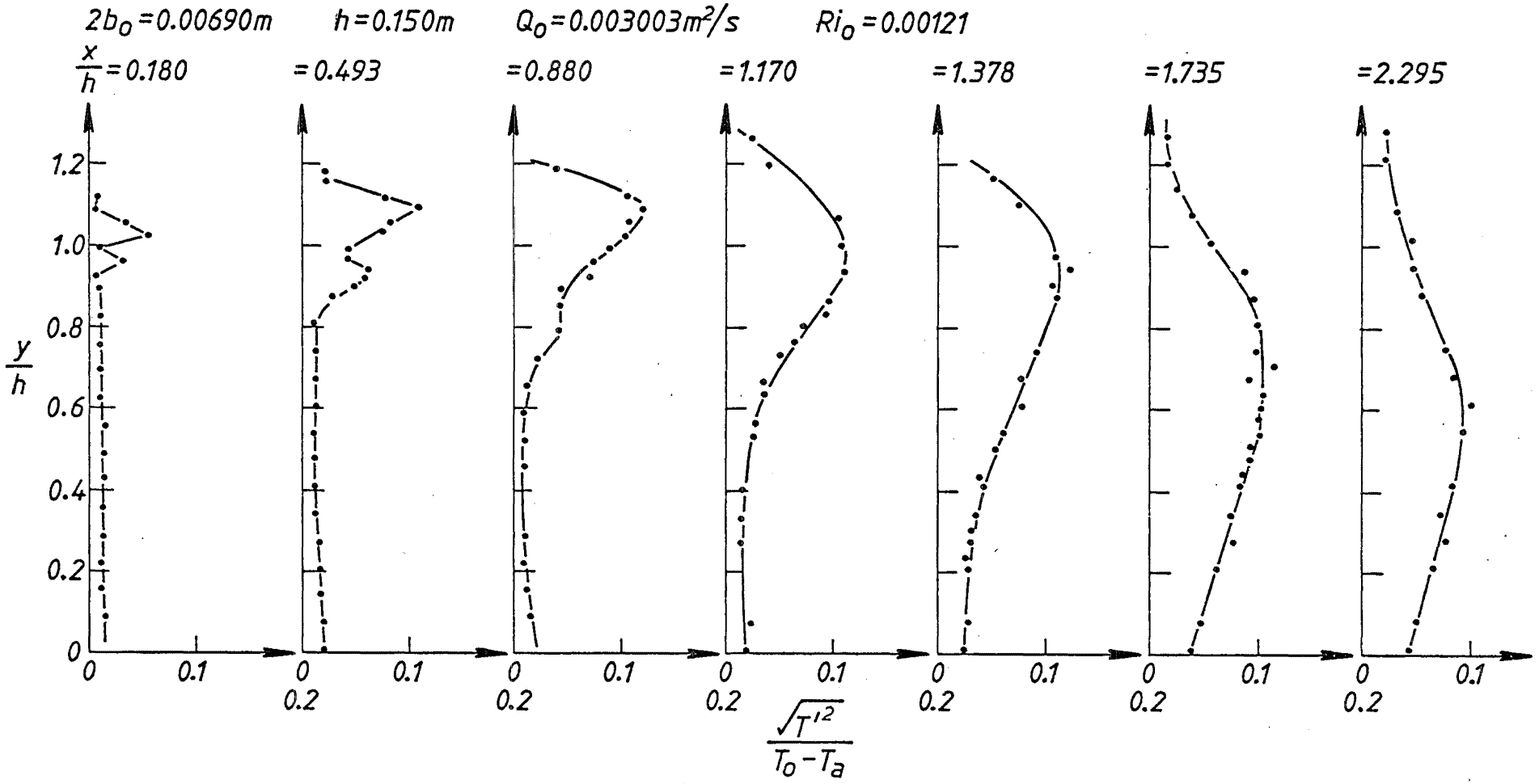

FIGURE E-4 Dimensionless turbulent intensity of temperature fluctuations in an attached buoyant jet. $h/b_o = 43.5$, Re ≃ 4650 and $Ri_o = 0.00121$.

h = 0.050 m

$2b_o$ = 0.00690 m

Q_o = 0.003003 m^2/s

Ri_o = 0.00126

x mm	T_o-T_a °C	y mm	$\bar{T}-T_a$ °C	$\sqrt{\overline{T'^2}}$ °C	$\frac{y}{h}$	$\frac{\bar{T}-T_a}{T_o-T_a}$	$\frac{\sqrt{\overline{T'^2}}}{T_o-T_a}$
7.5	23.38	64.5	1.38	0.25	1.290	0.059	0.011
	23.47	59.5	1.37	0.21	1.190	0.058	0.009
	23.38	54.5	14.74	1.38	1.090	0.630	0.059
	23.47	49.5	22.86	0.11	0.990	0.974	0.005
	23.65	47.0	23.01	0.18	0.940	0.973	0.008
	23.38	45.25	22.11	0.27	0.905	0.946	0.012
	23.47	42.0	18.12	0.30	0.840	0.772	0.013
	23.47	40.25	18.23	0.29	0.805	0.777	0.012
	23.65	37.0	18.38	0.30	0.740	0.777	0.013
	23.38	35.0	17.95	0.33	0.700	0.768	0.014
	23.47	32.0	18.20	0.31	0.640	0.775	0.013
	23.47	30.0	18.08	0.34	0.600	0.770	0.015
	23.65	27.75	18.38	0.34	0.555	0.777	0.014
	23.38	24.5	18.07	0.37	0.490	0.773	0.016
	23.47	22.75	18.12	0.36	0.455	0.772	0.015
	23.47	19.5	18.13	0.41	0.390	0.772	0.018
	23.65	17.5	18.04	0.58	0.350	0.763	0.025
	23.47	12.5	17.58	0.74	0.250	0.749	0.032
	23.65	7.0	17.26	1.26	0.140	0.730	0.053
	23.47	2.0	15.12	2.01	0.040	0.644	0.086
27.5	23.45	64.5	1.31	0.23	1.290	0.056	0.010
	23.49	59.5	2.30	1.26	1.190	0.098	0.054
	23.45	54.5	13.59	1.60	1.090	0.580	0.068
	23.49	49.5	21.58	0.85	0.990	0.919	0.036
	23.60	47.0	22.51	0.32	0.940	0.954	0.014
	23.45	45.25	21.77	0.36	0.905	0.928	0.015
	23.48	42.0	20.41	0.49	0.840	0.869	0.021
	23.49	40.25	19.41	0.55	0.805	0.826	0.024
	23.60	37.0	18.61	0.30	0.740	0.789	0.013

x mm	T_o-T_a °C	y mm	$\bar{T}-T_a$ °C	$\sqrt{T'^2}$ °C	$\frac{y}{h}$	$\frac{\bar{T}-T_a}{T_o-T_a}$	$\frac{\sqrt{T'^2}}{T_o-T_a}$
27.5	23.45	35.0	18.25	0.33	0.700	0.778	0.014
	23.48	32.0	18.54	0.28	0.640	0.789	0.012
	23.49	30.0	18.26	0.35	0.600	0.777	0.015
	23.60	27.75	18.64	0.34	0.555	0.790	0.014
	23.45	24.5	18.42	0.35	0.490	0.786	0.015
	23.48	22.75	18.59	0.32	0.455	0.792	0.014
	23.49	19.5	18.53	0.42	0.390	0.789	0.018
	23.60	17.5	18.49	0.44	0.350	0.783	0.019
	23.48	12.5	18.50	0.45	0.250	0.788	0.019
	23.60	7.0	18.85	0.56	0.140	0.799	0.024
	23.48	2.0	17.80	0.87	0.040	0.758	0.037
47.2	23.32	64.5	1.43	0.45	1.290	0.061	0.019
	23.36	59.5	4.43	1.84	1.190	0.190	0.079
	23.32	54.5	10.22	2.15	1.090	0.438	0.092
	23.36	50.25	15.24	1.76	1.005	0.653	0.075
	23.69	47.0	18.68	1.72	0.940	0.789	0.073
	23.32	45.25	20.07	1.01	0.905	0.860	0.043
	23.47	42.0	21.00	0.56	0.840	0.895	0.024
	23.36	40.0	20.47	0.52	0.800	0.876	0.022
	23.69	37.0	20.29	0.58	0.740	0.856	0.025
	23.47	32.0	18.86	0.31	0.640	0.804	0.013
	23.36	29.5	18.45	0.33	0.590	0.790	0.014
	23.69	27.75	18.98	0.26	0.555	0.801	0.011
	23.32	24.5	18.48	0.28	0.490	0.792	0.012
	23.47	22.75	18.85	0.21	0.455	0.803	0.009
	23.47	12.5	18.77	0.23	0.250	0.800	0.010
	23.69	7.0	19.34	0.24	0.140	0.816	0.010
	23.47	2.0	18.88	0.39	0.040	0.805	0.017
66.8	23.14	69.25	1.01	1.24	1.385	0.044	0.054
	23.14	59.25	3.68	1.74	1.185	0.159	0.075
	23.32	54.5	6.95	2.54	1.090	0.298	0.109
	23.14	50.0	10.71	2.17	1.000	0.463	0.094
	23.40	46.85	12.79	2.50	0.937	0.547	0.107
	23.32	45.25	14.46	2.02	0.905	0.620	0.087
	23.45	41.75	17.17	1.99	0.835	0.732	0.085

x mm	T_o-T_a °C	y mm	$\bar{T}-T_a$ °C	$\sqrt{\overline{T'^2}}$ °C	$\frac{y}{h}$	$\frac{\bar{T}-T_a}{T_o-T_a}$	$\frac{\sqrt{\overline{T'^2}}}{T_o-T_a}$
66.8	23.14	39.75	17.94	1.56	0.795	0.775	0.068
	23.40	36.85	19.69	1.10	0.737	0.841	0.047
	23.32	35.0	19.37	0.91	0.700	0.831	0.039
	23.45	31.75	20.07	0.54	0.635	0.856	0.023
	23.14	29.25	19.40	0.51	0.585	0.838	0.022
	23.40	27.6	19.66	0.45	0.552	0.840	0.019
	23.32	24.5	19.00	0.42	0.490	0.815	0.018
	23.45	22.5	19.24	0.30	0.450	0.820	0.013
	23.40	17.35	19.00	0.27	0.347	0.812	0.012
	23.45	12.25	19.01	0.31	0.245	0.811	0.013
	23.40	6.85	19.16	0.33	0.137	0.819	0.014
	23.45	1.75	18.83	0.40	0.035	0.803	0.017
86.9	23.13	59.5	2.51	1.55	1.190	0.109	0.067
	23.13	50.25	6.03	2.56	1.005	0.261	0.111
	23.64	47.0	7.56	3.20	0.940	0.320	0.135
	23.57	42.0	10.36	3.00	0.840	0.440	0.1273
	23.13	40.0	11.46	2.58	0.800	0.495	0.112
	23.64	37.0	13.64	2.72	0.740	0.577	0.115
	23.57	32.0	15.98	2.21	0.640	0.678	0.094
	23.13	29.5	16.09	1.95	0.590	0.696	0.084
	23.64	27.75	17.49	1.72	0.555	0.740	0.073
	23.57	22.75	18.45	1.27	0.455	0.783	0.054
	23.64	17.5	18.78	0.97	0.350	0.794	0.041
	23.57	12.5	18.60	0.89	0.250	0.789	0.038
	23.64	7.0	18.61	0.68	0.140	0.787	0.029
	23.57	2.0	18.25	0.66	0.040	0.774	0.028
118.0	22.81	77.0	0.58	0.17	1.540	0.025	0.008
	22.65	72.0	0.55	0.26	1.440	0.024	0.012
	22.81	67.75	0.66	0.31	1.355	0.029	0.013
	22.65	62.75	0.76	0.53	1.255	0.033	0.023
	22.81	47.0	2.84	2.01	0.940	0.125	0.088
	22.65	42.0	4.17	2.38	0.840	0.184	0.105
	22.85	37.0	6.42	2.74	0.740	0.281	0.120
	22.83	32.0	8.21	2.77	0.640	0.360	0.121

x mm	T_o-T_a °C	y mm	$\bar{T}-T_a$ °C	$\sqrt{\overline{T'^2}}$ °C	$\frac{y}{h}$	$\frac{\bar{T}-T_a}{T_o-T_a}$	$\frac{\sqrt{\overline{T'^2}}}{T_o-T_a}$
118.0	22.85	27.75	9.68	2.25	0.555	0.424	0.099
	22.83	22.75	11.40	2.11	0.455	0.499	0.093
	22.85	7.0	15.79	1.38	0.140	0.691	0.060
	22.83	2.0	16.63	1.03	0.040	0.728	0.045
147.8	23.05	77.0	0.88	0.24	1.540	0.038	0.010
	23.05	67.75	0.98	0.33	1.355	0.042	0.014
	23.05	47.0	2.35	1.65	0.940	0.102	0.072
	23.25	37.0	5.84	2.56	0.740	0.251	0.110
	23.22	32.0	7.65	2.48	0.640	0.330	0.107
	23.25	27.75	8.87	2.15	0.555	0.382	0.092
	23.22	22.75	10.41	2.05	0.455	0.448	0.088
	23.25	7.0	15.10	1.36	0.140	0.650	0.059
	23.22	2.0	16.17	1.05	0.040	0.697	0.045

h = 0.150 m

$2b_o$ = 0.00690 m

Q_o = 0.003003 m^2/s

Ri_o = 0.00121

x mm	T_o-T_a °C	y mm	$\bar{T}-T_a$ °C	$\sqrt{\overline{T'^2}}$ °C	$\frac{y}{h}$	$\frac{\bar{T}-T_a}{T_o-T_a}$	$\frac{\sqrt{\overline{T'^2}}}{T_o-T_a}$
27.0	23.45	168.15	2.06	0.42	1.121	0.088	0.010
	23.49	164.85	1.92	0.14	1.099	0.082	0.006
	23.47	163.55	2.07	0.16	1.090	0.088	0.007
	23.45	158.15	10.00	1.53	1.054	0.427	0.036
	23.49	154.85	15.89	1.40	1.032	0.676	0.059
	23.49	153.55	18.37	1.33	1.024	0.783	0.057
	23.45	148.9	22.06	0.45	0.993	0.941	0.011
	23.49	145.6	19.50	0.70	0.971	0.830	0.030
	23.47	144.3	18.15	0.78	0.962	0.773	0.033
	23.45	138.65	12.81	0.32	0.924	0.547	0.008
	23.49	135.35	12.82	0.27	0.902	0.546	0.012
	23.47	134.05	12.90	0.26	0.894	0.549	0.011
	23.48	123.55	12.13	0.29	0.824	0.517	0.012
	23.48	113.55	13.29	0.26	0.757	0.566	0.011
	23.48	104.3	13.23	0.26	0.695	0.563	0.011
	23.48	94.05	13.29	0.26	0.627	0.566	0.011
	23.50	83.55	12.07	0.40	0.557	0.514	0.017
	23.50	73.55	13.29	0.35	0.490	0.566	0.015
	23.50	64.3	13.22	0.34	0.429	0.562	0.015
	23.50	54.05	13.31	0.33	0.360	0.567	0.014
	23.63	43.25	12.25	0.34	0.288	0.518	0.014
	23.63	33.25	13.40	0.30	0.222	0.567	0.013
	23.63	24.0	13.19	0.32	0.160	0.558	0.013
	23.63	13.75	13.07	0.38	0.092	0.553	0.016
74.0	23.29	177.75	1.19	0.27	1.185	0.051	0.012
	23.16	174.35	1.32	0.32	1.162	0.057	0.014
	23.29	167.75	3.59	1.85	1.118	0.154	0.079
	23.16	164.35	5.84	2.57	1.096	0.252	0.111

x	T_o-T_a	y	$\bar{T}-T_a$	$\sqrt{T'^2}$	$\frac{y}{h}$	$\frac{\bar{T}-T_a}{T_o-T_a}$	$\frac{\sqrt{T'^2}}{T_o-T_a}$
mm	°C	mm	°C	°C			
74.0	23.29	158.5	11.09	1.95	1.057	0.476	0.084
	23.16	155.1	13.40	1.79	1.034	0.578	0.077
	23.29	148.5	17.18	1.06	0.990	0.738	0.045
	23.16	145.1	17.29	1.01	0.967	0.746	0.044
	23.55	141.1	16.29	1.49	0.940	0.692	0.063
	23.29	138.0	14.41	1.40	0.920	0.619	0.060
	23.16	134.6	13.26	1.16	0.897	0.573	0.050
	23.55	131.1	12.64	0.71	0.874	0.537	0.030
	23.55	121.8	12.29	0.31	0.812	0.522	0.013
	23.55	111.8	12.34	0.33	0.745	0.524	0.014
	23.55	101.3	12.73	0.34	0.675	0.540	0.014
	23.30	91.05	12.16	0.33	0.607	0.522	0.014
	23.30	81.05	12.67	0.28	0.540	0.544	0.012
	23.30	71.8	12.69	0.31	0.479	0.544	0.013
	23.30	61.8	12.68	0.30	0.412	0.544	0.013
	23.30	51.3	13.0	0.30	0.342	0.558	0.013
	23.33	41.25	12.07	0.40	0.275	0.517	0.017
	23.33	31.25	12.53	0.39	0.208	0.537	0.017
	23.33	22.0	12.59	0.42	0.147	0.540	0.018
	23.33	12.0	12.39	0.49	0.080	0.531	0.021
	23.33	1.5	12.45	0.50	0.010	0.534	0.021
132.0	23.35	178.5	1.50	0.94	1.190	0.064	0.040
	23.35	168.5	4.51	2.49	1.123	0.193	0.107
	23.24	163.5	5.77	2.84	1.090	0.248	0.122
	23.35	159.0	7.92	2.54	1.060	0.339	0.109
	23.24	153.5	10.30	2.43	1.023	0.443	0.105
	23.35	149.0	11.62	2.09	0.993	0.498	0.090
	23.24	144.0	12.89	1.75	0.960	0.555	0.075
	23.64	138.5	14.06	1.68	0.923	0.595	0.071
	23.24	134.0	14.81	1.04	0.893	0.637	0.045
	23.64	128.5	15.01	1.05	0.857	0.635	0.044
	23.64	119.0	13.89	1.02	0.793	0.588	0.043
	23.64	109.0	12.90	0.52	0.727	0.546	0.022
	23.46	98.5	11.86	0.29	0.657	0.505	0.013
	23.46	88.5	12.69	0.23	0.590	0.541	0.010

x	T_o-T_a	y	$\bar{T}-T_a$	$\sqrt{\overline{T'^2}}$	$\frac{y}{h}$	$\frac{\bar{T}-T_a}{T_o-T_a}$	$\frac{\sqrt{\overline{T'^2}}}{T_o-T_a}$
mm	°C	mm	°C	°C			
132.0	23.46	79.0	12.54	0.24	0.527	0.534	0.010
	23.46	69.0	12.68	0.23	0.460	0.540	0.010
	23.43	43.5	11.90	0.24	0.290	0.508	0.010
	23.43	33.5	12.80	0.22	0.223	0.546	0.009
	23.43	24.0	12.58	0.29	0.160	0.537	0.012
	23.43	14.0	12.59	0.35	0.093	0.538	0.015
175.5	22.80	190.1	0.91	0.57	1.267	0.040	0.025
	22.80	180.1	1.95	0.93	1.201	0.086	0.041
	22.80	160.6	4.30	2.42	1.071	0.189	0.106
	22.80	150.35	6.77	2.49	1.002	0.297	0.109
	23.15	140.1	8.77	2.60	0.934	0.379	0.112
	23.15	130.1	11.40	2.24	0.867	0.492	0.097
	22.78	125.0	11.45	2.15	0.833	0.502	0.094
	23.15	120.85	12.80	1.70	0.806	0.553	0.073
	22.78	115.0	12.97	1.47	0.767	0.569	0.065
	23.15	110.6	13.28	1.17	0.737	0.574	0.051
	23.15	100.35	13.42	0.82	0.669	0.580	0.036
	22.78	95.5	12.86	0.82	0.637	0.564	0.036
	22.78	85.25	12.69	0.63	0.568	0.557	0.028
	23.34	80.1	12.84	0.60	0.534	0.550	0.026
	23.34	60.6	12.51	0.35	0.404	0.536	0.015
	23.34	50.35	12.84	0.31	0.336	0.550	0.014
	23.28	41.0	11.78	0.33	0.273	0.506	0.014
	23.28	11.5	11.91	0.53	0.077	0.512	0.023
	23.28	1.5	11.88	0.43	0.010	0.510	0.019
206.75	22.80	175.5	1.28	1.16	1.170	0.056	0.051
	22.80	165.5	2.77	1.73	1.103	0.122	0.076
	22.80	146.0	4.82	2.51	0.973	0.211	0.110
	23.32	141.55	5.11	2.89	0.944	0.219	0.124
	22.80	135.75	5.81	2.43	0.905	0.255	0.107
	23.32	131.55	7.78	2.60	0.877	0.334	0.112
	23.32	112.05	10.48	2.15	0.747	0.449	0.092
	23.32	101.55	11.88	1.81	0.677	0.510	0.078
	23.30	91.55	12.13	1.84	0.610	0.521	0.079

x mm	T_o-T_a °C	y mm	$\bar{T}-T_a$ °C	$\sqrt{T'^2}$ °C	$\frac{y}{h}$	$\frac{\bar{T}-T_a}{T_o-T_a}$	$\frac{\sqrt{T'^2}}{T_o-T_a}$
206.75	23.30	81.55	12.91	1.41	0.544	0.554	0.061
	23.10	75.5	12.44	1.21	0.503	0.539	0.053
	23.10	65.5	12.88	0.87	0.437	0.558	0.038
	23.30	62.05	12.83	0.98	0.414	0.550	0.042
	23.30	51.55	12.87	0.81	0.344	0.552	0.035
	23.10	46.0	12.66	0.69	0.307	0.548	0.030
	23.08	41.75	11.77	0.69	0.278	0.510	0.030
	23.10	35.75	12.83	0.60	0.238	0.555	0.026
	23.08	31.75	12.21	0.64	0.212	0.529	0.028
	23.08	12.25	11.74	0.65	0.082	0.509	0.028
	23.08	1.75	11.86	0.56	0.012	0.514	0.024
260.25	23.33	191.15	0.91	0.35	1.274	0.039	0.015
	23.33	181.15	1.71	0.35	1.208	0.073	0.015
	23.33	171.9	2.00	0.59	1.146	0.086	0.025
	23.33	161.9	1.94	0.91	1.079	0.083	0.039
	23.33	151.4	2.74	1.32	1.009	0.117	0.057
	23.17	141.15	2.40	2.03	0.941	0.104	0.088
	23.17	131.15	4.11	2.24	0.874	0.177	0.097
	23.17	121.9	5.30	2.34	0.813	0.229	0.101
	23.17	111.9	5.98	2.29	0.746	0.258	0.099
	23.29	106.15	5.94	2.69	0.708	0.255	0.116
	23.17	101.4	7.22	2.15	0.676	0.312	0.093
	23.29	96.15	7.62	2.47	0.641	0.327	0.106
	23.28	91.15	7.16	2.65	0.608	0.307	0.114
	23.29	86.9	8.63	2.35	0.579	0.371	0.101
	23.28	81.15	8.77	2.36	0.541	0.377	0.102
	23.29	76.9	8.97	2.18	0.513	0.385	0.094
	23.28	71.9	9.90	2.16	0.479	0.425	0.093
	23.29	66.4	9.93	2.01	0.443	0.426	0.087
	23.28	61.9	10.08	1.99	0.413	0.433	0.085
	23.28	51.4	10.97	1.76	0.343	0.471	0.076
	23.39	41.75	10.48	1.82	0.278	0.448	0.078
	23.39	31.75	11.47	1.45	0.212	0.490	0.062
	23.39	12.5	11.51	1.10	0.083	0.492	0.047
	23.39	2.0	11.81	0.89	0.013	0.505	0.038

x mm	T_o-T_a °C	y mm	$\bar{T}-T_a$ °C	$\sqrt{\overline{T'^2}}$ °C	$\frac{y}{h}$	$\frac{\bar{T}-T_a}{T_o-T_a}$	$\frac{\sqrt{\overline{T'^2}}}{T_o-T_a}$
344.25	23.20	193.0	0.87	0.50	1.287	0.037	0.021
	23.20	183.0	1.74	0.49	1.220	0.075	0.021
	23.20	163.5	1.99	0.75	1.090	0.086	0.032
	23.20	153.0	2.70	1.07	1.020	0.117	0.046
	23.31	142.6	1.32	1.10	0.951	0.057	0.047
	23.31	132.6	2.48	1.27	0.884	0.106	0.055
	23.31	113.1	3.35	1.81	0.754	0.144	0.078
	23.31	102.6	4.44	2.00	0.684	0.191	0.086
	22.91	92.6	4.25	2.30	0.617	0.185	0.102
	22.91	82.6	5.69	2.15	0.551	0.248	0.095
	22.91	63.1	6.98	1.91	0.421	0.305	0.085
	22.91	52.6	8.11	1.67	0.351	0.354	0.074
	22.96	42.5	7.99	1.79	0.283	0.348	0.078
	22.96	32.5	9.25	1.52	0.217	0.403	0.066
	22.96	13.0	10.25	1.16	0.087	0.446	0.051
	22.96	2.5	10.90	1.00	0.017	0.475	0.044

APPENDIX F

A CHECK ON THE TWO-DIMENSIONALITY OF THE FLOW

In this study, the two-dimensional jet emerged from a slot nominally measuring 0.140 m x 0.007 m. The flow was subsequently confined by two walls to maintain two-dimensionality. Visual observations with dye confirmed that the flow was approximately two-dimensional. However, at large distances downstream, it was expected that the flow would lose its two-dimensionality.

Some experiments were conducted to check the two-dimensionality of the attaching jet. The mean temperature $\bar{T}$ (x,y,z) and the turbulent intensity of temperature fluctuations $\sqrt{\overline{T'^2}}$ (x,y,z) were measured for different y values across the jet (in the z direction) at some distance beyond the attachment point in the critical case. The origin of the (x,y,z) coordinate system was assumed to coincide with a position midway between the confining walls at the corner of the step. The measurements are shown in Figs. F-1 and F-2. They indicate that the assumption of two-dimensionality across the central portion of the flow is reasonable.

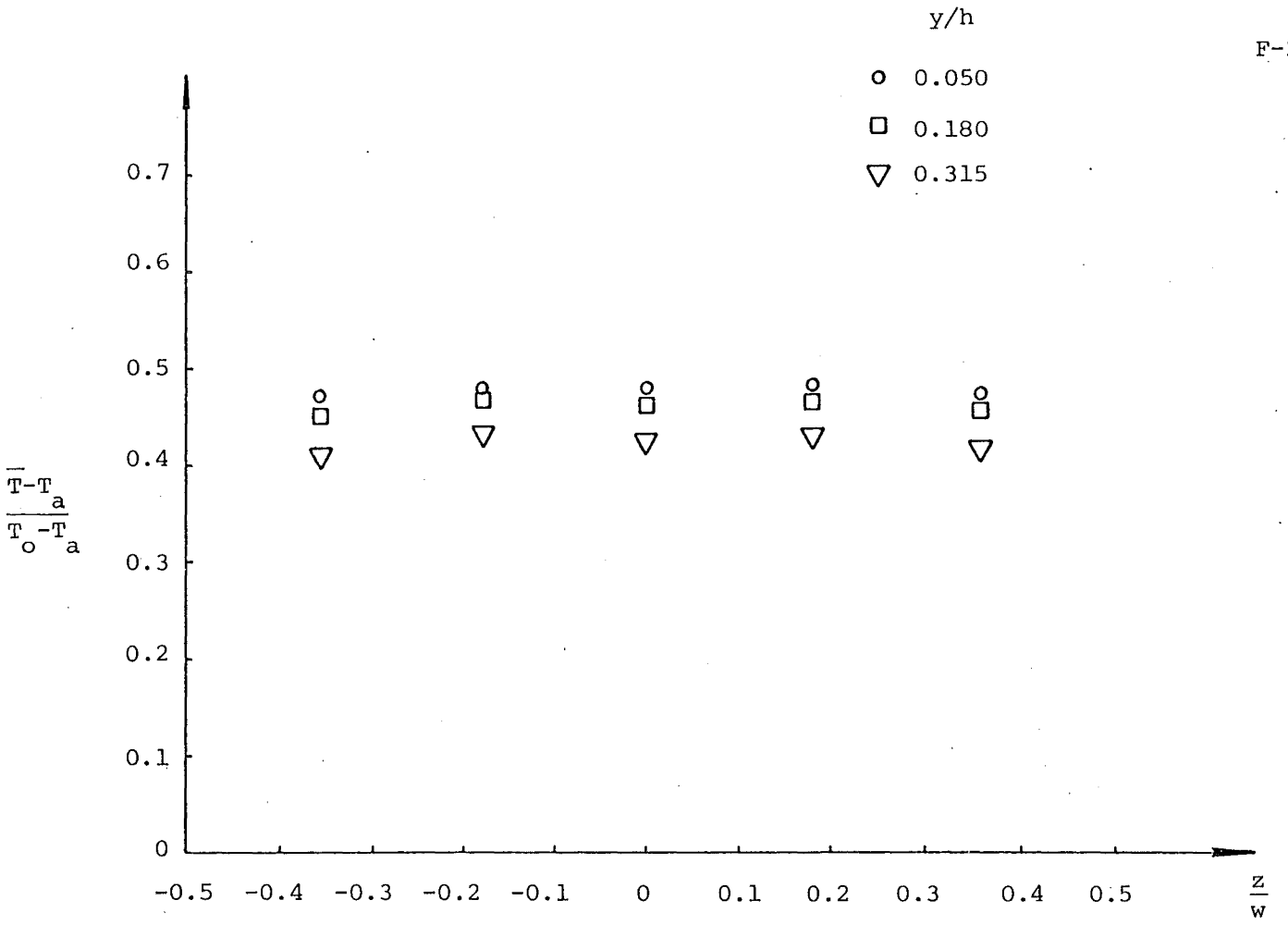

FIGURE F-1 Distribution of mean temperature across the downstream flow. x/h = 1.773.

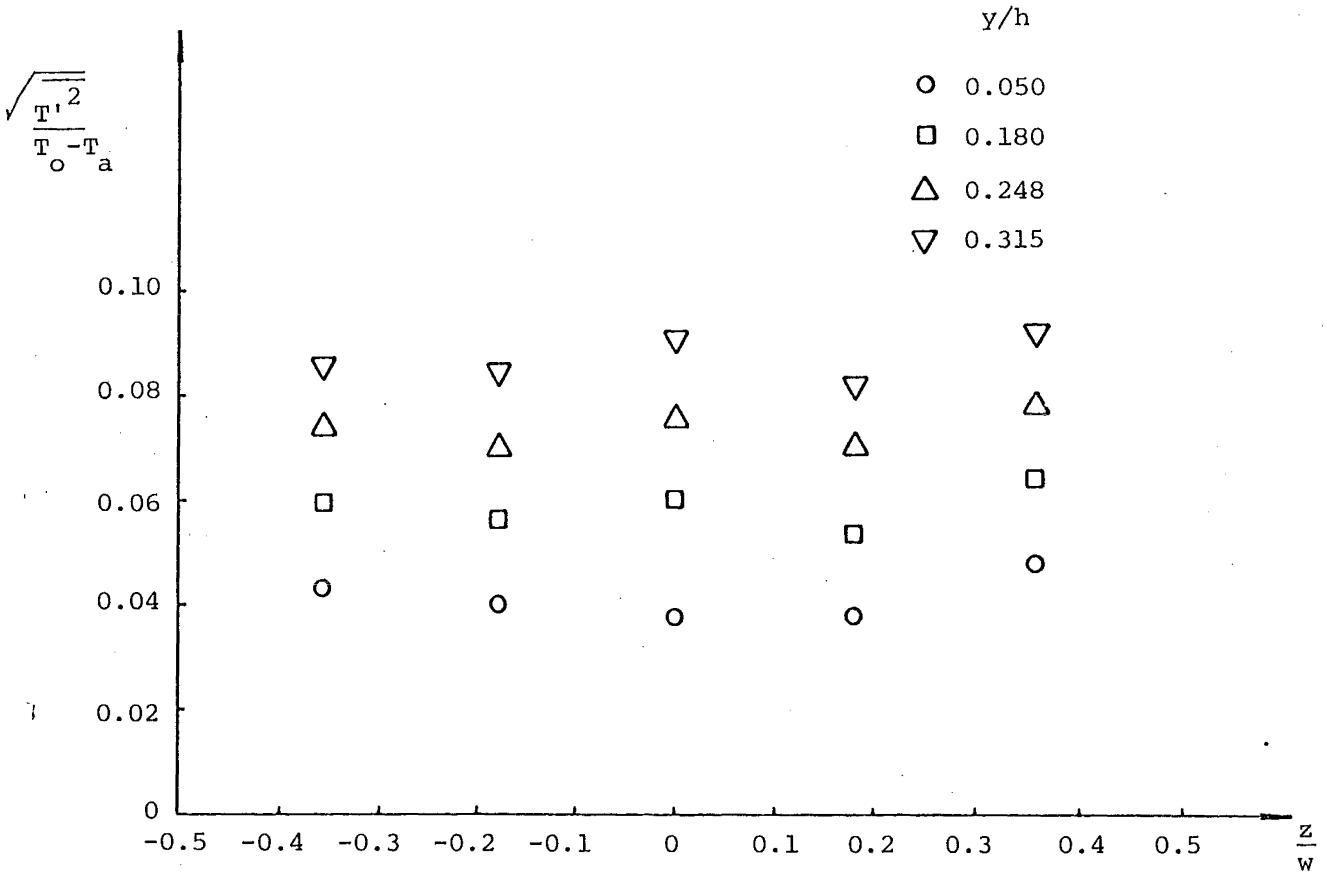

FIGURE F-2 Distribution of turbulent intensity of temperature fluctuations across the downstream flow. x/h = 1.773.

APPENDIX G

SENSITIVITY OF THE ATTACHED NON-BUOYANT JET MODEL TO THE CHOICE OF CERTAIN INPUT PARAMETERS

The attached jet model requires the input of certain empirical parameters. The sensitivity of the model to the choice of these parameters is examined in this appendix.

The effects of curvature on entrainment have been ignored in the model so that a value for the entrainment coefficient can be assumed on the basis of plane jet data. Now it is usual to measure experimentally the rate of spread of momentum in a jet and relate this to the entrainment coefficient. However, a wide range of spreading rates for a plane jet has been reported in the literature and the choice of a suitable entrainment coefficient is still a matter of conjecture.

In the present study, Sawyer's (1963) value of 0.065 for the entrainment coefficient has been assumed. The effect of varying this value has also been considered in view of the disagreement over a "correct" one. The predictions of the attached non-buoyant jet model for various values of entrainment coefficient are shown in Figs. G-1 and G-2. The value of the entrainment coefficient is apparently not critical.

The attached jet model also requires a definition of the inner jet edge. This is necessary for the location of the position at which the attaching jet senses the proximity of the boundary. In this study the edge has been arbitrarily defined as the locus of points for which the mean velocity is 15% of the centreline velocity. The effect of varying this criterion is illustrated by the model predictions in Figs. G-3 and

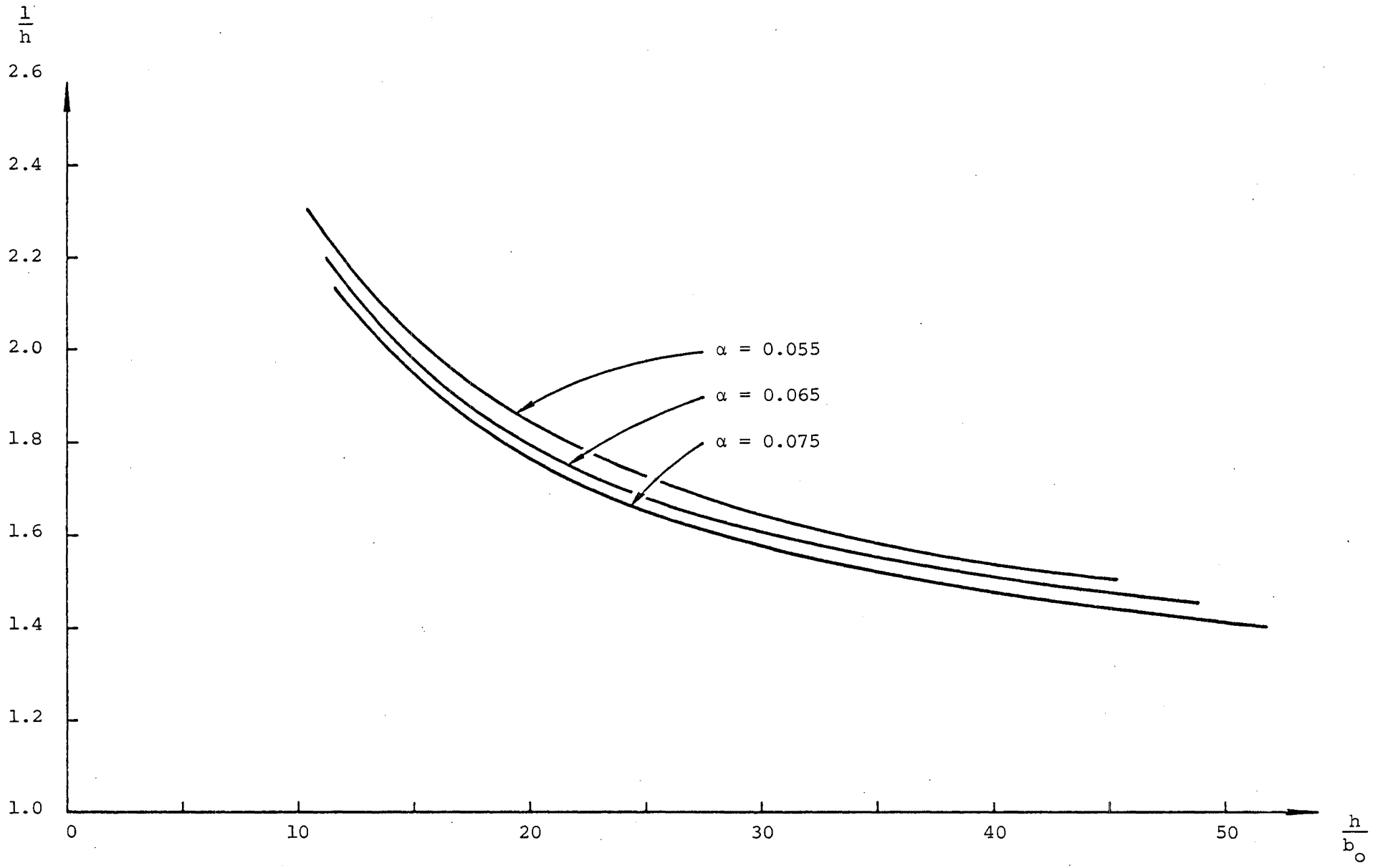

FIGURE G-1 Effect of varying the entrainment coefficient on the eddy geometry.

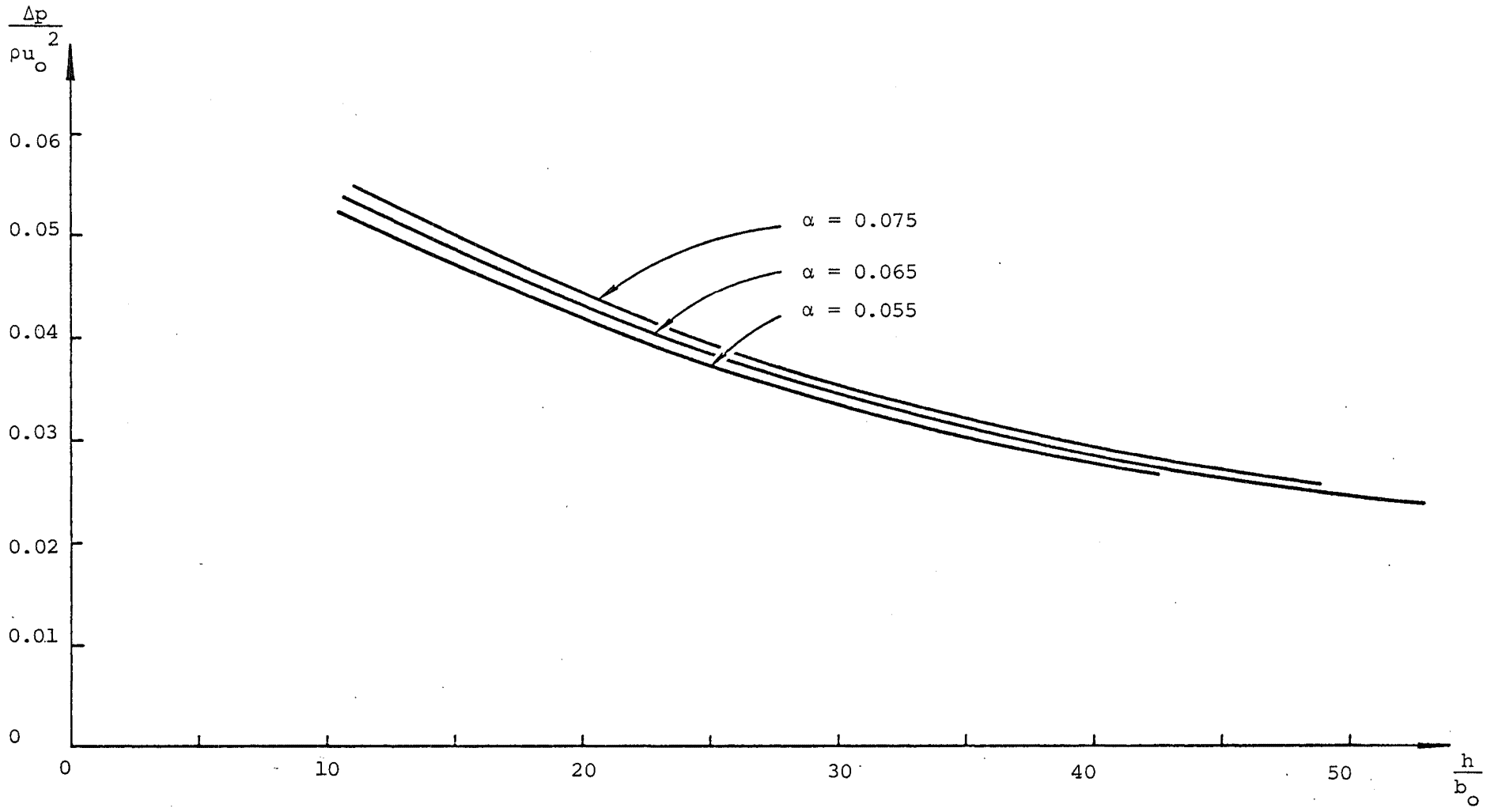

FIGURE G-2 Effect of varying the entrainment coefficient on the average underpressure.

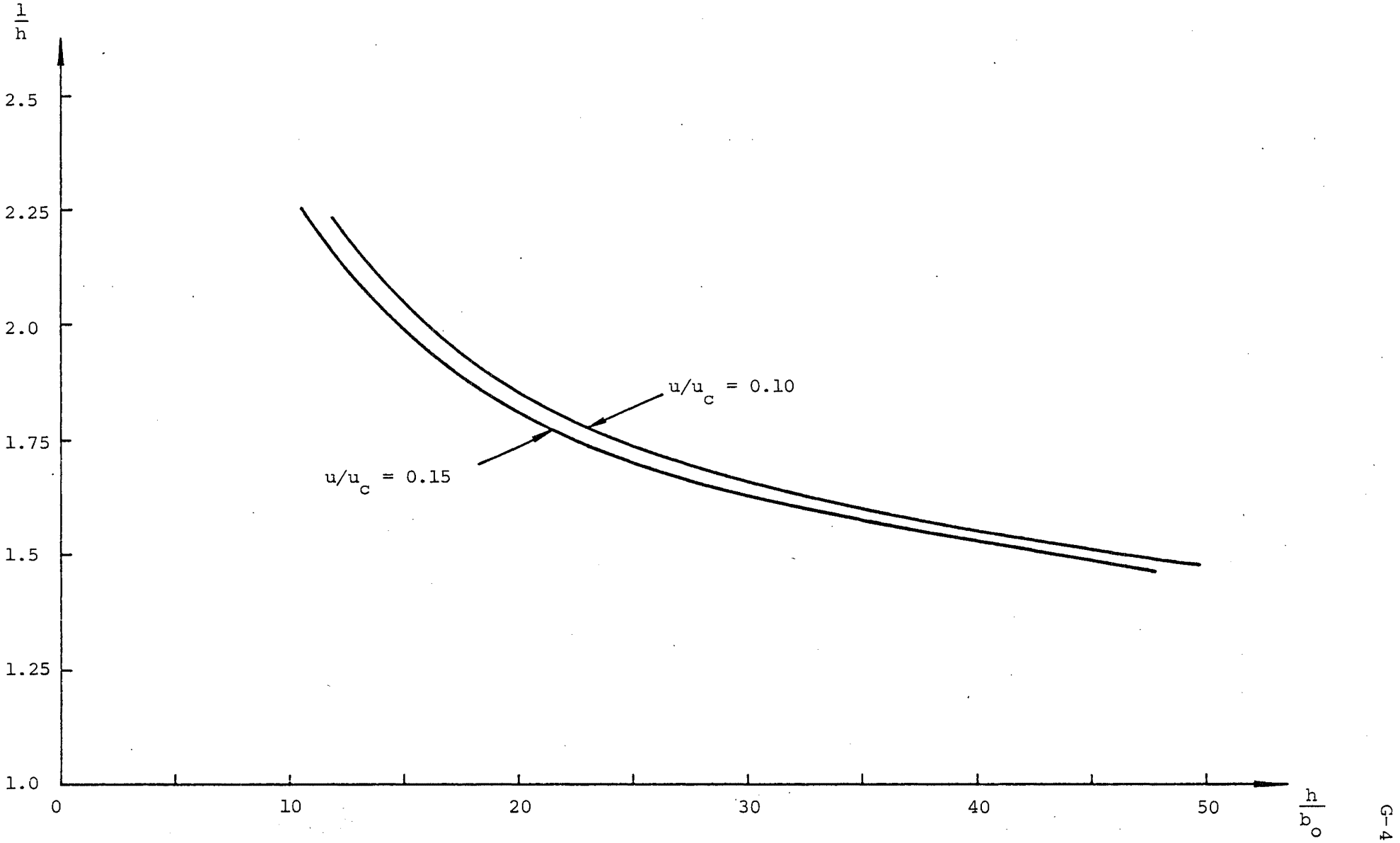

FIGURE G-3 Effect of changing the definition of the inner jet edge on the eddy geometry.

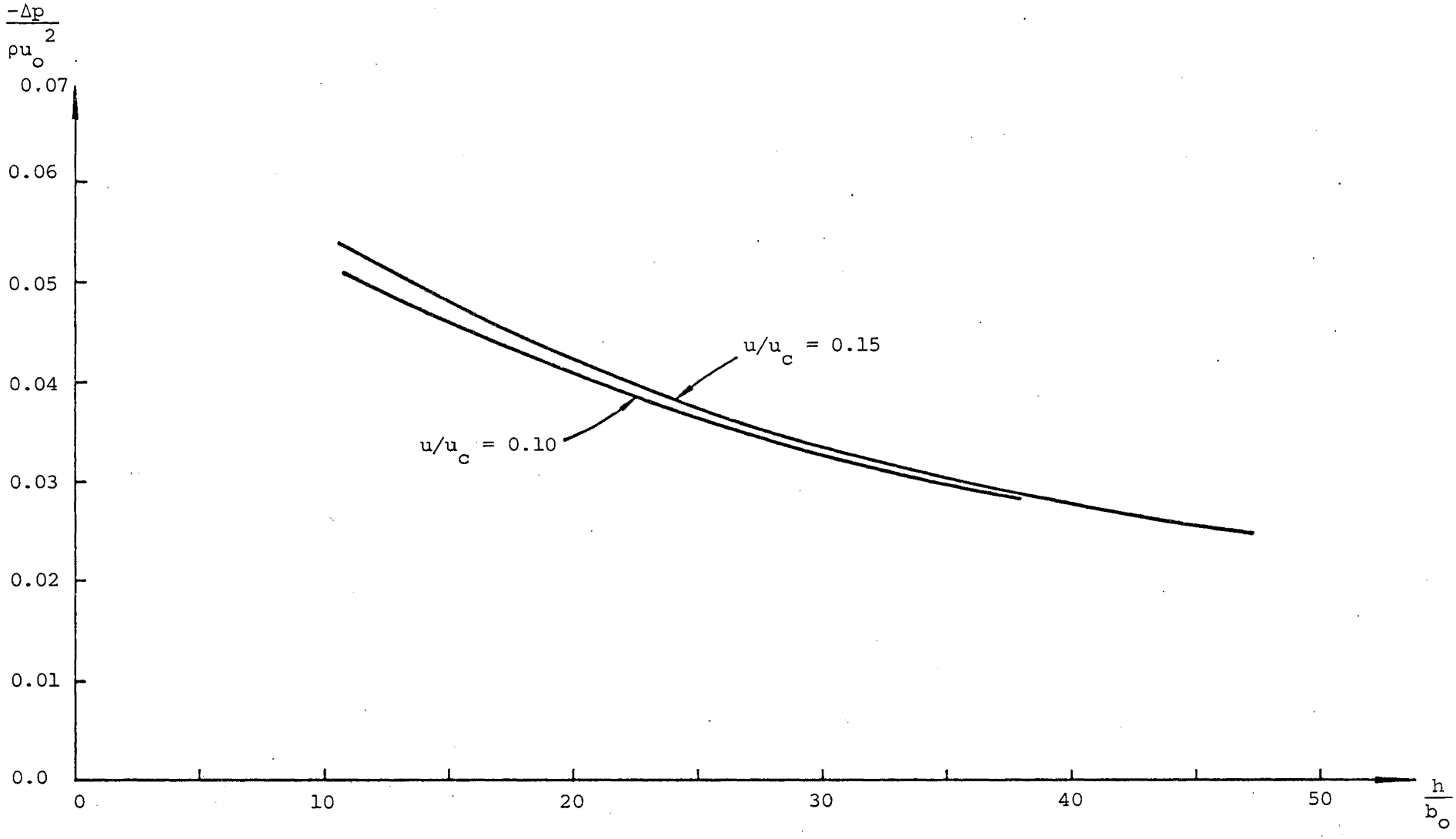

FIGURE G-4 Effect of changing the definition of the inner jet edge on the average underpressure.

G4. The model is seen to be insensitive to the definition of the edge.

The parameter γ_1 defines the growth of the shear layers towards the jet centreline in the initial flow region. The attached non-buoyant jet model is expected to be even less sensitive to the choice of a value for this parameter because the variability of the initial flow region length will be small.

APPENDIX H

COMPUTER PROGRAMME FOR THE ATTACHED BUOYANT JET MODEL

The following list defines the parameters used in the computer programme in terms of those used in the text.

ALPHA	α	GAM1	γ_1
ALPHA	α_i	HEIGHT	h_*
ANE	n_{e_*}	HGT3	V_*/l_{l_*}
ANX	n_{15_*}	LENGTH	l_*
ASPECT	l/h		
BRATIO	b_i/b	PS	Δp_*
B50	b	RI	Ri_o
		S	χ
DRHO	$(\rho_a-\rho_f)/(\rho_a-\rho_o)$	SF	χ_3
ETAE	η_e	SOR	χ_{or}
ETAX	η_{15}	S1	χ_1
F(1)	x_*	S2	χ_2
F(2)	y_*	THETA	δ
F(3)	θ	URATIO	$u/u_c = 0.15$
F(4)	Q_*	VOLUME	V_*
F(5)	M_*		
F(6)	B_*		

```
      DIMENSION F(6),FP(6)
      DIMENSION X(4,16),A(4,16),NP(4),NQ(4),C(4),SUM(4)
      COMMON/BLOCK1/RI,ALPHAI,ALPHA,PS,DRHO,IFLAG2,C6
      COMMON/BLOCK2/DX
      REAL LENGTH
C
C     INPUT PARAMETERS
      N=6
      PI=3.1415927
      ALPHA=0.065
      GAM1=4.8*PI/180.0
      ALPHAI=0.5*TAN(GAM1)
      S2=1.0/TAN(GAM1)
      SOR=S2-(0.75/ALPHA)
      RI=0.001
      IPRIN=50
      URATIO=0.15
      C5=2.0/PI
C
C     CALCULATE SIGMA
      SIG=1.0
      DO 800 I=1,20
      FSIG=COSH(SIG)-SQRT(2.0)
      FPSIG=SINH(SIG)
      DSIG=FSIG/FPSIG
      SIG=SIG-DSIG
  800 IF(ABS(DSIG)..LT.1E-6)GO TO 810
  810 CONTINUE
C
C     CALCULATE DISTANCE S1 DEFINING TRACER POTENTIAL CORE
      S1=S2
C     READ IN PARAMETERS FOR GAUSS-LEGENDRE FORMULA
      DO 820 L=1,4
      READ(5,10)NP(L)

      WRITE(6,20)NP(L)

      C(L)=NP(L)
      NQ(L)=AINT((C(L)/2.0)-0.5)+1
      DO 820 M=1,NP(L)
      IF(M.LE.NQ(L))READ(5,30)X(L,M),A(L,M)
      IF(M.GT.NQ(L))NM=NP(L)-M+1
      IF(M.GT.NQ(L))X(L,M)=-X(L,NM)
      IF(M.GT.NQ(L))A(L,M)=A(L,NM)
  820 WRITE(6,40)X(L,M),A(L,M)
      DO 830 K=1,50
      AMU1=(1.0-S1*TAN(GAM1))/(2.0*ALPHA*(S1-SOR))
      BRATIO=2.0*ALPHA*SIG*(S1-SOR)/
     C(S1*TAN(GAM1)*1.5*SIG)
      CALL LEGEND(X,A,NP,SUM,AMU1,BRATIO)
      WRITE(6,50)(SUM(I),I=1,4)
      FS1=2.0*ALPHA*(S1-SOR)*(ATAN(SINH(AMU1))+SUM(4))-1.0
      FPS1=2.0*ALPHA*(ATAN(SINH(AMU1))+SUM(4))
      DS1=FS1/FPS1
      S1=S1-DS1
  830 IF(ABS(DS1).LT.1E-6)GO TO 840
      STOP
  840 CONTINUE
C
C     WRITE OUT DATA
      WRITE(6,100)ALPHA,GAM1
      WRITE(6,110)S1,SIG
      WRITE(6,120)SOR
```

```
C
C     STARTING VALUES
      SF=20.0
      PS=-0.05
      DRHO=0.75
      HGT3=7.0
C
      DO 600 ITOTAL=1,5
      DO 580 ITER=1,25
      VOLUME=0.0
      IFLAG1=-1
      WRITE(6,190)SF,PS,DRHO
C
C     NON DIMENSIONAL INITIAL CONDITIONS
      S=0.0
      F(1)=0.0
      F(2)=0.0
      F(3)=0.0
      F(4)=1.0
      F(5)=1.0
      F(6)=1.0
      WRITE(6,200)
      WRITE(6,210)S,(F(I),I=1,6)
C
C     JET TRAJECTORY CALCULATIONS 0/S/S3
      IFLAG2=0
      C6=0.25*DRHO*HGT3*RI
  490 INDEX=0
      DS=0.1
      CALL RUNGS(S,DS,N,F,FP,INDEX)
      NCOUNT=0
      YL=ABS(F(2))
  500 CALL RUNGS(S,DS,N,F,FP,INDEX)
      IF(F(3).GT.0.0)STOP
      VOLUME=VOLUME+0.5*DX*(YL+ABS(F(2)))
      YL=ABS(F(2))
      NCOUNT=NCOUNT+1
      IF(NCOUNT.GE.IPRIN)WRITE(6,210)S,(F(I),I=1,6)
      IF(NCOUNT.GE.IPRIN)NCOUNT=0
      IF(S.GT.SF)GO TO 520
      IF(S.GT.S2)GO TO 500
      IF(ABS(S2-S).LT.1E-6)GO TO 510
      IF(S2-S.LT.DS)DS=S2-S
      GO TO 500
  510 WRITE(6,210)S,(F(I),I=1,6)
      IFLAG2=1
      GO TO 490
  520 WRITE(6,210)S,(F(I),I=1,6)
C
      X3=ABS(F(1))
      THETA=ABS(F(3))
      B50=2.0*SIG*F(4)*F(4)/(3.0*F(5))
C
C     CALCULATE POSITION OF INNER EDGE
      ETAX=1.0
      DO 530 J=1,20
      GETAX=(1.0/(COSH(ETAX)*COSH(ETAX)))-URATIO
      GPETAX=-2.0*TANH(ETAX)/(COSH(ETAX)*COSH(ETAX))
      DETAX=GETAX/GPETAX
      ETAX=ETAX-DETAX
  530 IF(ABS(DETAX).LT.1E-6)GO TO 540
```

```
      STOP
  540 ANX=ETAX*B50/SIG
C
C     CALCULATE POSITION OF EDDY STREAMLINE
      CALL STREAM(F(4),ETAE)
      ANE=ETAE*B50/SIG
      WRITE(6,220)URATIO,B50,ANX,ANE
C     CALCULATE HEIGHT OF DISCHARGE ABOVE FLAT PLATE
      HEIGHT=ABS(F(2))+ANX*(1.0+COS(THETA))-ANE
C     CALCULATE THE EQUIVALENT BUOYANCY VOLUME
      VOLUME=HEIGHT*ABS(F(1))-VOLUME
      HGT3=VOLUME/X3
C     CALCULATE NEW ESTIMATE OF PRESSURE DIFFERENCE
      C1=TANH(ETAE)
      PSN=(2.0/HEIGHT)*(1.5*F(5)*(C1-(C1*C1*C1/3.0))-1.0)
      DELTA1=ABS(PSN-PS)
      PS=(PS+PSN)/2.0
      IF(PSN.GT.0.0)STOP
C
C     EXTRAPOLATE JET TRAJECTORY TO FLAT PLATE
      DS=0.1
  550 CALL RUNGS(S,DS,N,F,FP,INDEX)
      CALL STREAM(F(4),ETAE)
      B50=2.0*SIG*F(4)*F(4)/(3.0*F(5))
      ANE=ETAE*B50/SIG
      IF(IFLAG1)560,560,570
  560 DELTA2=HEIGHT-ABS(F(2))-ANE*COS(ABS(F(3)))
      DELTAY=DS*SIN(ABS(F(3)))
      IF(DELTA2.LT.DELTAY.AND.IFLAG1.GE.0)DS=DELTA2/SIN(ABS(F(3)))
      IF(DELTA2.LT.DELTAY.AND.IFLAG1.GE.0)IFLAG1=1
      IF(DELTA2.LE.DELTAY.AND.IFLAG1.LT.0)DS=0.025
      IF(DELTA2.LE.DELTAY.AND.IFLAG1.LT.0)IFLAG1=0
      GO TO 550
  570 HGT2=ABS(F(2))+ANE*COS(ABS(F(3)))
      LENGTH=ABS(F(1))-ANE*SIN(ABS(F(3)))
      ASPECT=LENGTH/HEIGHT
      WRITE(6,230)HEIGHT,HGT2,LENGTH,ASPECT
C
C     CALCULATE NEW ESTIMATE OF DENSITY DEFICIT IN EDDY
      C2=1.0/COSH(-ETAE)
      C3=TANH(-ETAE)
      C4=ATAN(SINH(-ETAE))
      DRHON=(0.5*(1.0-C5*(C2*C3+C4))-1.0)/
     1(0.5*(0.5*F(4)-C5)*(C3-C5*(C4*C3+C2))+
     2C5*(C3-0.5*(C2*C3+C4)))
      DELTA3=ABS(DRHON-DRHO)
      DRHO=(DRHO+DRHON)/2.0
C
C     CONVERGENCE CRITERIA
      PS=PSN
      DRHO=DRHON
  580 IF(DELTA1.LT.1E-5.AND.DELTA3.LT.1E-4)GO TO 590
      STOP
  590 WRITE(6,240)PS,DRHO
C
C     CALCULATE DETACHMENT FACTOR
      FACTOR=RI*HEIGHT*HEIGHT
      WRITE(6,250)VOLUME,FACTOR
  600 SF=SF+5.0
C
   10 FORMAT(I2)
   20 FORMAT('0',T2,'N=',I2)
   30 FORMAT(2E17.10)
   40 FORMAT('0',T2,2E17.10)
   50 FORMAT('0',T2,4E17.10)
  100 FORMAT(/////,1X,'ENTRAINMENT COEFFICIENT FOR FULLY DEVELOPED REGIO
```

```
     1N ASSUMED TO BE ',F6.4,//,1X,'ANGLE GAMMA1 DEFINING EDGE OF VELOCI
     2TY POTENTIAL CORE ASSUMED TO BE',F9.6)
  110 FORMAT('0','LENGTH OF CONCENTRATION POTENTIAL CORE IS',F9.6,
     1//,1X,'SIGMA HAS VALUE',F9.6)
  120 FORMAT('0','POSITION OF VIRTUAL ORIGIN IS ',F9.6)
  190 FORMAT(/////,1X,'CENTRELINE DISTANCE TO WHERE JET SENSES PLATE IS'
     1,F9.5,//,1X,'AVERAGE UNDER PRESSURE IS ',F8.5,//,1X,'DENSITY DEFIC
     2IT IN EDDY IS ',F6.4)
  200 FORMAT('0',T6,'S',T16,'X',T26,'Y',T36,'THETA',T46,'VOL',T56,'MOM',
     1T66,'BUOY')
  210 FORMAT('0',7F10.5)
  220 FORMAT('0','FOR URATIO OF ',F4.2,1X,'AND B50 OF ',F8.5,2X,
     1'ANX IS ',F8.5,//,1X,'ANE IS ',F8.5)
  230 FORMAT('0','STEP HEIGHT IS ',F8.5,5X,'CHECK ',F8.5,//,1X,'EDDY LEN
     1GTH IS ',F9.5,//,1X,'ASPECT RATIO IS ',F7.5)
  240 FORMAT('0','FINAL UNDER PRESSURE IS ',F8.5,//,1X,
     1'FINAL EDDY DENSITY DEFICIT IS ',F6.4)
  250 FORMAT('0','EDDY VOLUME IS ',F7.2,//,1X,'DETACHMENT FACTOR IS ',F7
     1.5)
C
      END
```

```
C
      SUBROUTINE LEGEND(X,A,NP,SUM,AMU1,BRATIO)
      DIMENSION X(4,16),A(4,16),NP(4),SUM(4),F(16),U(16),P(16)
C
      DO 10 I=1,4
      SUM(I)=0.0
      DO 10 K=1,NP(I)
      U(K)=(X(I,K)+1.0)/2.0
      P(K)=2.0*(U(K)**BRATIO)/(1.0+(U(K)**(2.0*BRATIO)))
      F(K)=(1.0/(EXP(AMU1)+U(K)*U(K)*EXP(-AMU1)))*P(K)*P(K)
   10 SUM(I)=SUM(I)+A(I,K)*F(K)
      RETURN
      END
```

```
C
      SUBROUTINE RUNGS(X,H,N,Y,YPRIME,INDEX)
C
C     RUNGS - RUNGE - KUTTA SOLUTION OF SET OF FIRST ORDER O.D.E. FORTRA
C     N II
C     DIMENSIONS MUST BE SET FOR EACH PROGRAM
C     X    INDEPENDENT VARIABLE
C     H    INCREMENT DELTA X, MAY BE CHANGED IN VALUE
C     N    NUMBER OF EQUATIONS
C     Y    DEPENDENT VARIABLE BLOCK     ONE DIMENSIONAL ARRAY
C     YPRIME  DERIVATIVE BLOCK  ONE DIMENSIONAL ARRAY
C     THE PROGRAMMER MUST SUPPLY INITIAL VALUES OF Y(1) TO Y(N)
C     INDEX IS A VARIABLE WHICH SHOULD BE SET TO ZERO BEFORE EACH
C     INITIAL ENTRY TO THE SUBROUTINE, I.E., TO SOLVE A DIFFERENT
C     SET OF EQUATIONS OR TO START WITH NEW INITIAL CONDITIONS.
C     THE PROGRAMMER MUST WRITE A SUBROUTINE CALLED DERIVE WHICH COM-
C     PUTES THE DERIVATIVES AND STORES THEM
C     THE ARGUMENT LIST IS SUBROUTINE DERIVE(X,N,Y,YPRIME)
C
      DIMENSION Y(6),YPRIME(6),Z(6),W1(6),W2(6),W3(6),W4(6)
      COMMON/BLOCK2/DX
C
      IF (INDEX)5,5,1
    1 DO 2 I=1,N
      W1(I)=H*YPRIME(I)
    2 Z(I)=Y(I)+(W1(I)*.5)
      A=X+H/2.
      CALL DERIVE(A,N,Z,YPRIME)
      DO 3 I=1,N
      W2(I)=H*YPRIME(I)
    3 Z(I)=Y(I)+.5*W2(I)
      A=X+H/2.
      CALL DERIVE(A,N,Z,YPRIME)
      DO 4 I=1,N
      W3(I)=H*YPRIME(I)
    4 Z(I)=Y(I)+W3(I)
      A=X+H
      CALL DERIVE (A,N,Z,YPRIME)
      DO 7 I=1,N
      W4(I)=H*YPRIME(I)
      IF(I.EQ.1)DX=(2.0*(W2(I)+W3(I))+W1(I)+W4(I))/6.0
    7 Y(I)=Y(I)+(((2.*(W2(I)+W3(I)))+W1(I)+W4(I))/6.)
      X=X+H
      CALL DERIVE (X,N,Y,YPRIME)
      GO TO 6
    5 CALL DERIVE (X,N,Y,YPRIME)
      INDEX=1
    6 RETURN
      END
```

```
C
      SUBROUTINE STREAM(FLUX,ETAE)
C
      ETAE=0.0
      DO 10 I=1,20
      GETAE=FLUX*TANH(ETAE)-1.0
      GPETAE=FLUX*(COSH(ETAE)*COSH(ETAE))
      DETAE=GETAE/GPETAE
      ETAE=ETAE-DETAE
   10 IF(ABS(DETAE).LT.1E-6)GO TO 20
      STOP
   20 RETURN
      END
```

```
C
      SUBROUTINE DERIVE(X,N,Y,YP)
C
      DIMENSION Y(6),YP(6)
      COMMON/BLOCK1/RI,ALPHAI,ALPHA,PS,DRHO,IFLAG,C2
C
      YP(1)=COS(Y(3))
      YP(2)=SIN(Y(3))
      IF(IFLAG)10,10,20
   10 ALPHA2=ALPHAI+1.5*C2*SIN(Y(3))
      YP(3)=(0.5*PS+C2*COS(Y(3)))/Y(5)
      YP(4)=ALPHA2
      YP(5)=C2*SIN(Y(3))
      YP(6)=0.5*ALPHA2*DRHO
      RETURN
   20 C1=C2+RI*Y(4)*(2.0*Y(6)-DRHO*Y(4))/(3.0*Y(5))
      YP(3)=(0.5*PS+C1*COS(Y(3)))/Y(5)
      YP(4)=1.5*ALPHA*Y(5)/Y(4)
      YP(5)=C1*SIN(Y(3))
      YP(6)=0.75*ALPHA*DRHO*Y(5)/Y(4)
      RETURN
      END
```